Hybrid methods of space radiation shielding for astronauts against deep-space radiation

by

Rajarshi Pal Chowdhury

M.Tech., Indian Institute of Technology Kanpur, 2013

M.S., Missouri S & T, 2016

AN ABSTRACT OF A DISSERTATION

submitted in partial fulfillment of the
requirements for the degree

DOCTOR OF PHILOSOPHY

Alan Levin Department of Mechanical and Nuclear Engineering
Carl R. Ice College of Engineering

KANSAS STATE UNIVERSITY
Manhattan, Kansas

2020

Abstract

Protecting astronauts against the harsh radiation environment of space is one of the major hurdles to human presence in space in the twenty-first century. Future exploration class missions to the Moon and Mars will require a long-duration presence of astronauts in space outside of the protective barrier of the Earth's atmosphere and geomagnetic field. Space radiation outside of the protection of Earth is a complex hybrid environment of highly energetic and heavy charged cosmic ions and energetic protons generated as a result of solar activity.

It was established in previous studies that conventional radiation shielding methods that use materials to slow down and fragment the heavy charged ions are incapable of protecting per NASA's career space radiation limit, for deep-space, long-term missions. Therefore, other strategies must be used to shield astronauts on long-duration space missions adequately.

Electrostatic radiation shielding, in which an electrostatic field is used to deflect charged particles, was investigated as an alternative by various researchers. All prior investigations concluded that the magnitude of potentials needed to generate a field that can provide significant protection is beyond the reach of present-day technology.

In this work, a set of configurations for electrostatic radiation shielding was investigated. This work proposes a novel concept of using multiple conductors of lower-magnitude electric field and repetitively arranging them in three-dimensional space to generate a cumulative electric field, which, together with passive shielding, can provide significant protection. Multiple combinations of such configurations were identified. A set of optimized electrostatic settings and passive shielding materials were used to characterize shielding efficacy against deep-space radiation.

Hybrid methods of space radiation shielding for astronauts against deep-space radiation

by

Rajarshi Pal Chowdhury

M.Tech., Indian Institute of Technology Kanpur, 2013

M.S., Missouri S & T, 2016

A DISSERTATION

submitted in partial fulfillment of the
requirements for the degree

DOCTOR OF PHILOSOPHY

Alan Levin Department of Mechanical and Nuclear Engineering
Carl R. Ice College of Engineering

KANSAS STATE UNIVERSITY
Manhattan, Kansas

2020

Approved by:

Major Professor
Amir A. Bahadori

Copyright

© Rajarshi Pal Chowdhury 2020.

Table of Contents

List of Figures x

List of Tables xvi

Acknowledgements xviii

Dedication xix

1 Introduction and Background 1

1.1 Motivation 1

1.1.1 Organization of the Dissertation 3

1.2 Types of Space Radiation 4

1.2.1 Trapped Radiation 4

1.2.2 Solar Energetic Particles 5

1.2.3 Galactic Cosmic Rays 8

1.3 Radiation Dosimetry Concepts 13

1.3.1 Stopping Power 13

1.3.2 Linear Energy Transfer 15

1.3.3 Absorbed Dose 15

1.3.4 Dose Equivalent 16

1.3.5 Effective Dose 16

1.3.6 RBE-weighted Dose 18

1.4 Space Radiation Dosimetry and Concept of Risk 20

1.4.1 Risks Associated with Space Radiation 20

1.4.2 Exposure Guidelines Relevant to Space Radiation 21
1.4.3 Brief History of Cohorts and the Dosimetry Models 22
1.4.4 Radiation Risk Model Concepts 23
1.4.5 BEIR VII Models 25
1.4.6 UNSCEAR Model 27
1.4.7 Risk of Exposure Induced Cancer and Death 27
1.4.8 NASA Space Cancer Risk Code (NSCR)-2012 Model 28
1.5 Radiation Transport Tools 29
1.5.1 Stochastic Radiation Transport Methods 29
1.5.2 Deterministic Radiation Transport Methods 30
1.5.3 Active Shielding Transport Tool 33
1.6 Radiation Shielding Methods 36
1.6.1 Passive Radiation Shielding Methods 36
1.6.2 Active methods of radiation shielding 39
1.6.3 Comparative Analysis of Different Active Shielding Methodologies . . 45

2 Population-based Approach to Astronaut Radiation Risk Assessment 49
2.1 Motivation 49
2.1.1 Ethics in Space Radiation Protection 50
2.1.2 Study Scope and Purpose 52
2.2 Methods 53
2.2.1 Representation of Astronaut Corps Reference Population 53
2.2.2 Space Missions Addressed in the Present Work 54
2.2.3 Space Radiation Environments 55
2.2.4 Computational Phantoms and Vehicle Shielding 55
2.2.5 Radiation Transport and Dosimetry 56
2.2.6 Risk Assessment 57
2.3 Results 57

2.3.1 Analysis of Different Fitting Methods . . . 57
2.3.2 Low Earth Orbit and Cis-Lunar Missions . . . 58
2.3.3 Mars Missions . . . 59
2.3.4 Age-specific vs. Population-combined REID Distributions . . . 60
2.4 Discussion . . . 61
2.4.1 Analysis of Different Fitting Methods . . . 61
2.4.2 Low Earth Orbit and Cis-Lunar Missions . . . 62
2.4.3 Mars Missions . . . 63
2.5 Summary . . . 65

3 Formulation of Scaling Law for Beam-like Configuration . . . 68
3.1 Motivation . . . 68
3.2 Hypothesis . . . 69
3.2.1 Source Configuration . . . 71
3.3 Simulation Geometry . . . 73
3.4 Simulation Domain . . . 73
3.4.1 Radiation Transport . . . 75
3.5 Image Processing Algorithm . . . 76
3.5.1 Simulation Tools . . . 77
3.6 Results . . . 78
3.6.1 Scaling Law for Accelerator-based Parameters . . . 78
3.6.2 Scaling Law for Space-based Parameters . . . 80
3.6.3 Scaling Law for Combined Parameters . . . 81
3.6.4 Comparison of Protected Area . . . 82
3.6.5 Explanation for the Knee Region . . . 84
3.7 Summary . . . 85

4 Evolution of 3-D Electrostatic Radiation Shielding Configurations . . . 88

4.1 Simulation Geometry . . . 89
4.2 Computing Flux Reduction . . . 90
4.3 Simulation Strategy . . . 91
4.4 Dipole Configuration . . . 92
4.5 Multi-pole configuration . . . 93
4.6 Monopole Configuration . . . 94
4.7 Multi-layered Spherical Configuration . . . 96
4.8 3-D Charged Array Configuration . . . 99
4.8.1 Effect of Addition of Layers . . . 104
4.8.2 3-D Charged Arrays with Shifted Layers . . . 106
4.8.3 3-D Stacked Array-Cubic Configuration . . . 106
4.8.4 3-D Stacked Spherical Sector Configurations . . . 106
4.8.5 3-D Charged Arrays with Extended Negative Points . . . 108
4.8.6 3-D Stacked Arrays with Isolated Negative Charges Placed on Diagonal 110
4.8.7 Relative Performance Analysis of the Configurations Tested . . . 111
4.8.8 Charged Plane and Line Configuration . . . 113
4.9 Formulation of 3-D Configuration Scaling Law . . . 114
4.10 Summary . . . 123

5 Hybrid Methods of Radiation Shielding against an Extreme SPE . . . 127
5.1 Motivation . . . 127
5.2 Description of Electrostatic Field Configurations . . . 128
5.3 Proton Angular Distribution . . . 131
5.4 Hybrid Shielding Configurations . . . 133
5.5 Ion Scaling . . . 139
5.5.1 Surface Charge Density Scaling . . . 140
5.6 Passive Radiation Transport . . . 142
5.6.1 Description of the Computational Phantoms . . . 143

5.6.2 Active-Passive Configuration . . . 143
5.6.3 Passive-Active Configuration . . . 143
5.6.4 Passive-Active-Passive Configuration . . . 144
5.6.5 Computation of Effective Dose . . . 144
5.7 Results . . . 145
5.8 Summary . . . 149

6 Hybrid Methods of Radiation Shielding against GCRs . . . 155
6.1 Motivation . . . 155
6.2 Description of Hybrid Shielding Configuration . . . 156
6.3 Methods . . . 158
6.4 Results . . . 160
6.5 Summary . . . 162

7 Conclusions and Future Work . . . 169

Bibliography . . . 174

List of Figures

1.1 Different layers of the Sun, from Ref. [1] 5

1.2 Fluence spectra for historically significant SPEs [2, 3] 7

1.3 Flux density of significant ions in case of solar minimum (solid line) and maximum (dashed line) conditions [2, 3] 9

1.4 Relationship between SSN and solar modulation parameter, from Ref. [4] . . 13

1.5 Quality factor as a function of LET for different publications of ICRP, from Ref. [5, 6] 17

1.6 Electrostatic shielding configuration using 6-sphere and 3-toroid configuration, from Ref. [7] 46

1.7 Shielding performance comparison between 12-sphere and 6-sphere-3-toroid configuration, from Ref. [7] 47

2.1 Comparison of different fitting methods for 900-day Mars mission in solar minimum and solar maximum boundary conditions. 58

2.2 REID for male and female astronauts for 1-year space mission at ISS Airlock in solar minimum condition. 59

2.3 REID for male and female astronaut for 1-year space mission at ISS Airlock in solar maximum condition. 60

2.4 Combined risk for the Astronaut Corp for Different Space missions. 61

2.5 Risk profile for male and female astronauts for 900-day Mars mission in solar minimum condition. 62

2.6 Risk profile for male and female astronauts for 900-day Mars mission at solar maximum condition. 63

2.7 REID probability density functions for 30-year-old male, 60-year-old female, and combined population for 900-day Mars mission at solar maximum conditions. 64
2.8 Organ-specific REID for 30-year-old male, 60-year-old female, and combined population for 900-day Mars mission at solar maximum conditions. 65
2.9 Organ-specific REID for 60-year-old male, 30-year-old female and combined population for 900-day Mars mission at solar maximum conditions. 66
2.10 Organ-specific REID for astronaut corps males, astronaut corps females, and combined population for 900-day Mars mission at solar maximum conditions. 67

3.1 Shape of the protected area below knee region 71
3.2 Shape of the protected area above knee region 72
3.3 Coordinate system and schematic for all simulations 73
3.4 1-D Scaling law with $\ell_{DD} = 1.2\,\mathrm{m}$ for accelerator-based energies. 79
3.5 Validation of 1-D Scaling law with $\ell_{DD} = 2.2\,\mathrm{m}$ for accelerator-based energies. 80
3.6 1-D Scaling law with Dipole to Detector Distance equal to 10 m for space-based energies. 82
3.7 1-D Scaling law with Dipole to Detector Distance equal to 100 m for space-based energies. 83
3.8 1-D Scaling law with Dipole to Detector Distance equal to 400 m for space-based energies. 84
3.9 Comparison of Scaling law for accelerator-based and space-based parameters for Dipole to Detector distance equal to 1.2 m and charged sphere diameter 0.2 inch. 85
3.10 Comparison of protected area for two different sizes of charges sphere conductor for all ions where dipole-detector distance equal to 10 m. 86

4.1 Source Geometry for 3-D radiation transport, after Ref. [8] 89

4.2 Distribution of dipoles over a spherical surface using Thomson's algorithm ($N = 400$, $R_0 = 400$ m) 94
4.3 Distribution of quadrupoles over a spherical surface using Thomson's algorithm ($N = 400$, $R_0 = 400$ m) 95
4.4 Distribution of sextupoles over a spherical surface using Thomson's algorithm ($N = 400$, $R_0 = 400$ m) 96
4.5 Distribution of monopoles over a spherical surface using Thomson's algorithm ($N = 400$, $R_0 = 400$ m) 97
4.6 Example of charge distribution for multi-layered spherical geometry 99
4.7 Single layer charged array configuration 101
4.8 3-D charged array configuration with multiple stacked 2D arrays 102
4.9 Distribution of negative charge points within a 2D charged array 103
4.10 Cubic Configuration 107
4.11 Stacked Spherical Sector Arrays 108
4.12 3-D charged Array Configuration with laterally extended negative points . . 109
4.13 3-D charged Array Configuration with extended negative points 110
4.14 Stacked Arrays with Negative Diagonal 111
4.15 Electric field plot for 3-D stacked array configuration 114
4.16 Electric field plot for cubic configuration 115
4.17 Electric field plot for 3-D stacked arrays with extended negative points . . . 116
4.18 Electric field plot for 3-D stacked arrays with negative diagonals 117
4.19 3-D electrostatic shielding configuration with charged planes and rods 118
4.20 3-D scaling parameter for plane-rod combination (with three planes) without distance scaling 119
4.21 3-D scaling parameter for plane-rod combination (with three planes) with distance scaling 120

4.22 3-D scaling parameter for plane-rod combination (with three planes) without a normalized gap (G) scaling . . . 121
4.23 3-D scaling parameter for plane-rod combination (with three planes) with normalized gap (G) scaling . . . 122
4.24 3-D scaling parameter for plane-rod combination (with three planes) without normalized distance to the proximal plane (d_{pos}) scaling . . . 123
4.25 3-D scaling parameter for plane-rod combination (with 3 planes) with normalized distance to the proximal plane (d_{pos}) scaling . . . 124
4.26 3-D scaling parameter for plane-rod combination (with three planes) with basic scaling . . . 125
4.27 3-D scaling parameter for plane-rod combination (with three planes) with updated 3-D scaling law . . . 126

5.1 3-D electrostatic shielding configuration with charged planes and rods . . . 128
5.2 Flux density reduction factor for protons for different active shielding configurations . . . 130
5.3 Unshielded and shielded proton fluence spectra . . . 132
5.4 Degree of angular reduction in 10×10 angular bin for 50 MeV proton in Configuration 3 . . . 133
5.5 Degree of angular reduction in 10×10 angular bin for 100 MeV proton in Configuration 3 . . . 134
5.6 Degree of angular reduction in 10×10 angular bin for 200 MeV proton in Configuration 3 . . . 135
5.7 Degree of angular reduction in 10×10 angular bin for 500 MeV proton in Configuration 3 . . . 136
5.8 Passive shielding configuration . . . 137
5.9 Hybrid Active-Passive configuration . . . 137
5.10 Hybrid Passive-Active configuration . . . 138

5.11 Hybrid Passive-Active-Passive configuration 138
5.12 Flux density reduction factor for different GCR ions without scaling 140
5.13 Flux density reduction factor for different GCR ions with scaling 141
5.14 Flux density reduction factor normalized with the surface charge density . . 142
5.15 Comparison of organ dose equivalent for different important female organs (part 1) 146
5.16 Comparison of organ dose equivalent for different important female organs (part 2) 147
5.17 Comparison of organ dose equivalent for different important male organs (part 1) 148
5.18 Comparison of organ dose equivalent for different important male organs (part 2) 149
5.19 Comparison of tissue effects for different organs under different shielding for female (lightly shielded) 150
5.20 Comparison of tissue effects for different organs under different shielding for female (heavily shielded) 151
5.21 Comparison of tissue effects for different organs under different shielding for male (lightly shielded) 152
5.22 Comparison of tissue effects for different organs under different shielding for male (heavily shielded) 153
5.23 Comparison of effective dose for all the tested shielding configurations for male and female 154

6.1 Flux density reduction factor for protons for different active shielding configurations relevant for GCR 157
6.2 Validation of Method 2 in terms of annual organ-specific dose equivalent for solar minimum conditions for female 159

6.3 Validation of Method 2 in terms of annual organ-specific dose equivalent for solar minimum conditions for male 160
6.4 Organ dose equivalent for different important organs for female for GCR solar minimum annual exposure 161
6.5 Organ dose equivalent for different important organs for male for GCR solar minimum annual exposure 162
6.6 Organ dose equivalent for different important organs for female for GCR solar maximum annual exposure 163
6.7 Organ dose equivalent for different important organs for male for GCR solar maximum annual exposure 164
6.8 Effective dose for different configurations for GCR solar minimum conditions 165
6.9 Effective dose for different configurations for GCR solar maximum conditions 166
6.10 Contribution of different particles towards the total effective dose for female computational phantom in solar minimum condition for different shielding configurations 167
6.11 Contribution of different particles towards the total effective dose for male computational phantom in solar minimum condition for different shielding configurations 168

List of Tables

1.1 Fractional Contribution (f) of each element in GCR at solar minimum, after Ref. [9] . . . 10

1.2 Model parameters used for BON2014, after Ref. [4] . . . 12

1.3 Tissue weighting factors from recent ICRP publications, after Ref. [6, 10] . . . 18

1.4 RBE values for different types of radiation, after Ref. [11] . . . 19

1.5 Parameter values for NASA solid cancer and leukemia . . . 20

1.6 Dose and RBE-weighted dose limits for short-term and career non-cancer effects (mGy-Eq or mGy, where specified), after Ref. [11] . . . 22

1.7 E fective dose to reach 3% REID for never-smoker population, after Ref. [12] 22

1.8 NSCR-2012 models for site-specific risk models, after Ref. [12] . . . 29

1.9 Relative Contribution (%) to effective dose from different energy and charge groups without any passive shielding, after Ref. [13] . . . 37

1.10 Relative Contribution (%) to effective dose equivalent from different energy and charge groups behind 20 g cm^{-2} of aluminum passive shielding, after Ref. [13] . . . 38

1.11 Effective dose equivalent for different incidence conditions and passive shielding, after Ref. [12] . . . 38

3.1 Accelerator-based parameter space . . . 75

3.2 Space-based parameter space. . . . 75

3.3 The knee-values for different accelerator- and space-based parameters . . . 79

4.1 Names and corresponding symbols of the parameters that have been used for the 3-D electrostatic field configuration optimization . . . 92

4.2 Flux reduction values for spherical electrostatic configuration using monopoles 97

4.3 Flux reduction values for multi-layer spherical configuration using monopoles 100

4.4 Flux density reduction results three different negative charge distributions for 200 MeV protons in case of 3-D stacked configuration where the intra-node gap (G) was fixed at 7.5 m and the the array span was 30 m × 30 m with q_+ = 0.005 C, q_- = −26.25 mC, S = 7.5 m, R_1 = 22.5 m, and N_p = 5 103

4.5 Flux reduction results for 200 MeV protons in case of 3-D stacked configuration where the intra-node gap (G) was 20 m and array span was 80 m × 80 m, S = 20 m 104

4.6 Flux reduction results for 200 MeV protons in case of 3-D stacked configuration where the intra-node gap (G) was 10 m and array span was 40 m × 40 m, S = 10 m 104

4.7 Flux reduction results for 200 MeV protons in case of 3-D stacked configuration where the intra-node gap (G) was 7.5 m and array span was 30 m × 30 m, R_1 = 22.5 m, N_p =5, S = 7.5 m 105

4.8 Flux reduction results for 200 MeV protons in case of 3-D stacked configuration where the intra-node gap (G) was fixed at 7.5 m and the the array span was 30 m × 30 m, S = 7.5 m, R_1 = 22.5 m, and Q = 3.15 C 105

4.9 Flux reduction results for 200 MeV protons in case of 3-D cubic configuration where the intra-node gap (G) was fixed at 20 m, N = 456 107

4.10 Flux reduction results for 200 MeV protons in case of 3-D stacked configuration with extended negative nodes (figure 4.12) where nodes were stacked on each side of a cube with each 2D charged array being 5 × 5 in size. N = 750, R_0 = 60 m, and N_p = 5. 109

4.11 Flux reduction results for 200 MeV protons in case of 3D stacked hyperbolic configuration where each 2D charged array was of size 7x7 and each positive point was 5 m from each other while negative charges were placed along a diagonal far from the stacked arrays (Figure 4.14). In this configuration, each diagonal was placed from 35 m to 173 m from the origin along a diagonal. N = 1248, R_1 = 20 m, N_p = 4. The span of each 2D array was 30 m × 30 m . 112

4.12 Relative performance analysis of different configurations 113

4.13 Parameter space for the charged plane and rod configuration studies 119

5.1 Parameter space for the charged plane and rod configuration studies 129

5.2 Tissue weights for NASA 2010 model for never smokers, after Ref. [12] . . . 145

6.1 Parameter space for the charged plane and rod configuration studies 156

Acknowledgments

I would first express my sincere gratitude to my advisor and mentor, Prof. Amir Bahadori, for allowing me to work with him on space radiation protection and shielding research. I learned a lot from his advising and his way of addressing a difficult problem, which will help me further in my career and in my life. I thank him for thinking me worthy of working on the NASA project, from which I gained substantial experience.

I would also like to thank Dr. Dan Fry, the principal investigator of the project and a member of my dissertation committee. He gave me valuable knowledge and first-hand experience working in a laboratory facility. I appreciate the opportunity to go to Brookhaven National Laboratory to conduct research and meet with world-class scientists and technicians.

I would thank Prof. Roberts for sharing his experience in scientific computation methods and the parallelization of codes. I would like to also thank him for letting me use his computational nodes on Beocat for my simulations.

I would also thank Mr. Luke Stegeman for his help in making codes for the active shielding project, which helped me obtain results faster. Also, I thank him for being always helpful in my research, for being a good colleague, and for being the best travel partner for the last three years. I would also like to thank my other colleagues, Mike Pfeifer, Rabab Elzohery, and Ye Cheng for meaningful discussions and their help in research.

I express my full gratitude to my parents, my sister and her family, friends, and my girlfriend Chandrima for being helpful, understanding, and supportive in my work and personal life.

I would finally like to acknowledge that the presented work is supported in part by the NASA Human Health and Performance Contract NNJ15HK11B.

Dedication

Dedicated to my mother, Mrs. Himani Pal Chowdhury, my father, Mr. Ranjan Pal Chowdhury, and my sister Mrs. Reshmi Bhattacharya for their immense sacrifices and hard work which helped me to the reach where I am today.

Chapter 1

Introduction and Background

1.1 Motivation

In December 2017, the president of the United States, Donald J. Trump, signed the Space Policy Directive-1 (SPD-1) [14]. This policy created a pathway for the NASA administrator to implement strategies that would bring back crewed missions to different locations in the solar system with the combined efforts of the Federal Government and the private sector. SPD-1 boosted the United States' approach towards making crewed missions a priority in the near future.

It is vital to know the potential challenges of space travels to determine its future. NASA has identified space radiation as one of the primary roadblocks for future exploration missions [15]. The risks associated with space radiation are assigned the highest priority. Mitigation of space radiation risks is complicated by two factors: the first is the uncertainties associated with extrapolation methods of risk computation from databases available for terrestrial radiation, which are qualitatively and quantitatively different from space radiation, and the second is the lack of effective radiation shielding methods to protect against the highly energetic, chronic background space radiation. A proper understanding of free-space radiation and the radiation environment behind various types of shielding, along with radiobiological effects on the human body, is also required to understand and mitigate the risk of space

radiation. The radiation environment in deep space mainly consists of two components: 1) random bursts of energetic particles (mostly protons) generated by solar activity and 2) the low flux density but highly energetic charged ions that originate from outside the heliosphere. Trapped particle radiation is encountered in Earth's vicinity and is thus a minor contributor for missions beyond Earth orbit.

The nature of space radiation is unique compared to any other terrestrial radiation, and the data on the effects of this radiation on human bodies are incredibly sparse. To date, only the exposure data for 24 astronauts for a 12-day mission outside of the lower-Earth orbit (LEO) environment are available [16]. Because radiation exposure data in deep space are sparse, space radiation risk models rely on exposure data from terrestrial radiation, which may have different biophysical effects compared to radiation encountered in space.

Because space radiation risk assessment is based on mathematical models, and there are significant uncertainties associated with these models, an essential focus of space radiation protection is lowering astronaut exposure. As enumerated by the International Committee on Radiological Protection (ICRP), the principles of radiation protection are justification, optimization, and limitation [5]. Space missions are essential for the progress of science, technology, and engineering, and have great importance in terms of national pride; thus, they are justified. The optimization method follows the 'As low as reasonably achievable' (ALARA) principle by focusing on mitigating the risk due to space radiation exposure. ALARA is often implemented via three methods: 1) increasing the distance from the source, 2) reducing exposure time, and 3) increasing shielding. It is practically impossible to increase the distance from the mostly isotropic space radiation, so the last two principles of ALARA are of prime importance. The United States Nuclear Regulatory Commission (USNRC) has specified the limit of 50 mSv per year for radiation workers [17]. The National Aeronautics and Space Act of 1958 [18] gives NASA the right to set its regulation limits. Based on this act, NASA has set the regulation limit of career-integrated 3% excess risk of mortality at the upper 95% tolerance interval [19]. The NASA space permissible exposure limits (SPEL) differ from the limits of terrestrial radiation workers and can be altered based on the requirement of the mission, especially for exploration missions (long-term). In addition to the mortality

risk, there are regulations in place to restrict doses to prevent tissue reactions, as described later in this chapter [19].

It has been shown in previous studies that conventional radiation shielding methods that use materials such as polyethylene or aluminum are incapable of providing sufficient protection against the highly energetic and heavy charged (HZE) ion component that poses the greatest threat on deep-space missions [13, 20]. The mass shielding needs to be increased to reduce the radiation risk below the regulated limit [19]. The increased mass penalty surpasses the launch constraints specified by NASA [21, 22]. Therefore, an alternative solution is required to resolve this issue.

1.1.1 Organization of the Dissertation

Chapter 1 of this dissertation contains background information regarding types of space radiation, relevant dosimetric quantities, the risks associated with space radiation, regulation of space radiations, and types of space radiation transport and shielding methodologies. Chapter 2 describes the risks associated with male and female astronauts of different ages for various space missions and a novel method of computing population-based risk. Chapter 2 also demonstrates why an improved space radiation shielding system is required to lower the accumulated risk over a long-term deep space mission. Chapter 3 establishes the simulation framework and mathematical foundation of the one-dimensional (1-D) scaling law in a beam-like facility. Chapter 4 discusses different three-dimensional (3-D) active shielding configurations in detail and shows the evolution to the best performing current configuration. Chapters 5 and 6 demonstrate the effect of hybrid shielding on extreme case solar particle events (SPEs) and galactic cosmic rays (GCRs), respectively. Finally, Chapter 7 discusses the conclusions and limitations of this work and also identifies future work that should be performed.

1.2 Types of Space Radiation

To understand space radiation risk, one must first understand different categories of space radiation. Space radiation is generally categorized as: 1) geomagnetically trapped radiation; 2) solar energetic particles (SEPs); and 3) galactic cosmic rays (GCRs). The high energy SEP and GCR components are of primary concern for deep-space radiation shielding. In this section, these three components are discussed in details.

1.2.1 Trapped Radiation

Trapped radiation consists of charged particles that get trapped near Earth due to the presence of the geomagnetic field. Trapped radiation is formed when charged particles interact with the magnetopause region of the Earth and slow down due to the presence of the magnetic field [23]. Each particle then rotates at a certain gyro-radius based on its rigidity [24]. The other source of trapped radiation is when HZE ions outside of LEO collide with Earth's atmosphere and generate secondary radiation. These secondary radiations then get trapped due to the magnetic field. Due to the fragmentation of HZE ions, neutrons are generated. Neutrons further decay to create protons and electrons that get trapped in the near-Earth environment. Trapped radiation can be a concern for LEO missions such as missions to the International Space Station (ISS) due to the presence of South Atlantic Anomaly (SAA) [**?**]. This radiation can impact humans and sensitive electronics on spacecraft [25]. It has been estimated that of the total dose equivalent on ISS that is incurred by astronauts, almost half is contributed by trapped radiation in LEO [26]. Earth's radiation belts consist of these hazardous radiations, which can create problems for space missions. The electrons are generally found in the outer belt because they have a greater gyro-radius, whereas protons are found in the inner belt because of their smaller gyro-radius. The energy of protons in the trapped radiation environment can exceed 500 MeV, whereas the energy of electrons can exceed 20 MeV [27]. Trapped radiation is a concern for missions involving substantial time in Earth orbit. For deep-space missions, trapped radiation exposure is neglected since the majority of the risk results from SEPs and GCRs. Therefore, for most of this work, trapped

radiation is not addressed.

1.2.2 Solar Energetic Particles

The Sun is the nearest star to Earth and is the energy source that life on Earth requires. The source of the Sun's energy is thermo-nuclear fusion reactions. Due to the Sun's large mass and gravity, a sufficiently large gravitational pull restricts charged particle escape and provides the pressure sufficient to maintain the thermo-nuclear reactions among charged nuclei [23]. The Sun's atmosphere can be divided into three parts from the center of the Sun outward, as shown in Figure 1.1.

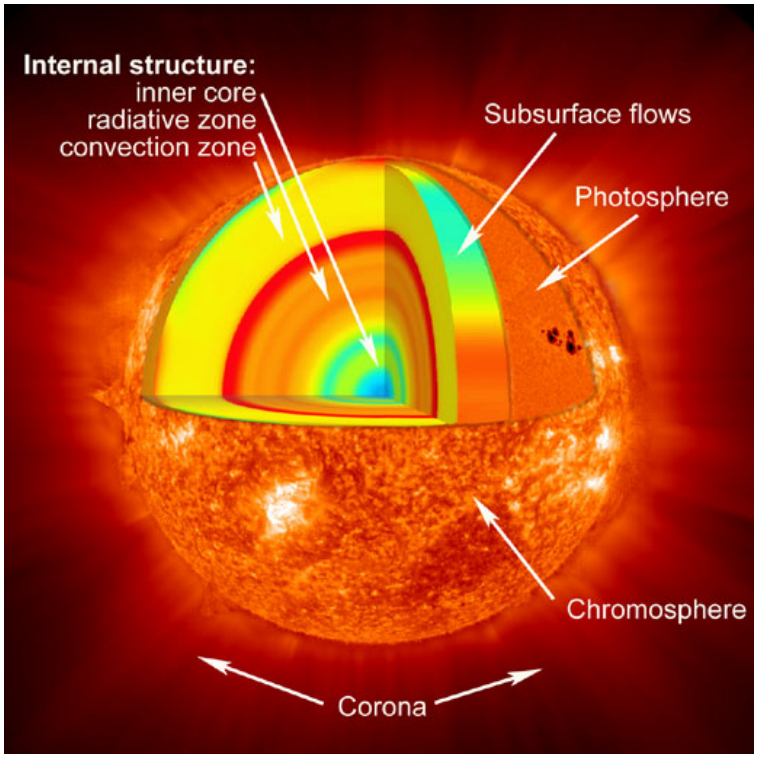

Figure 1.1: Different layers of the Sun, from Ref. [1]

Solar wind consists of highly energetic protons and electrons emitted from the corona layer of the Sun. They are emitted at a very high speed in the interplanetary region due to the supersonic expansion of the plasmas located in the corona region.

SPEs are time-integrated spectra of SEPs. Based on the definition of the National

Oceanic and Atmospheric Administration (NOAA), an SPE occurs when solar proton angular flux density equals or exceeds the value of $10\,\mathrm{cm^{-2}\,s^{-1}\,sr^{-1}}$ at energy equal to or higher than 10 MeV [28]. SPEs can be differentiated into multiple categories, from minor to extreme, based on the intensity and hardness of the fluence spectra. SPEs can be detected on Earth when sufficiently energetic protons collide with the atmosphere and create secondary neutrons that can be sensed by the neutron monitors that are located at some specific locations on the ground. These events are known as Ground Level Enhancements (GLEs). GLEs are rare, and the probability of occurrence is less than one per solar cycle (around 11 years) [29]. They are essential from the point of view of radiation shield design [30]. Most SPEs are limited to a maximum proton kinetic energy of a few hundred MeVs, but sometimes the maximum proton kinetic energy with substantial fluence can exceed a few GeVs [29, 31]. SEPs originate either via magnetic reconnection events during solar flaring or emissions from the corona [32]. SPEs associated with magnetic reconnection events tend to be smaller and impulsive, but SPEs related to coronal mass ejections (CMEs) tend to be large and gradual. The second type of SPE is usually more dangerous for the protection of astronauts and sensitive space electronics. CME driven events generally accelerate interplanetary (IP) shock waves that can accelerate other charged particles in space and thereby can cause more damage in comparison to impulsive events where the damage can only occur if the observer is directly located along magnetic field lines connecting the observer to the Sun. Gradual events have more longitudinal spread compared to impulsive events [29].

There are some historically significant SPEs which could have caused significant exposure to astronauts. Examples of such historically significant SPEs include those of February 1956, August 1972, and October 1989. From a dosimetric point of view, the October 1989 SPE is considered the most important as it had a significant fluence spectrum at energies that can penetrate conventional passive radiation shielding [30]. Spectra for these SPEs are shown in Figure 1.2 [2, 3].

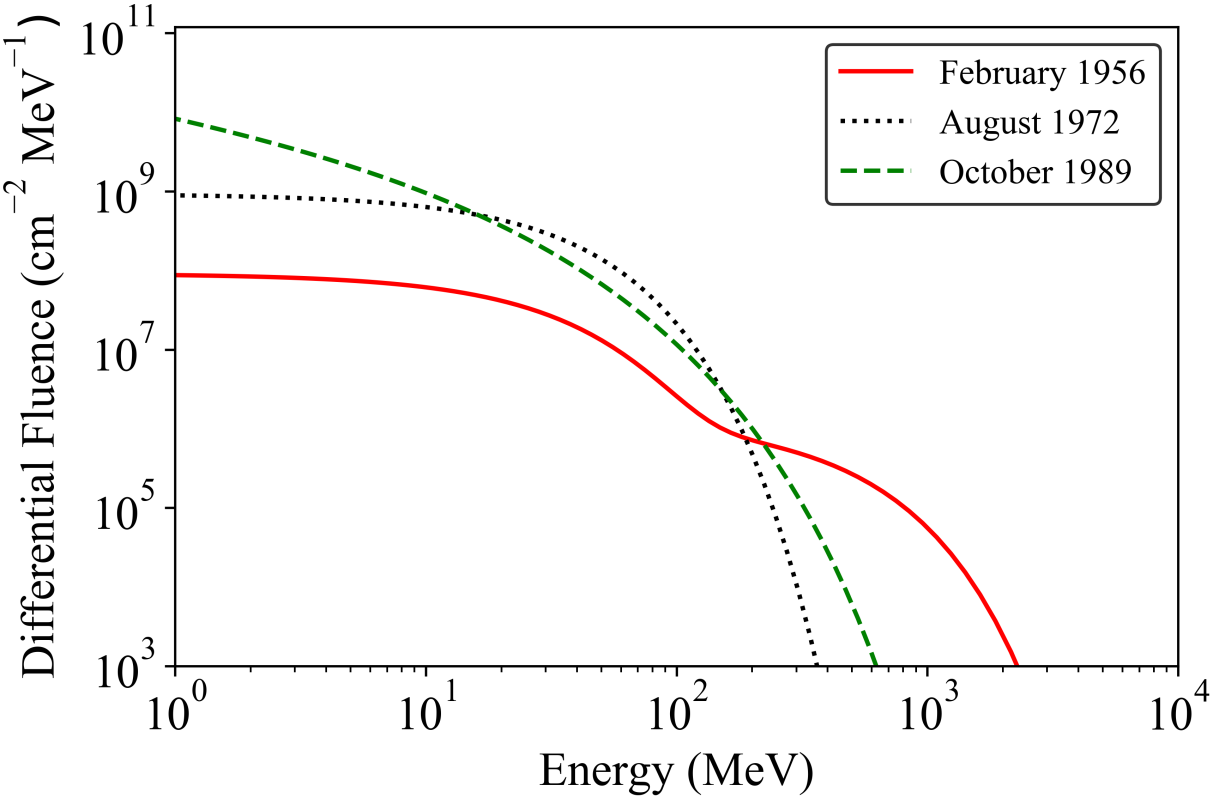

Figure 1.2: Fluence spectra for historically significant SPEs [2, 3]

1.2.3 Galactic Cosmic Rays

Galactic cosmic rays are HZE particles traveling from both inter-galactic and intra-galactic spaces [33]. They thought to be generated from supernova explosions and are accelerated due to the intergalactic magnetic field. GCRs are comprised of fully-stripped nuclei of isotopes for elements ranging from hydrogen to plutonium as well as electrons and positrons, although significant dosimetric contributions result only from heavy charged particles up to Z of 28 (nickel) [34, 35]. Ninety-eight percent of GCR components are baryons. Of them, around 87% are protons, 12% are alpha particles, and the rest are heavy charged particles [34, 35]. Kinetic energies of positively charged ions of GCR range from about 1 MeV/n to greater than 1 TeV/n, with 50 GeV/n being a reasonable upper limit for astronaut dosimetry [2, 3]. The rest of the GCR components are made up of energetic electrons and positrons [36]. The intensity of GCRs varies based on the solar cycle, which is around 11 years in duration [37]. During the solar cycle, the plasma density changes based on emissions from the Sun. The galactic radiation field is altered based on the intensity of the Sun's magnetic field at that time. Parker showed that the moderation of GCRs by the Sun's magnetic field could be accurately represented by Equation 1.1[38]

$$\frac{\partial U}{\partial t} = \nabla(k^s \nabla U) - \vec{V}\nabla U + \frac{1}{3}\nabla\vec{V}\frac{\partial}{\partial E}[(1 + \frac{m}{E+m})UE] = 0, \tag{1.1}$$

where U denotes the cosmic ray number density, E is the particle energy, V is the particle velocity vector, and m is the mass of the particle [4]. The spectra for GCR for some important ions are shown in Figure 1.3.

The components of different ions in the GCR spectra in the case of solar minimum conditions are shown in Table 1.1. The highly ionizing nature of GCRs poses the greatest threat in terms of radiation risk for long-term deep-space missions. To estimate the radiation risk for exploration space missions, a robust computational model for the flux density of the GCR's nucleonic component is necessary. There are a few mathematical models of GCR that accurately represent the real data. These models are generated using the experimental data obtained from high-altitude balloons and experiments conducted in space. Of these models,

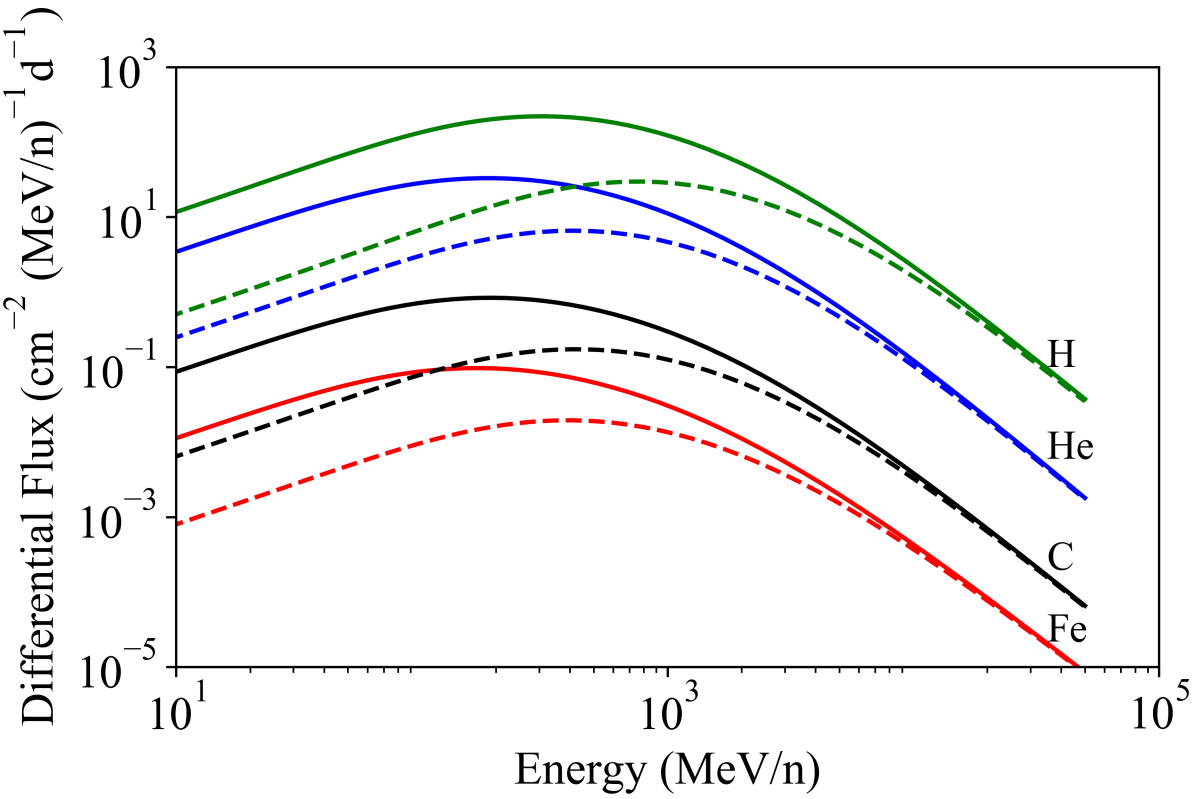

Figure 1.3: Flux density of significant ions in case of solar minimum (solid line) and maximum (dashed line) conditions [2, 3]

the most accepted ones in the scientific community are: CREME96 [37], CREME2009 [39], Burger-Usoskin [40], Badhwar-O'Neill 2010 [41], and Badhwar-O'Neil 2014 [4] models [42].

Cosmic Ray Effects of Microelectronics Code (CREME96)

CREME96 is a model that was developed in 1996 to compute the effect of space-borne radiation on electronics. This model uses a mathematical model formulated by Nymmik et al. in 1992 to characterize cosmic ray flux density [37]. In this model the flux density for elements with $Z = 1$ to $Z = 28$ are formulated. The basic mathematical formula for CREME96 model is given in Equation 1.2,

$$\phi_i(R) = D_i R^{-\gamma_i} \beta^{\alpha_i}, \tag{1.2}$$

Table 1.1: Fractional Contribution (f) of each element in GCR at solar minimum, after Ref. [9]

Element	f	Element	f	Element	f
H	0.8976	Ne	3.71×10^{-4}	K	2.0×10^{-5}
He	0.0935	Na	7.46×10^{-5}	Ca	5.33×10^{-5}
Li	3.37×10^{-4}	Mg	4.86×10^{-4}	Sc	1.01×10^{-5}
Be	2.1×10^{-4}	Al	8.06×10^{-5}	Ti	3.66×10^{-5}
B	6.89×10^{-4}	Si	3.66×10^{-4}	V	1.71×10^{-5}
C	2.56×10^{-3}	P	3.66×10^{-4}	V	1.71×10^{-5}
N	6.78×10^{-4}	S	6.9×10^{-5}	Mn	2.24×10^{-5}
O	2.42×10^{-4}	Cl	1.32×10^{-5}	Fe	2.52×10^{-4}
F	4.36×10^{-5}	Ar	2.65×10^{-5}	-	-

where ϕ_i is the flux density of particle type i, R is the rigidity of the particle, and D_i and α_i are constants defined for each particle in the model. γ_i and β represent the Lorentz factor and the ratio of the particle's velocity to that of the speed of light in vacuum. An update of the CREME96 model was done in the CREME2009 model. The CREME2009 uses a 12-month average of the Wolf numbers instead of the monthly average of the Wolf numbers as in the case of the CREME96 model.

Badhwar-O'Neil 2010 Model

The Badhwar-O'Neill model (BON2010) is the previous model that was accepted as the benchmark by NASA [41]. The differential flux density for a particle type is defined by the following mathematical formula in Equation 1.3,

$$\phi(E) = j_0 \beta^{\delta} (E + E_0)^{-\gamma}, \tag{1.3}$$

where j_0, δ, and γ are constants which are dependent on the particle type. The variables E and E_0 represent the kinetic and rest mass energies of the particles respectively. This model predicts the flux density of GCR particles from $Z = 1$ to $Z = 94$ with energy range between 1 MeV/n to 1000 GeV/n in interplanetary space [42]. This model used data obtained from

Advanced Composition Explorer (ACE) and Interplanetary Monitoring Platform-8 (IMP-8).

Badhwar-O'Neil 2014 Model

The underlying mathematical base for the updated Badhwar-O'Neill 2014 model (BON2014) is the same as that of the BON2010 model. The difference lies in how the constants were computed [4]. In the BON2010 model, the constants were based on data gathered by the Cosmic Ray Isotope Spectrometer (CRIS) on the ACE. The data were limited to 50 MeV/n to 500 MeV/n, and the prediction of higher energy components was made via extrapolation. In this model, a multitude of data was examined from different satellite and balloon measurements during Solar Cycle 20-24, and based on all of the data, the model parameters were fit with higher accuracy than the BON2010 model. The parameters used for this model for different GCR ions are shown in Table 1.2.

The solar modulation parameter is a measure of how much the GCR spectra will be modified by solar activity. Numerical solution of Equation 1.1 gives the measure of alteration of the GCR spectra in the presence of the heliospheric magnetic field and solar wind. The parameter k is impacted by solar activity and is represented in Equation 1.4,

$$k(r,t) = \frac{k_0}{V_s}\beta P[1 + (\frac{r}{r_0})^2]/\phi(t), \tag{1.4}$$

where V_s is the constant solar wind speed ($400\,\mathrm{km\,s^{-1}}$), r represents the distance from the Sun in astronomical units (AU), t is the time in years, k_0 is the diffusion constant which is equal to $1.6 \times 10^{21}\mathrm{cm^2\,s^{-1}}$, and P and $\phi(t)$ are respectively the particle rigidity and solar modulation parameter. The solar modulation parameter is given by Equation 1.5,

$$\phi(r,t) = \frac{1}{3}\int_r^{r_B} \frac{V_W(r',t)}{k(r',t)}\mathrm{d}r', \tag{1.5}$$

where r_B is the extent of the heliosphere, $V_W(r,t)$ is the speed of the solar wind, and $k(r,t)$ is the diffusion parameter. A quasi-steady state and spherically symmetric interplanetary medium were assumed to solve this equation. In case of solar minimum conditions, the value of $\phi(t)$ is approximately equal to 475 MV, and in case of solar maximum conditions, the solar

Table 1.2: Model parameters used for BON2014, after Ref. [4]

Z	γ	δ	j_0 [MV]
1	2.75	-2.82	9.50×10^{-4}
2	2.80	-2.00	4.53×10^{-5}
3	3.21	-0.69	6.37×10^{-8}
4	2.93	1.50	1.20×10^{-7}
5	3.00	-0.40	2.40×10^{-7}
6	2.70	-2.0	1.60×10^{-6}
7	2.95	-0.60	2.65×10^{-7}
8	2.73	-1.90	1.50×10^{-6}
9	3.08	0.40	1.63×10^{-8}
10	2.75	-1.60	2.35×10^{-7}
11	2.73	-1.80	4.60×10^{-8}
12	2.70	-2.40	3.03×10^{-7}
13	2.75	-1.40	5.30×10^{-8}
14	2.65	-2.40	2.65×10^{-7}
15	3.15	2.00	5.68×10^{-9}
16	2.70	-1.00	5.78×10^{-8}
17	3.13	2.00	5.99×10^{-9}
18	2.90	0.60	1.68×10^{-8}
19	3.13	2.00	5.68×10^{-9}
20	2.75	-1.60	3.23×10^{-8}
21	3.15	0.40	3.50×10^{-9}
2 22	3.0	-0.5	1.44×10^{-8}
23	3.0	-0.50	7.14×10^{-9}
24	2.90	-1.00	1.39×10^{-8}
25	2.80	-1.00	1.39×10^{-8}
26	2.60	-2.50	1.11×10^{-9}
27	2.60	-2.50	1.11×10^{-9}
28	2.55	-2.40	1.19×10^{-8}

modulation parameter is approximately equal to 1150 MV.

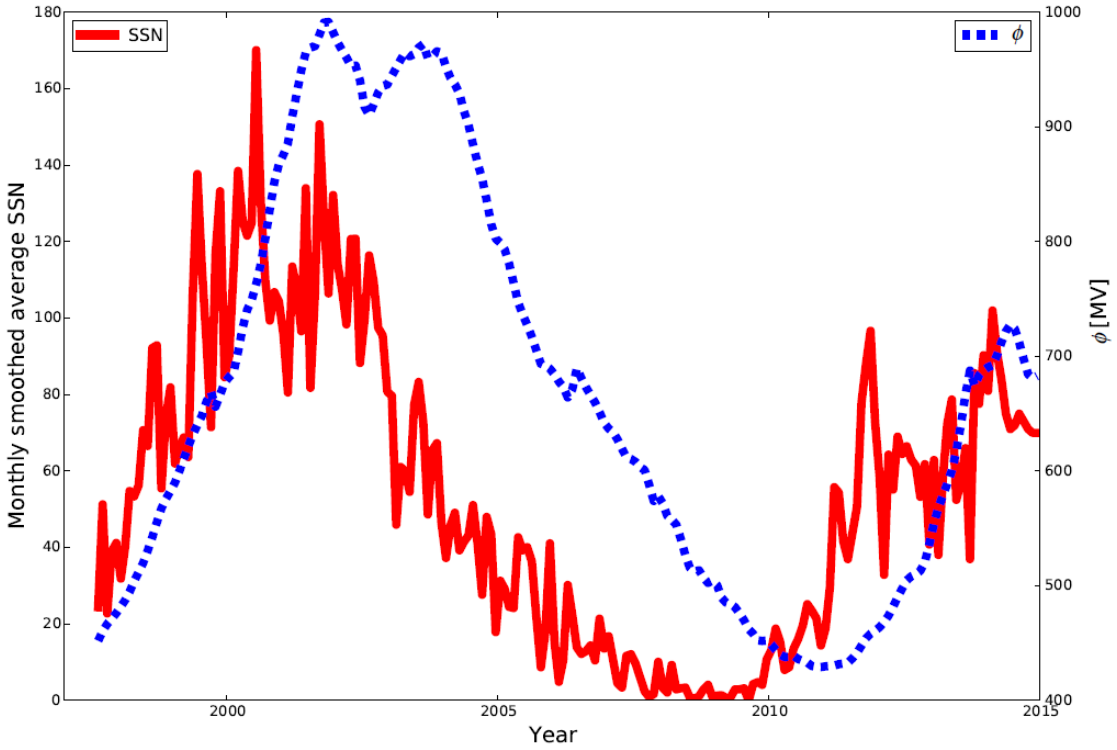

Figure 1.4: Relationship between SSN and solar modulation parameter, from Ref. [4]

Figure 1.4 represents the relationship between the Sunspot number (SSN) and the solar modulation parameter. It is clear that there is a time-lag between the SSN and ϕ. This time lag occurs because the solar magnetic field takes some time to disturb the galactic component. The solar modulation parameter only alters the lower-energy components of the GCR (up to around 1000 MeV) as shown in Figure 1.3, and the higher energy component (with higher rigidity) remains unchanged.

1.3 Radiation Dosimetry Concepts

1.3.1 Stopping Power

Stopping power is defined by the International Commission on Radiation Units and Measurements (ICRU) as the average energy dissipated by ionizing radiation in a medium per

unit path length of travel by the radiation [43]. The mechanisms by which ionizing radiation dissipates energy can be classified into three sub-categories: 1) energy loss via interactions with electrons, 2) energy dissipation via radiation, and 3) energy loss via interactions with nucleus. Another important parameter called mass stopping power is defined as the energy dissipated per unit length per unit density. In dosimetry, often, the latter parameter (mass stopping power) is used extensively. The total mass stopping power is represented as shown in Equation 1.6,

$$\frac{S_{tot}}{\rho} = \frac{S_{el}}{\rho} + \frac{S_{rad}}{\rho} + \frac{S_{nucl}}{\rho}, \tag{1.6}$$

where $\frac{S_{el}}{\rho}$, $\frac{S_{rad}}{\rho}$, and $\frac{S_{nucl}}{\rho}$ represent the mass electronic, mass radiative and mass nucleonic stopping power. These three variables are explained here. Mass electronic stopping power is defined as energy lost per unit length and per unit density by the ionizing radiation via Colulombic interactions with the electrons of the interacting medium. The mass electronic stopping power is given by Equation 1.7 [44],

$$\frac{S_{el}}{\rho} = 4\pi {r_e}^2 m_e c^2 N_A \frac{Z}{A} \frac{z^2}{\beta^2} [\ln(\frac{2m_e c^2}{\beta^2} I) - \ln(1-\beta^2) - \beta^2], \tag{1.7}$$

where r_e and m_e are the radius and mass of electron, c is the velocity of light in vacuum, N_A is Avogadro's number, Z and A are the atomic number and mass number of the target material respectively, z is the atomic number of the projectile, and I is the mean excitation energy, dependent on target material. This formula in Equation 1.7 is popularly known as Bethe-Bloche formula for computing stopping power of an ionizing radiation in a medium. The other two stopping powers are radiative stopping power and nuclear stopping power. The definitions of the mass radiative stopping power is given in Equation 1.8 [44],

$$\frac{S_{rad}}{\rho} = 4\alpha {r_e}^2 N_A \frac{Z^2}{A} E_{tot} [\ln(\frac{E_{tot}}{m_e c^2}) - \frac{1}{3}], \tag{1.8}$$

where E_{tot} is the total rest mass and kinetic energy of the particle and α is a constant. The last parameter is the nuclear mass stopping power where the ionizing radiation loses its

energy via elastic collisions with the nucleus of the interacting medium. The mathematical expression for the mass nuclear stopping power is given in Equation 1.9 [44],

$$\frac{S_{nucl}}{\rho}(E) = 2\pi \frac{N_A}{A} \int_0^{W_{max}} Q(\theta, E) \frac{d\sigma_{elas}}{d\Omega} \sin\theta \mathrm{d}\theta, \tag{1.9}$$

where $Q(\theta, E)$ is the recoil energy received by the target atom, and θ is the deflection angle of the projectile.

1.3.2 Linear Energy Transfer

Linear energy transfer (LET) is an important quantity in radiation dosimetry. It is defined as the energy absorbed per unit distance by the local medium when ionizing radiation traverses it [43]. The mathematical representation of the LET is shown in Equation 1.10,

$$L(E) = (-\mathrm{d}E/\mathrm{d}x)_{avg}. \tag{1.10}$$

The negative sign in Equation 1.10 indicates that the energy of the particle is reduced with increasing distance traveled in the medium. The right hand side of Equation 1.10 represents the average energy locally imparted to the medium per unit path length. The LET is a function of particle type and energy. Although the mathematical formulation is similar, there is a difference between LET and stopping power. Stopping power denotes the energy lost by the ionizing particle per unit length, whereas the LET refers to the energy that is imparted to the local medium per unit length. Therefore, LET is either less than or equal to the stopping power, as some energy loss may be radiative in nature, e.g., Bremsstruhlung.

1.3.3 Absorbed Dose

Absorbed dose is defined as the mean energy imparted to material of mass m when the mass is infinitesimally small. In practice, it is a measure of amount of energy deposited per unit mass. For heavy charged particles traversing a medium, absorbed dose can be calculated as

$$D = \frac{1}{\rho} \int_0^\infty L(E)\Phi(E)\mathrm{d}E, \tag{1.11}$$

where $L(E)$ and $\Phi(E)$ are the LET and differential fluence spectrum of the particle that imparts its energy to the medium. Here, ρ represents the density of the medium. The SI unit of absorbed dose is gray ($1\,\mathrm{J\,kg^{-1}}$). For HZE ions with minimal radiative losses, the LET in the definition can be replaced with the stopping power.

1.3.4 Dose Equivalent

Absorbed dose provides information on the amount of energy deposited locally in a tissue or medium. To assess the radiobiological damage that this absorbed energy does to a tissue, absorbed dose must be modified by a quantity known as the quality factor. This factor is a dimensionless weight that takes into account the degree of damage caused by different kinds of radiation. The mathematical definition of the dose equivalent is shown in Equation 1.12

$$H = \frac{1}{\rho} \int_0^\infty L(E)\Phi(E)Q(L(E))\mathrm{d}E, \tag{1.12}$$

where Q(L(E)) is the LET-dependent quality factor. Different versions of ICRP publications have defined the quality factors differently[5, 6]. Early works established that the quality factors are a function of LET. Figure 1.5 represents the quality factor formulated by different ICRP publications [5, 6]. The unit for dose equivalent is the sievert (Sv), which is also equal to $1\,\mathrm{J\,kg^{-1}}$.

1.3.5 Effective Dose

Another important quantity frequently used in space radiation dosimetry is the effective dose. The dose equivalent indicates the different biological effects of different types of radiation. The dose equivalent in different tissues gives the measure of biological harm to the particular tissue. To determine the cumulative damage to the body, another weight factor is needed. Organs have varying importance in terms of total damage to the body. Effective dose allows

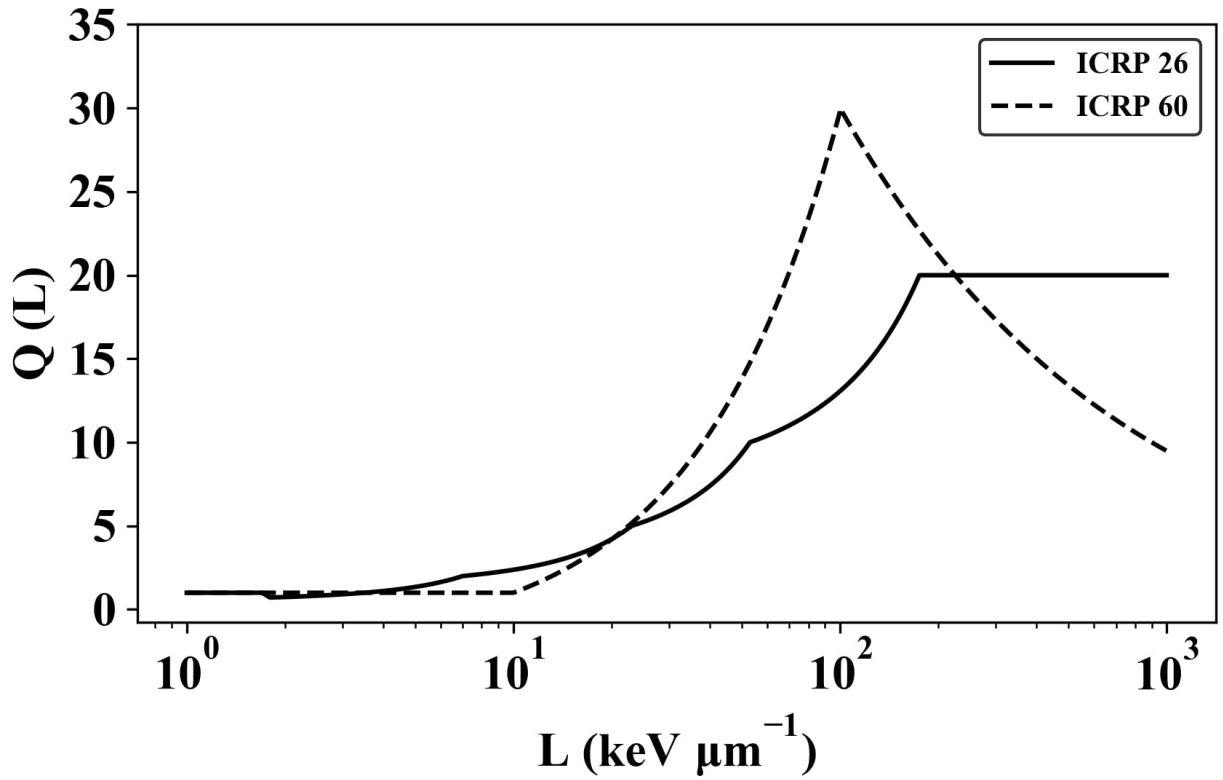

Figure 1.5: Quality factor as a function of LET for different publications of ICRP, from Ref. [5, 6]

one to compute the cumulative damage to the body using different tissue weight factors. The mathematical definition of effective dose is given in Equation 1.13,

$$E = \sum_T w_T H_T, \tag{1.13}$$

where w_T and H_T represent the tissue-specific weight factor and organ dose equivalent in tissue T respectively for the tissue T. The values of these weight factors are listed in Table 1.3 based on ICRP 60 [6] and ICRP 103 [10] publications. The expression for organ equivalent dose (H_T) is given by Equation 1.14,

$$H_T = \sum_R w_R D_{T,R}, \tag{1.14}$$

where the term w_R is the radiation weighting factor, $D_{T,R}$ is the organ absorbed dose due to radiation type R in the tissue T [10]. For space radiation dosimetry, the quality factor approach (as shown in Equation 1.12) is used to determine organ dose equivalent, whereas for terrestrial radiation, the radiation weighting factor is used to compute organ dose equivalent [10].

Table 1.3: Tissue weighting factors from recent ICRP publications, after Ref. [6, 10]

Tissue	Tissue weighting factor (w_T) [6]	Tissue weighting factor (w_T) [10]
Gonads	0.2	0.08
Bone Marrow (red)	0.12	0.12
Colon	0.12	12
Lung	0.12	0.12
Stomach	0.12	0.12
Bladder	0.05	0.04
Breast	0.05	0.12
Esophagus	0.05	0.04
Thyroid	0.05	0.04
Skin	0.01	0.01
Bone	0.01	0.01
Remainder	0.05	0.12
Total	1.0	1.0

Effective dose is useful for comparing overall detriment for different exposure situations but is not used to compute risk [45].

1.3.6 RBE-weighted Dose

In addition to dose equivalent, which is used extensively for characterizing stochastic effects, there is another quantity, RBE-weighted dose, which is used to characterize tissue reactions. Appropriate RBEs are provided by NCRP Report 132 [46]. RBE-weighted dose for a particular organ is calculated by weighting the absorbed dose with energy dependent radiobiological effectiveness values and integrating them over the energy range. The unit of RBE-weighted dose is gray-equivalent (Gy-Eq). Table 1.4 shows the RBEs of different particles.

Table 1.4: RBE values for different types of radiation, after Ref. [11]

Radiation Type	RBE
1 - 5 MeV neutrons	6.0
5 - 50 MeV neutrons	3.5
Heavy Ions ($Z > 1$)	2.5
Protons > 2 MeV	1.5

Updated Track Structure-based Quality Factors

In previous section, the definitions of quality factors have been discussed. It was shown that the quality factor is a function of the LET. In recent years, studies have found that quality factor is also dependent on the track structure of the particle. Since the majority of space radiation consists of charged particles with varying track structures, an updated definition of quality factor was required. Extensive research done by the NASA Human Resource Program (HRP) resulted an updated quality factor, which is based on the track-structure produced by ions passing through any tissue. The quality factors are defined for different ions for solid cancer and leukemia [47]. The updated NASA quality factor formula is given by Equation 1.15,

$$Q_{NASA} = (1 - P(Z, E)) + \frac{6.24(\Sigma_0/\alpha_\gamma)}{LET} P(Z, E), \tag{1.15}$$

where the terms of Equation 1.15 are given in Equations 1.16, 1.17, and 1.18,

$$P(Z, E) = (1 - e^{-\frac{(Z^*/\beta)^2}{k}})^m P_{TD}, \tag{1.16}$$

$$Z^* = Z(1 - e^{-(\frac{1.25\beta}{Z^{2/3}})}), \tag{1.17}$$

$$P_{TD} = (1 - e^{-(\frac{E}{E_{TD}})}), \tag{1.18}$$

where the quantity Z^* represents ion effective charge, P_{TD} represents the decrease of the radial dimensions of the track near the termination point, k determines the location of the maximum value of Q, α_γ is the slope of the linear part of the dose response curve for reference photons, and E_{TD} is an empirical parameter set from experimental values. The values of these parameters for solid cancer and leukemia are given in Table 1.5.

Table 1.5: Parameter values for NASA solid cancer and leukemia

Parameter	Solid Cancer		Leukemia	
	$Z \leq 4$	$Z > 4$	$Z \leq 4$	$Z > 4$
m	3	3	3	3
κ $[Z/\beta^2]$	1000	550	1000	550
Σ_0 [μm^2]	7000	7000	1750	1750
α_γ [Gy^{-1}]	6.24	6.24	6.24	6.24
E_{TD} [MeV/n]	0.2	0.2	0.2	0.2

1.4 Space Radiation Dosimetry and Concept of Risk

1.4.1 Risks Associated with Space Radiation

NASA has classified space radiation effects into four categories [16]: cancer [48], damage to central nervous system [49], degenerative tissue damage [50], and radiation sickness [51]. Space radiation effects are also categorized as acute or long term. Acute effects include nausea, vomiting, skin-burn, and for very high exposures, non-carcinogenic mortality. Long-term effects include deterministic outcomes such as cataract formation, damage to the central nervous system, and cardiovascular disease, as well as stochastic effects, such as cancer. A major concern with stochastic effects is that there are no known dose thresholds [52] and thus it is possible that these effects can occur at relatively low exposure levels. The primary concern for GCR exposure is stochastic effects such as cancer whereas deterministic effects may be caused by SEPs. Recently, advancements have been made in predicting the occurrence of SPEs [53]. For long-term deep space missions, "storm shelters" are designed to

protect astronauts during the course of SPE, which usually lasts between hours to days [29]. Most SPEs do not pose a significant threat unless astronauts are performing extravehicular activities (EVA) outside of the protection of the spacecraft. The most worrisome radiation effects are stochastic effects such as cancer which may be caused due to low flux density HZE components which are highly penetrating and thus cannot be removed. Since this component is ever-present, accumulated effects over the span of years can increase the risk of exposure-induced death beyond the permissible limit. The different radiation risk concepts and models are discussed in detail in the following section.

1.4.2 Exposure Guidelines Relevant to Space Radiation

Radiation workers have a very strict limit on what is acceptable in terms of organ dose equivalent and effective dose. For astronauts, these limits are higher compared to those for terrestrial radiation workers. The effects for astronauts can be cancerous and non-cancerous. For stochastic effects, the NASA regulation is a 3% career integrated risk of exposure induced death (REID, discussed in a later section) at the upper 95% tolerance interval [19]. For non-cancerous effects, the regulation limit was set by the NASA Space Flight Human System Standard Volume 1 (NASA-STD-3001v1) [19]. These radiation limits were set to prevent deterministic effects from occurring in astronauts in spaceflight. These acute and deterministic effects are associated with tissue damage and not with cancer risk. To differentiate the effects of tissue damage from that of cancer, a new unit (Gy-Eq) was introduced, which uses the RBE-weight factors (as shown in Table 1.4) instead of quality factors. Current NASA dose limits for these deterministic effects are attributed to organs such as eyelens, skin, BFO, and circulatory system. The tissue damage to the central nervous system (CNS) is computed using absorbed dose (Gy) as the RBEs for CNS are mostly unknown. Table 1.6 shows the dose and RBE-weighted dose limits for deterministic tissue effects.

In case of stochastic effects, such as cancer, it is generally postulated that these are caused by the low flux density, high energy, slowly and steadily varying GCR component. Although the approach of the current SPEL restricts excess risk of death, effective doses

Table 1.6: Dose and RBE-weighted dose limits for short-term and career non-cancer effects (mGy-Eq or mGy, where specified), after Ref. [11]

Organ	30-day limit	1-year limit	Career limit
Lens	1000	2000	4000
Skin	1500	3000	4000
BFO	250	500	Not applicable
Heart	250	500	1000
CNS	500 mGy	1000 mGy	1500 mGy
CNS ($Z \geq 10$)	-	100 mGy	250 mGy

corresponding to the NASA career limit can be calculated for astronauts of different ages for both sexes [12]. Table 1.7 shows the effective dose limit per year to achieve 3% REID for male and female astronauts. It is evident from the table that females, especially younger females are more susceptible to space radiation.

Table 1.7: E fective dose to reach 3% REID for never-smoker population, after Ref. [12]

Age [y]	Male [mSv]	Female [mSv]
30	780	600
40	880	700
50	1000	820
60	1170	980

1.4.3 Brief History of Cohorts and the Dosimetry Models

Since available data on radiation exposure to human beings in space are very scarce, radiation risk models are dependent on existing databases containing the history of exposure of human beings of varying ages and both sexes to radiation encountered on the Earth. Such a database should contain detailed information about a large number of people, including age, sex, radiation exposure, and a control group of people with similar demographics who were not exposed to the radiation. The Life Span Study (LSS) cohort data are useful for this purpose [54]. The LSS cohort comprises around 120000 survivors of Hiroshima and Nagasaki atomic

bombs detonated in 1945. Meticulous records have been kept by the Radiation Effects Research Foundation (RERF), a collaboration between Japan and the United States. The database contains all the people's exposure data based on their distance from the epicenter of the blast at the time of the explosion. A total of four groups were constructed, with varying distances: 1) less than 2 km, 2) between 2 km and 2.5 km, 3) between 2.5 km and 10.0 km, and 4) people who were not present in the cities at the time of the bombing (greater than 10.0 km). Among these groups, people with identical age and sex were chosen to compare the effects of radiation. The last group served as the control group, which included the unexposed population. A separate group consisting of the survivors' progenies was also tracked to understand the hereditary effects of radiation exposure. The dosimetry was computed using several models over the years. The latest model, known as "DS02", includes Monte Carlo computation of radiation exposure via neutron and photon fluences using data for initial locations of the individuals and detailed shielding configurations that were designed using reconstructed models of the cities [55]. Three different computational phantom models, representing infants, adult men, and adult women were used to account for body self-shielding. Organ absorbed doses were computed by adding the contributions of photon dose and neutron dose multiplied by a factor of 10 to account for the neutron RBE in an approximate way [54].

1.4.4 Radiation Risk Model Concepts

There are multiple radiation risk models that have been developed over the past half century. To understand these radiation risk models, first it is important to understand definitions of quantities commonly used in these models.

Incidence Rate

The first definition is known as cancer incidence rate or hazard function. It is denoted by the new cases of cancer occurring among previously healthy group of people. The incidence

rate at a certain time t_j is expressed as:

$$\lambda_j(t_j) = \frac{d_j}{n_j T_j}, \tag{1.19}$$

where d_j denotes the number of cancer occurrence at time t_j in j^{th} group due to the effect of radiation exposure among a group of sample size n_j in a time period of occurrence is T_j [56].

Risk

Probability that an individual develops a certain diseases over a specified amount of time, given the individual is disease free at $t = 0$. The risk at time t_j is defined by

$$p(t_j) = \frac{d_j}{n_j}. \tag{1.20}$$

It is clear that the risk is the multiplication of the incidence rate with the time period of concern (T_j) [56].

Instantaneous Incidence Rate (continuous)

Continuous instantaneous incidence rate is a probabilistic model used in the studies of risk. It is also known as hazard function. It is given by

$$\lambda(t) = \frac{f(t)}{1 - F(t)}, \tag{1.21}$$

where *F(t)* is the probability of the occurrence of the disease from beginning of time $(t = 0)$ to time t, and $f(t)$ is the time rate of change of *F(t)*. It gives the probability of disease to occur at time t, provided the subject is disease free up to that time point. This function is very important in the studies of risk as all risk quantities are derived from the hazard function [56].

Cumulative Incidence Rate

Cumulative incidence rate is the time integral of the hazard function and it gives total incidence rate over time t:

$$\lambda_C(t) = \int_0^t \lambda(t')\mathrm{d}t'. \tag{1.22}$$

Excess Absolute Risk

Excess absolute risk is one quantity that is used extensively in risk models. It is given by the difference between hazard functions for an unexposed group and a group which is exposed to a particular type of radiation. It is given as

$$EAR(t) = \lambda_{exposed}(t) - \lambda_{unexposed}(t). \tag{1.23}$$

The subtraction is strictly valid if all other conditions between the exposed and unexposed groups are identical. If they are not, there are different mathematical models that can be applied to compare the data from the exposed and unexposed groups. The risk for an unexposed group sometimes referred to as baseline risk.

Excess Relative Risk

There is one other quantity that is often cited in the studies of radiation risk. This is called excess relative risk (ERR). It is defined as

$$ERR(t) = \frac{\lambda_{exposed}(t)}{\lambda_{unexposed}(t)} - 1. \tag{1.24}$$

1.4.5 BEIR VII Models

The BEIR VII models are a collection of well-established, site-specific, mostly linear no-threshold (LNT) based radiation risk models that give the ERR and EAR. These risk models were suggested by the BEIR committee in 2007 to compute risk based on data from LSS

cohort [56]. Based on the BEIR committee's recommendation, the LSS data from the period 1958-1998 were considered for cancer incidence, whereas for site-specific mortality, the data from 1950-1997 were studied. The models provide numerical fits to the data using Poisson regression analysis to compute EAR and ERR. Equation 1.25 gives the most common mathematical form of the BEIRVII solid cancer risk models for most of the organs except breast and thyroid,

$$ERR(s,e,a) \; or \; EAR(s,e,a) = \beta D \exp(\gamma e^*)(a/60)^{\eta}, \tag{1.25}$$

where e is the age at exposure, e^* is equal to $e-30$ years when $e \geq 30$ and equal to 0 when $e \geq 30$, a and s are the attained age and sex of the exposed person, and the parameters β, γ, and η are obtained by parameter fitting. There are some site-specific risk models such as breast and thyroid that have a slightly different radiation risk form than Equation 1.25. The breast cancer model is obtained from a different cohort to represent American women characteristics more accurately [57]. The ERR model (Sv^{-1}) for breast cancer is given by Equation 1.26,

$$ERR/Sv = \beta D(a/60)^{-2}, \tag{1.26}$$

and the EAR (10^{-4} woman years per Gy) for breast cancer is given by Equation 1.27,

$$EAR = 9.9D \exp(-0.05(e-25))(a/50)^{-2}. \tag{1.27}$$

The thyroid model provides only the ERR as recommended by the committee. Five different cohorts including the LSS cohort were studied for this purpose. The BEIRVII recommended thyroid ERR model (Gy^{-1}) is given by Equation 1.28,

$$ERR/Gy = \beta \exp(-0.083(e-30))(a/50)^{-2}, \tag{1.28}$$

where β is equal to 0.53 for females and 1.05 for males. These models of cancer risk do not take into account the effect of e above the age of 30 for while computing the risk.

1.4.6 UNSCEAR Model

The United Nations Scientific Committee on the Effects of Atomic Radiation (UNSCEAR) provides risk estimate models from LSS and other cohorts for solid cancer and leukemia [58]. The most common form for the EAR and ERR for UNSCEAR model is given by Equations 1.29 and 1.30,

$$EAR(a, e, D, s) = [1 + (\alpha D + \beta D^2) \exp [\kappa_1 1_{s=female} + \kappa_2 \ln[a - e] + \kappa_3 \ln[a]], \tag{1.29}$$

$$ERR(a, e, D, s) = [(\alpha D + \beta D^2) \exp [\kappa_1 1_{s=female} + \kappa_2 \ln[a - e] + \kappa_3 \ln[a]], \tag{1.30}$$

where D is the organ dose equivalent (Sv), a is attained age, e is the age at exposure, and s represents the sex. The parameters κ_1, κ_2, κ_3, α and β are obtained from fitting to cohort data. The parameter κ_1 is dependent on the sex; that is, it is zero if the sex is male, and it is equal to κ_1 otherwise.

1.4.7 Risk of Exposure Induced Cancer and Death

Risk of Exposure Induced Cancer (REIC) and Risk of Exposure Induced Death (REID) are two essential quantities in terms of regulation of space radiation risks. The first quantity reflects the risk of cancer incidence as a result of the exposure, while the second quantity reflects the risk of mortality from cancer as a result of exposure [59]. The mathematical expression of REIC is given by Equation 1.31,

$$REIC_T(a_E, H_T) = \int_{a_E+L_T}^{\infty} \mathrm{d}t \lambda_{IT}(a_E, t, H_T) S_0(t) e^{-\sum_T \int_{a_E+L_T}^{t} \mathrm{d}z \lambda_{MT}(a_E, z, H_T)}, \tag{1.31}$$

where λ_{IT} and λ_{MT} are the tissue-specific incidence and mortality hazard functions, a_E is the age at exposure, H_T is the tissue-specific dose equivalent function, $S_0(t)$ is the background survival function conditional on surviving to age a_E, L_T represents the cancer-specific latency period, and the variable z is a dummy variable used to describe possible attained ages

between the exposure [12].

The quantity REID is more important in terms of astronaut career risk limitation and mission crew assignment. The mathematical expression for REID is given by Equation 1.32,

$$REID_T(a_E, H_T) = \int_{a_E+L_T}^{\infty} \mathrm{d}t \lambda_{MT}(a_E, t, H_T) S_0(t) e^{-\sum_T \int_{a_E+L_T}^{t} \mathrm{d}z \lambda_{MT}(a_E, z, H_T)}. \tag{1.32}$$

The incidence hazard function is calculated as

$$\lambda_{IT}(a_E, a, H_T) = [\nu_T ERR_T(a_E, a) + (1 - \nu_T) EAR_T(a_E, a)] \frac{H_T}{DDREF}, \tag{1.33}$$

where the term ν_T represents the tissue-specific transfer model weight governing the relative contributions of the EAR and ERR models. The dose and dose rate effectiveness factor (DDREF) accounts for reduced cancer incidence at doses and dose rates lower than that experienced by the LSS population and is applied to all solid cancers.

1.4.8 NASA Space Cancer Risk Code (NSCR)-2012 Model

The NSCR-2012 model is the adaptation of NASA's risk strategy roadmap in terms of determining the space radiation risks. A non-smoking population of healthy men and women was used as the reference population. The value of DDREF was taken to be equal to 1.5 based on the suggestions of BEIR VII committee [12]. Table 1.8 shows the NSCR-2012 models for site-specific cancers.

Uncertainty Quantification for NSCR-2012 Model

There can be multiple sources of uncertainties for the NSCR-2012 model. These uncertainties include statistical errors, uncertainties in the incident data, errors in dosimetry models, tissue weight factor (v_t), DDREF, physics uncertainties (uncertainties related to determination of particle fluence), and uncertainties related to quality factors that have been used in this model. It has been observed that among all the sources of uncertainties, the largest

Table 1.8: NSCR-2012 models for site-specific risk models, after Ref. [12]

Organ/Tissue	Risk-model	Tissue weight factor (v_T)
Lung	UNSCEAR	0.5
Stomach	UNSCEAR	0.7
Colon	UNSCEAR	0.7
Liver	UNSCEAR	0.7
Bladder	UNSCEAR	0.7
Esophagus	BEIR	0.7
Breast	UNSCEAR	0
Thyroid	BEIR	1.0
Leukemia	UNSCEAR	0.5

uncertainty comes from the quality factors. Uncertainty quantification of these risk models is important as it is determines the number of safe days in space for astronauts.

1.5 Radiation Transport Tools

1.5.1 Stochastic Radiation Transport Methods

In this section, a brief overview of stochastic radiation transport methods is presented. Stochastic radiation transport tools are effective at 3-D radiation transport, including the effects of material shielding and enabling computation of dosimetric quantities inside different computational phantoms. Several such stochastic codes are used in case of space radiation transport. These include Particle and Heavy Ion Transport Code (PHITS) [60], developed by Japan Atomic Energy Agency (JAEA), and other European collaborators, FLUktuating Cascade (FLUKA) [61], Geant4 [62], developed by CERN, and Monte Carlo N-Particle Code (MCNP), developed at Los Alamos National Laboratory in the USA [63]. Stochastic radiation transport codes tend to be more accurate than deterministic codes but time consuming. With the progress of high performance cluster systems and parallel processing, that problem has been reduced substantially. In this section, the details of the PHITS simulation software are discussed, as it is the stochastic radiation transport tool used in this work.

PHITS

PHITS is a general-purpose Monte Carlo code system that can simulate the transport of radiation, including neutron, photon, pion, and muon, to all heavy charged particles, including protons, which are important for space radiation transport. This code is a Fortran based code that can be compiled and executed on Windows, macOS, and Linux operating systems. PHITS can be executed in parallel mode using either message passing interface (MPI) or OpenMP mode. It has a wide variety of physics reaction models based on particle type and energy. The intra-nucleus cascade models such as JAM [64] and INCL4.6 [65], and quantum molecular dynamics nuclear model such as JQMD [66] are used for charged ion and nucleus collisions for space radiation. This code uses continuous slowing down approximation with physics model such as SPAR [67] and ATIMA [68] to simulate the motion of charged particles. Another important feature of this code is that it uses an event generator mode to transport neutrons below the energy of 20 MeV to preserve the energy conservation and enables dosimetry via secondary particles produced by the interactions and not by using neutron cross-section libraries [69]. Using this method enables the calculation of the secondary particles' quality factors so the user can calculate the dose equivalent with better precision. Also, another physics module, known as Electron Gamma Shower (EGS), is used to simulate the transport of photons and electrons [70]. In the simulations presented in this work, heavy charged ions were transported as low as 1 keV. Photons were transported from 1 keV to 1000 MeV. Lynch's formula was used for angular straggling [71], and Landau Vavilov's energy straggling was used at the time of transport[72, 73]. The default quality factor for PHITS is the ICRP Publication 60 definitions [6]. Updated track-structure based quality factors [47] were used for computation of solid cancer and leukemia dose equivalent in the simulations involved in this work.

1.5.2 Deterministic Radiation Transport Methods

NASA uses a deterministic code named HZETRN-2015 [2, 3] for radiation transport and calculation of doses. The deterministic code provides approximate solutions to Boltzmann's

equation for charged particle transport using the straight-ahead approximation. Previous versions of deterministic radiation transport codes BRYNTRN [74] and HZETRN-2010 [75] were upgraded to the present version known as 3D-HZETRN or HZETRN-2015. This code has been validated for deep-space radiation environment inside thick material shielding [2]. Earlier versions of the code involved the assumption that the projectile as well as secondaries travel forward along the direction of the projectile [75]. The code was later updated to accurately simulate the secondary particles that travel in forward and backward directions as well as propagte isotropically. This code has been validated extensively with more reliable but time-consuming 3-D stochastic transport codes such as PHITS [60], FLUKA [61] and Geant4 [62] for space-like boundary conditions [2, 3].

The basic equation behind the formation of this code lies in the solution of time-independent form of the Boltzmann equation using conservation of particles in 3-D. The basic principle of phase space conservation is shown in Equation 1.34. This transport equation is derived by assuming that a region of space is filled with different materials with atomic and nuclear cross-sections.

$$\vec{\Omega}\nabla\phi_j(\vec{x},\vec{\Omega},E) = \sum_k \int_E^\infty \int_{4\pi} \sigma_{jk}(\vec{\Omega},\vec{\Omega}',E,E')\phi_k(\vec{x},\vec{\Omega}',E')\mathrm{d}\vec{\Omega}'\mathrm{d}E' - \sigma_j(E)\phi_j(\vec{x},\vec{\Omega},E). \tag{1.34}$$

Here $\phi_j(x,\vec{\Omega},E)$ is the flux density of j^{th} particle at solid angle $\vec{\Omega}$ and energy E at position $\vec{x}$. $\sigma_{jk}(E)$ and $\sigma_j(E)$ are the differential macroscopic and macroscopic cross-section respectively. The first term in the RHS denotes gain from all other particles of type k with energy E' and initial direction Ω' that converts to particle of type j with energy E and direction Ω after collision. The second term of the RHS is a loss term that signifies particle of type j getting lost due to interaction in the medium. The interactions can be of multiple types such as collisions with atomic electrons, elastic scattering from the nuclei and inelastic scattering by the nuclei. In this section, the required theory to calculate the 1-D approximation for space radiation transport is discussed. In case of space radiation transport, especially in case of SPE, the Boltzmann's equation can be solved using straight-ahead approximation. It was

assumed that the differential cross-section of the atomic processes can be expressed as

$$\sigma_{jk}(\vec{\Omega},\vec{\Omega}',E,E') = \sum_n \sigma_{jn}^{at}(E')\delta(\vec{\Omega}.\vec{\Omega}'-1)\delta_{jk}(E+\epsilon_n-E'), \tag{1.35}$$

where n is the number of electronic excitation levels and ϵ_n represents the corresponding excitation energies. The atomic term can be further represented in Equation 1.36 as

$$\sum_k \int \sigma_{jk}^{at}(\vec{\Omega},\vec{\Omega}',E,E')\phi_k(x,\vec{\Omega}',E')\mathrm{d}\vec{\Omega}'\mathrm{d}E' - \sigma_j(E)\phi_j(\vec{x},\vec{\Omega},E) = \frac{\partial}{\partial E}[S_j(E)\phi_j(\vec{x},\vec{\Omega},E)], \tag{1.36}$$

where the stopping power $S_j(E)$ of type j ion with energy E is defined as

$$S_j(E) = \sum_n \sigma_{jn}^{at}(E)\epsilon_n, \tag{1.37}$$

and the atomic cross section is defined as

$$\sigma_j^{at}(E) = \sum_n \sigma_{jn}^{at}(E). \tag{1.38}$$

From Equation 1.37 and 1.38, Equation 1.34 can be re-written as the Boltzmann equation with continuous slowing down approximation (Equation 1.39) as

$$\vec{\Omega}\nabla\phi_j(\vec{x},\vec{\Omega},E) - \frac{\partial}{\partial E}\frac{1}{A_j}[S_j(E)\phi_j(\vec{x},\vec{\Omega},E)] + \sigma_j(E)\phi_j(\vec{x},\vec{\Omega},E) = \sum_k \int_E^\infty \sigma_{jk}(E,E')\phi_k(\vec{x},E')\mathrm{d}E', \tag{1.39}$$

where $\sigma_{jk}(E,E')$ is the differential cross-section of a particle of type k, A_j is the atomic mass of the particle of type j and energy E' producing a particle of type j with energy E. $\phi_k(x,E')$ is the flux density of particle type k. The left hand side of Equation 1.39 is known

as the Boltzmann operator and using it, Equation 1.39 can be re-defined as [76]

$$B[\phi_j(\vec{x},\vec{\Omega},E)] = \sum_k \int_E^\infty \sigma_{jk}(E,E')\phi_k(x,E')\mathrm{d}E'. \tag{1.40}$$

To solve this integro-differential equation (Equation 1.40), the double-differential cross sections are separated for forward and backward directions in case of HZETRN. The forward component is first solved using a straight ahead approximation, where it was assumed that all particles travel along the path of the projectile. It was hypothesized that the forward components are associated with high-energy the projectile and target fragmentation, whereas the secondaries are isotropically distributed [77]. The differential cross section can be represented as

$$\sigma_{jk}(\vec{\Omega},\vec{\Omega}',E,E') = \frac{1}{4\pi}\sigma_{jk,iso}(E,E') + \sigma_{jk,for}(\vec{\Omega},\vec{\Omega}',E,E'), \tag{1.41}$$

where the first and second terms in the RHS represent the isotropic and forward components respectively. 3D-HZETRN provides the numerical solution of the Boltzmann equation along different forward and backward directions. The latest version of HZETRN can do particle transport along multiple angular directions specified by the user, as well as transport more exotic particles such as pions and muons [78].

1.5.3 Active Shielding Transport Tool

Charged particle transport in electromagnetic fields follows the Lorentz formula for charged particle transport. Relativistic charged particle transport equation is governed by Equation 1.42,

$$\frac{d(\gamma m\vec{u})}{dt} = q(\vec{E} + \vec{u}\times\vec{B}), \tag{1.42}$$

where $\vec{u}$ is the velocity vector of the particle, $\vec{E}$ and $\vec{B}$ are the electric and magnetic fields, and m and q represent the rest mass and total charge of the particle, respectively. The

Lorentz factor, γ, is calculated as

$$\gamma = 1 + \frac{E_k}{E_0}, \tag{1.43}$$

where E_k and E_0 are the kinetic and rest mass energies of the particle, respectively. For this study, $\vec{B} = \vec{0}$ for all simulations.

Active Shielding Particle Pusher Code (ASPP)

The ASPP code is an in-house code developed by NASA Lyndon B. Joshnson Space Center, University of Utah, and Kansas State University [79] for relativistic and charged particle transport within an electromagnetic field. This code is the backbone of all of the novel active methods of radiation shielding discussed in this dissertation work. It was validated in the experimental facilities of Idaho National Laboratory and the Tandem Van de Graaff facility of Brookhaven National Laboratory. The ASPP input file has six different sections: the selection of source geometry, initial particle position and velocity assignment, choice of the electric or magnetic field, selection of particle motion integrator, selection of particle propagation parameters (e.g. number of time steps and time-step width), and finally the tallying parameters. The simulation methods of charged particles in a mono-directional beam through a specified electric field in an accelerator-based facility are explained below:

1. Choose number of particle histories,
2. Choose a disk shaped source with fixed radius,
3. Initialize the particle position and velocity as well as direction of propagation,
4. Choose the electric field (in this case a dipole electric field),
5. Choose parameters like type of ion, energy, distance between the source and the dipole configuration, time step length (Δ_t) and number of time steps,
6. Choose the type of integrator to be used for propagation,

7. Choose the position of the detector plane, and

8. For each particle history:

   (a) Propagate each particle history via the electric field and update the position and velocity using the type of integrator chosen for the required number of time steps,

   (b) Tally the position of the particle on the detector plane, and

   (c) Tally the final position of the particle.

In the case of particle propagation along one direction in a beam-like source, the location of particle interaction with the detector plane is tallied. In contrast, in the case of particle propagation from an isotropic source, the number of particles penetrating a spherical volume of a given radius is the tallied parameter, which is discussed in Chapter **??**. Multiple particle motion integrators such as the Runge-Kutta method, Velocity-Verlet method, Boris-Buneman method, and Leap-frog method are available in ASPP. It was observed in studies that in case of the presence of electric field alone, the Velocity-Verlet algorithm [80] is most efficient, whereas in case of particle propagation under the sole influence of magnetic fields, the Boris algorithm is the most effective [81]. Since this work involved particle propagation under the electric field, a brief description of the Velocity-Verlet algorithm is discussed in the next section.

Particle Propagation

In this section, the particle propagation algorithm used to simulate particle propagation under the influence of the electric field is discussed. The Velocity-Verlet algorithm is a popular particle integrator in the field of molecular dynamics [80]. The particle propagation can be divided into the following steps:

1. Update the position using one time step,

2. Velocity is computed using half time step,

3. The acceleration is computed using full-step position and half-step velocity, and

4. Finally the velocity is updated for full time step using half-time step velocity and acceleration.

The fundamental particle propagation model of the Velocity-verlet algorithm is shown below in Equation 1.44,

$$\begin{aligned}
\vec{r}(t+\Delta t) &= \vec{r}(t) + \Delta t\vec{u}(t) + \tfrac{\Delta t}{2}\vec{a}(t), \\
\vec{u}(t+\Delta t/2) &= \vec{u}(t) + \tfrac{\Delta t}{2}\vec{a}(t), \\
\vec{a}(t+\Delta t) &= \tfrac{\vec{F}(\vec{r}(t+\Delta t)}{m}, \\
\vec{u}(t+\Delta t) &= \vec{u}(t+\Delta t/2) + \tfrac{\Delta t}{2}\vec{a}(t+\Delta t).
\end{aligned} \tag{1.44}$$

where $r(t)$ is the position at time t and Δt is a time interval chosen by the user, which is used to represent the position and velocity after this time interval. $\vec{F}$ and $\vec{a}$ represent the electric field force and acceleration. Here, the velocity vector is updated twice once at the half time step and once at full time step to give a better approximation. This method provides a fourth-order accuracy in terms of time and second order accuracy in terms of position.

1.6 Radiation Shielding Methods

Space radiation shielding methods are of two types: 1) conventional passive methods using materials, and 2) active methods of radiation shielding. In this section, details regarding these two approaches are discussed.

1.6.1 Passive Radiation Shielding Methods

Passive shielding means using materials to slow down or stop ionizing radiation before it affects the human body. Passive shielding works via slowing down and fragmentation of high-Z ions. With the type of radiation encountered in space, it is almost impossible to ultimately reduce the flux density to zero with any realistic shielding thicknesses of material [49]. Additionally, slowing HZE ions might have energy decreases resulting in a higher LET and, therefore, greater energy depositions. Fragmentation results in lower LET particles with higher penetration capability compared to the primary incident radiation. Thus, increasing

the shielding thickness beyond a particular value could be counter-productive in the case of space radiation. It has been shown in previous studies that even a thick shielding of $20\,\mathrm{g\,cm^{-2}}$ of aluminum or polyethylene would provide a reduction of effective dose due to GCR by only 25% and 35% respectively [82] in the free-space radiation environment. Also, it has been shown that increasing material shielding thickness could increase dose equivalent beyond a specific value of thickness, especially for materials like aluminum [83].

Understanding the contribution of different ions to the total effective dose beyond material shielding and without shielding is vital to gain insight on material protection against GCR. Table 1.9 and Table 1.10 show the breakup of contribution from different ions without any material shielding and behind a standard $20\,\mathrm{g\,cm^{-2}}$ of aluminum shielding [13]. It is evident that with the introduction of passive shielding, the contribution of lighter ion towards total contribution increases because of the fragmentation effect. The BON2010 GCR model for solar minimum conditions was used to compute the data in Table 1.9 and Table 1.10. Table 1.9 shows that around 65% of the contribution comes from energy range 0 - 1.5 GeV/n and therefore shielding efforts should be concentrated on protecting against this energy range as it seems more reasonable in comparison to higher energy ions.

Table 1.9: Relative Contribution (%) to effective dose from different energy and charge groups without any passive shielding, after Ref. [13]

Energy / Ions	0 - 0.25 [GeV/n]	0.25 - 0.5 [GeV/n]	0.5 - 1.5 [GeV/n]	1.5 - 4.0 [GeV/n]	>4.0 [GeV/n]	Total
Z =1	2.1	3.7	11.6	10.5	7.7	35.6
Z = 2	2.1	1.4	2.5	1.6	0.9	8.4
Z = 3 -10	4.1	5.5	2.6	1.0	0.6	13.8
Z = 11 - 20	1.4	6.0	7.7	2.7	1.5	19.3
Z = 21 -28	0.4	3.0	11.1	5.5	3.0	22.9
Total	10.0	19.5	35.6	21.3	13.6	100

Table 1.11 shows the shielding performance for different passive shielding against a historically significant August 1972 SPE (Figure 1.2) and GCR spectra under solar minimum conditions (Figure 1.3).

Table 1.10: Relative Contribution (%) to effective dose equivalent from different energy and charge groups behind 20 g cm^{-2} of aluminum passive shielding, after Ref. [13]

Ions \ Energy	0 - 0.25 [GeV/n]	0.25 - 0.5 [GeV/n]	0.5 - 1.5 [GeV/n]	1.5 - 4.0 [GeV/n]	>4.0 [GeV/n]	Total
Z = 1	1.2	5.4	18.3	18.4	14.8	58.1
Z = 2	1.2	2.2	4.1	2.9	1.7	12.2
Z = 3 -10	< 0.1	3.3	3.8	1.3	0.8	9.1
Z = 11 - 20	< 0.1	< 0.2	6.6	2.0	1.1	10.0
Z = 21 -28	< 0.1	< 0.1	4.7	3.8	2.1	10.6
Total	2.5	11.1	37.4	28.4	20.5	100

Table 1.11: Effective dose equivalent for different incidence conditions and passive shielding, after Ref. [12]

Passive radiation shielding thickness of Al [g cm^{-2}]	Effective dose for August 1972 SPE	Annual Effective dose for GCR at Solar Minimum
5	676.2	620.7
20	48.4	496.7

It is evident from Table 1.11 that the effective dose (with ICRP 2007 Publication definition 103) in case of August 1972 SPE reduces drastically (from 676.2 mSv to 48.45 mSv) with the increase in thickness of shielding from 5 g cm^{-2} to 20 g cm^{-2}, whereas in case of the GCR at solar minimum, the annual effective dose is only reduced from 620.7 mSv to 496.74 mSv, which is only around 20%. The reason behind this is that GCRs have a significantly harder energy spectrum than even extreme SPEs; it is practically impossible to shield them using any reasonable shielding thickness and materials. 20 g cm^{-2} of aluminum is considered a standard shielding thickness that can be achievable in the future for long-term deep space missions. This result indicates that an alternative pathway needs to be explored to solve this problem. Using very large thicknesses of radiation shielding for a spacecraft would surpass the launch constraints imposed by NASA [21, 22]. Therefore, passive radiation shielding can not be the only method of radiation shielding, especially for long duration deep space missions.

1.6.2 Active methods of radiation shielding

Magnetic Shielding

In the beginning phase of active shielding research in the early 1960s, extensive focus was placed on using a magnetic field as the way to prevent charged particles from reaching the spacecraft [84–86]. The idea emulated Earth's protection ability, the geomagnetic field, to deflect HZE ions. The magnetic shielding realm can be divided into two broad categories: 1) Confined field approach, and 2) Unconfined field approach. This section discusses the historical development of concepts and their advantages and disadvantages.

Early work on magnetic methods of radiation shielding was done by Levy [84]. In his paper of 1961, the comparative analysis between passive shielding and magnetic shielding was discussed. The study revolved around a futuristic magnetic shielding concept which used a superconductor and a magnetic field of 12 T produced by a 13 m-radius coil with a current requirement of 3.7×10^7 A. The energy stored by the system was approximately 3.4×10^{12} J. This theoretical model of magnetic shielding exhibited a smaller mass penalty

compared to a hydrogenous passive radiation shielding system protecting against protons of the same energy. The concept of using superconductors to reduce the power requirement in the case of magnetic shielding was later discussed [85]. The major components of magnetic shielding are superconducting wires, structure for supporting the shielding configuration, and the cryogenic environment that maintains the low temperature for the essential operation of the superconductors. After the initial work of Levy in 1961, which showed the magnetic field as a promising method, there was work done by the joint initiative of NASA and AVCO-EVERETT Research laboratory [86]. This work analyzed different configurations of confined and non-confined magnetic fields using superconductors. They predicted the efficiency of the shielding system and the mass required to achieve this efficiency. It was postulated that using a magnetic field with superconductor materials from combining metals such as Nb and Zr can be beneficial. The magnetic field strength used in this study was in the range of 10 T. The magnetic energy that was stored in the system was in the order of thousands of joules. After the initial works are done in the field of magnetic radiation shielding that emphasized that to lower mass penalty, superconductors should be used, additional investigations were performed in the early 2000s by NASA as well as the European Space Agency (ESA) which led to various superconductor based magnetic shielding architectures [87].

The extensive work done by Hoffman et al. was dedicated to protecting the crew volume from particles with an energy range between 2-4 GeV/n by using a magnetic field of strength around 9 T [88]. The crew volume was assumed to be a cylindrical object with a diameter of 7 m and a height of 7 m. A toroidal magnetic field was chosen with the thickness of the magnetic field equal to 1.5 m - 3 m. This configuration provided 100% protection against all protons below the energy of 2 GeV and around 50% protection for protons with energy 3 GeV. Although the protection using the magnetic field was significant, the mass required to generate the 9 T is more than the passive shielding needed to provide similar protection. While this study was not successful in identifying an active shielding configuration to solve the mass penalty, it paved the way for future modifications in which a similar magnetic field can be generated using low-mass materials, and it also created a simulation methodology which can be used for future. This study represented a very thorough implementation of 3-D

simulation of HZE particles passing through a magnetic field as well as a shielding material. However, it failed to address the generation of secondary radiation from the substantial mass of the magnetic structure, which can be an important factor for long-term space missions where GCR exposure dominates.

Later research done by Geng et al. used a confined toroidal magnetic field in the range of 2 T to 6 T for a cylindrically shaped crew volume [89]. Effective dose reduction for GCR particles for a combined magnetic field of 6 T and 10 g cm^{-2} was around 32%. The magnitude of the field for this work was varied between 2 T to 6 T.

The European Space Agency (ESA) in 2002 created Topical Team (TT) to recommend a pathway to solve the space radiation shielding issue using active shielding methods, primarily focusing on magnetic shielding methods. Their study was dedicated to the critical idea that instead of trying to protect against HZE particles from galactic cosmic rays (GCR), which are chronic radiation, the primary goal should be building a magnetic "storm shelter" for protection against random SPEs. This purpose would require a less intense of the magnetic field, in the range of 1 T to 2 T. It was shown that the mass used to build this magnetic field based "storm shelter" is almost one-third of that required for a passive absorber based shelter. A critical assumption that this study made was that SEPs are mostly directional, and the orientation of the magnetic lens can be changed based on the direction of the incoming solar particle storm direction. Although some component of SPEs is directional, large SPEs have isotropic SEPs for the majority of the event, and therefore this sort of configuration is not ideal for these scenarios [29]. Also, this study depends on the successful detection of upcoming SPEs to change the orientation of the magnetic field, introducing complexity in the risk mitigation procedure. This study showed that a magnetic field of around 2.5 T is needed if the outer radius of the toroidal field is set to 3 m [90].

Plasma Shielding

Another method of active shielding which gained momentum is the use of plasma to protect against space-borne charged particles. The concept of plasma shielding is a hybrid of electro-

static and magnetic shielding. The electrostatic force is used to repel positively charged HZE ions, while a weaker magnetic field is used to prevent electrons from accelerating towards the spacecraft, reducing the discharge of conductors and Bremmstruhlung production [91]. The potential required for these configurations is in the range of hundreds of megavolts. There can be instabilities stored in the plasma cloud due to collisions of ions, and the considerable energy that is stored in the system, on the order of 10 MJ, makes this radiation shielding approach unrealistic.

In the 20^{th} century, significant plasma radiation shielding research involved a combination of plasma with a magnetic field. Unlike previous research in the field of plasma shielding, current work does not provide the combination of an electrostatic and weak magnetic field. Instead, modern studies in plasma were concentrated on the formation of mini-magnetosphere, inspired by Earth's geomagnetic field [92, 93]. In this concept, greater protection is achieved by extending the magnetic field and the artificially injected plasma. Without the presence of the plasma, the magnetic field dissipates rapidly with increasing distance from the center of the magnetic field. This concept avoids the previous issue with plasma shielding, where extreme electrostatic potential was required, and the system was unstable as a high amount of energy was stored in the plasma system. Experimental studies have shown that the magnetic field can be extended further out, and therefore, a lower magnitude field to deflect charged particles of a given rigidity [92, 93]. Also, an electrostatic field is created at the plasma boundary, which helps further deflect energetic particles away from the spacecraft.

Electrostatic Radiation Shielding

In the beginning phase of active shielding, pioneering work was done by F. H. Vogler in 1964 in terms of using electrostatic shielding to protect astronauts from harmful space radiation [94]. This study focused on protecting trapped proton environments but can easily be extended to protection against SPE and GCR. Although the configuration tested in this work was very basic and used only electrostatic repulsive forces to deflect highly energetic and heavily charged ions, this study listed the first detailed analysis on using an electrostatic

field as a means of radiation shielding.

An electrostatic field provides shielding against charged particles through deflecting or reflecting them. The electric field vectors have to be strong enough to stop the particles and reverse their trajectories completely. On the other hand, to deflect a particle gradually away from the spacecraft or crew volume, a lower-magnitude of the electrostatic field is required. Unlike magnetic fields, electric fields can slow the particles, causing more damage due to increasing LET. In Vogler's work, a concentric spherical configuration was used where the protected region was located inside the inner spherical shell. The potential difference that was applied between these two different spherical shells was on the range of tens of megavolts. The potential was chosen in such a manner that the electric field between the two concentric spheres remained lower than $1\,\mathrm{MV\,cm^{-1}}$. This study also concentrated on assessing the pressure that the spherical shells may place on each other. The attraction force faced by the spherical conductors was used to compute the design constraints of this configuration. At the end of the study, it was concluded that this sort of concentric spherical structure is extremely unstable, and any minor deviation from being concentric will result in substantial mechanical stress on the structure. This research showed that for electrostatic radiation shielding to be successful, there is a need for new sets of configurations that provide significant shielding and are stable from a structural point of view.

In 1985, independent research done by W. Frisina improved the electrostatic radiation shielding scenario [95]. This configuration also relied on the concentric spherical model. It used three spherical electrodes with the electrode closest to the spacecraft being positively charged, whereas the second layer of electrodes is negatively charged, and the third (outermost) layer is a slightly positively charged electrode. The field between the first and the second electrode is used to deflect positively charged HZE ions, whereas the electric field between the second electrode and the third electrode is used to generate a field that will protect against the thermal electrons that might get attracted by the presence of the highly positively charged electrode. In this work, the electrodes that were chosen were a meshed instead of solid and materials that were chosen to minimize the thermionic emissions from the electrodes in the presence of solar thermal radiation. It was also shown that the radius

of the second electrode carrying the negative charge should be at least twice that of the positively charged spherical electrode. This study established a relationship between the size of the spherical electrode and the maximum potential generated between the positively and negatively charged electrodes. This configuration demonstrated a way to stabilize the electrostatic shielding configuration by adjusting the dimension of it.

There was another surge of research in the early 21st century on electrostatic shielding in the United States for NASA's plan to send crewed missions to the Moon, Mars and beyond. The goal was to reduce the mass penalty and improvement of the radiation shielding capabilities. Previous works done in the area of electrostatic shielding showed that the concerns towards its successful implementation lies in the requirement of power which is at least two orders of magnitude greater than possible with present technology. Also, in order to prevent any structural instability and potential breakdown, the dimensions of these configurations have to be large, which becomes unrealistic.

Studies done by Tripathi et al in the early 2000s introduced a new concept where the whole shielding configuration was decoupled from the protected volume and spread over a distance in the order of 50 m to 160 m [96]. This concept was novel and it shaped a way to implement the active shielding without the possibilities of a potential breakdown. Here, twelve electrostatically charged spheres were used. Of them, six spheres of radius equal to 10 m were placed 50 m away from the protected volume. These spheres were charged with 300 MV, whereas the negatively charged spheres were of radius equal to 20 m and placed at 160 m from the protected area. The negatively charged spheres also were charged with equal negative potential. The protected volume was also energized with a positive potential of 300 MV. In terms of efficiency, it was observed that this configuration provides around 50% more protection in terms of effective dose in comparison to a 20 g cm^{-2} spherical polyethylene shielding when subjected to solar minimum GCR spectra of 1977. It is true that this sort of decoupled asymmetric configuration had the advantage of negating any potential breakdown or structural instabilities. However, the potential applied was still two orders higher than what can be achieved. The mass penalty of this configuration was postulated to be equal to around 20-40 t. This study was followed by similar studies concentrating on reducing

the mass penalty of the previously discussed active shielding configuration with lightweight gossamer structure [7]. This work also modified the previous twelve sphere configuration to a hybrid of three toroidal rings and six spheres, where the previously positively charged spheres were replaced by the positively charged toroidal rings. The updated configuration is demonstrated in Figure 1.6. The potential profile comparison in Figure 1.7 shows that the toroidal rings perform better than the charged spheres. A Monte Carlo based code that simulates the particle positions in an electromagnetic field was used to characterize the flux density reduction within the spacecraft. These works demonstrates a comparative analysis in terms of flux density reduction between the twelve sphere configuration and three toroidal rings and six sphere configuration (Figure 1.6). In the first case, the potential applied on each positively and negatively charged spheres was 100 MV and in case of second configurations, the toroids were kept at 50 MV, whereas the negatively charged spheres were kept at -100 MV. It was shown that the transmission probability for energetic protons were reduced in case of the second configuration (toroidal rings) in Figure 1.6.

The most recent work on electrostatic shielding was done by Joshi et al, who improved the performance of the electrostatic shielding configurations by combining both electrostatic as well as magnetic shielding methods [97]. This study did a comparative analysis by adding a magnetic field in the form of a toroid with the earlier twelve sphere electrostatic field configuration. The magnetic field of the toroid shaped structure was chosen such that the amplitude of the magnetic field within the protected volume does not go beyond 0.4 T, which is the recommended limit set for public to reduce the adverse biological effects [98].

1.6.3 Comparative Analysis of Different Active Shielding Methodologies

To do a comparative analysis between magnetic, plasma, and electrostatic field, it can be argued that plasma methods of radiation shielding generally result in an unstable system. However, recent advances in plasma shielding coupled with a magnetic field have some potential that can be explored in the future. On the other hand, active shielding using the magnetic

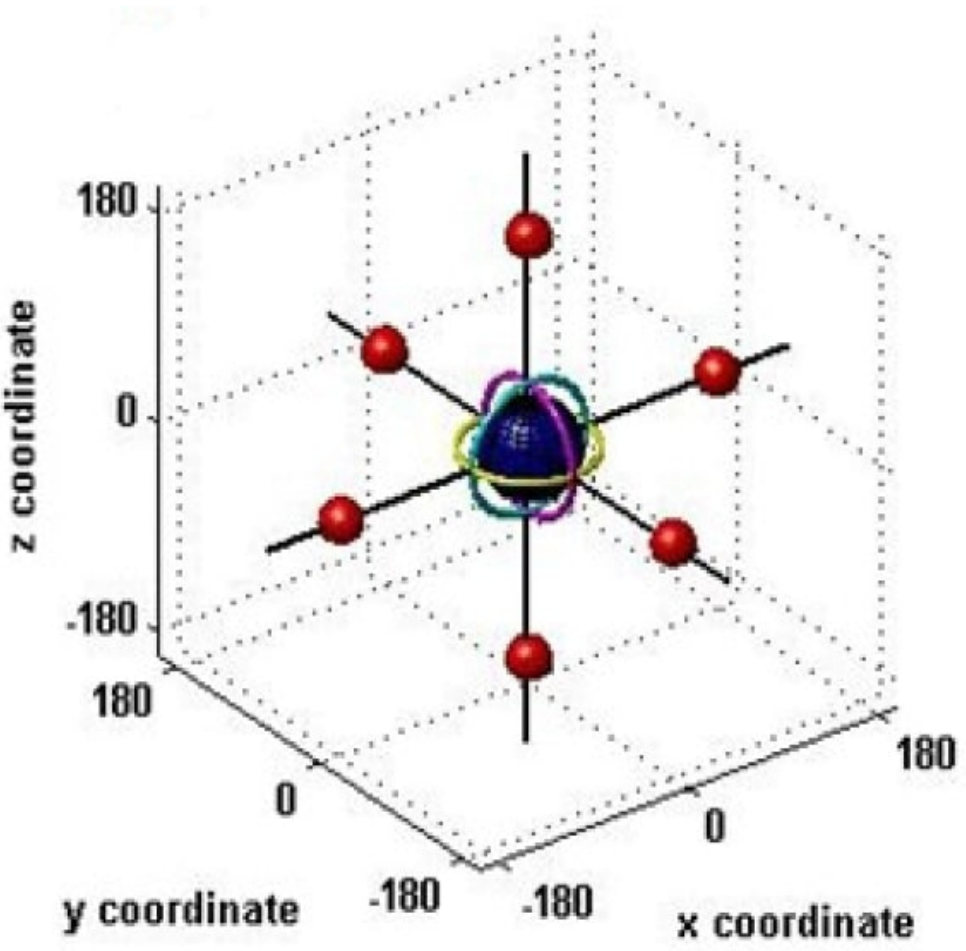

Figure 1.6: Electrostatic shielding configuration using 6-sphere and 3-toroid configuration, from Ref. [7]

field alone requires several teslas to provide sufficient protection against the GCR component. To generate a magnetic field that strong, several technological advancements such as high temperature superconductors or extensive cryogenic systems are required. Magnetic shielding methods have inherent problems such as the generation of the magnetic quench, high mass magnets, and large currents as are necessary for operation. Recent studies demonstrated a shift of focus in terms of the implementation of magnetic shielding. Magnetic shielding is being considered as an alternative for storm shelters against SPEs compared to past where it was considered as a protection against GCRs. This change of magnetic shielding application towards protection from SPEs lowered the requirement of the magnetic field and made it more feasible to implement [87]. Also, there have been some major advance-

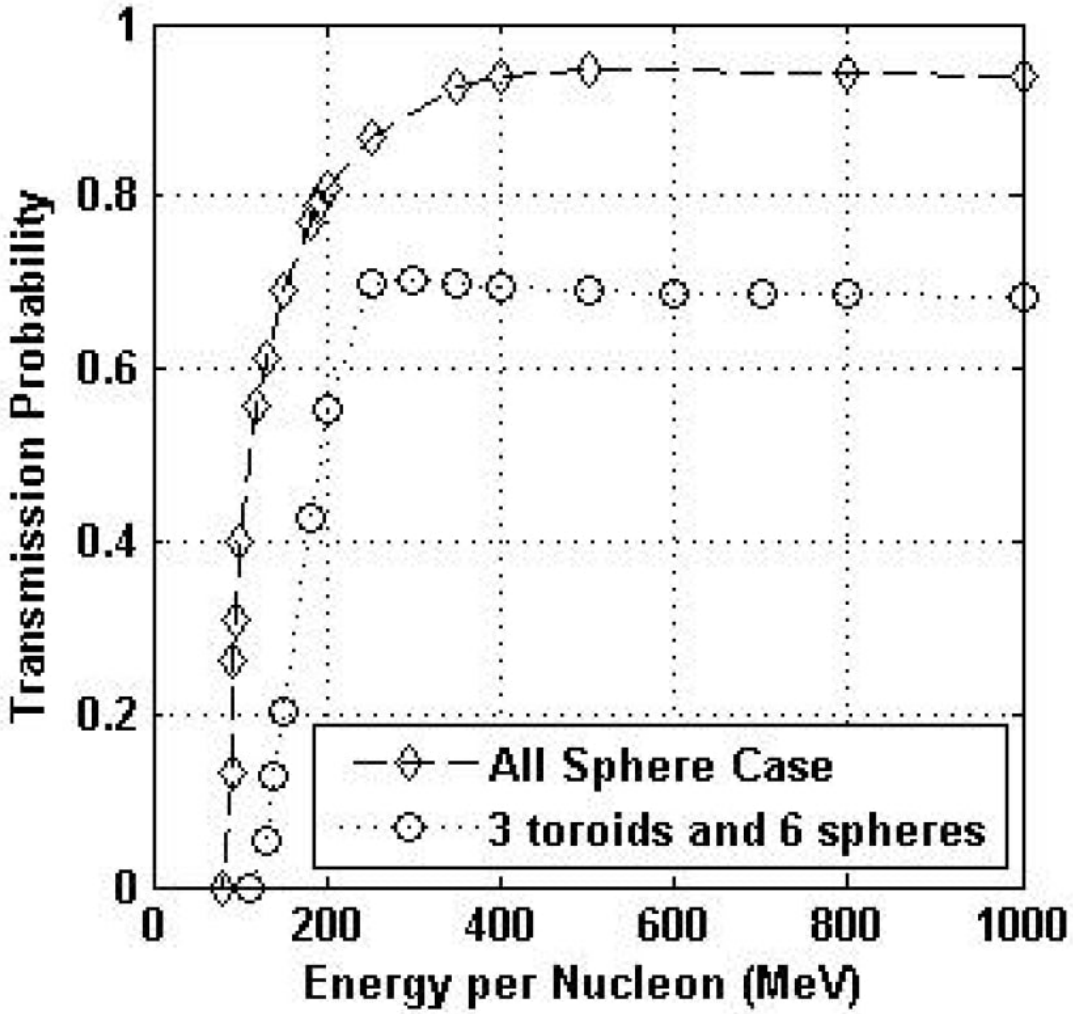

Figure 1.7: Shielding performance comparison between 12-sphere and 6-sphere-3-toroid configuration, from Ref. [7]

ments in high-temperature superconductor alloys in recent years that can be beneficial in the area of magnetic shielding [90]. In comparison, the electrostatic shielding configuration has only one major issue: it is impossible to generate hundreds of megavolt potential supplies that can power the system. However, there may be a way to reduce the power requirement by aligning multiple conductors sequentially in space with potential in the range of < 10 MV, which is within the grasp of current technology. Electrostatic radiation shielding alone may not be capable of protecting astronauts in deep-space missions, but when combined with passive shielding materials, it may be effective. The work done in this dissertation involves finding such hybrid configurations that can reduce the risk for astronauts and an

arrangement or a set of physically realizable configurations within the grasp of present-day or emerging technologies.

Chapter 2

Population-based Approach to Astronaut Radiation Risk Assessment

2.1 Motivation

This chapter is dedicated to inform the reader on the risks associated with different space missions of varying length for male and female astronauts of different age. These space missions vary from LEO-ISS missions to deep-space long term missions. In case of ISS missions, the LEO radiation environment is encountered. For deep-space missions, GCR boundary conditions at solar minimum and solar maximum, and the radiation environment at Mars surface, are encountered. This chapter also presents a novel population-based risk computation approach that can be later used to address the risks using hybrid radiation shielding system. Sex and age dependence in existing radiation risk models and large uncertainties, mostly due to lack of knowledge of biological effects of highly energetic and heavy charged particles, presently limit demographics to older, male astronauts for participation in long-duration missions to Mars. To address this issue, a novel method is introduced for evaluating radiation risk for proposed missions, where the combined risk for the population is used in place of age- and sex-specific risks. The age and sex distribution of active and trainee astronauts as of 2018 and operational NASA tools for evaluating astronaut radiation risk are

used to demonstrate the proposed method for a variety of missions. Discrete and continuous methods representing the population probability density function are tested. Mission-specific astronaut population risk distributions are constructed using random sampling from the astronaut age and sex distributions, which are then used to calculate the corresponding upper 95% tolerance limit.

2.1.1 Ethics in Space Radiation Protection

Radiation protection in all scenarios, including space exploration, is guided by three principles: justification, limitation, and optimization. For an exposure to be justified, the benefits must outweigh the associated risks. The scientific, technological, and societal benefits of space exploration are considered to outweigh all associated risks, including those resulting from radiation exposure. As previously described, NASA limits exposures to astronauts to prevent deterministic effects and keep stochastic effects, in this case cancer, to a level considered acceptable by all stakeholders. NASA keeps radiation exposure As Low As Reasonably Achievable (ALARA) through shielding and mission design with the use of radioprotectants expected in the near future. As described in ICRP publication 138 [46], the foundation of these three principles is science, ethics, and experience. The recent emphasis on crewed, long-duration exploration missions, particularly a mission to Mars, has brought the concept of space radiation protection ethics to the forefront.

The constitution of the NASA astronaut corps has changed considerably over the 60 years of its existence. The Mercury 7 astronauts comprised a remarkably homogeneous population by design; among other criteria, they were required to be less than 40 years of age, in excellent physical condition, and test pilots [99]. At the time of selection, all of these Caucasian males were between the ages of 32 and 37. Substantial diversification of the astronaut corps was achieved during the Space Transport System, or Shuttle, Program. Astronaut Group 8, selected in 1978, included Sally Ride, the first American woman in space; Guion Bluford, the first African-American in space; and Ellison Onizuka, the first Asian-American in space. Astronaut Group 22, the most recently-selected group of astronauts

(2017), consists of seven men and five women ranging in ages from 29 to 42 with diverse racial and ethnic backgrounds. Diversification of the astronaut corps was accompanied by changes to career radiation exposure limits. In 1967, no limits were recommended by the National Research Council of the National Academies of Sciences (NAS/NRC) [100] due to a concern that such limits would jeopardize mission success. By 1989, the National Council on Radiation Protection and Measurements (NCRP) recommended a 3% increase in cancer mortality as the career radiation exposure limit [101], and in 2000, a recommendation was made to account for uncertainties in the limit [102], with NASA implementation of the uncertainty portion occurring in 2007 [19].

For a given mission, REID at the upper 95% tolerance limit for younger, female astronauts is substantially greater than that for older, male astronauts. Enforcement of a career radiation risk limit based on radiation risk models that show substantial sex and age dependence has led to a fundamental ethical dilemma: *Should an otherwise qualified astronaut be restricted from participating on certain missions on the basis of his or her sex or age?* In the absence of additional information, modern society has decided that the answer to this question should definitely be "No". However, the ethical dilemma arises when balancing NASA's ethical principles of avoiding harm, respect for autonomy, and fairness, and NASA's ethical responsibilities of equality of opportunity and long-term astronaut care [103], as they relate to the astronaut's REID. This is in stark contrast with Title 10 of the Code of Federal Regulations Part 19 [104], which explicitly prohibits exclusion from activities on the basis of sex for workers under the purview of the US Nuclear Regulatory Commission. Additionally, recent research has shown that inclusion of personalized genetic information and family history might improve radiation risk assessment for astronauts, although there are serious ethical and legal questions arising from this approach [105].

In an attempt to address this dilemma and more generally the large values of REID associated with long-duration exploration missions, NASA developed a three-level crew health and safety medical waiver implementation framework as recommended by the US Institute of Medicine (IOM). First, a decision must be made as to whether health and medical standards should be exceeded for any mission (Level 1). Former NASA Administrator

Charles F. Bolden, Jr., authorized the NASA Office of Chief Health and Medical Officer to implement the IOM report recommendations in 2016 [103], serving as approval for Level 1. Second, a decision must be made on whether to undertake a mission that exceeds existing health and medical standards (Level 2). Finally, if Level 2 is passed, a decision must be made on crew assignments considering risk assessment for individual crew members (Level 3). Levels 2 and 3 are evaluated per NASA Procedural Requirement 8900.1B [106]. While this waiver implementation framework now makes it possible to assign any astronaut to any mission passing Level 2, certain classes of astronauts may be subjected to a more stringent crew assignment process (i.e., Level 3) than other classes of astronauts.

2.1.2 Study Scope and Purpose

One possible resolution to this persistent ethical dilemma is to apply the existing REID limit to the astronaut population instead of individual astronauts. This approach accommodates existing risk limits and risk assessment infrastructure; harmonizes NASA's approach with other US agencies, such as the USNRC; and is similar in philosophy to the "primary reference risk" concept recommended by the NAS/NRC in 1970 [107]. The proposed approach proceeds as follows:

1. Define a reference population that reflects the current NASA astronaut corps,

2. Compute the reference population mission REID probability distribution for the mission under consideration. If this value exceeds the NASA standard, decide whether to undertake mission (Level 2),

3. If mission passes Level 2, apply the reference population mission REID when making crew assignments based on reference population career REID (Level 3). Age- and sex-specific REIDs should be calculated and presented to all stakeholders for informed consent purposes (but are not used for crew assignment).

The purpose of the present study is to demonstrate the proposed astronaut radiation risk assessment process for a variety of existing or planned space missions. Various methods

of representing the reference population for the current astronaut corps are first explored. Next, the space radiation environments are determined and transported through appropriate vehicle and astronaut body self-shielding. Organ dose equivalents, based on NASA-defined quality factors pertinent for HZE radiation, are calculated, and REID distributions are found for specific astronaut age and sex combinations. Finally, the reference population mission REIDs are compared with age- and sex-specific REIDs to demonstrate the overall impact of adopting the revised risk assessment process.

2.2 Methods

2.2.1 Representation of Astronaut Corps Reference Population

Current NASA candidate and active astronauts were considered for the present study. There are currently 49 astronauts in these categories. Of them, 32 are men and 17 are women. At the end of 2018, the males ranged in age from 33 to 63, while the females ranged in age from 30 to 53.

The probability density function (pdf) and cumulative distribution function of male and female astronauts were fit using a discrete binning method as well as two continuous density approximation methods (Gaussian mixture models [108] and kernel density estimators (KDEs) [109]). The discrete pdf is given by

$$f(x_{i-1} < x_0 < x_i) = \frac{1}{N}\frac{M}{x_i - x_{i-1}}, \tag{2.1}$$

where the x_0 is the point of interest, N is the number of samples, and M is the number of occurrences of x_0 inside the interval $x_{i-1} < x < x_i$ with corresponding bin-width equal to $x_i - x_{i-1}$.

The Gaussian mixture model is a semi-parametric probabilistic model in which the pdf is approximated by a weighted sum of multiple Gaussian pdfs. In the case of Gaussian Mixture Modeling (GMM), *a priori* knowledge of the data is required. For the KDE, the probability density of a random variable at a certain point is a weighted average of all distribution

points that fall under a certain distance from the point of interest. The weight, or kernel, is adjusted based on the distance of the sample points from the point of interest. The density function of the KDE is given by:

$$f(x_0) = \frac{1}{Nh} \sum_{i=1}^{N} K(x_i) \frac{x_i - x_0}{h}, \tag{2.2}$$

where x_0 is the point of interest, N is the sample size, and h is the chosen distance from the point of interest and also known as the bandwidth of the system. The parameter K is the system kernel. In this work, the Epanechnikov and Gaussian kernels were used. The Epanechnikov kernel is given by

$$K(x) = \frac{3}{4}(1 - x^2), \tag{2.3}$$

where $|x| < 1$ while, Gaussian kernel is given by

$$K(x) = \frac{1}{\sqrt{2\pi}} \exp(-\frac{x^2}{2}), \tag{2.4}$$

where $|x| < \infty$.

2.2.2 Space Missions Addressed in the Present Work

Three mission profiles were considered, ranging from short term to long term. These missions included a one-year ISS mission, with REID evaluated in the ISS crew quarters in Node 2 (nominal shielding); at the ISS Radiation Assessment Detector location in the US Lab (heavily shielded); and in the ISS airlock (lightly shielded). Missions outside of LEO that were considered included a 21 d mission to cis-Lunar space and a 900 d mission to Mars, consisting of 200 d transit from Earth to Mars, a 500 d surface stay on Mars, and then a 200 d transit from Mars to Earth. The Mars mission was separated into three mission segments (two transits and one surface stay) for analysis. Both of the transit missions were heavily shielded while the surface stay mission was lightly shielded with shielding levels similar to that of ISS airlock location.

Each mission was specified to take place during solar minimum and solar maximum to evaluate the impact of changes in solar activity on REID. These periods were defined by inspecting historical monthly Oulu Neutron Monitor (http://cosmicrays.oulu.fi) count rates. The maximum in count rate was found to occur in August 2009, while the minimum in count rate was found to occur in November 1989. The time periods for all missions were centered on August 1, 2009, for solar minimum and November 1, 1989, for solar maximum.

2.2.3 Space Radiation Environments

Analyses for the present study were executed using the Multi-environment cancer Risk analysis Tool (MeRiT) infrastructure [110], developed and maintained by the Space Radiation Analysis Group at NASA Lyndon B. Johnson Space Center. MeRiT is an end-to-end space radiation assessment tool that encompasses environment specification, shield specification, radiation transport, radiation dosimetry, and radiation risk calculations.

In this study, geomagnetically-shielded GCR and trapped protons were used as the boundary condition environments in LEO, while free-space GCR was used for the other missions. To generate the appropriate free-space GCR environments, the Badhwar-O'Neill 2014 [4] model was used with direct date input. For the ISS missions, the GCR spectrum was modified to account for geomagnetic shielding throughout the ISS orbit. The AP8 [111] trapped proton model, which has been modified by NASA to account for solar activity levels intermediate to solar minimum and solar maximum, was used to generate the trapped proton environment. An updated model of the trapped proton environment is available [112], but it has not yet been incorporated into NASA's radiation risk assessment infrastructure.

2.2.4 Computational Phantoms and Vehicle Shielding

To properly represent astronaut organ dose equivalent, shielding from both the space vehicle and astronaut body must be considered. Body-self shielding distributions were represented using the Male Adult voXel (MAX) and Female Adult voXel (FAX) computational human phantoms [113]. Previously, convergence studies for organ dose point sampling in the context

of space radiation exposure evaluations were performed by other researchers [114]. For the present work, 42 rays and 968 rays per organ dose point were sampled for ray tracing the computational human phantoms to account for astronaut body self-shielding.

Vehicular shielding varied according to mission. For ISS missions, an advanced computer-aided design (CAD) model of the ISS was ray traced to generate one-dimensional shield distributions. For the cis-Lunar space missions, a CAD model of Orion Multi-Purpose Crew Vehicle (MPCV) was coupled with a CAD model of the European Service Module, and one crew seat location was ray traced. Finally, for the transit segments of the Mars missions, the MPCV was coupled with a notional Deep Space Habitat (DSH) consisting of ISS laboratory, node, and airlock modules, while the Mars surface vehicle shielding consisted only of the DSH. One vehicle point was ray traced for the Mars transit configuration and one vehicle point was ray traced for the Mars surface vehicle configuration. All vehicle shielding distributions were expressed in terms of aluminum equivalent thickness.

2.2.5 Radiation Transport and Dosimetry

NASA's high charge and energy deterministic space radiation transport code, HZETRN [2, 3], is used by MeRiT to simulate transport and dosimetry. HZETRN simulates transport of heavy ion spectra through user-defined material shielding and computes point absorbed dose and point dose equivalent using NASA-defined quality factors [12]. For ISS, cis-Lunar, and transit segments of the Mars missions, HZETRN was used to generate an interpolation database for heavy ion fluxes at various material thicknesses. For the Mars surface segment of the Mars missions, the GCR spectra were transported through the Martian atmosphere on a ray-by-ray basis to more accurately represent the radiation environment impinging on the DSH. Organ dose equivalents were then calculated as an average of the point dose equivalents computed by HZETRN.

2.2.6 Risk Assessment

MeRiT incorporates the NSCR-2012 [12] methodology for calculating REID point estimates and distributions taking into account the numerous sources of uncertainty. For each mission, a database of organ-specific and total REID for males and females of astronaut-relevant ages was constructed, each with 50,000 entries. To calculate the population-combined REID for a particular mission, the following steps were taken:

1. Randomly select sex using the relative fractions of male and female astronauts,
2. Randomly select astronaut age given the astronaut sex,
3. Construct the total REID cumulative distribution function (CDF) for selected age and sex,
4. Randomly select total REID for selected age and sex using inverse CDF method and store value.
5. Repeat previous steps for N samples, and
6. Calculate upper 95% tolerance limit from N samples of total REID.

2.3 Results

In this section, the effect of choice of population age distribution fitting method is examined. REID associated with various space missions are presented. The REID probability distribution functions for various ages of both sexes for the Mars mission at solar maximum and the pdf of the population-combined REID for this mission are shown.

2.3.1 Analysis of Different Fitting Methods

Figure 2.1 shows the population-combined REIDs for Mars mission in solar minimum and solar maximum boundary conditions using various curve-fitting tools investigated in our study. The 42-ray and 968-ray dose point sampling methods were evaluated. Discrete and

continuous curve-fitting methods provide almost identical results. The population-combined REID was calculated for all these cases using five different random seeds each with the sample size of 100000. In Figure 2.1, averages of these simulations are shown, with the error bars representing one standard deviation.

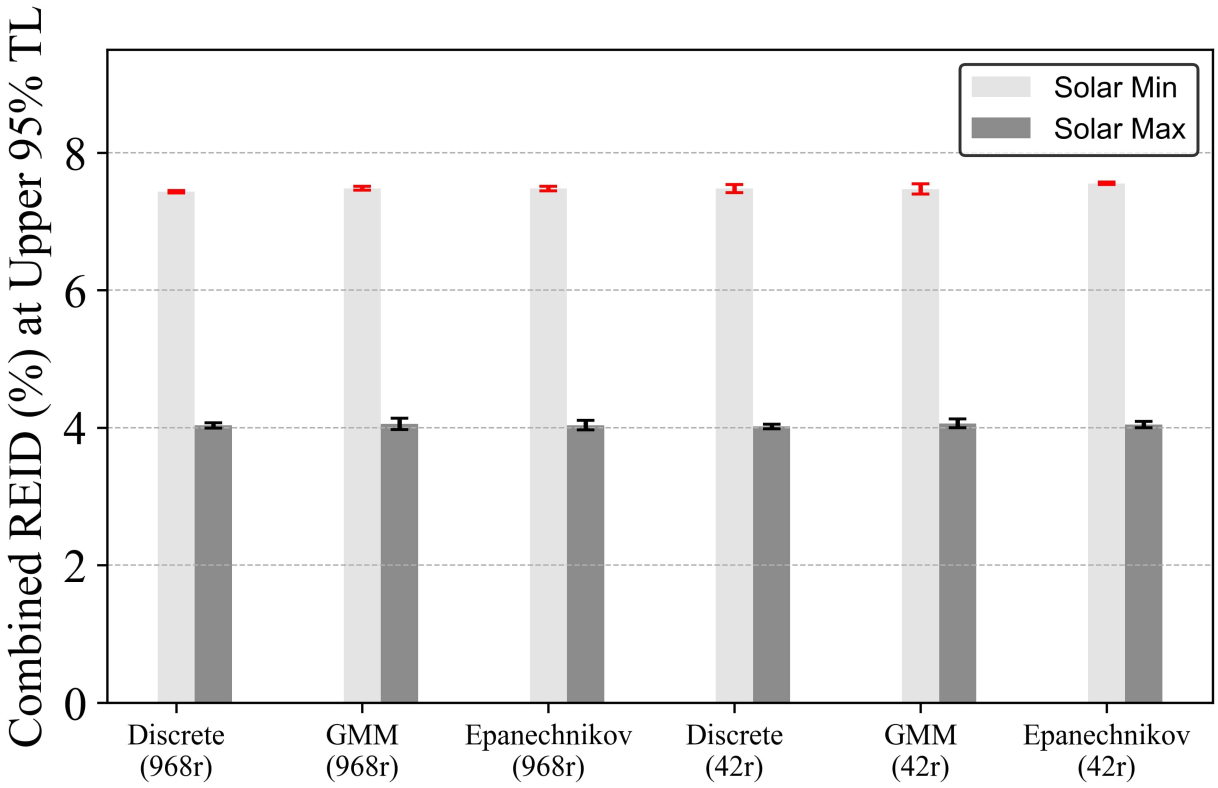

Figure 2.1: Comparison of different fitting methods for 900-day Mars mission in solar minimum and solar maximum boundary conditions.

2.3.2 Low Earth Orbit and Cis-Lunar Missions

In Figures 2.2 and 2.3, the age-dependent REIDs for male and female astronauts for one-year mission in the ISS airlock location are shown for the LEO radiation environment, consisting of a combination of GCR and trapped proton radiation. Similar results are observed for the other ISS locations. The age-dependent REIDs are all below NASA's REID limit. At a particular age, the female REID is higher than the corresponding male REID due to higher radiosensitivity as indicated by the underlying epidemiology. The population-

combined REID lies somewhere in between male and female risk distributions for ages less than about 55 years. Figure 2.4 shows that for all one-year LEO missions and the cis-Lunar missions, the REID is well below NASA's limit. Depending on age and sex, NASA astronauts could participate in anywhere between one and six one-year ISS missions with no need for waiver.

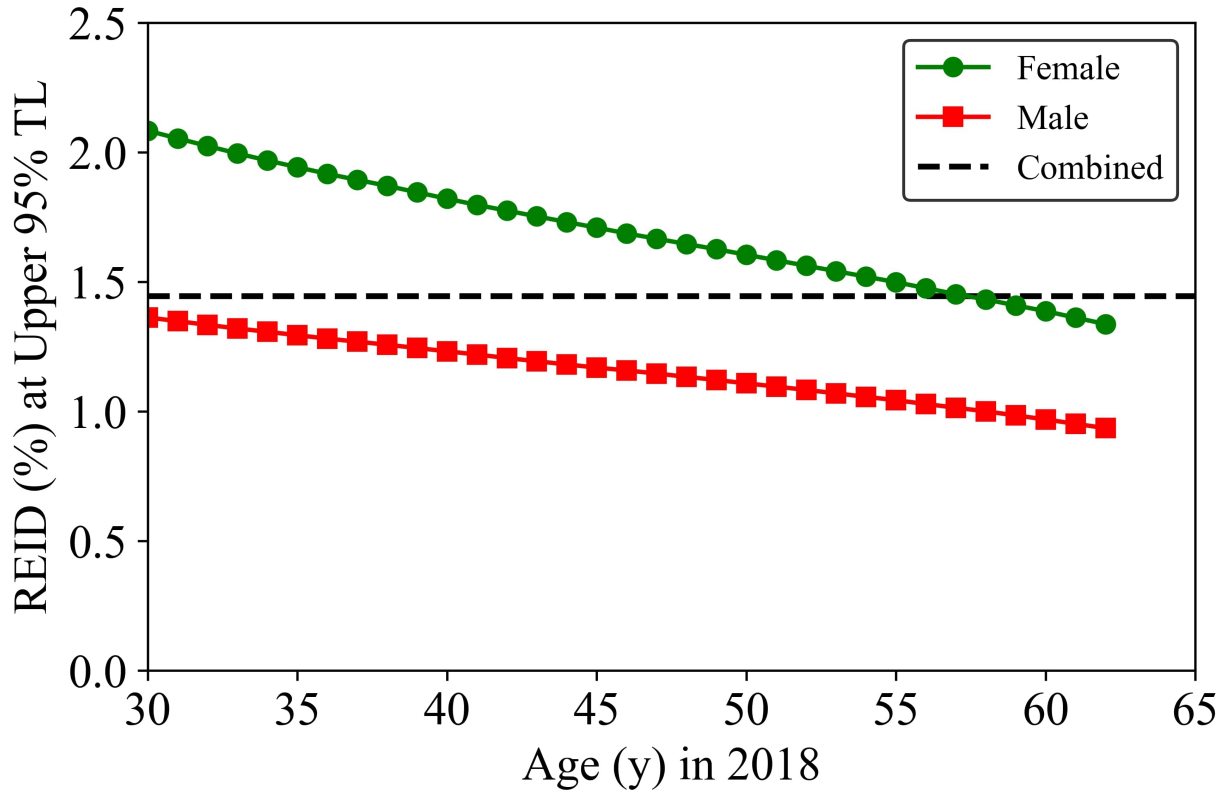

Figure 2.2: REID for male and female astronauts for 1-year space mission at ISS Airlock in solar minimum condition.

2.3.3 Mars Missions

Long-term deep space missions are of greatest concern for lifetime risk of radiation-induced health effects. For the solar minimum Mars mission, it is evident that the male, female, and population-combined risks surpass the NASA REID limit as shown in Figure 2.5. For the solar maximum Mars mission (Figure 2.6), only male astronauts 54 and older without previous spaceflight experience would be allowed to participate without a waiver. The population-

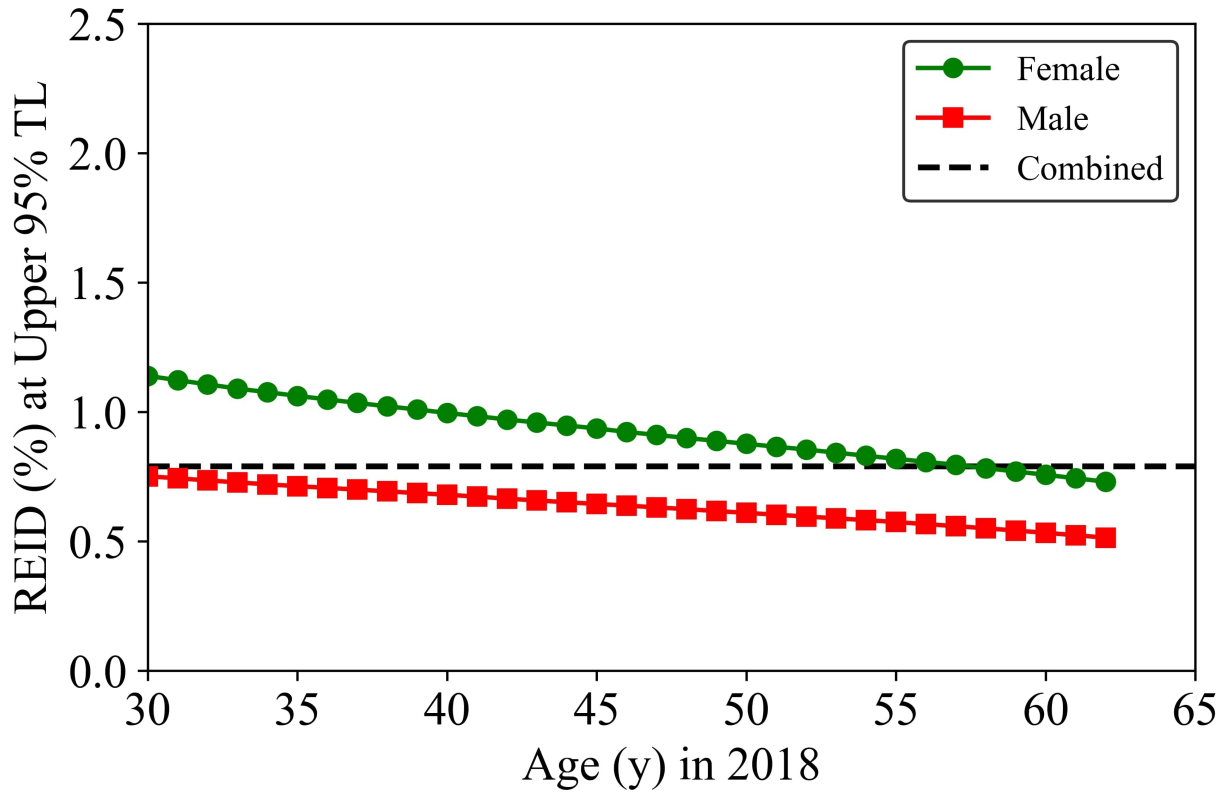

Figure 2.3: REID for male and female astronaut for 1-year space mission at ISS Airlock in solar maximum condition.

combined REID at the upper 95% TL is around 4%, which would require a mission waiver according to the proposed protocol.

2.3.4 Age-specific vs. Population-combined REID Distributions

Comparing the age-specific and population-combined REID distributions for the solar maximum Mars mission, it is observed that the population-combined distribution closely follows that of a 30-year-old male and 60-year-old female astronaut in case of Mars mission at solar maximum conditions (Figure 2.7). The organ-specific point estimate REIDs for 30-year-old male and 60-year-old female astronauts, shown in Figure 2.8, demonstrates how risks for different cancers compensate to result in very similar total risks. On the other hand, the comparison of organ-specific point estimate REIDs for the same mission at same boundary conditions for a 30-year-old female and 60-year-old male (Figure 2.9) shows that

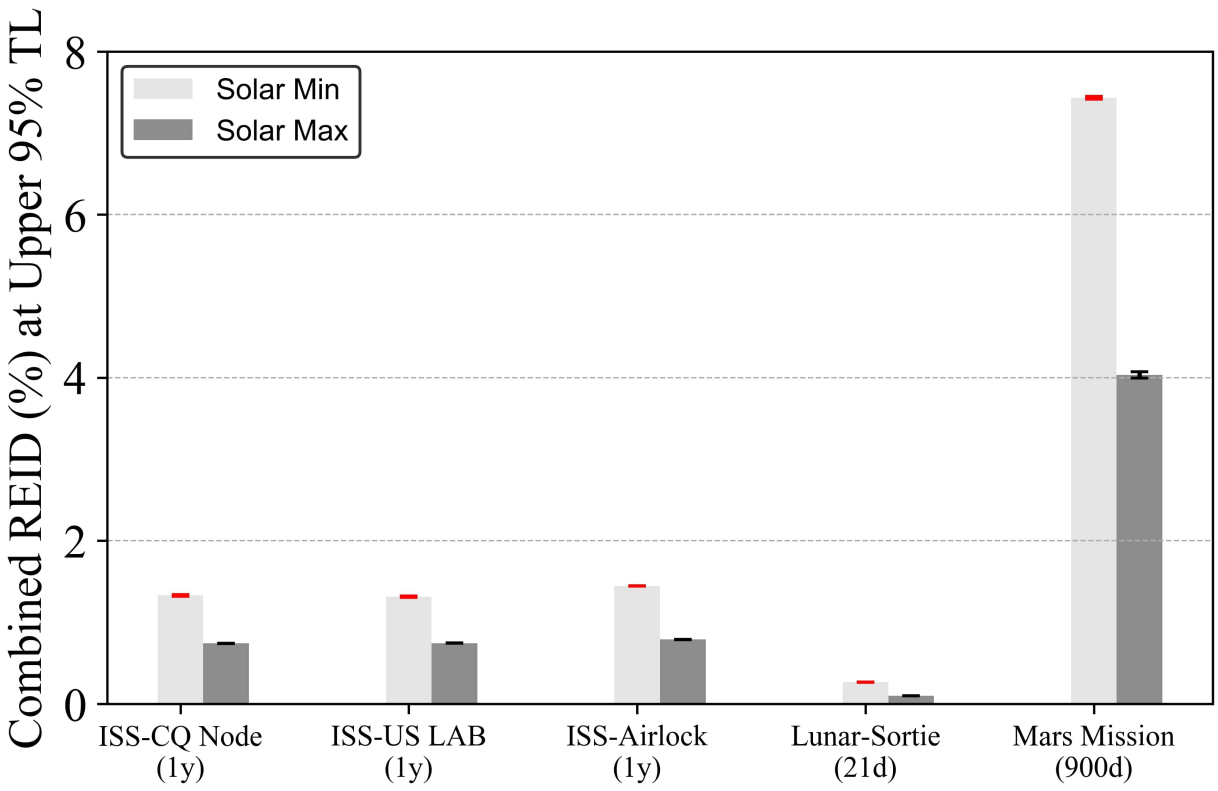

Figure 2.4: Combined risk for the Astronaut Corp for Different Space missions.

the organ-specific risks for 30-year-old female are higher compared to 60-year-old male and population-combined REID for each organ except BFO; therefore the total risk is also higher. The compensating effect is not observed in this comparison. In Figure 2.8 and Figure 2.9, the term Others represents the cumulative risk from organs such as thyroid, brain, esophagus, oral cavity, bladder and remainder organs. The population-combined total REID lies in between the REID of male- and female-only population-combined REIDs, as shown in Figure 2.10.

2.4 Discussion

2.4.1 Analysis of Different Fitting Methods

This work involves choosing discrete and continuous fitting methods for sampling the probability density function of age for the male and female astronauts in the astronaut corps.

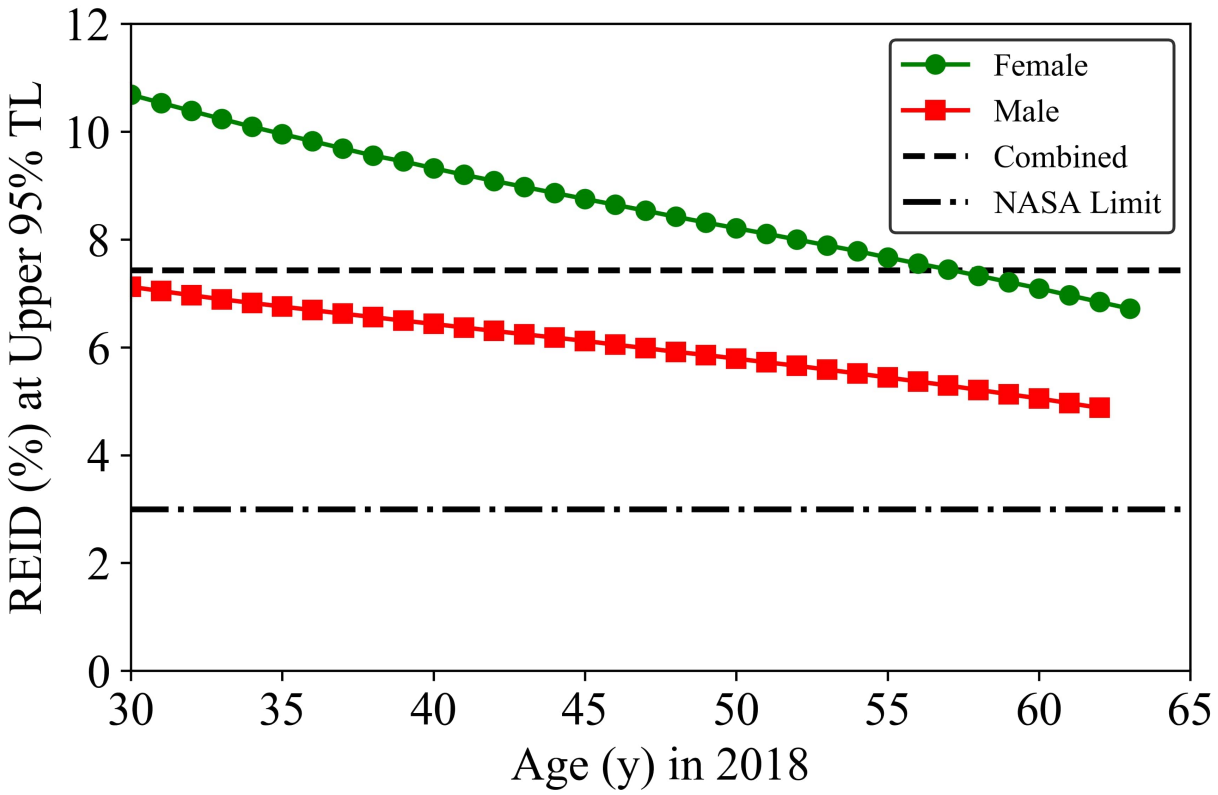

Figure 2.5: Risk profile for male and female astronauts for 900-day Mars mission in solar minimum condition.

Continuous distributions do not suffer from discretization errors in distribution sampling. Discrete methods are simple, but introduce errors as one point can only be inside a particular bin and outside of that bin it does not have any contribution. From Figure 2.1, it is evident that the continuous and discrete methods show minimal differences, demonstrating that discretization error in this system is negligible. Additionally, the results for 42 rays per dose point are very similar to the results for 968 rays per dose point.

2.4.2 Low Earth Orbit and Cis-Lunar Missions

REID for one-year ISS missions and short-term cis-Lunar missions for astronauts of both sexes and all ages is below the NASA limit; however, the crew member's career REID may exceed the limit depending on career mission profile. The REID associated with one-year ISS missions at solar minimum is almost twice that for the same missions at solar

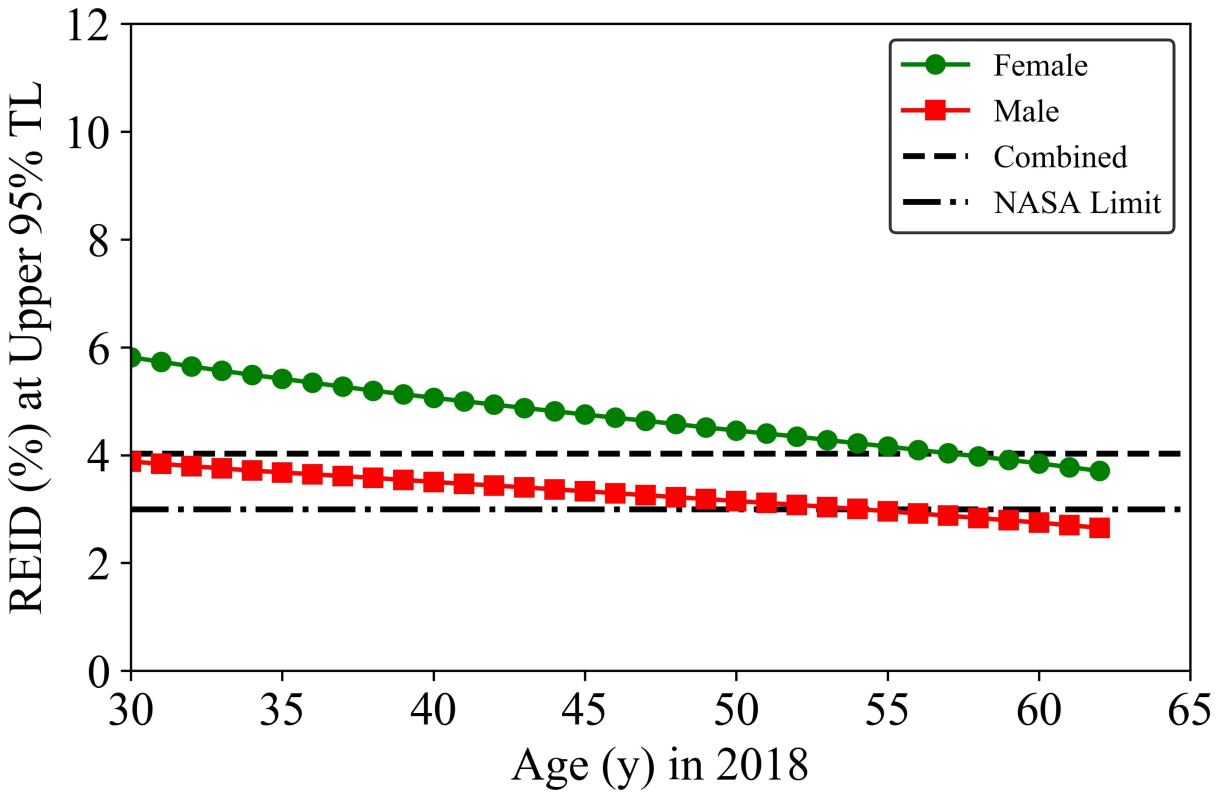

Figure 2.6: Risk profile for male and female astronauts for 900-day Mars mission at solar maximum condition.

maximum. REID is a strictly monotonically decreasing function of age for both male and female astronauts, and differences in REID for the two sexes decrease as age progresses.

2.4.3 Mars Missions

REIDs for the Mars missions mostly exceed NASA's career REID limit at the upper 95% TL, ranging from around 11% for 30-year-old females during solar minimum to less than 3% for older males during solar maximum. It is clear from the results that none of the female astronauts would be permitted to participate in a Mars mission without an individual waiver, while some males would be permitted to participate in the mission without a waiver during solar maximum. With the proposed approach, individuals are not restricted from participating in missions on the basis of age and sex; instead, the population-combined REID for their particular career mission profile is the determining factor.

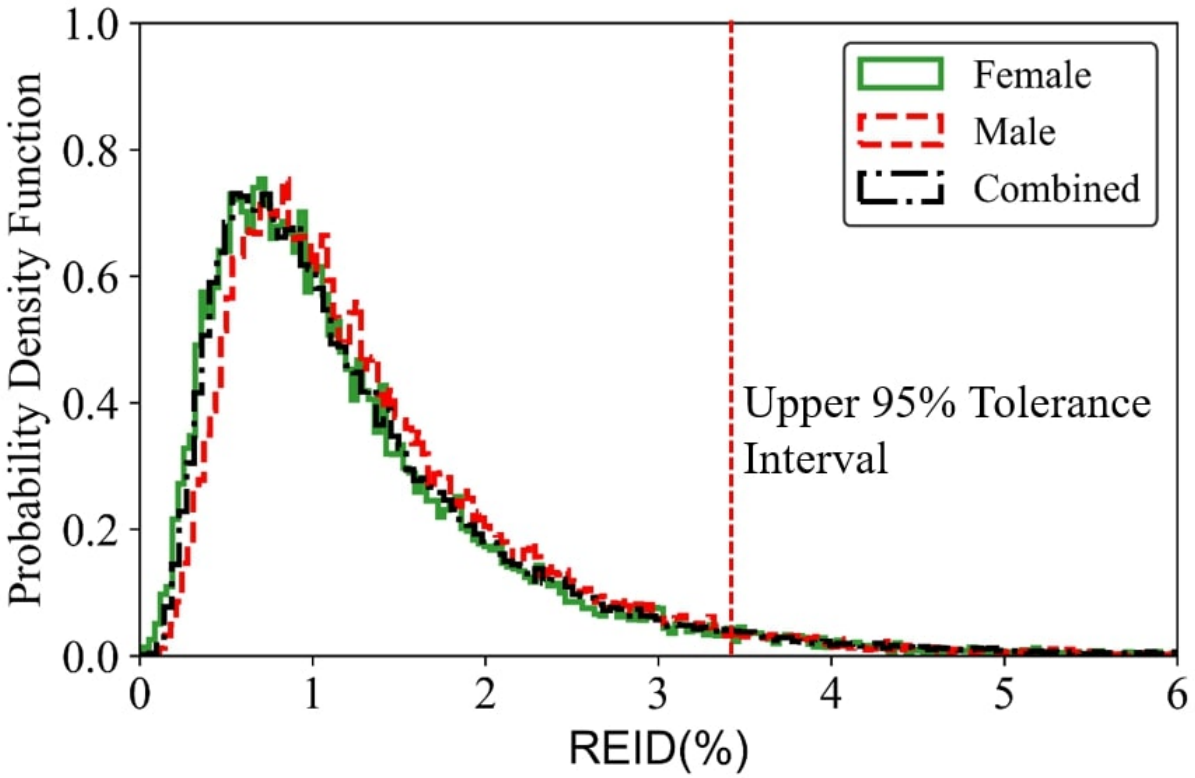

Figure 2.7: REID probability density functions for 30-year-old male, 60-year-old female, and combined population for 900-day Mars mission at solar maximum conditions.

When examining distributions of total REID, it is observed that the distributions for a 30-year-old male astronaut and 60-year-old female astronaut are very similar to the distribution for the population-combined REID. Inspection of organ-specific and point-estimate REIDs shows that while the 30-year-old male and 60-year-old female have similar total REIDs, there are compensating risks from different cancers. Specifically, the 60-year-old female REID from lung cancer and sex-specific cancers are larger than that for the male, while the 30-year-old male REID for leukemia (BFO), colon cancer, and those in the "Others" category are larger than that for the female. This is not observed when comparing the organ-specific REIDs for a 30-year-old female and a 60-year-old male, as most of the organ-specific risks and the cumulative risk of a younger female are higher than that of an older male. This difference is mostly attributed to the higher radiosensitivity of sex-specific organs and lungs for the younger female. While differences in radiosensitivity due to presence or absence of sex organs is reasonable, sex differences in organs that are present in both males and females

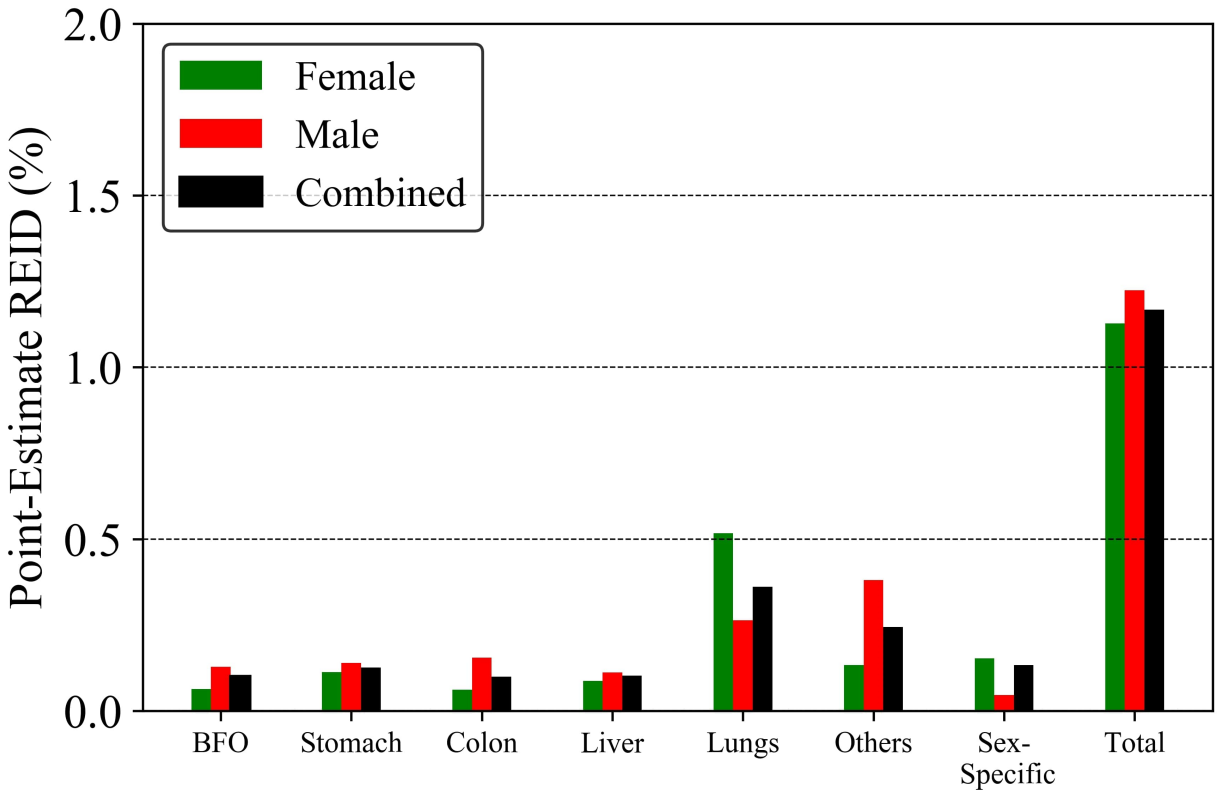

Figure 2.8: Organ-specific REID for 30-year-old male, 60-year-old female, and combined population for 900-day Mars mission at solar maximum conditions.

must be investigated to determine whether confounders, such as smoking status of the LSS population, are artificially enhancing or suppressing risk estimates for one sex. The proposed methodology ensures that these types of unexplained differences do not result in biased crew assignments. Similar differences are observed when comparing the male and female astronaut populations. As expected, the organ-specific REID for the total population appears to be consistent with a weighted average of the two sexes.

2.5 Summary

A novel, population-based approach to astronaut radiation risk assessment has been proposed to address persistent ethical issues with NASA's current implementation of the career REID limit due to radiation exposure. The approach was demonstrated for a variety of missions,

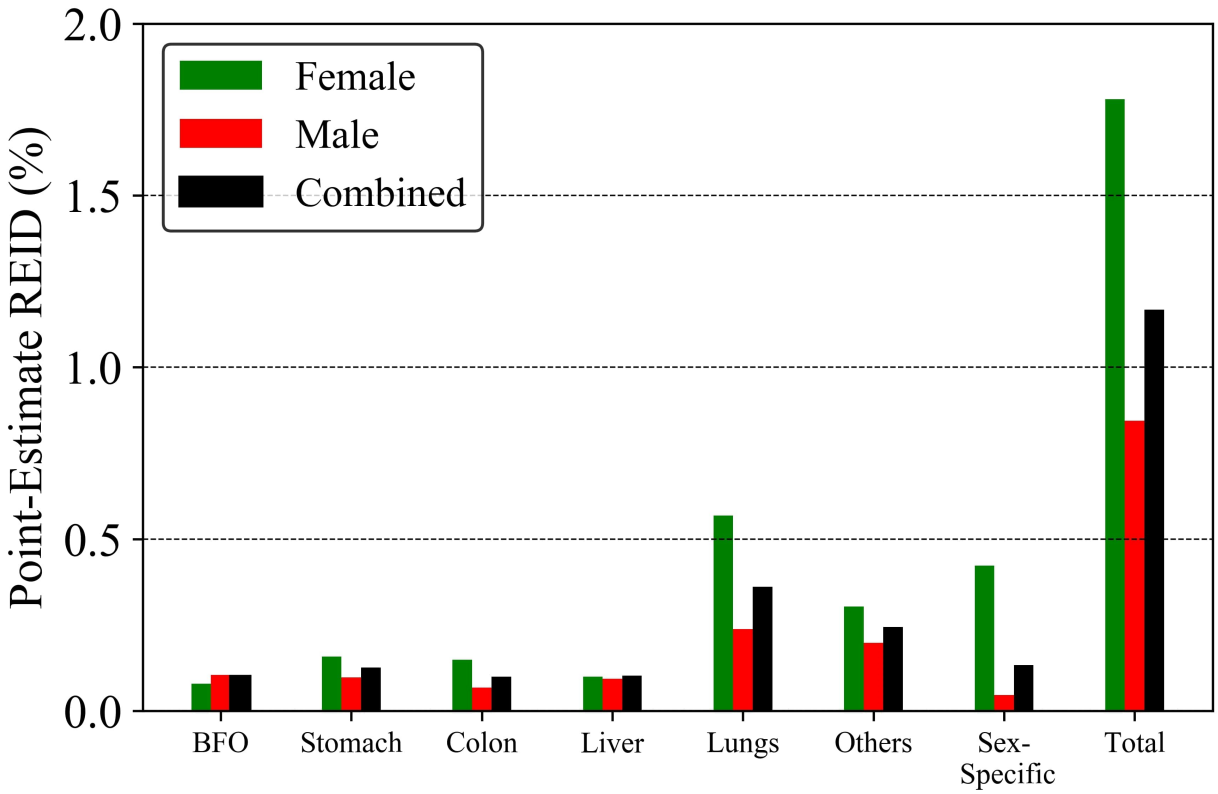

Figure 2.9: Organ-specific REID for 60-year-old male, 30-year-old female and combined population for 900-day Mars mission at solar maximum conditions.

and detailed analyses of total REID distributions and organ-specific REID at the upper 95% TL were investigated. The proposed methodology is consistent with NASA standards and risk evaluation infrastructure. Age- and sex-specific REID estimates would be retained for informed consent purposes but not used to determine crew eligibility for flight. It should be noted that astronaut career REID must be considered by evaluating lifetime risk from all space missions. Crew career mission profile therefore becomes the determining factor in crew assignments instead of the astronaut's age and sex.

For individual missions, only the Mars missions presented a challenge to NASA's 3% REID at the upper 95% TL limit. The population-combined REID for a Mars mission during solar maximum, during which time GCR fluxes are lowest, results in a 4% REID at the upper 95% TL. Examination of cancer-specific REIDs showed that lung cancer is the major contributor to both male and female radiation risks, with REID for female lung substantially

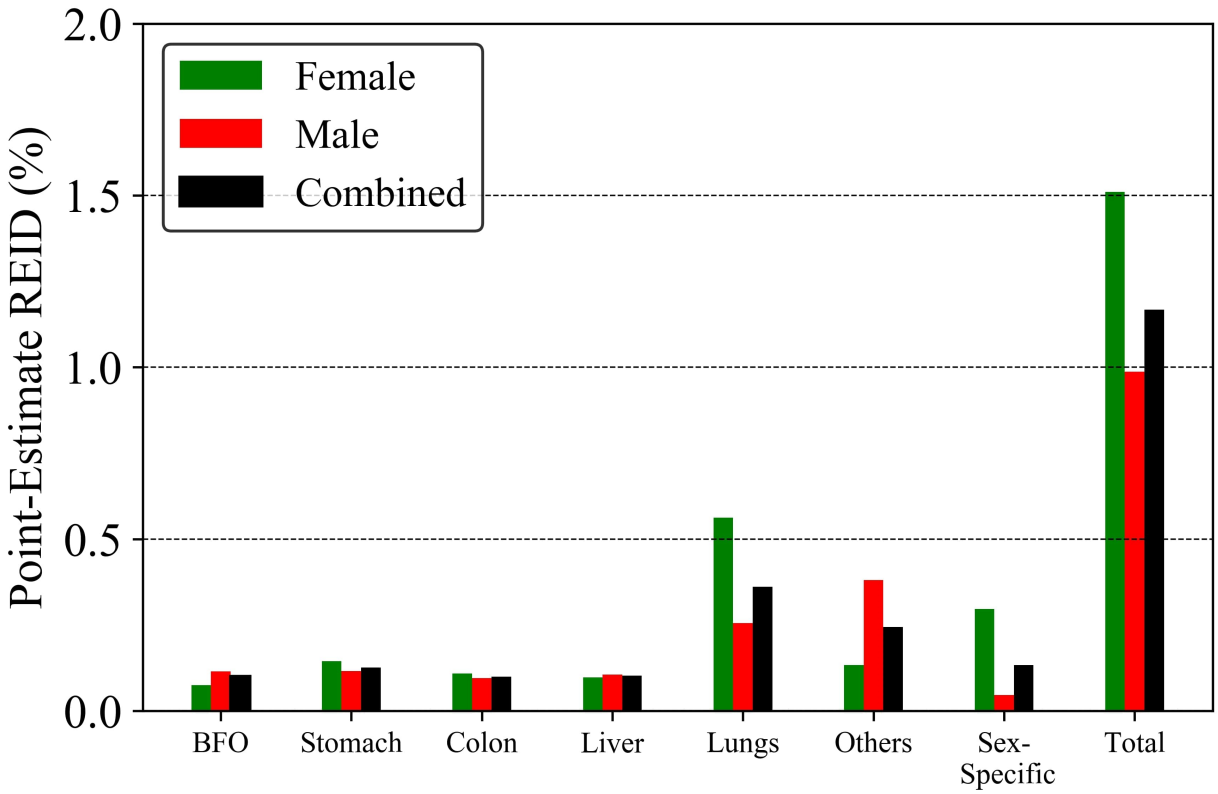

Figure 2.10: Organ-specific REID for astronaut corps males, astronaut corps females, and combined population for 900-day Mars mission at solar maximum conditions.

greater than that of the male lung. The differences in risks in organs common between males and females, which are not readily explained, are less important in the proposed methodology due to population averaging.

Chapter 3

Formulation of Scaling Law for Beam-like Configuration

3.1 Motivation

In this chapter, a scaling law, which is an essential computational tool for rapid evaluation of active shielding configurations, has been developed. This law establishes a mathematical relationship between a dimensionless scaling parameter that characterizes the active shield, the incoming ion, and a void area formed on a downstream detector due to the deflection of HZE ions by the applied field. This chapter examines a so-called one-dimensional (1-D) scaling law since the incoming ions are directed along a single vector to first investigate fundamental aspects of electrostatic active shielding. A simple dipole electric field was chosen to represent the active shielding configuration. It is observed that as the value of the scaling parameter increases, the linear relationship transforms into a sub-linear relationship. This chapter conclusively demonstrates a prototype method to experimentally evaluate the efficacy of an active shielding configuration in existing laboratory beamlines.

Experimental validation of the previously described active shielding configurations is unrealistic. No facility on Earth is capable of generating space-like, isotropic radiation environments. Therefore, determining the shielding efficacy of any active shielding configuration

is highly dependent on simulation prior to deploying the configuration in space. Previous work by Fry et al. [115] established a mathematical relationship between the electrostatic shielding and the corresponding protected area. The scope of that study was limited to validating the particle propagator code [79] over a small subset of ion-energy combinations and applied potential available at a typical accelerator-based facility. In this work, that scope is extended by investigating combinations of ions, energies, and applied potentials encountered at accelerator-based facilities on Earth (accelerator-based parameters) as well as parameters relevant for space (space-based parameters).

Any useful electrostatic shielding configuration is likely to be too large to test at beamline facilities on Earth, and so the configurations would need to be significantly scaled down for testing purposes. To ensure that the scaled-down tests conducted on Earth (and corresponding simulations) are translatable to actual shielding configurations to be eventually deployed in space, a scaling law must be established. This scaling law relates the properties of the electrostatic shield, the incoming ions, and the resulting shielding efficacy. Although the scope of this work is limited to simulation in a beam-like configuration, the results have implications for three-dimensional (3-D) active shielding configurations, as will be discussed in later chapters.

3.2 Hypothesis

To establish a relationship between active shielding configuration characteristics and corresponding deflection ability, a dimensionless scaling parameter, f_s, is proposed. This parameter is proportional to the applied potential and inversely proportional to the rigidity of the incoming ion. The mathematical expression of the scaling parameter is defined as

$$f_s = \frac{ZeV_{dip}}{(\gamma^2 - 1)E_0/\gamma}, \tag{3.1}$$

where Z, E_0, and γ respectively refer to the charge state, rest mass energy, and Lorentz factor (as described in Equation 1.43) for the incident ions. The elementary charge is denoted by

e. The active shielding configuration of interest in this study is a simple electric dipole, consisting of two oppositely charged spheres of the same charge magnitude $|Q|$. The applied potential V_{dip} refers to the magnitude of the potential applied to each sphere with respect to a common reference point. The scaling parameter represents ratio of the impulse of the electric field (V_{dip}/v), and the rigidity of the particle, where v is the relativistic speed of the particle. Rigidity of the particle is defined by the ratio of momentum and total charge of the particle (p/Ze). Therefore, the scaling parameter is a quantity that indicates the ability of the electric field to deflect a charged particle of a given rigidity. The lower the value of f_s, the more efficient is the electrostatic field, as less magnitude of electric field is required to deflect a particle of certain rigidity.

As incoming charged particles are acted upon by the electric field generated by the dipole, an area devoid of radiation appears downstream from the radiation source. This region is referred to as the "void region" or "protected area". Two different types of protected areas are shown by the low-flux density contiguous region bounded by the red curves in Figures 3.1 and 3.2, demonstrating the shapes of the protected areas in the linear and sub-linear regions of the 1-D scaling law, respectively. The shape and the size of the void region changes with the properties of the beam and the active shielding configuration. The area of the void region was chosen to represent the shielding efficacy of the active shielding configuration. This quantity is calculated using data from simulation. For convenience, a normalization of the protected area is defined as A/a, where A is the true area of the void region and a is the radius of the identical dipole spheres comprising the dipole. This normalization is performed to account for differences in conductor sphere size, as it is later shown that the area of the void region depends upon the total charge on the dipole conductor surfaces and the total charge is linearly proportional to the radius of the spherical conductors. A number of simulations were performed to formulate the 1-D scaling law. The following paragraphs describe the methods used to conduct these simulations and perform the analysis necessary to extract the normalized protected area (A/a), which is used to characterize the shielding effectiveness.

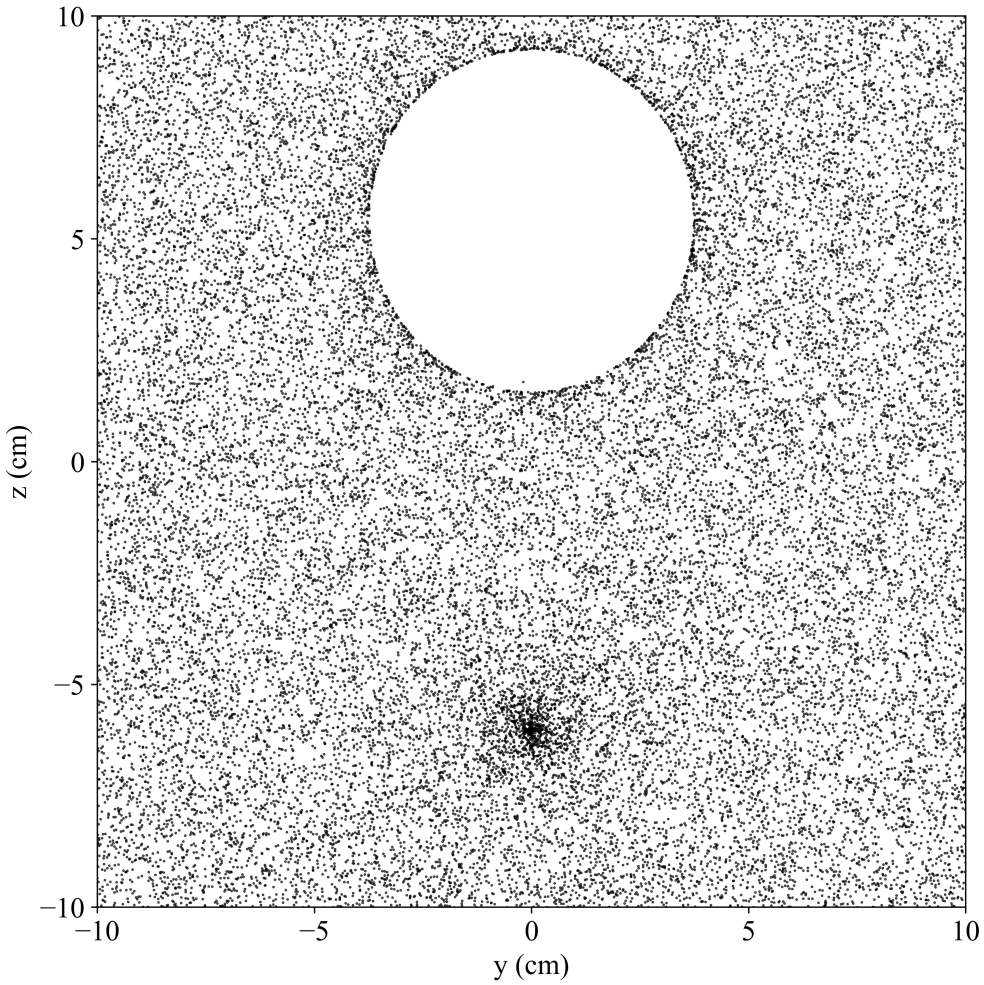

Figure 3.1: Shape of the protected area below knee region

3.2.1 Source Configuration

All simulations were performed with mono-directional beams of fully-stripped positively charged ions. The ion beam was simulated using a disk-shaped source with 0.15 m radius. Initial particle positions were randomly generated on the plane of the disk. The beam radius remained constant over most of the simulation domain except in some cases where the protected area surpassed the beam size. In these cases, the beam radius was increased to better characterize the protected area. Changes in the beam radius greater than half the center-to-center distance between the two dipole spheres had no discernible effects on the calculation of the void area as long as the flux density of the source was constant. Once

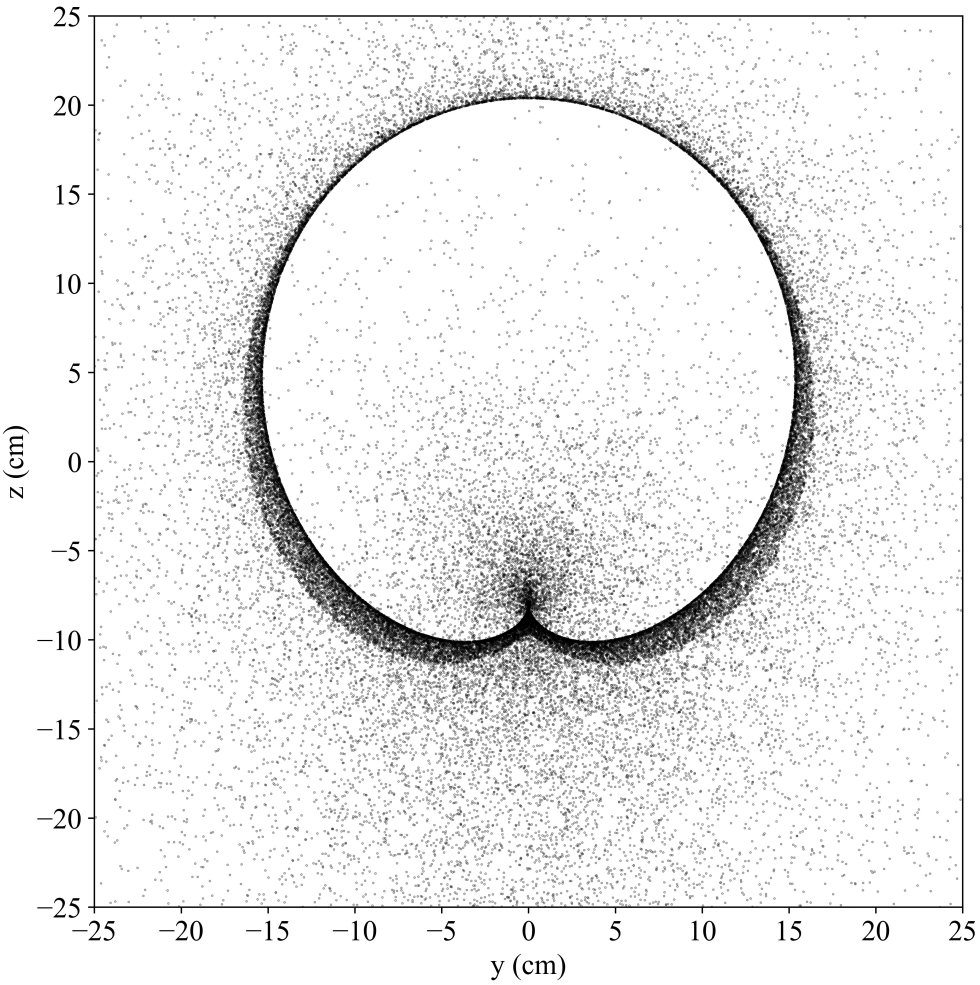

Figure 3.2: Shape of the protected area above knee region

generated, the particles were directed along the $-x$-axis toward the detector plane. The distance between the center of the source disk and the center of the dipole axis was set to 2.0 m throughout this work. This distance was selected because the source disk was far enough away from the dipole such that the electric field can be considered negligible, but close enough to limit the total number of time steps required to accurately transport each particle.

3.3 Simulation Geometry

Figure 3.3 represents the physical configuration for the simulations conducted in this study. The dipole was placed along the z-axis with the dipole centroid located at the origin. The sphere radius of the virtual spherical conductors was set to be equal to the surface-to-surface distance between them (ℓ_{SS}). A mono-directional beam of fully-stripped positive ions are directed in the $-x$-direction. A thin detector volume of thickness Δx is located at a distance D downstream from the dipole structure; this volume is used to record the (y, z) position of each particle as it passes through. The (y, z) positions on the detector plane are eventually used to generate images of the void area.

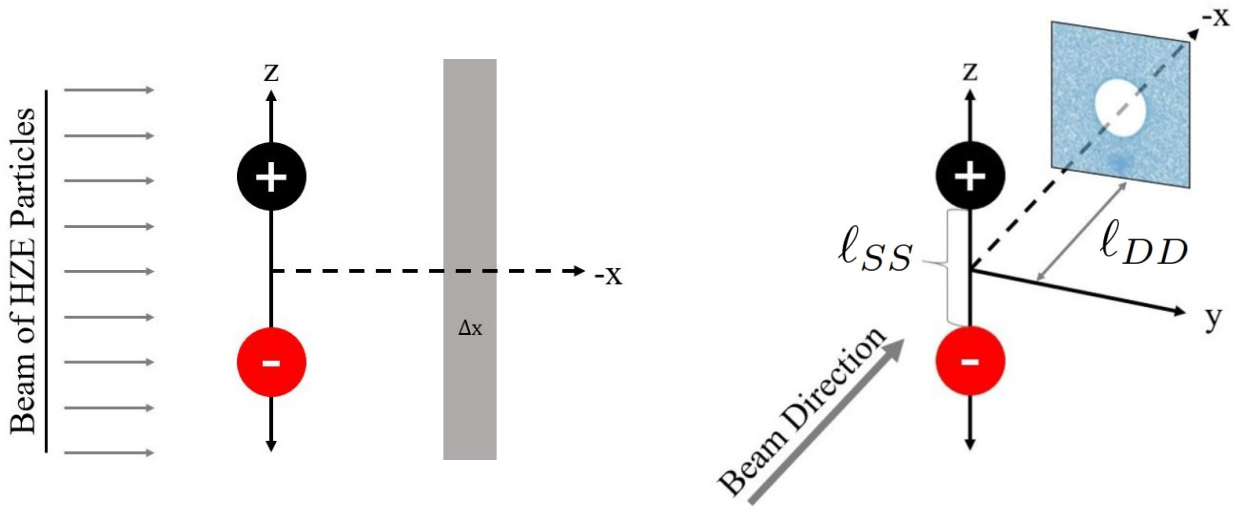

Figure 3.3: Coordinate system and schematic for all simulations

3.4 Simulation Domain

The simulation domain for this chapter was divided into two categories: accelerator-based ion energies and space-based ion energies. For accelerator-based ion energies, the maximum kinetic energy was chosen to be equal to 28 MeV/n. This energy range was chosen because the experimental facility which will be used to validate the simulation (Brookhaven National Laboratory's Tandem Van de Graaff facility) has maximum energy of protons equal to

28.5 MeV(https://www.bnl.gov/tandem/capabilities/ions.php). For space-based energies, it was hypothesized that 1.5 GeV/n is the maximum energy of the ion that could be shielded against using active shielding methods, while keeping the power requirement within a realistic limit. The energy range that contributes a significant fraction total effective dose is 30 MeV/n to 1.5 GeV/n [13]. For these reasons, the range of accelerator-based energies was restricted to the range 1 MeV/n to 28 MeV/n, whereas the range of in-space energies was defined as 28 MeV/n to 1500 MeV/n as shown in Tables 3.1 and 3.2 to keep continuity between accelerator-based and space-based parameters. Two values of sphere radius equal to 0.1 in and 1.0 in were chosen for simulation as these two values of sphere diameter are the minimum and the maximum sphere diameters that were used for the validation phase of the ASPP code [79]. For each of the sphere diameter values, the surface-to-surface distance (ℓ_{SS}) between two monopole spheres was kept equal to the radius of the charged sphere. These two particular dimensions were used for the simulations as spheres with these dimensions were available for the measurement at the experimental facility.

The greatest potentials that can be applied to the surface of the isolated spheres were chosen to be ±75 kV and ±1000 kV for accelerator- and space-based energies respectively. This assumption was supported by the fact that in the case of accelerator-based facility, 75 kV was the highest potential available. The reason for choosing ±1000 kV as the upper limit for the space-based parameters was that this value was thought to be realizable for application in space using current high-voltage power supply technology. In simulation, the ℓ_{SS} was kept equal to the radii of the charged monopole spheres (Tables 3.1 and 3.2). Therefore, the denominator term in Equation 3.3 becomes equal to 2 for a value of $\delta = 1$. To account for the charge scaling factor of 2, the potential applied to each sphere in the dipole structure was varied from ±1 kV to ±37.5 kV for the accelerator-based parameter space. For the space-based parameter space, the potential was varied from ±1 kV to ±500 kV. Both parameter spaces are shown in Tables 3.1 and 3.2. The HZE projectiles $^{1}H^{+}$, $^{4}He^{2+}$, $^{12}C^{6+}$, and $^{56}Fe^{26+}$ were chosen for the simulation. The rationale behind selecting these ions is that they have substantial GCR abundances and/or high quality factors that can result in significant organ dose equivalent and radiation risk [13, 20].

Table 3.1: Accelerator-based parameter space

Species	$^{1}H^{+}$, $^{4}He^{2+}$, $^{12}C^{6+}$, $^{56}Fe^{26+}$
Kinetic Energy [MeV/**n**]	1 - 28
Dipole Sphere Voltage (V_{dip}) [kV]	1 - 37.5
Dipole-to-Detector Distance (ℓ_{DD}) [**m**]	1.2 - 2.2
Dipole Sphere radius (a) [in]	0.1 and 1.0
Dipole Sphere Surface-to-Surface Distance (ℓ_{SS}) [in]	0.1 (for $a = 0.1$) and 1.0 (for $a = 1.0$)

Table 3.2: Space-based parameter space.

Species	$^{1}H^{+}$, $^{4}He^{2+}$, $^{12}C^{6+}$, $^{56}Fe^{26+}$
Kinetic Energy [MeV/**n**]	28 - 1500
Dipole Sphere Voltage (V_{dip}) [kV]	1 - 500
Dipole-to-Detector Distance (ℓ_{DD}) [m]	1.2 - 400
Dipole Sphere radius (a) [in]	0.1 and 1.0
Dipole Sphere Surface-to-Surface Distance (ℓ_{SS}) [in]	0.1 (for $a = 0.1$) and 1.0 (for $a = 1.0$)

3.4.1 Radiation Transport

For radiation transport, ASPP [79], a relativistic charged particle code was used for all simulations. This code allows the user to simulate the motion of charged particles with relativistic velocities under the influence of electromagnetic fields. The Velocity-Verlet method was used to perform particle propagation. The advantages of the Velocity-Verlet method are that the method is symplectic and sufficiently balances memory-storage with computational speed [80]. The radiation transport algorithm begins by assigning each particle a position and velocity based on the ion energy and source details specified by the user. These particles are propagated through the electric field, which is calculated for each particle at every time step, for a fixed number of time steps. The length of each time step is specified by the user. For this study, the time step was set to be 5×10^{-12} s, as this was determined to be small enough to produce accurate results in terms of each particle's momentum phase space subjected to the electric field and large enough to limit computation time. The number of time steps in each simulation was varied according to the predicted amount of time necessary for a particle to cross the detector volume, depending upon the initial velocity of each

particle and the dipole-to-detector distance (ℓ_{DD}). As previously mentioned, when particles intersect the detector volume of depth Δx, their (y, z) positions are recorded. The depth Δx was selected such that Δx was always greater than the distance traversed by a particle in a single time step to ensure that no particle would skip the detector volume.

The active shielding configuration used to conduct this work employs spherical, charged conductors. The electric field vector $\vec{E}$ at position $\vec{r}$ is calculated by assuming the spheres can be represented by a collection of N point charges Q_i located at $\vec{r_i}$, i.e.

$$\vec{E}(\vec{r}) = \frac{1}{4\pi\epsilon_0} \sum_{i}^{N} \frac{Q_i(\vec{r} - \vec{r_i})}{\|\vec{r} - \vec{r_i}\|^3}. \tag{3.2}$$

The total charge of each conductor can be related to its supplied potential, V_{dip} as

$$Q = \frac{4\pi\epsilon_0 a V_{dip}}{1 - \frac{1}{1+\delta}} \tag{3.3}$$

where Q is the total charge on the surface of the sphere, ϵ_0 is the vacuum permittivity, a is the radius of the spheres, and δ is the inner surface-to-surface between the two oppositely charged monopole spheres in units of a [79]. The term in the denominator arises because of the image charge effect of the two opposite polarity charges. It is evident from Equation 3.2 and Equation 3.3 that both the total charge on a sphere as well as the resulting electric field are linearly proportional to the sphere radius.

3.5 Image Processing Algorithm

The simulation domain for the 1-D scaling law is substantially large, with tens of thousands of distinct physical scenarios. To rapidly determine the void area for each simulation, an automated image-analysis method was developed. The image-analysis algorithm takes in coordinates from the detector and attempts to calculate the area of the void. The image segmentation and void area calculation method is described in detail below:

1. After completing an ASPP simulation, a simulated detector planar image is generated

using the (y, z) coordinates (Image 1),

2. Apply the Canny edge-detection algorithm [116] to Image 1 with a Gaussian smoothing parameter of 1 to generate Image 2, the edge,

3. Apply dilation and closing techniques to Image 2 using linear and circular structural elements to attempt to close the edge, generating Image 3, the closed edge,

4. Fill the closed edge and calculate the total number of pixels within it, and

5. Use the total number of pixels within the closed edge and a pixel-area to actual-area conversion factor to calculate the area of the void.

This image-analysis method gave accurate results for about 90% of cases.

Figure 3.1 and Figure 3.2 represent the different shapes of voids forms, an effect which manifests before and after a specific value of the scaling parameter, identified as the "knee value". The image-analysis algorithm used here is capable of capturing the shapes of the circular- and cardioid-shaped void areas and computing the respective areas.

3.5.1 Simulation Tools

This work required substantial computational resources to execute simulations. The Beocat high-performance computing system (HPC) located at Kansas State University was used for simulation. This substantial computational resource helped to run thousands of simulations in both shared and distributed memory (OpenMP and MPI) parallelization. The software 'Dakota' (Sandia National Laboratory, Albuquerque, NM) was used in conjunction with Beocat HPC to simulate all input files for both parameter spaces. Dakota can be used for parameter study, multi-dimensional optimization, and many other relevant applications [117]. Dakota is a software that can interface among multiple codes and run them in the desired manner. In our work, Dakota was utilized for reading the parameter space, generating the input files, executing the ASPP code, transferring the ASPP output (surface tally data) to the image-processing algorithm, and saving the output in a pre-defined location for user access.

3.6 Results

In this section, scaling laws for both accelerator- and space-based energies are developed and discussed. To demonstrate applicability across variations in dipole/detector geometry, scaling laws for several dipole-detector distances were developed. The full parameter space was divided into three sub-categories to establish a relationship between the scaling parameter and the protected area. For accelerator-based parameters, the energies and potentials were simulated where dipole-detector distance range was kept similar to what can be achieved experimentally (1.2 m to 2.2 m). In case of the space-based parameters, the energies and potentials were simulated, and the dipole-detector distance was set to a range relevant for actual space-based active shielding configurations (10 m to 400 m). The last set of simulations demonstrates the scaling law for both accelerator- and space-based parameters for a fixed dipole-detector distance (1.2 m). All results shown here were simulated with each sphere diameter set to 0.2 in unless otherwise specified. Also, the effect of changing conductor sizes for all ions was observed for a fixed dipole-detector distance in case of space-based energies to establish that the area increase in area is linearly proportional to an increase in the size of the conductor.

3.6.1 Scaling Law for Accelerator-based Parameters

Figures 3.4 and 3.5 demonstrate the 1-D scaling law for the accelerator-based parameters category. It is evident from the figures that the scaling law follows two trends, both of which can be described by a power-law curve-fit of the form $y = C_0 x^b$, where the fitting parameters are C_0 and b. The dashed and solid lines in these figures show the curve-fit using non-linear least-squares optimization. They show a linear function where the exponent is approximately 1 up to a certain value of f_s. For f_s greater than this value, a sub-linear trend is apparent where the exponent is approximately 0.67. This trend is reflected in Figures 3.4 and 3.5 where data were associated with the accelerator-based parameter space. The value of f_s where this phenomena occurs is identified as the knee value ($f_{s_{knee}}$). Table 3.3 demonstrates the knee-values for different accelerator-based parameters for various values of ℓ_{DD}. For

accelerator-based parameters, where ℓ_{DD} is equal to 1.2 m, this value (f_{sknee}) is around 10^{-3}. With higher value of ℓ_{DD}, the value of f_{sknee} decreases.

Table 3.3: The knee-values for different accelerator- and space-based parameters

Parameter space	ℓ_{DD} [m]	f_{sknee}	A/a [cm] at f_{sknee}
Accelerator	1.2	9.2×10^{-4}	5.56
Accelerator	1.6	7.4×10^{-4}	6.02
Accelerator	2.2	5.6×10^{-4}	7.07
Space	10.0	1.4×10^{-4}	5.71
Space	100.0	8.9×10^{-5}	47.26
Space	400.0	3.2×10^{-5}	64.21

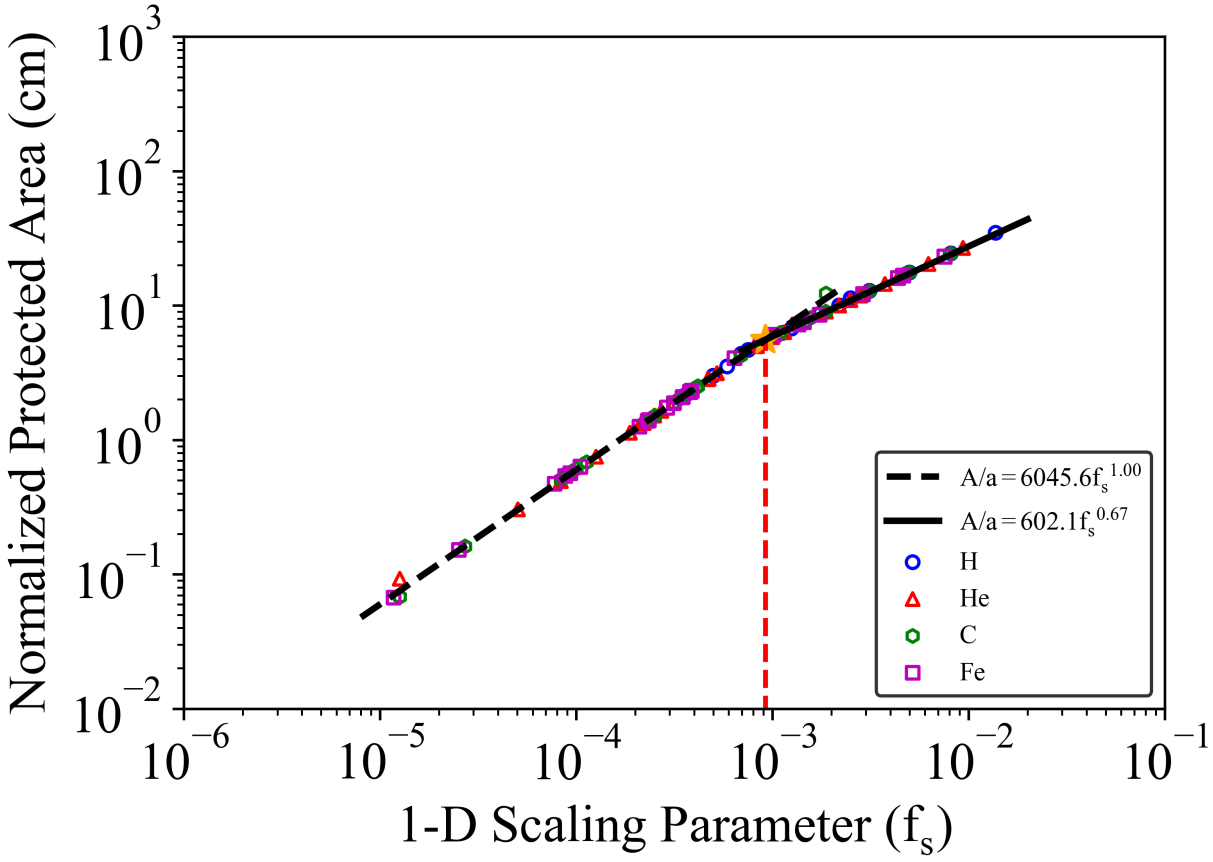

Figure 3.4: 1-D Scaling law with $\ell_{DD} = 1.2$ m for accelerator-based energies.

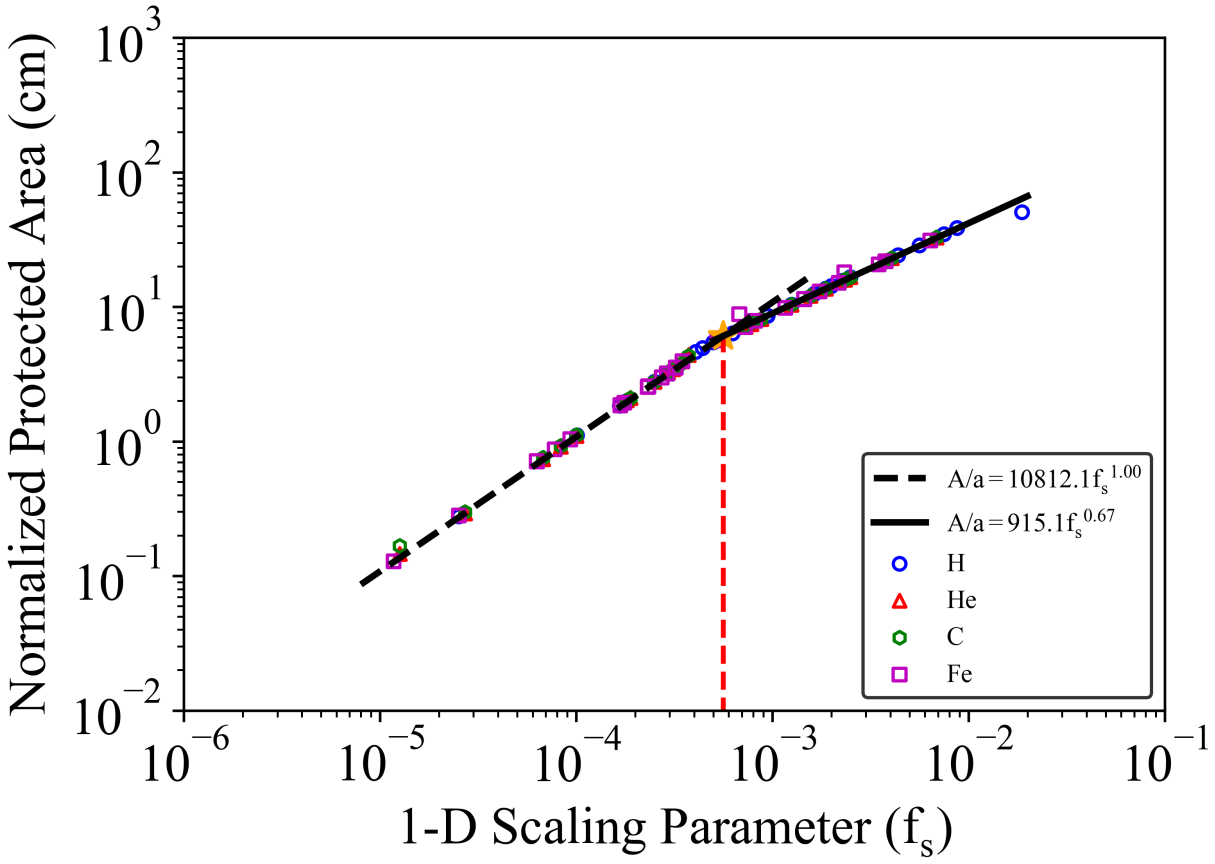

Figure 3.5: Validation of 1-D Scaling law with $\ell_{DD} = 2.2\,\text{m}$ for accelerator-based energies.

3.6.2 Scaling Law for Space-based Parameters

Figures 3.6, 3.7, and 3.8 demonstrate the 1-D scaling law for space-based scaling parameters. It was hypothesized that in order to reduce the required potential (power) without compromising the shielding efficacy, the source of the electric field needed to be placed further away from the spacecraft. To evaluate this claim, the value of ℓ_{DD} was varied from 10 m to 400 m. A similar partial linear trend was observed for these data. However, the value of f_{sknee} observed in the figures corresponding to the second parameter space category was reduced to about 10^{-4} (Table 3.3) for these sets of simulations, which is an order of magnitude smaller compared to the knee value of observed in the first category. A similar relationship between the ℓ_{DD} and f_{sknee} was also observed in case of space-based parameters as the value of the latter decreases with the increase in the value of the former. The phenomenon can be explained as the ℓ_{DD} was increased in the case of accelerator- and space-based parameters,

the deflected charged ions had to travel greater distances before coinciding with the detector after the initial deflection by the localized electric field. As the particles in the case of greater ℓ_{DD} get to travel more along the direction of initial deviation, the degree of deflection gets increases the time they reach the detector plane. This implies that for the same value of the 1-D scaling parameter, the protected area will be higher, explaining why the knee effect can be observed at a lower potential (lower value of scaling parameter) in case of the space-based parameters (significantly higher values of ℓ_{DD} compared to the accelerator-based parameters), as less electric field is required to achieve a similar degree of deflection compared to accelerator-based parameters. Larger void areas are observed at lower values of f_s for greater value of ℓ_{DD}. This also means that the shape of the void changes from circular to cardioid-like at lower values of f_s. In case of space-based parameters, there are some outliers in the scaling law plot especially at low value of f_s (around 10^{-6}), where A/a does not match the scaling law fit. The reason behind these scattered points is that the protected areas are so small for these values of f_s, the image processing algorithm did not accurately segment the protected area from background within a reasonable computation time.

3.6.3 Scaling Law for Combined Parameters

Figure 3.9 shows the 1-D scaling law for both the accelerator- and space-based parameter domains for ℓ_{DD} equal to 1.2 m for all ions. It is evident from Figure 3.9 that both data sets coincide and therefore demonstrates that deflection of a high-energy ion by a high-magnitude potential can be modeled using a low-energy ion and low-potential if the scaling parameter and the value of ℓ_{DD} between two cases are identical. This outcome instills confidence that a space-based active shielding configuration can be validated using accelerator-based facilities with a scaled-down configuration for future space applications. In later chapters, 3-D active shielding configurations are discussed which can be expressed as a function of a scaling law and their scaled-down versions can be tested in a accelerator facility. Also, it is noticeable that in Figure 3.9, the value of the knee for space-based as well as accelerator-based parameters is $\sim 10^{-3}$. This phenomenon shows that the magnitude of ℓ_{DD} has a strong

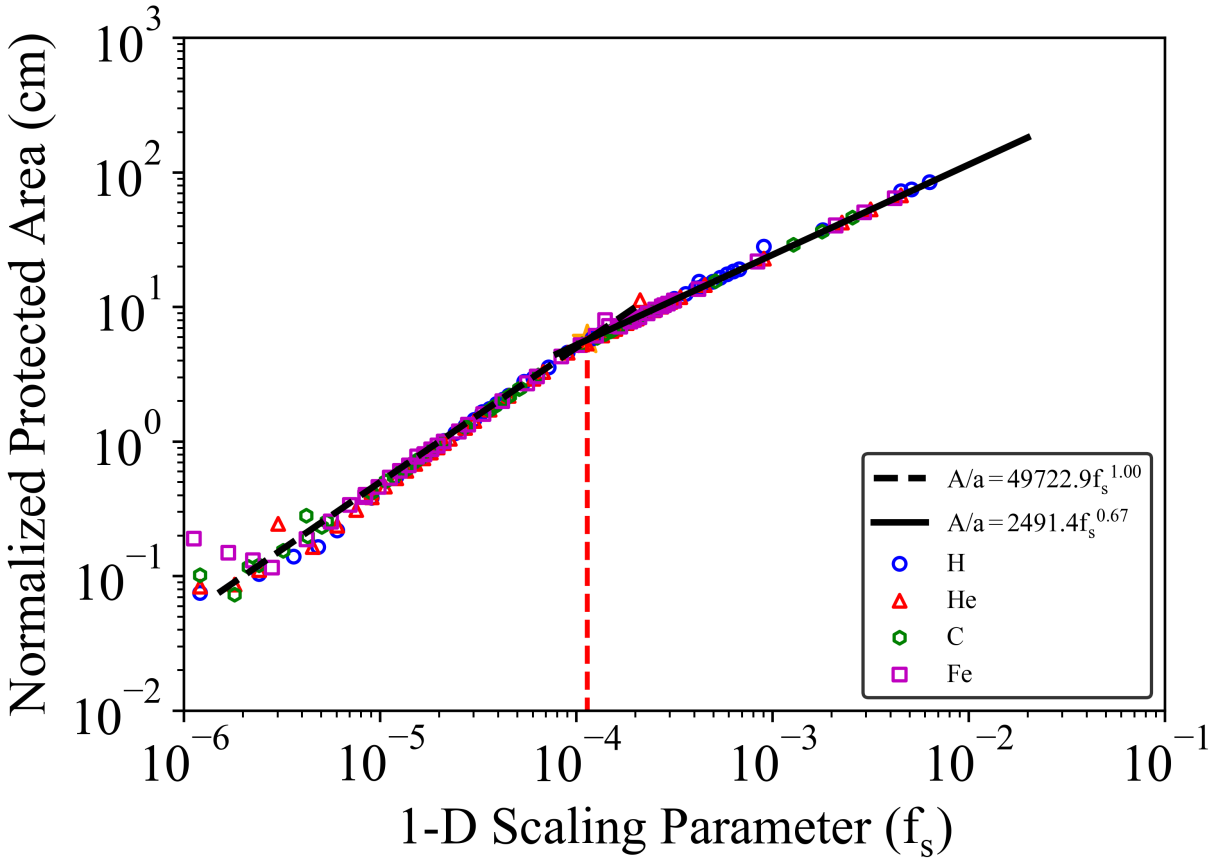

Figure 3.6: 1-D Scaling law with Dipole to Detector Distance equal to 10 m for space-based energies.

influence on where the knee occurs in the 1-D scaling law plot–increasing the ℓ_{DD} shifts this value to the left.

3.6.4 Comparison of Protected Area

It was mentioned previously that increasing the value of a should result in a linear increase in the protected area. Figure 3.10 shows the effect of increasing the value of a from 0.1 in to 1.0 in for space-based parameters, considering a fixed ℓ_{DD} of 10 m. In the Figure 3.10, the dashed and solid black lines represent the numerical fit corresponding to the region below and above the knee where a is equal to 0.1 in, whereas the dashed orange line represents the numerical fit to the region below the knee where a is equal to 1.0 in. It is observed from the comparison of the area between the dashed black and dashed orange lines that the

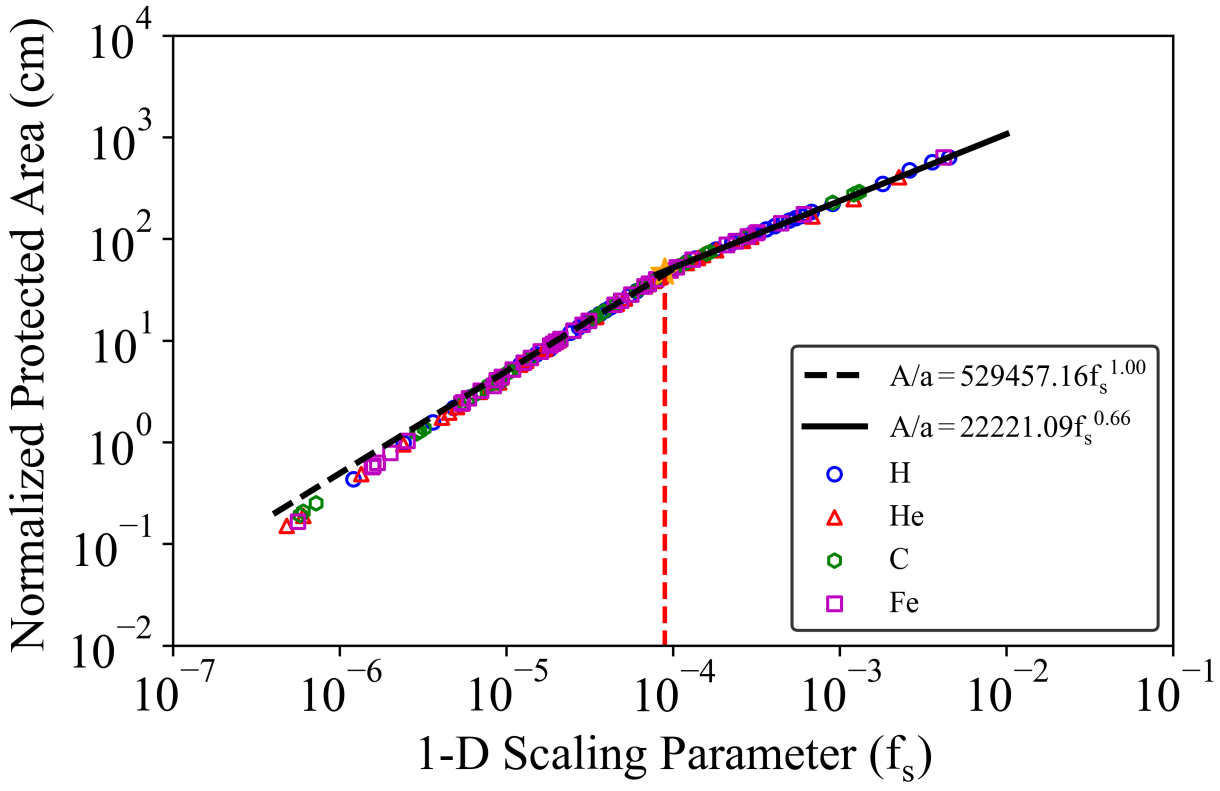

Figure 3.7: 1-D Scaling law with Dipole to Detector Distance equal to 100 m for space-based energies.

increase in protected area is approximately a factor of 10, which is the ratio of the sphere radii for the two sets of data. This effect was observed for all iterations in the value of ℓ_{DD}. In Figure 3.10, in the case of 1.0 in sphere radius, only the linear part of the data is shown (dashed orange line), and the part above the knee region (sub-linear) is not shown. The reason for not showing the full set of data is that the image-processing algorithm failed to compute protected areas greater than around 100 cm^2 within reasonable computation time. Future work includes updating the image-processing algorithm to address this issue. Also, it is evident from Figure 3.10, that increasing the magnitude of a from 0.1 in to 1.0 in shifts the knee value to the right of the scaling law curve. The reason of that can be explained by the altered value of ℓ_{SS} between two sets of simulations.

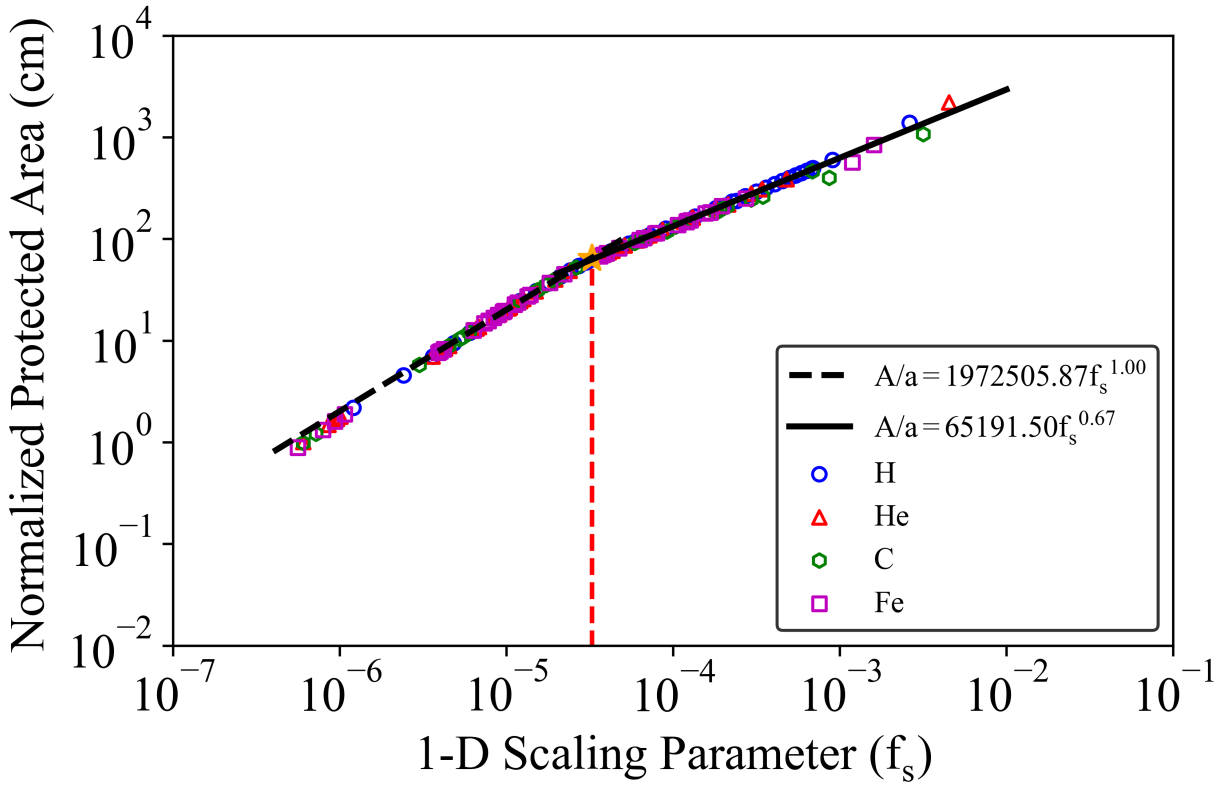

Figure 3.8: 1-D Scaling law with Dipole to Detector Distance equal to 400 m for space-based energies.

3.6.5 Explanation for the Knee Region

Observing the image data in conjunction with the scaling law plots shows that the shape of the protected area changes from a circular to a cardioid-like shape at a value of the scaling parameter where the knee occurs, f_{sknee} (Figures 3.1 and 3.2). The change in shape is evident for all ions, energies, and dipole-to-detector distances (ℓ_{DD}) simulated. At the lower potential-to-rigidity ratios, the two-point charges (positive and negative) appear to act independently. In these cases, the void shape is circular and centers around the positive point charge. A concentration of particles is apparent around the negative point charge. As the potential-to-rigidity ratio increases, the void area covers both of the point charges. At this point, the effect of the negative charge is observed as it attracts positively charged particles and thereby reduces the size of the void region. The void transitions from a circular shape to a cardioid shape, as shown in Figures 3.1 and 3.2.

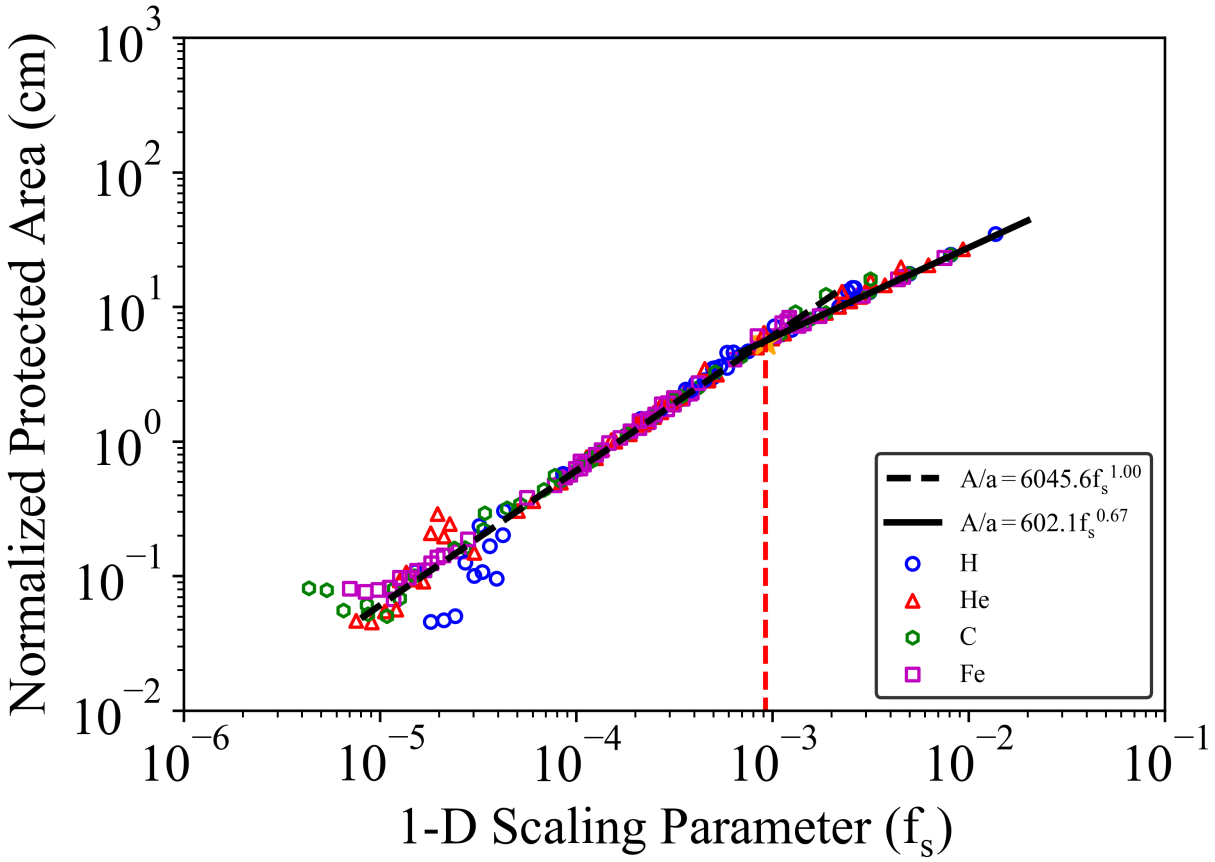

Figure 3.9: Comparison of Scaling law for accelerator-based and space-based parameters for Dipole to Detector distance equal to 1.2 m and charged sphere diameter 0.2 inch.

3.7 Summary

The objective of this study was to establish an explicit relationship between the magnitude of the scaling parameter (representing particle rigidity and applied potential) and shielding efficacy (represented by normalized void areas) for accelerator-based and space-based parameters. The results shown in Figures 3.4 to 3.8 effectively establish a scaling relationship. The outcomes demonstrate that the scaling law is linear for accelerator-based and space-based energies up to a particular value (knee-value), that is a function of ℓ_{DD}. The exponents of the power-law curve fitting for two observed trends are around 1 and 0.67 which represent the circular and cardioid shaped voids, respectively. Minor differences observed in the values of the linear and sub-linear exponents across ground-based and space-based energies as well as different values of ℓ_{DD} is due to uncertainties with image processing.

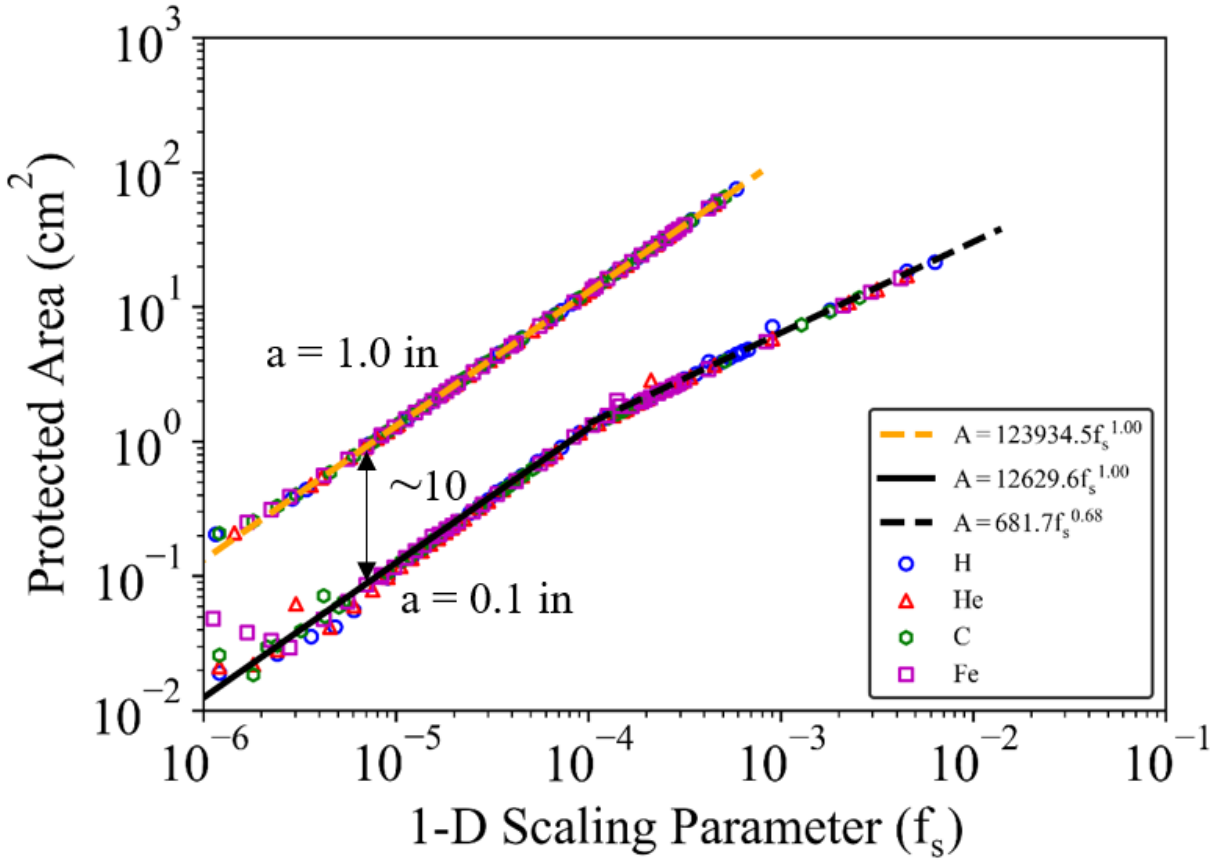

Figure 3.10: Comparison of protected area for two different sizes of charges sphere conductor for all ions where dipole-detector distance equal to 10 m.

One of the other objectives was to investigate whether a lower magnitude electrostatic field can deflect a lower-energetic ion (which can be generated in any accelerator facility), a higher-magnitude potential can deflect a higher-energy particle (which cannot be generated or tested in a laboratory or accelerator like facility) of the same species by the same amount as long as the dimensionless scaling parameter f_s between these two cases are identical. This result is shown in Figure 3.9. It is evident from the schematic of the simulation geometry (Figure 3.3) that this type of dipole electric field is simplistic and only capable of providing protection against mono-directional energetic particles directed towards the center of the dipole configuration. In space-like isotropic incidence condition, this type of simplified electric field configuration will be ineffective. The goal of the study was not to find the electric field configuration for space radiation protection, but to establish a mathematical

model which can be used for computation of radiation shielding using the measured values of scaled-down parameters.

The third important implication of this work is that it was shown that the area of the protected region is a function of the conductor dimension, and it increases linearly with the dimension of the conductor. This outcome is significant in terms of designing 3-D active shielding configurations, since the degree of protection can be increased by merely increasing the size of the conductor instead of the applied potential, assuming that the total charge needed can be supplied by the power supply in space. It was also shown that the occurrence of this knee region is also a function of the total charge or the dimension of the dipole spheres. At higher total charges or higher dimension, the influence of the negatively charged sphere becomes effective at a higher value of applied potential.

This chapter also establishes that increasing the distance between field generating nodes and spacecraft increases the protected area. Although this study was conducted for a beam-like configuration where the particles are streaming along a particular direction, the results have importance in designing and testing scaled models of active 3-D space radiation shielding configurations, which will be discussed in later chapters.

Chapter 4

Evolution of 3-D Electrostatic Radiation Shielding Configurations

In this chapter, a detailed description of different 3-D electrostatic configurations is presented. Previous work in Chapter 3 described an electrostatic shielding system in a beam-like setting and established a mathematical formulation between 1-D scaling law parameter and normalized protected area. The electric field configuration in the case of 1-D is insufficient to protect an isotropic radiation environment. Therefore, a suitable 3-D electric field configuration must be identified to provide full 4π protection. The present functionality of the ASPP code is limited to computing the electric field from multiple point charges or from a conductor for which the electric field can be computed using an analytic method. In this section, a detailed description of different 3-D charge configurations and their corresponding performance is described in detail. In these simulations, it was assumed that each point's total charge remained unaltered, i.e., the interdependence of these charges was not considered. It was assumed that the power supply used to charge these configurations would maintain the original charges set by the user. The electric field was computed using Equation 3.2 in Chapter 3.

4.1 Simulation Geometry

The simulation geometry is shown in Figure 4.1. The source geometry is chosen in a manner that space like isotropic incidence conditions are maintained.

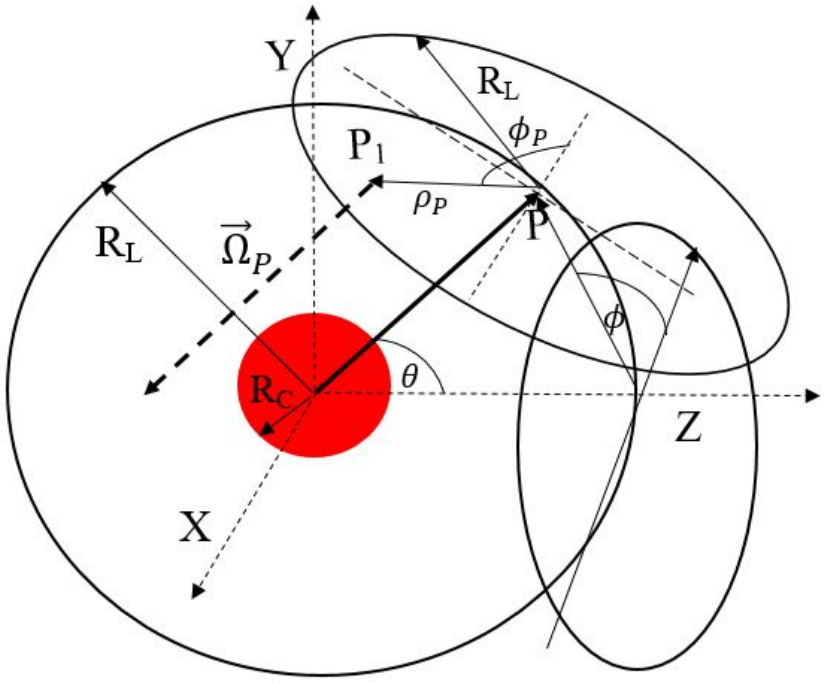

Figure 4.1: Source Geometry for 3-D radiation transport, after Ref. [8]

The algorithm that is used to generate particles isotropically is described below [8]:

1. Choose the radius of the source sphere (also known as launch radius) (R_L),
2. Choose number of simulated particles,
3. Initialize a random number generator,
4. For each particle:
   (a) Choose four pseudo-random numbers,

(b) Compute two angles θ and ϕ from two random number to define the disk center (P),

(c) Generate a disk with radius equal to R_L which is tangential to the point P,

(d) Compute an angle ϕ_P and radius ρ_P from the other two random numbers and find a point on the disk which acts as the starting position of the particle (P_1),

(e) Choose a inward direction (Ω_P) normal to the disk using the first two random numbers,

(f) Store the coordinates of the generated point and velocity components,

(g) Propagate the particle via that direction (Ω_P).

5. Compute the number of particle histories that enter the crew volume with radius R_c,

6. Compute the flux density reduction using Equation 4.1.

4.2 Computing Flux Reduction

It is important to know how the flux density reduction is computed to assess the flux density reduction capability of various electrostatic shielding systems. At first, the number of particle histories is chosen in such a manner that a certain number of particles would reach the crew volume (Shown as the red sphere in Figure 4.1). Equation 4.1 describes the flux density reduction calculation method used in this study,

$$F(E) = 1 - \frac{N(E)}{N_0}, \tag{4.1}$$

where $F(E)$ is the measure of flux density reduction of a particle with energy E, N_0 is the number of particles entering the crew volume in the absence of the electric field, and $N(E)$ is the number of particles with energy E entering the crew volume in the presence of the electric field. The number N_0 is not dependent on the particle's energy, as all particles irrespective of their initial energy will propagate along with the same directions as long as they have the same initial velocity-position distribution specified by the random seed.

4.3 Simulation Strategy

A single species and energy was chosen to compare the performance of different electrostatic radiation shielding systems. Since protons are the most abundant species in space radiation, they were chosen for the initial evaluation of the configurations. 200 MeV was chosen as the energy of the protons for simulations, as this energy is high enough to penetrate conventional shielding thickness (around $10\,\mathrm{g\,cm^{-2}}$) of any spacecraft hull, and the fluence spectra of any significant SPEs, as well as the flux spectrum of protons of GCR below this energy, are quite substantial from a dosimetric point of view. Additionally, based on the prior work in the field of active electrostatic shielding, the potential required to provide protection against 200 MeV protons was within the range of potentials that have been used in the literature [96, 118]. The goal was to start with a high potential known to provide protection against energetic protons and then optimize the configuration to get better or similar reduction with smaller potential. It was obvious that if a configuration does not provide protection even with a very high magnitude of electric field, it will not provide protection with a lower value of an electric field, and therefore, these configurations were not tested further. Since the ASPP code computes the electric field of multiple charge points, the aim was to find a 3-D charge distribution that can generate the required electric field, minimizing the radiation risk. The focus of this work was to minimize the requirement of charge, both individual and cumulative. Also, it was assumed that the conductor shape used to generate the electric field is spherical because the analytical formula required to compute the potential on the surface of a sphere is straightforward if the total charge on the surface of the sphere is known. The total charge on the surface of each hollow conductor was assumed to be concentrated at the center of the sphere and is given by

$$Q = 2\pi\epsilon_0 d_{sph} V_{dip}, \tag{4.2}$$

where Q is the total charge on the surface of the sphere, ϵ_0 is the vacuum permittivity, d_{sph} is the diameter of the sphere and V_{dip} is the voltage applied on each monopole sphere. The initial priority was to find a suitable electric field, created by a combination of multiple

charges distributed in space. The next sections describe the origin and evolution of different 3-D charged configurations and how an optimized charge/electric field configuration was chosen for computation of organ dose equivalent and effective dose under different radiation environments.

Table 4.1: Names and corresponding symbols of the parameters that have been used for the 3-D electrostatic field configuration optimization

Name of the parameter	Symbol
Number of Nodes	N
Radius of the tiling sphere	R_0
Distance of the proximal charged array from the origin	R_1
Gap between charged planes	d_p
Positive charge/node	q_+
Negative charge/node	q_-
Total positive charge of the system	Q
Potential on dipole spheres	V_{dip}
Potential on monopole spheres	V_{mon}
Number of charged 2-D arrays	N_p
Array size of 2-D arrays	$A\ (n \times n)$
Gap between nodes within an array	G
Gap between consecutive charged arrays	S
Distance of the negative nodes from the origin	d_{neg}

4.4 Dipole Configuration

The first approach used in this study was to implement the dipole electric field concept from the beam-like configuration to a suitable 3-D configuration. The initial ideal configuration tested was a spherical configuration where multiple dipoles were placed along a spherical surface of fixed radii. Throughout the simulation procedure, the radius of the virtual sphere on which the dipoles were tiled and the number of dipoles were varied to improve the flux density reduction. For multiple configurations, the placement of these dipoles (also known as nodes) was based on Thomson's algorithm [119]. A restriction of this algorithm was a

maximum of 400 nodes (dipoles), as shown in Figure 4.2, since only 400 positions for these nodes were available. To place more than 400 nodes, the Fibonacci method of placements was used [120]. The red and black points in Figure 4.2 indicate the locations of positive and negative charges, respectively. To place a dipole, first, a point on the sphere was chosen based on either Thomson or Fibonacci algorithm. That point was defined as the center of the dipole. The positive and negative monopoles were then placed so that the dipole axis was a tangent to the surface of the sphere. Random directions were chosen for dipole alignment. Each dipole consisted of two 5 m diameter spheres with the potentials on them varying from ± 5 MV to ± 100 MV. The starting point of the simulation was with 100 MV, as this potential was most likely to provide protection, and if the flux density reduction was observed, the potential was reduced. If there was no reduction observed at 100 MV, then the configuration was modified by increasing or decreasing the radius (R), and increasing the number of nodes (N). The gap between the positive and negative monopoles was kept at 7.5 m. It can be concluded from this configuration that whereas dipole configuration was effective in providing a protected area in case of beam-like configuration, placing multiple dipoles nodes in 3-D did not reduce the proton flux density. This type of dipole orientation was chosen initially as this was the simplest form of orientation. Orientations of the dipoles were varied throughout the simulation but no advantages were observed in comparison to the initial orientation. Table 4.1 shows all the symbols that have been used to describe different parameters that are used for simulations.

4.5 Multi-pole configuration

After observing no flux density reduction using multiple dipoles, the multi-pole configurations were extended from dipoles to include quadrupoles and sextupoles. Different numbers of quadrupoles and sextupole configurations were used instead of dipole configurations. Placement of these different types of nodes was achieved using previously described methods. Figures 4.3 and 4.4 show the placement of quadrupoles and sextupoles on a spherical surface. These configurations also did not provide any flux reduction when tested with potential

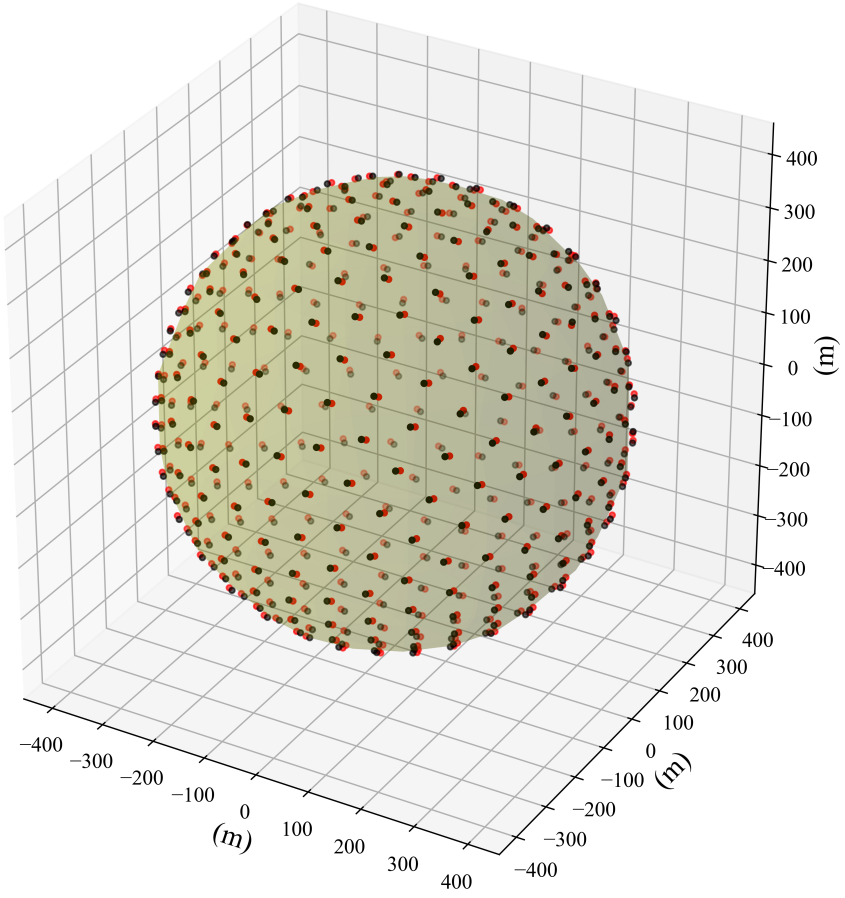

Figure 4.2: Distribution of dipoles over a spherical surface using Thomson's algorithm ($N = 400$, $R_0 = 400$ m)

ranging from ± 5 MV to ± 100 MV.

4.6 Monopole Configuration

After the failure of the multi-pole system, monopole configurations were tested next. These monopoles were charged with positive potentials. It is impractical to have isolated positive monopoles only, without any charge sink (negative charge) in space like conditions. In previous configurations, each node (dipole, quadrupole, sextupole) was a combination of equal positive and negative charges. To demonstrate that the lack of flux density reduction ob-

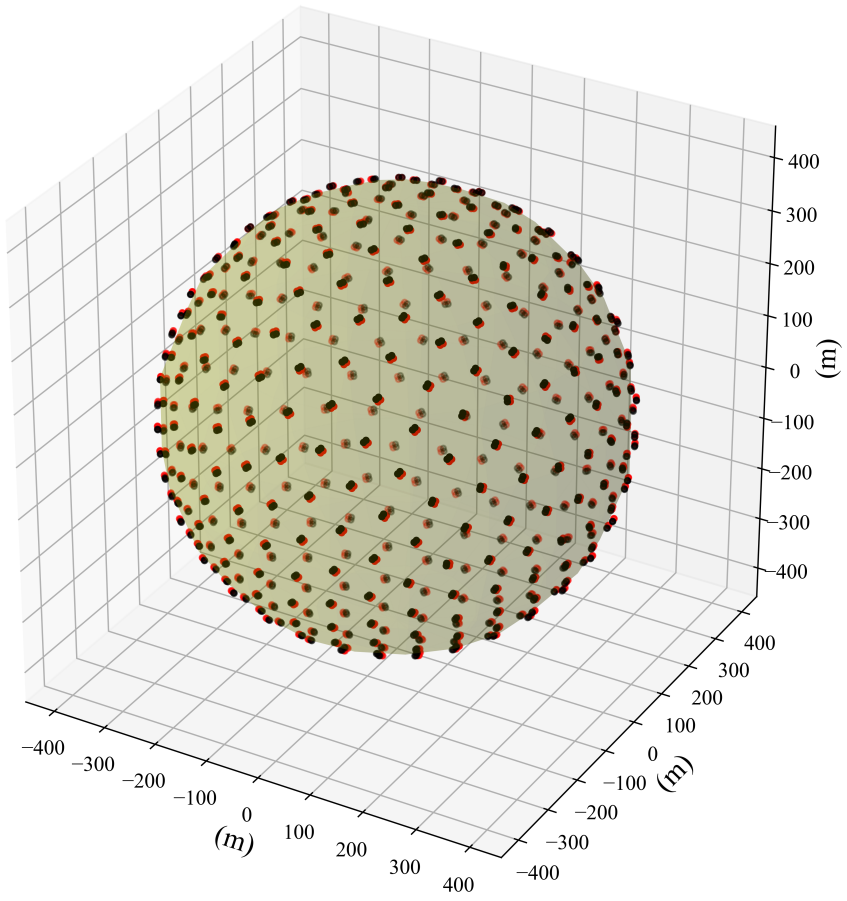

Figure 4.3: Distribution of quadrupoles over a spherical surface using Thomson's algorithm ($N = 400$, $R_0 = 400$ m)

served with these multi-pole configurations is due to the presence of the negative charges and not due to the distribution of the nodes across the spherical surface, only positively charged monopoles were used. The arrangement of monopoles over a spherical surface was made using Thomson's algorithm. Figure 4.5 shows different monopole configuration. Table 4.2 shows the monopole configurations that were investigated and the corresponding flux density reductions. It was observed that with 100 MV, sufficient flux density reduction was observed with more than 150 nodes, which was not observed using multi-pole nodes. Multiple simulations were done using different random seeds. The number of particles per simulation was chosen in such a way that around 1000 particles reach the crew volume in the absence of the

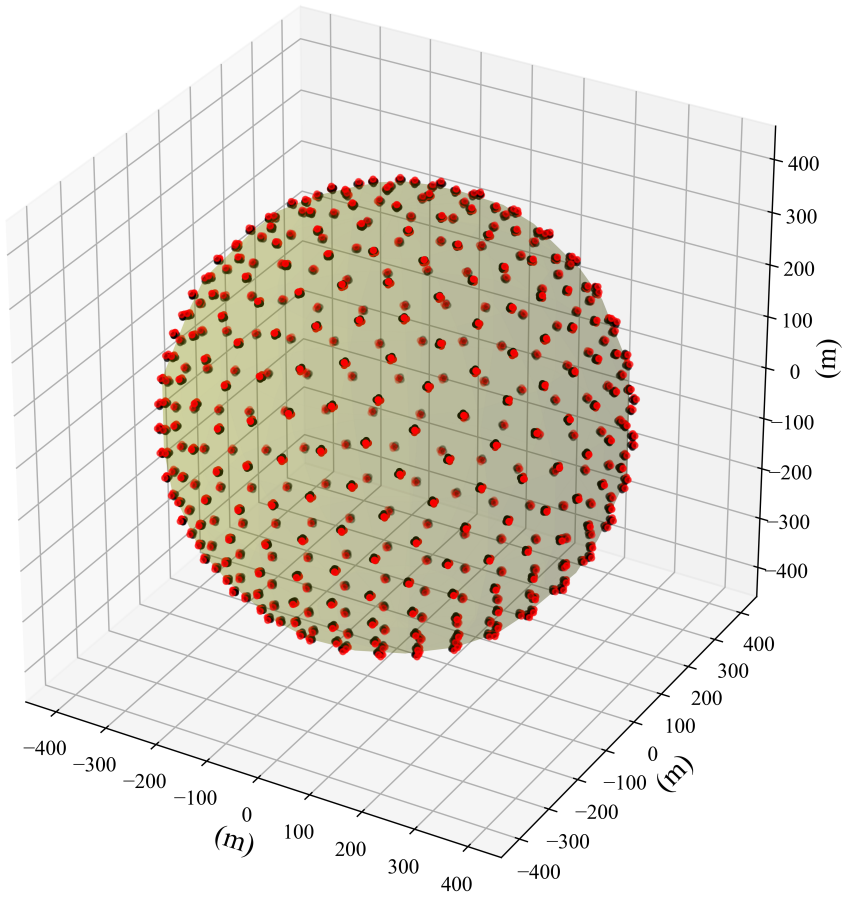

Figure 4.4: Distribution of sextupoles over a spherical surface using Thomson's algorithm ($N = 400$, $R_0 = 400$ m)

electric field, which means the number of simulated particles would be equal to $1000 \times (\frac{R_L}{R_c})^2$. For each case, at least three different random seeds were used for simulation. In the column of 'Reduction,' the average and one standard deviation values are shown. The average value is rounded to the nearest decimal place.

4.7 Multi-layered Spherical Configuration

It was observed that monopoles, when arranged in a spherical configuration, provided non-zero flux density reduction in comparison to the rest of the configurations. However, the

Table 4.2: Flux reduction values for spherical electrostatic configuration using monopoles

N	R_0 [m]	V_{mon} [MV]	Reduction [%]
20	400	100	5 ± 2
50	400	100	9 ± 2
100	400	100	18 ± 3
150	400	100	30 ± 2
200	400	100	39 ± 2
250	400	100	51 ± 1
400	400	100	98 ± 1

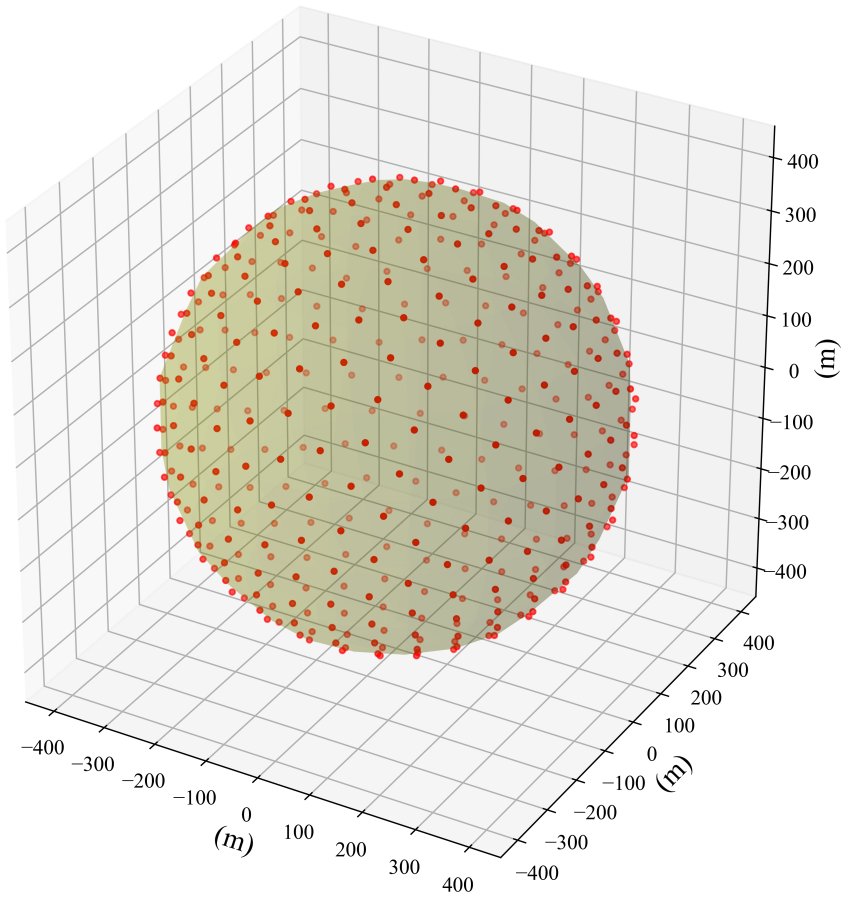

Figure 4.5: Distribution of monopoles over a spherical surface using Thomson's algorithm ($N = 400$, $R_0 = 400$ m)

potential requirement for each node was very high. It was observed that the potentials required to gain any significant reduction were on the order of hundreds of MVs. The potential requirement was at least one order of magnitude larger than the potential that can be achieved using present technology. Therefore, there needs to be a configuration or a set of arrangements that provides significant protection against HZE particles with potentials that can be achieved using present-day technology. The goal was to achieve a similar degree of flux density reduction by increasing the number of nodes (monopoles) and reducing the potential. This configuration depicts a pathway of lowering the potential requirements by using multi-layers of node distribution instead of single layer node distribution. In this configuration, the monopole nodes were tiled across the surfaces of multiple spheres with different radii (R_i) in such a manner that they form a multi-layered cascaded structure. Figure 4.6 shows an example of this multi-layered spherical configuration where each node is a positively charged monopole.

Flux reduction factors as a function of proton kinetic energy for spacecraft represented by spheres with radii of 5 m, was simulated as they represent the standard radius range of a spacecraft. The electrostatic monopoles were placed on the surfaces of spheres of radii ranging from 25 m to 400 m concentric with the spacecraft. Use of multiple spheres for electrostatic monopole placement is considered to be a cascaded geometry since it does not rely on a single layer of positive charge to deflect energetic protons. An example geometry is shown in Figure 4.6, where the red sphere represents the spacecraft. Nodes were placed on the spherical surface such that they are equally distributed over the surface area. For the present study, Thomson's method of charge distribution was used to distribute the point charges equally on each spherical surface. The performance of this configuration is shown in Table 4.3, where the column 'N_i', and 'R_i' represent the number of monopoles tiled across the surface of different virtual spheres and the radius of these spheres respectively.

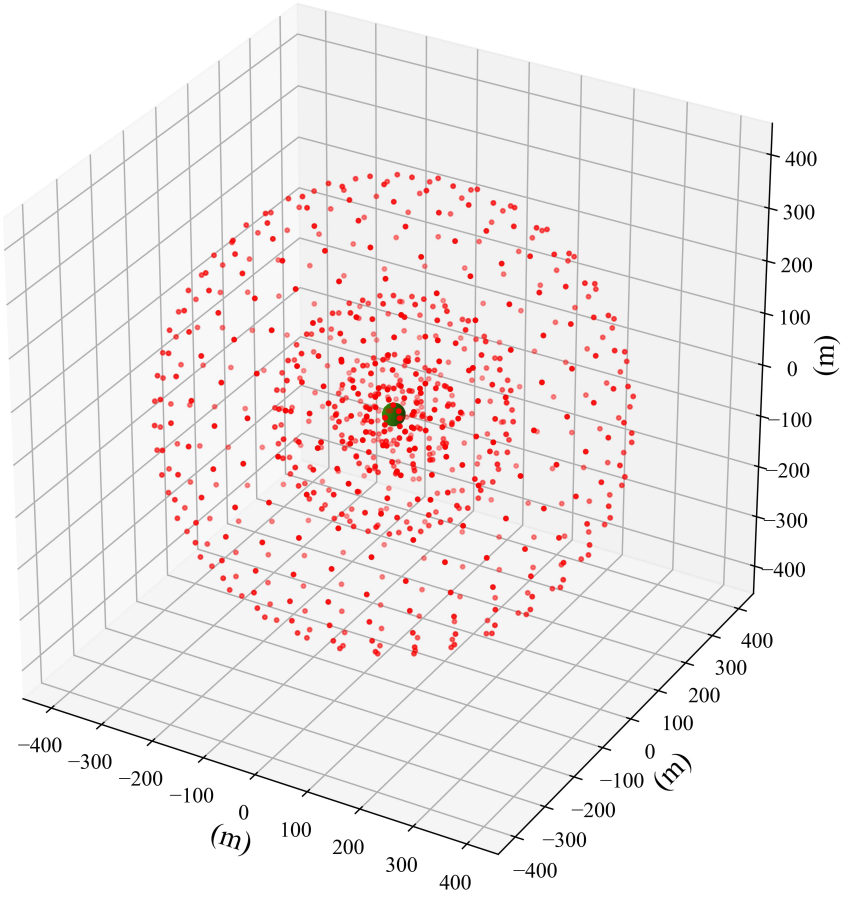

Figure 4.6: Example of charge distribution for multi-layered spherical geometry

4.8 3-D Charged Array Configuration

It was observed in the spherical configurations that the flux density reductions can be achieved when only positively charged monopoles are used. Additionally, to lower the potential requirement, the monopoles were required to be distributed in multiple layers. While the multi-layer monopole distributions reduced the potential requirement and provided flux density reductions, they were not suitable configurations as they were not charge neutral. It is practically impossible from an engineering point of view to implement an electrostatic radiation shielding system with that kind of angular distribution. Therefore, a configuration needed to be investigated to satisfy the following three criteria: 1) provides significant

Table 4.3: Flux reduction values for multi-layer spherical configuration using monopoles

N_i	R_i [m]	V_{mon} [MV]	Reduction [%]
50,100,200,400	50, 100, 200, 400	5	25 ± 3
25,50,100,200,400	25,50,100,200,400	5	30 ± 2
100, 200, 300, 400	100, 200, 300, 400	5	20 ± 2

flux density reduction for 200 MeV protons, 2) the system should be charge neutral, and 3) multi-layer distribution can be achieved to lower potential/charge requirement per node. A charged 2-D array configuration was hypothesized to achieve these three requirements. Here, a 2-D array shaped structure was placed instead of on each side of a cube shaped geometry covering the crew volume. It was observed in the 1-D studies that when charged spheres of equal and opposite polarity are placed close to one another, void regions develop. However, because the void region is localized, regions of localized concentrated particle flux develop simultaneously around the outer edge of the void region. Thus, if the void region generated by a dipole node is not expansive enough, the resultant reduction in particle flux ends up being negligible. In order to remove the gain-compensating effects of negatively charged spheres, an asymmetric charge configuration was chosen. Positive charges were decoupled from negative charges, and the charges were no longer uniformly distributed over a sphere. Figure 4.7 shows the basic configuration of this charged array. The black points represent the negative charge in this configuration. Several such 2-D charged arrays were stacked together to create a 3-D charged array, as shown in Figure 4.8. The charge values of the negatively charged nodes were chosen such that the integral charge of each 2-D array as well as the whole system was zero. This was done to minimize the probability that negatively charged ions would accelerate and collide with positively charged conductors and, in turn, create Bremsstrahlung radiation.

Several parameters can be optimized to improve the performance of the electrostatic shielding system. These parameters can be the size of the 2-D array, the intra-array gap (G) between charged nodes, Orthogonal distance from the center to the 2-D array (R), and the gap between each 2-D array (S).

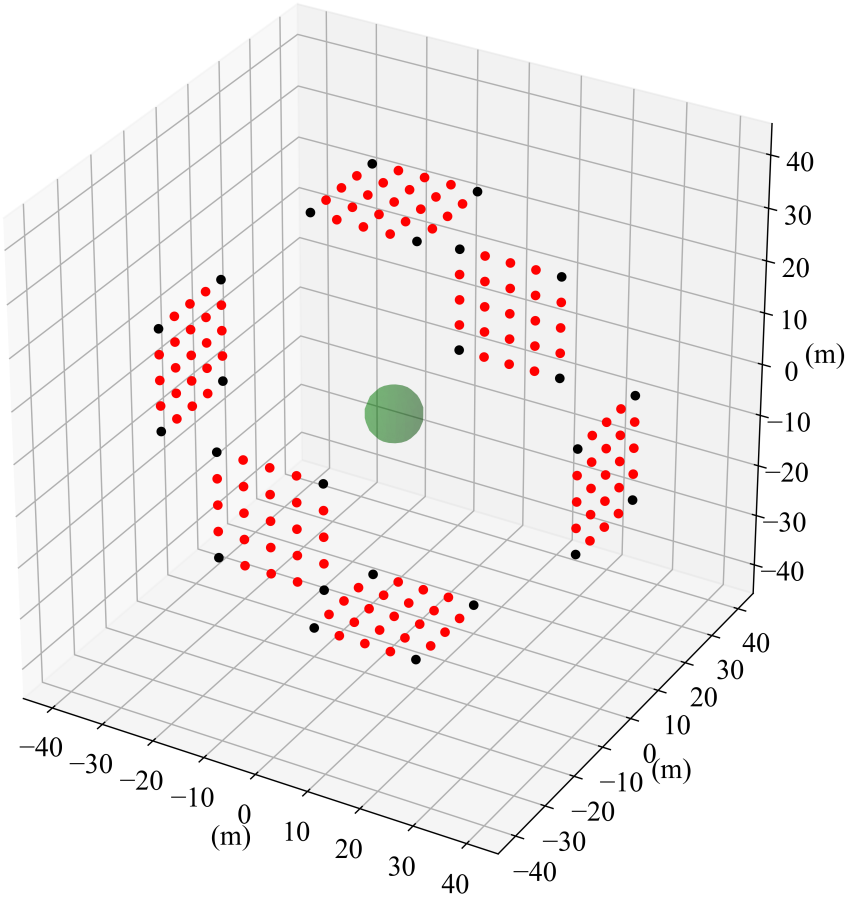

Figure 4.7: Single layer charged array configuration

The first and simplest configuration constructed under these guiding principles is shown in Figure 4.8. This family of charge configurations consists of planar arrays, each made up of a square matrix of charged spheres. If the crew volume is centered on the origin, planar arrays are oriented such that their normal vectors are parallel or anti-parallel with one of the Cartesian coordinate axes, resembling the six sides of a cube. The charge distribution for each array was allowed to change, but negative charges were generally clustered toward the edges of each planar array. Multiple planar arrays were stacked together by maintaining a fixed gap between each 2-D array such that the normal vectors of these planar arrays are collinear. This method was based on the previous strategy of using multi-layered charge distribution to gain flux density reduction by using lower positive charge (Table 4.8). Stacking 2-D

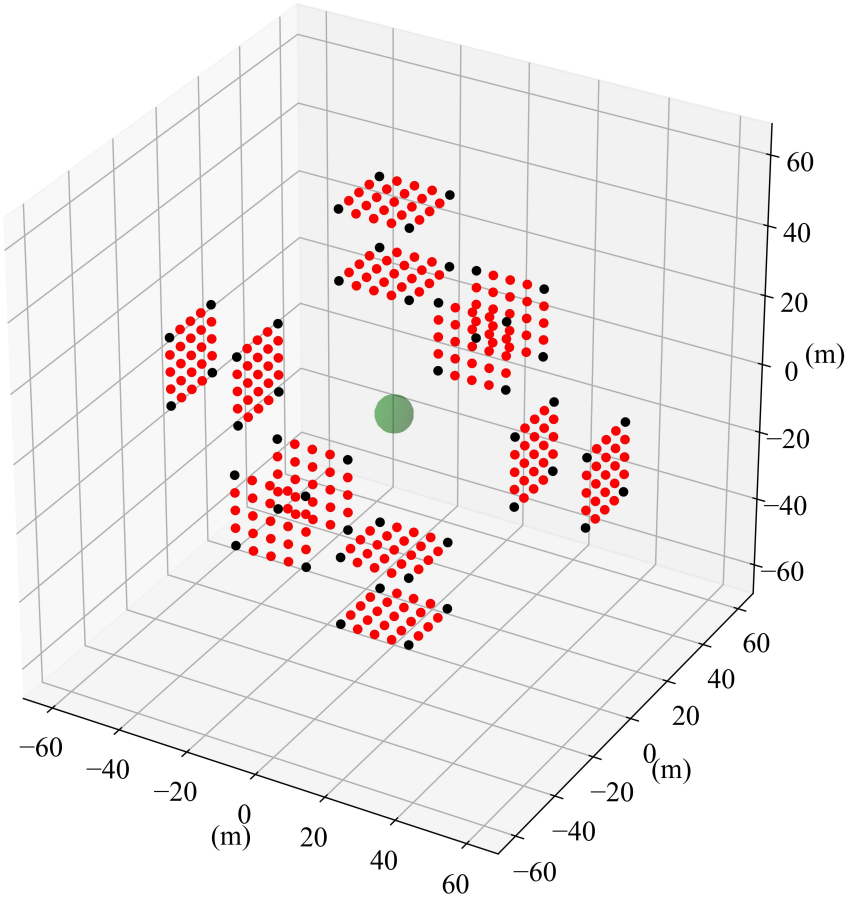

Figure 4.8: 3-D charged array configuration with multiple stacked 2D arrays

charged arrays increases the extent of the electric field and improves flux density reduction capabilities.

Distribution of negative charges was tested for different configurations as shown in Figure 4.9. The effectiveness of these three different negative charge distributions was computed for different combinations of the 3-D stacked arrays, and it was observed that the first distribution among the three works best. Table 4.4 shows the relative performance of these three different charge distributions.

As evident from Table 4.4, Distribution 1 works the best among all three negative charge distribution shown in Figure 4.9. The reason behind that is, as the negative charge per node (q_{-}) is highest for Distribution 1, it acts as a negative potential well to attract charged par-

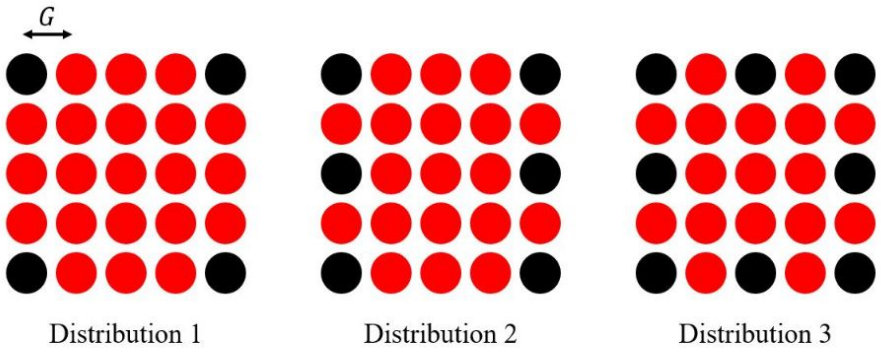

Figure 4.9: Distribution of negative charge points within a 2D charged array

Table 4.4: Flux density reduction results three different negative charge distributions for 200 MeV protons in case of 3-D stacked configuration where the intra-node gap (G) was fixed at 7.5 m and the the array span was 30 m × 30 m with $q_+ = 0.005$ C, $q_- = -26.25$ mC, $S = 7.5$ m, $R_1 = 22.5$ m, and $N_p = 5$

Distribution Name	Reduction [%]
Distribution 1	41 ± 2
Distribution 2	35 ± 3
Distribution 3	30 ± 2

ticles away from the crew volume more efficiently compared to the other two negative charge distributions (Distribution 2 and 3). In this configuration, protons with energy 200 MeV were simulated with multiple 2-D stacked array configurations where the gap between nodes (G) and the distance of the first 2-D charged array (S) were varied from 7.5 m to 20 m. The distance to the proximal 2-D charged array (R_1) was varied from 22.5 m to 60 m. The value of R_1 was chosen so that the 2-D charged arrays on each side of the crew volume do not overlap and maintain the minimum gap equal to the value of G. Unlike in the case of 1-D simulations, it was observed that the flux density reduction reduces when the charged 2-D arrays are placed further away from the crew volume. Additionally, it was observed that as the value of G and S increases, the value of flux density reduction factor decreases.

Tables 4.5, 4.6, and 4.7 demonstrate that the value of flux density reduction factor decreases with increasing values of R_1, G, and S respectively. The explanation of this phenomenon can be drawn from the effect that with increasing gap between nodes, the electric field between the gaps decreases and affects the shielding's performance. Additionally, with an increasing value of R_1, the solid angle coverage that the electrostatic shielding provides to the crew volume is reduced. The total number of nodes in these configurations was equal to 750, with 630 positively charged nodes and 120 negatively charged nodes. For each configuration, multiple (at least three) simulations were done using different random seeds, and the average value and one standard deviation are shown in the flux density reduction column.

Table 4.5: Flux reduction results for 200 MeV protons in case of 3-D stacked configuration where the intra-node gap (G) was 20 m and array span was 80 m × 80 m, S = 20 m

q_+ [C]	q_- [C]	Q [C]	Reduction [%]
0.001	-0.00525	0.63	0
0.002	-0.0105	1.26	5 ± 3
0.003	-0.01575	1.89	10 ± 2
0.005	-0.02625	3.15	18 ± 3

Table 4.6: Flux reduction results for 200 MeV protons in case of 3-D stacked configuration where the intra-node gap (G) was 10 m and array span was 40 m × 40 m, S = 10 m

q_+ [C]	q_- [C]	Q [C]	Reduction [%]
0.001	-5.25×10^{-3}	0.63	0
0.002	-10.5×10^{-3}	1.26	15 ± 3
0.003	-15.75×10^{-3}	1.89	18 ± 2
0.005	-26.25×10^{-3}	3.15	35 ± 2

4.8.1 Effect of Addition of Layers

Here, adding layers on a particular configuration by keeping the total positive charge constant was examined. The objective was to determine whether the same reduction can be

Table 4.7: Flux reduction results for 200 MeV protons in case of 3-D stacked configuration where the intra-node gap (G) was 7.5 m and array span was 30 m × 30 m, R_1 = 22.5 m, N_p =5, S = 7.5 m

q_+ [C]	q_- [C]	Q [C]	Reduction [%]
0.001	-5.25×10^{-3}	0.63	10 ± 3
0.002	-10.5×10^{-3}	1.26	18 ± 2
0.003	-15.75×10^{-3}	1.89	27 ± 2
0.005	-26.25×10^{-3}	3.15	41 ± 1

achieved by reducing individual charge values and increasing the number of charged points. For this purpose, one of the first configurations with charge value per positive node equal to 0.005 C was chosen since it provided the best reduction. Protons with kinetic energy equal to 200 MeV were simulated to compare the efficacy between different active shielding configurations. The value of N_p was varied from 5 to 10, and the flux density reduction results are shown in Table 4.8. The value of q_+ and q_- were changed in such a manner that the total positive charge remains same in all cases. It is shown that the even if the total positive charge value is constant, lowering individual charge values by increasing number of nodes does not improve performance of the active shielding configuration and the performance decreases with the increase of layers until the value of flux density reduction factor remains constant with increase in the number of 2-D charged arrays.

Table 4.8: Flux reduction results for 200 MeV protons in case of 3-D stacked configuration where the intra-node gap (G) was fixed at 7.5 m and the the array span was 30 m × 30 m, S = 7.5 m, R_1 = 22.5 m, and Q = 3.15 C

N_p	q_+ [C]	q_- [C]	Reduction [%]
5	0.005	-26.25×10^{-3}	41 ± 2
6	0.0041	-21.52×10^{-3}	37 ± 2
7	0.0035	-18.75×10^{-3}	37 ± 2
8	0.0031	-16.4×10^{-3}	32 ± 2
9	0.0027	-14.58×10^{-3}	27 ± 3
10	0.0025	-13.12×10^{-3}	25 ± 3

4.8.2 3-D Charged Arrays with Shifted Layers

In this configuration family, each 2-D array is shifted with respect to its neighboring 2-D charged array such that the dip in the electric field created by the gap between two nodes for each array is compensated by the presence of node in the consecutive 2-D charged array. Multiple simulations where the intra-node gap (G) was kept between 7.5 m to 20 m were done in this study. It did not improve the performance, but, to some extent, deteriorated it (in the case where the gap between nodes was higher, for example, around 20 m). No flux density reduction was observed in this configuration. It is clear that shifting the layers with respect to each other nullifies the flux density reduction. It may be due to the effect of placing the negative charges in the middle section of the 2-D charged arrays.

4.8.3 3-D Stacked Array-Cubic Configuration

In previous configuration (3-D Charged Array Configuration), it was shown that the more the charge points are concentrated together, the better the performance. Thus it was hypothesized that the stacked 3-D arrays were not providing any protection from the particles with trajectories are directed towards the diagonals of the cube. In order to prevent this streaming, a stacked cubic configuration was chosen. In this case, the nodes at the sides and corners of each array overlapped the nodes located on the other orthogonal side, and therefore, the charge values were adjusted accordingly. The positive charge values of each side of the array were doubled where negative values at each corner of the cube were multiplied by a value of three. The cubic configuration is shown in Figure 4.10. Table 4.9 shows the simulation results for the cubic configurations, which demonstrated improved performance compared with previous arrangements in terms of gaining more reduction for less value of total charge, but it increases the charge on individual nodes unrealistically.

4.8.4 3-D Stacked Spherical Sector Configurations

In this case, curvature was added to the 3-D stacked arrays. They were placed in a manner that resembles a fractional solid angle, shown in Figure 4.11. No reduction was observed in

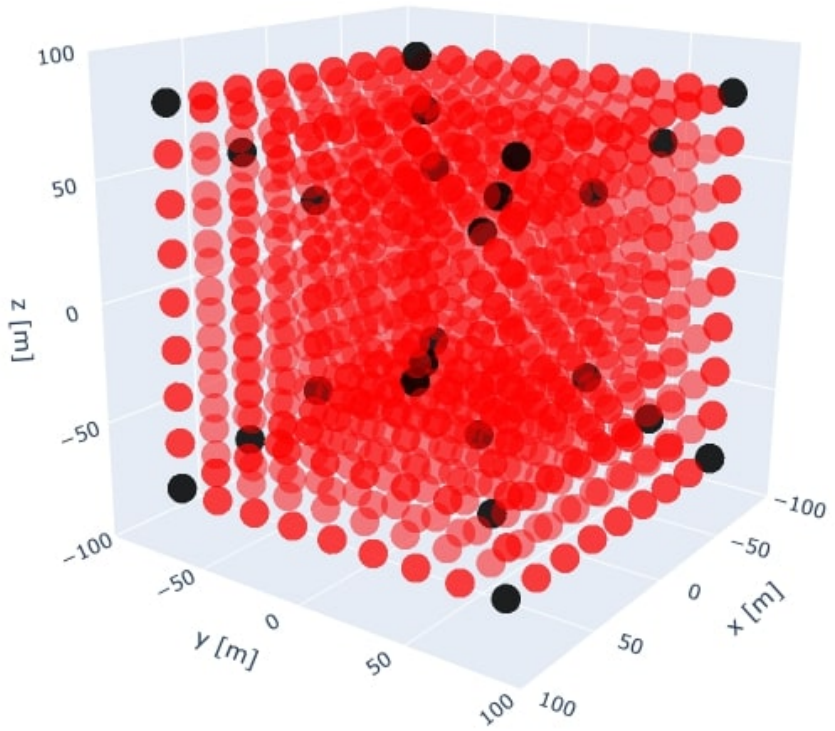

Figure 4.10: Cubic Configuration

Table 4.9: Flux reduction results for 200 MeV protons in case of 3-D cubic configuration where the intra-node gap (G) was fixed at 20 m, $N = 456$

R_i	A	q_+ [C]	q_- [C]	Reduction [%]
20, 40, 60	3x3, 5x5, 7x7	0.001	0.426	12 ± 3
20, 40, 60	3x3, 5x5, 7x7	0.002	0.852	25 ± 3
20, 40, 60	3x3, 5x5, 7x7	0.003	1.278	44 ± 2
20, 40, 60	3x3, 5x5, 7x7	0.005	2.13	50 ± 1

this case for the same charge values as 3-D stacked arrays. One possible explanation is that the negative charges in this configuration direct positively charged particles towards crew volume. Another possible reason may be, the greater distance to the crew volume.

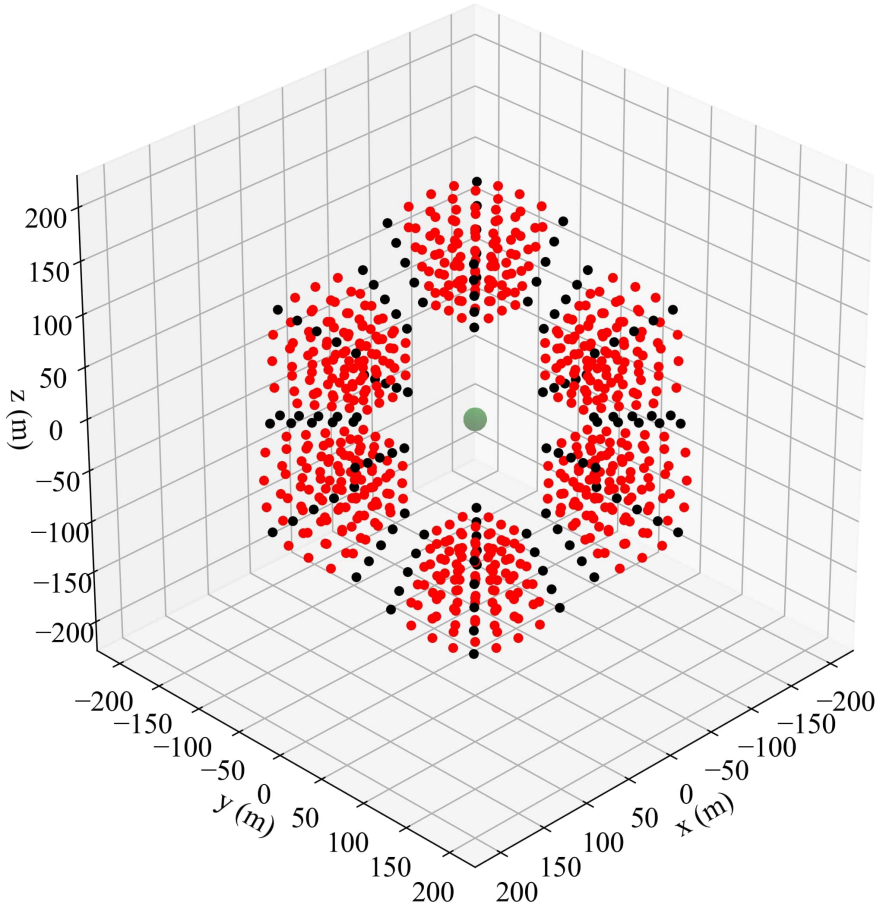

Figure 4.11: Stacked Spherical Sector Arrays

4.8.5 3-D Charged Arrays with Extended Negative Points

This configuration was a modified version of the stacked arrays. Here, the gaps between each node within an array was kept constant. In this configuration, the gap between positive nodes and negative nodes were increased, and negative nodes was stretched away, as shown in Figure 4.12 so that the positively charged particles are directed further away from the crew volume.

The flux density reduction for these types of configurations are shown below in Table 4.10. It is clear from the outputs that for similar configuration of stacked arrays in terms of charge values, and number of charges, this configuration provides better performance. Therefore, in later configurations, the negative charges were placed further away in each 2-D charged

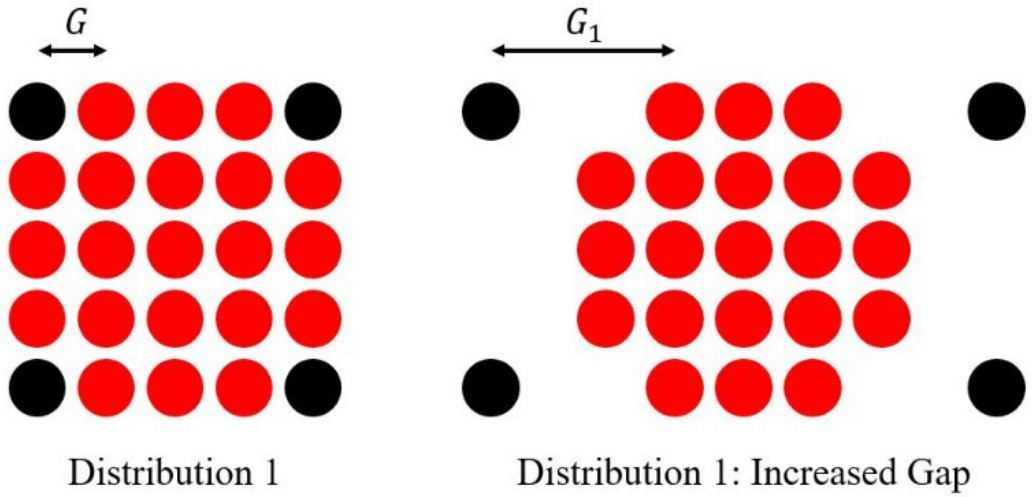

Figure 4.12: 3-D charged Array Configuration with laterally extended negative points

array to improve performance. The 3-D charge configuration is shown in Figure 4.13.

Table 4.10: Flux reduction results for 200 MeV protons in case of 3-D stacked configuration with extended negative nodes (figure 4.12) where nodes were stacked on each side of a cube with each 2D charged array being 5×5 in size. $N = 750$, $R_0 = 60\,\text{m}$, and $N_p = 5$.

q_+ [C]	q_- [C]	Q [C]	D_N [C]	Reduction [%]
0.003	-0.01575	1.89	50, 60, 70, 80, 90	10 ± 3
0.005	-0.02625	3.15	50, 60, 70, 80, 90	32 ± 1

It is evident from Table 4.7 and Table 4.10 that for the same value of total positive charge (Q), 3-D Charged Arrays with Extended Negative Point performs better. From these 3-D charge distributions, it is clear that to find a suitable configuration, one needs to confine the positive charge points in a smaller volume in space equally around the crew volume and distribute the negative charge points away from the positive charges. This finding was utilized in the following configuration.

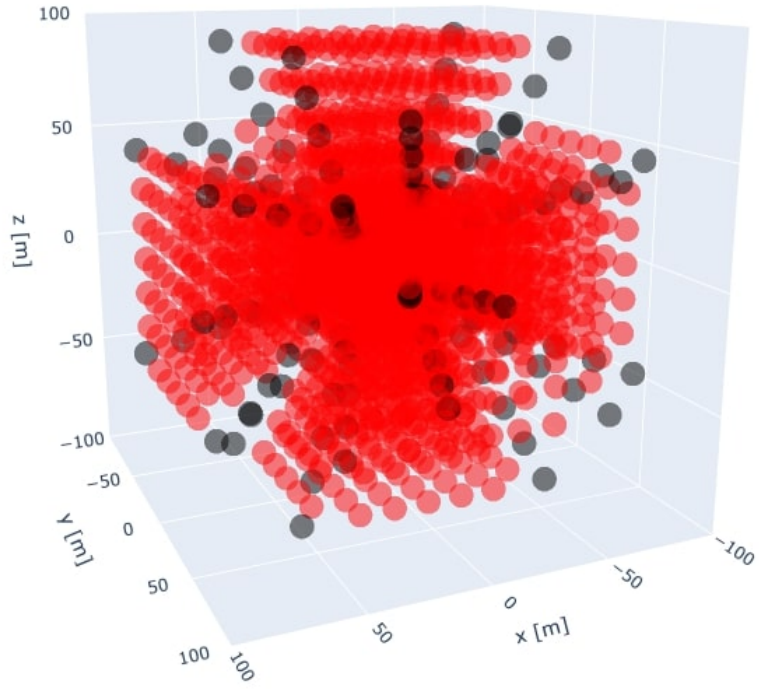

Figure 4.13: 3-D charged Array Configuration with extended negative points

4.8.6 3-D Stacked Arrays with Isolated Negative Charges Placed on Diagonal

This configuration further demonstrated improvement in flux density reduction. Here, the orthogonal stacked arrays were chosen to be all positive and negative charge points were separated and placed along the diagonal of a large cube as shown in Figure 4.14.

The flux density reduction factor for different configurations in this family are shown Table 4.11. Protons of kinetic energy 200 MeV was simulated for each combination to determine the flux density reduction. The best configuration provides almost 30% reduction for a charge values as low as 0.0003 C.

The simulation results of Table 4.11 show improved reduction using a lower amount of total charge and individual charge. The gap between the positively charged nodes were

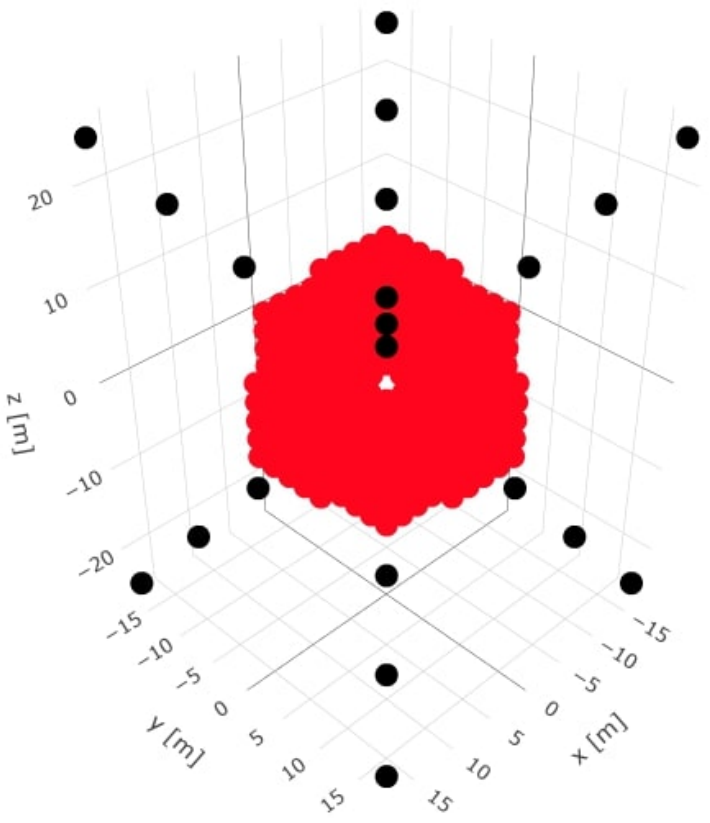

Figure 4.14: Stacked Arrays with Negative Diagonal

lowered to 5 m to achieve better flux density reduction. In practice, this configuration can be achieved using plane charge instead of point charges and charged rods that can are placed along the diagonal of a cube decoupled from the system.

4.8.7 Relative Performance Analysis of the Configurations Tested

In this section, the relative performance among the best performing configuration has been shown. Here, the spherical configurations are not included as it was decided that from a practical point of view, generating spherical shielding would be next to impossible. To analyze which configuration would be best, four different metric were chosen: 1) amount of

Table 4.11: Flux reduction results for 200 MeV protons in case of 3D stacked hyperbolic configuration where each 2D charged array was of size 7x7 and each positive point was 5 m from each other while negative charges were placed along a diagonal far from the stacked arrays (Figure 4.14). In this configuration, each diagonal was placed from 35 m to 173 m from the origin along a diagonal. $N = 1248$, $R_1 = 20$ m, $N_p = 4$. The span of each 2D array was 30 m $\times$ 30 m

q_+ [C]	q_- [C]	Q [C]	Reduction [%]
0.0001	-0.001633	0.117	0
0.0002	-0.00326	0.324	15 $\pm$ 3
0.0003	-0.0049	0.351	26 $\pm$ 2
0.0005	-0.008167	0.585	49 $\pm$ 1
0.00075	-0.01224	0.877	82 $\pm$ 1
0.001	-0.01633	1.17	98 $\pm$ 2

total positive charge on the system (an indicator of the total power requirement), 2) how far are these charges spread (relates to the compactness of the system), 3) the amount of positive charge per node (represents the amount of potential required to generate them), and 4) the amount of flux density reduction it provides for 200 MeV protons. Table 4.12 shows the summary of the best configurations of all the configurations tested and which provided non-zero flux density reduction. From Table 4.12 it is evident that the last configuration is the best among all and therefore in the next work, as it provides better reduction at lower value of q_+ and Q even though the extent of the configuration is increased from 60 m to 80 meter. A modified version of this configuration with charged planes and rods instead of point charges are presented in later sections.

Comparison of Electric Field Distribution

In this section, the representational electric field plots for different configurations that provided non-zero flux density reduction are described. Figures 4.15, 4.16, 4.17,and 4.18 represent the electric field plot for four configurations that worked best. Both the colors and size of the field vectors (cones) represent the magnitude of the electric field vector at the point at which they're located. Bright yellow + large cone means the magnitude of the electric field is

Table 4.12: Relative performance analysis of different configurations

Configuration Name	Q [C]	q_+ [C]	Maximum extent [m]	Reduction [%]
3-D stacked arrays	1.26	0.002	52.5	18 ± 2
Cubic configuration	0.852	0.002	60	25 ± 3
3-D stacked arrays with extended negative points	3.15	0.005	90	32 ± 1
3-D stacked arrays with negative diagonals	0.585	0.0005	80	32 ± 2

large at that position. Dark/black + small cone means the magnitude of the electric field is small at that position. The dimension of the cones represents the magnitude of the electric fields. The magnitude of the electric field is normalized by the highest magnitude of the electric field vectors. It is clear from these figures that the best configuration among them has a higher value of electric field around the corner and isotropic spread of electric field surrounding the crew volume. Further studies need to be done to get a better idea regarding the relationship between the orientation of the electric field and corresponding flux density reductions.

4.8.8 Charged Plane and Line Configuration

With the success of the 3-D charged array with coupled negative charges, the key issue was to find a set of suitable conductors that can generate the required field. To move from charge based configurations to conductors, a simple model was chosen. The positively charged arrays were replaced by positively charged 2-D planes and the negatively charged points were replaced by negative line charges. Analytic functions describing the electric field of a square plane with finite dimensions and finite charged lines were added to ASPP code [79] to

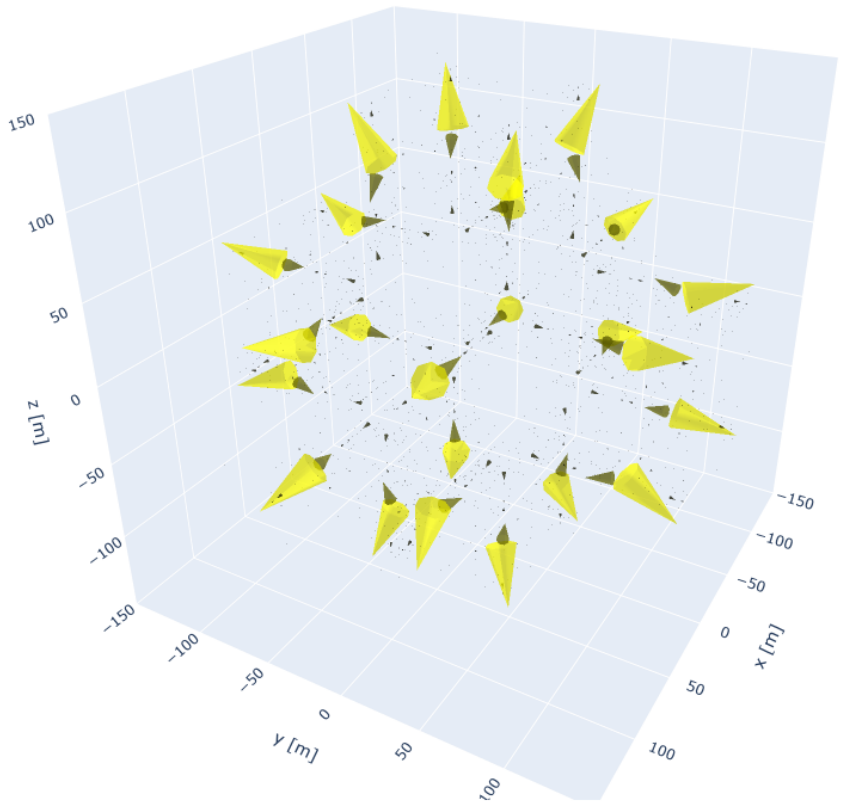

Figure 4.15: Electric field plot for 3-D stacked array configuration

compute the resulting electric field. It is true that in reality, the charged planes will have some finite thicknesses and will not be truly 2-D and the charged rods will have some thickness, but these finite characteristics are unimportant for present applications. Figure 5.1 shows the standard charged plane and rod combination. Here, the red square regions represent the positively charged plane and black lines represent the negatively charged rods. The parameter space for all the configurations that were tested is shown in Table 4.13.

4.9 Formulation of 3-D Configuration Scaling Law

This section discusses the formulation of a 3-D scaling law for the chosen family of electrostatic shielding configuration in a step-by-step manner. In Chapter 3, a scaling law was

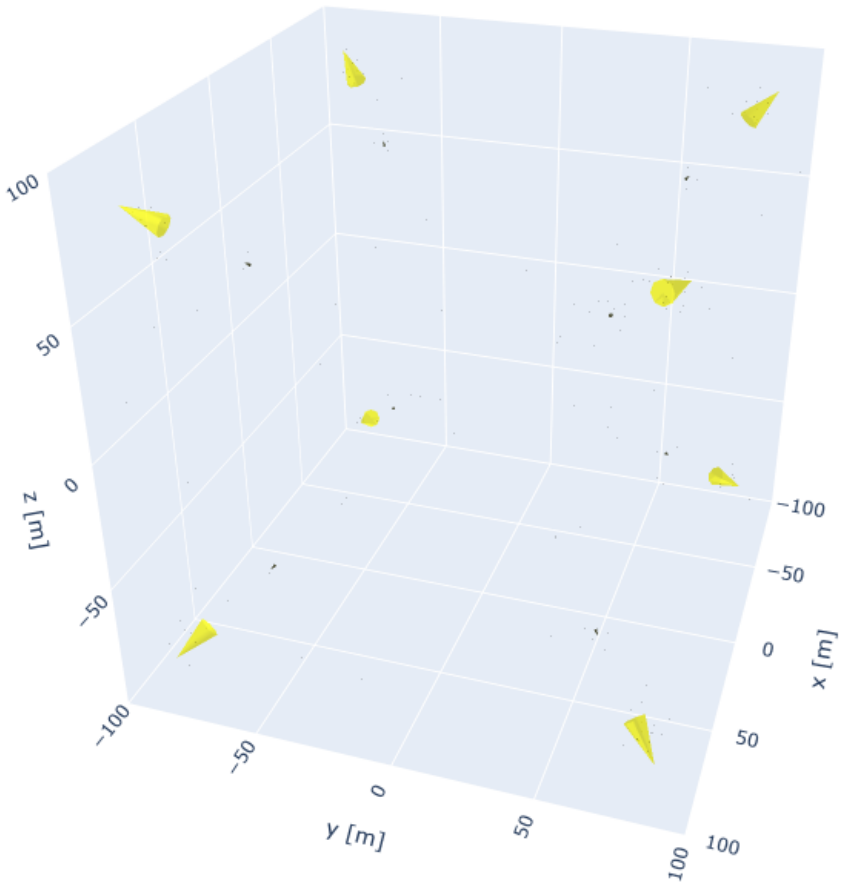

Figure 4.16: Electric field plot for cubic configuration

formulated for a beam-like configuration, relating the performance of the dipole electric field and its ability to deflect a stream of energetic ions. Similarly, a 3-D scaling law was established to formulate a mathematical relationship between different subsets of active shielding configurations of a family of configurations (shown in Table 4.13) and the corresponding flux density reduction factor for various energies. This mathematical relationship can be later used to demonstrate the performance of a scaled-down version of 3-D active shielding configuration in an accelerator-based facility. In order to establish the law, a set of configurations that are a combination of positively charged planes and negatively charged lines were used for simulations. The shielding efficacy of these sets of electrostatic shielding was calculated

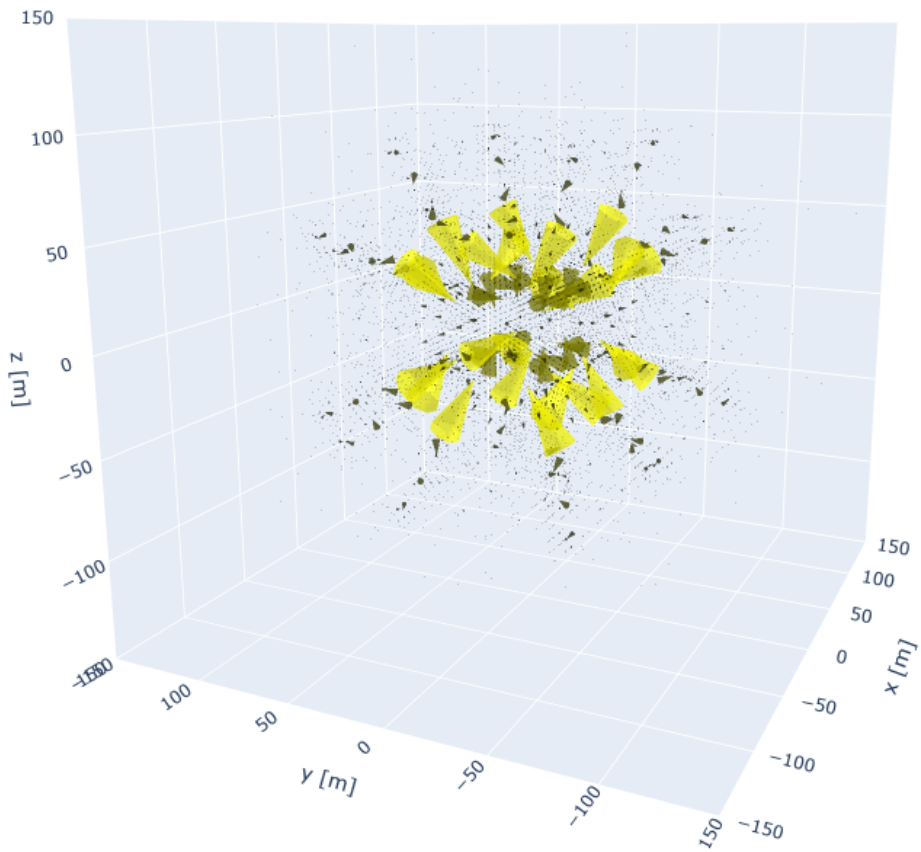

Figure 4.17: Electric field plot for 3-D stacked arrays with extended negative points

for protons and other high-Z particles relevant for space radiation. The energy range of the projectiles was varied from 10 MeV/n to 1000 MeV/n as no flux density reduction was observed above the energy of 1000 MeV/n for all the three active shielding configurations.

A new concept of 3-D scaling parameter is formed, which can be used to calculate the efficacy of different configurations. The initial definition of the 3-D scaling parameter can be seen in Equation 4.3,

$$f_s = \frac{KQZ}{((\gamma^2 - 1)E_0)/\gamma}, \tag{4.3}$$

where Z is the incident ion charge, Q is the cumulative positive charges on the planes, E_0 is the rest mass energy of the projectile, and γ is the Lorentz factor. K is a constant

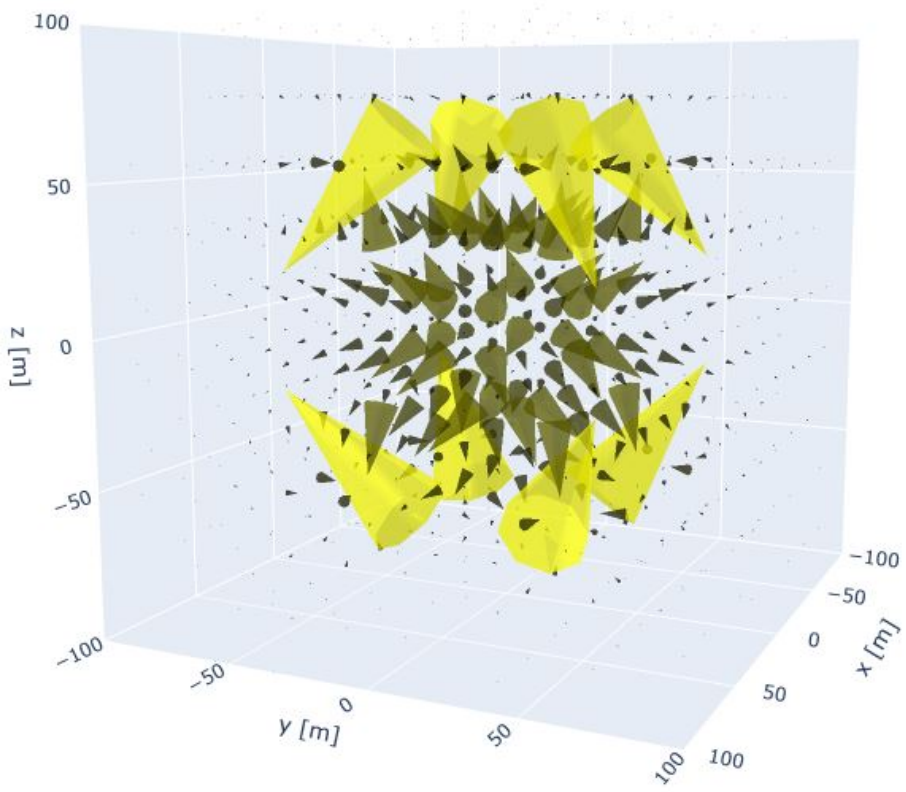

Figure 4.18: Electric field plot for 3-D stacked arrays with negative diagonals

which is used for magnitude scaling. The numerator of the 3-D scaling parameter includes total positive charge, which is used to deflect the ions, whereas the denominator represents the momentum of the incoming ions per unit atomic number (Z). The denominator in Equation 4.3 represents how difficult it is for the electric field to deflect the ions. In this case, the value of K is a scaling factor equal to 1000 to normalize the values of 3-D scaling parameter. Figure 4.20 shows the flux density reduction factor (F(E)) versus parameter for protons for different values of distance between crew volume center and the negative charges. Unlike the 1-D scaling parameter, the 3-D scaling parameter is not dimensionless. The unit of 3-D scaling parameter is $\mathrm{C\,MeV^{-1}}$. Therefore, the scaling parameter needs to be modified to incorporate the variation of reduction with distance of the negative line charges. The updated scaling parameter is shown in Equation 4.4

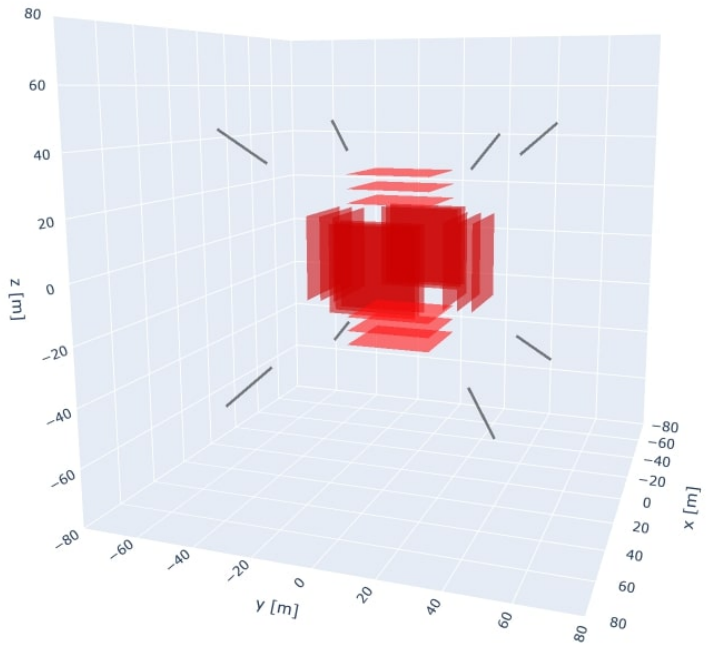

Figure 4.19: 3-D electrostatic shielding configuration with charged planes and rods

$$f_{s1} = \frac{KQZd^{0.33}}{((\gamma^2 - 1)E_0)/\gamma}, \tag{4.4}$$

where d is the distance of the negative rod to the crew volume center, normalized by the highest distance of the negative rod to the crew volume center that were simulated ($d = d_{neg}/d_{neg_{max}}$). The updated scaling law plot with new scaling parameter is shown in Figure 4.21. The power of the normalized distance of the negative rod is 0.33 for the modified 3-D scaling law. This is an empirical factor which may be related to the physics of the electrostatic shielding. Further studies should be done to provide an accurate explanations for these empirical parameters.

It is evident that the updated scaling parameter takes account of the variation of distance between the center of the crew volume and the negative charge. However, there are other two other parameters that influence the reduction and needs to be associated with the 3-D scaling parameter. These two parameters are the gap between the charged planes (d_p) which were varied between 5 m to 10 m, and the proximal distance between the crew volume center and

Table 4.13: Parameter space for the charged plane and rod configuration studies

Parameter	Range
Distance of the negatively charged rod (d_{neg}) [m]	60 - 140
Number of plane charged per side (N_p)	3 - 5
Surface charge density (σ) [μC m^{-2}]	2.27 - 15.1
Planar charge dimension	30 m $\times$ 30 m
Distance of proximal plane (d_{pos}) [m]	20, 25, 30
Distance between consecutive planes (d_p) [m]	5, 7.5, 10
Proton energy [MeV]	10, 30, 50, 75, 100, 150, 200, 300, 500, 750, 1000

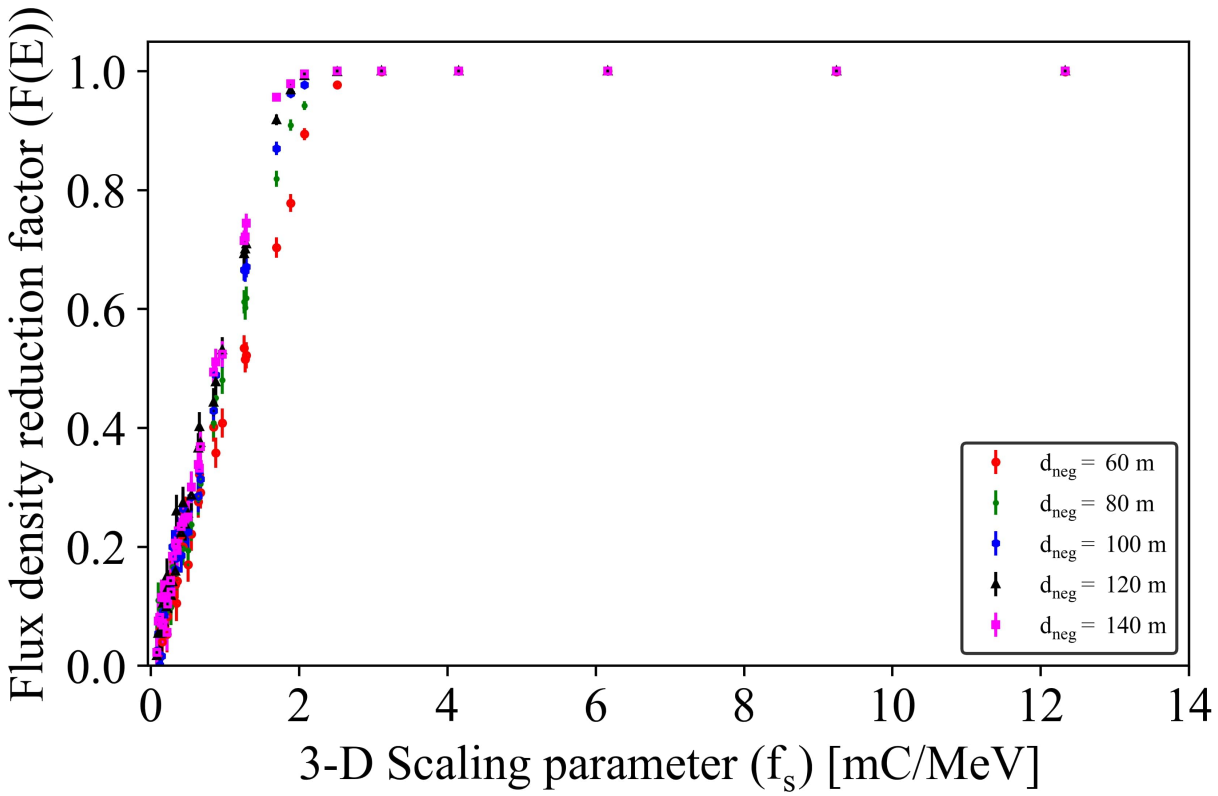

Figure 4.20: 3-D scaling parameter for plane-rod combination (with three planes) without distance scaling

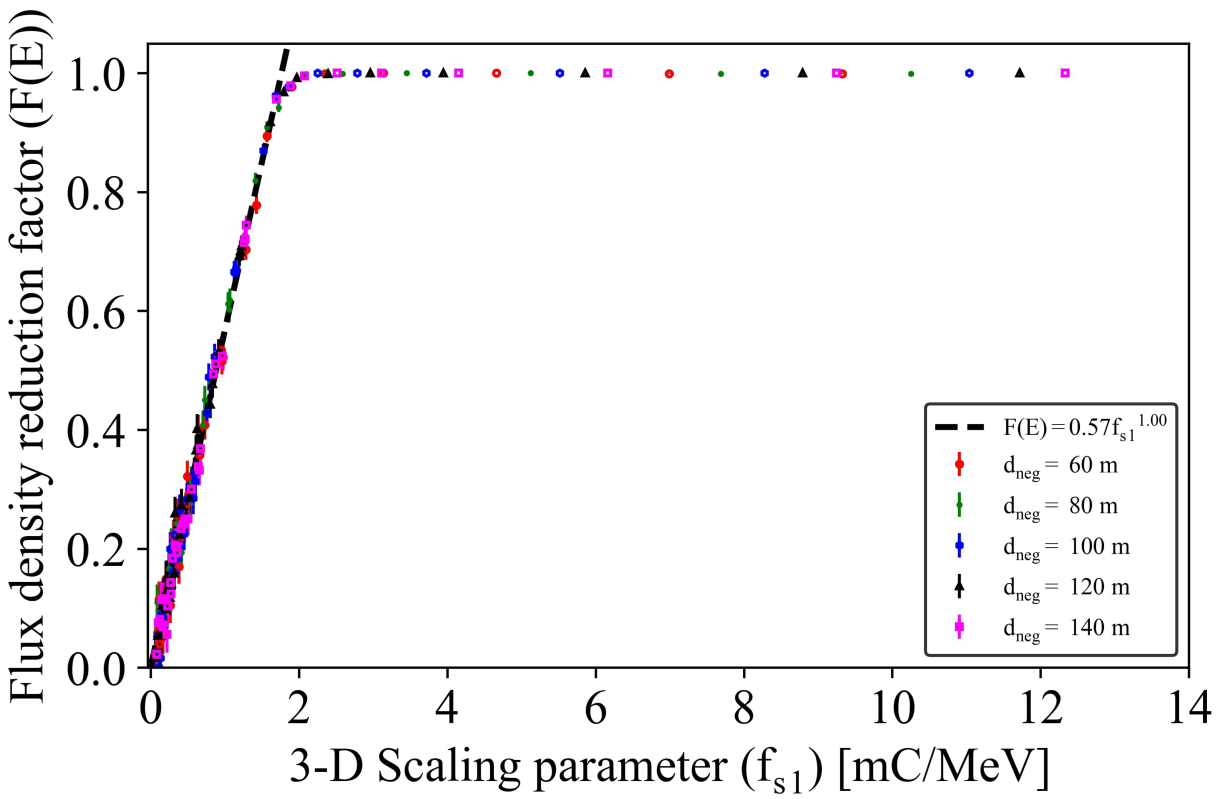

Figure 4.21: 3-D scaling parameter for plane-rod combination (with three planes) with distance scaling

the first charged plane (d_{pos}). The variation of the flux density reduction factor for different values of d_p is shown in Figure 4.22. The 3-D scaling parameter used in Equation 4.4 was used in this case. Figure 4.22 shows that the flux density reduction value changes with different values of d_p. To account for these changes, the 3-D scaling law in Equation 4.4 was modified, and the modified form is shown in Equation 4.5

$$f_{s2} = \frac{KQZd^{1/3}}{(g^{0.2}(\gamma^2 - 1)E_0)/\gamma}, \tag{4.5}$$

where f_{s2} is the updated 3-D scaling parameter and g is the normalized inter-plane gap ($g = d_p/d_{p_{max}}$).

Figure 4.24 shows that the flux density reduction is a function of d_{pos}. To account for the variation in d_{pos}, Equation 4.4 was modified to Equation 4.6

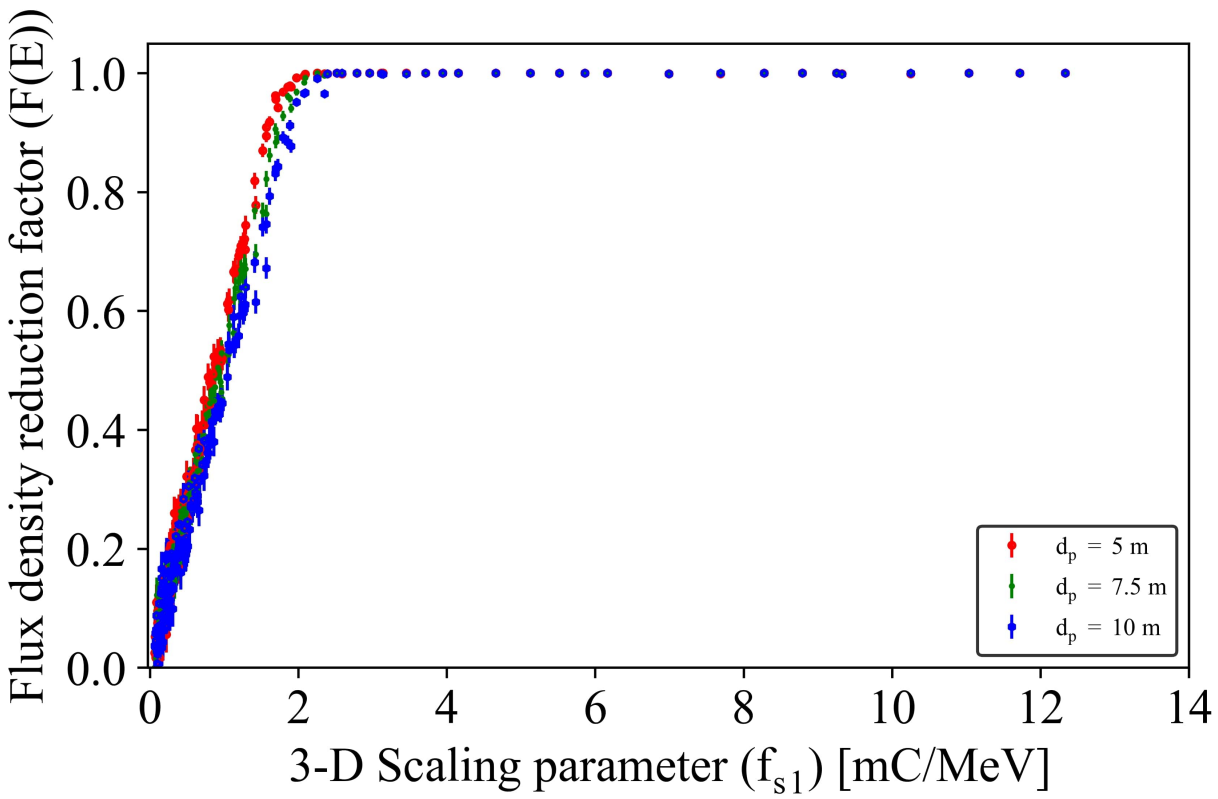

Figure 4.22: 3-D scaling parameter for plane-rod combination (with three planes) without a normalized gap (G) scaling

$$f_{s3} = \frac{KQZd^{1/3}}{(s(\gamma^2 - 1)E_0)/\gamma}, \tag{4.6}$$

where f_{s3} was the modified 3-D scaling parameter to counter the variation in d_{pos}, and s is the normalized distance to the proximal plane from the crew volume center ($s = d_{pos}/d_{pos_{max}}$).

Figures 4.24 and 4.25 show the effect of modified 3-D scaling parameter that takes account of the variation of d_{pos}. A curve-fitting is also done to show the linear relationship between the flux density reduction factor and the 3-D scaling parameter in each of these figures (Figure 4.21, 4.23, and 4.25). For the final stage, to test the 3-D scaling law for all relevant parameters, three separate active shielding configurations were tested with non-identical distance to the negative charged rod (d_{neg}), distance to the proximal plane (d_{pos}), and gap between plane (d_p). Figure 4.26 shows the plot of reduction for three different active shielding

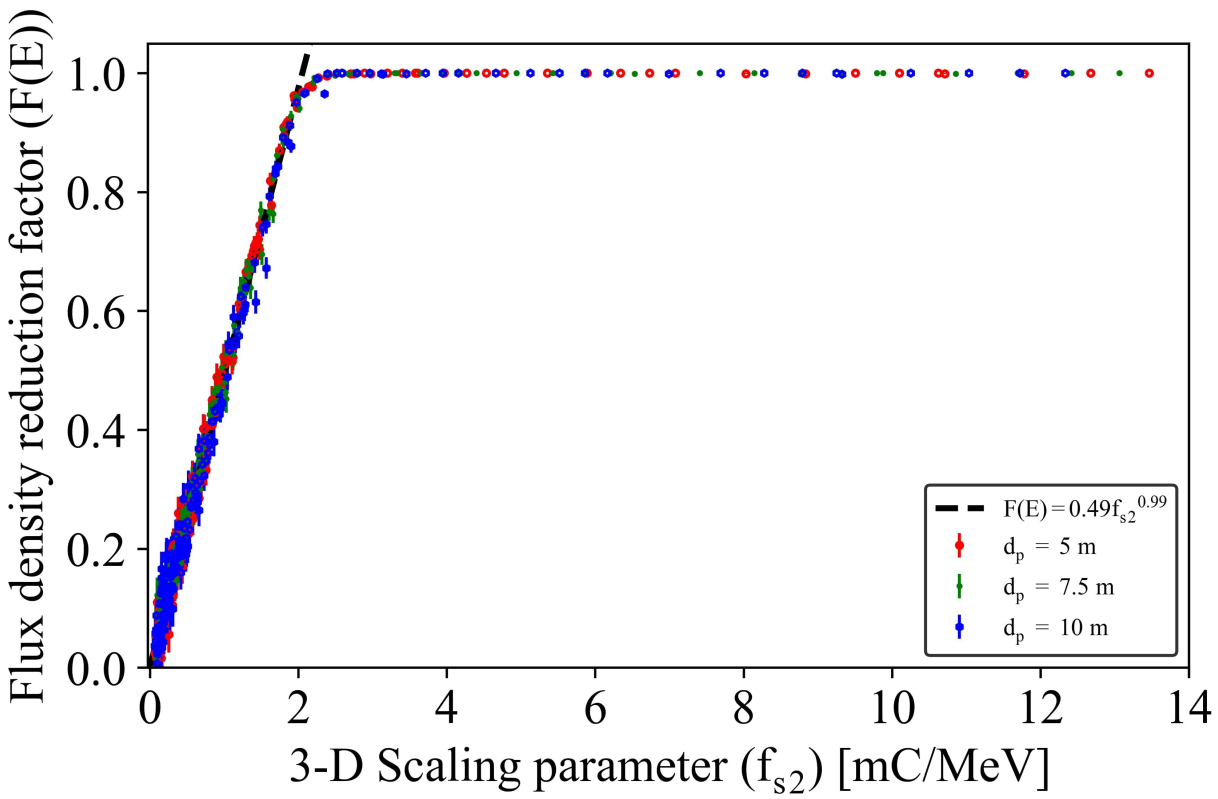

Figure 4.23: 3-D scaling parameter for plane-rod combination (with three planes) with normalized gap (G) scaling

configurations.

To scale these three different configurations, an updated 3-D scaling parameter was chosen which account the variations in all these three parameters using Equation 4.7

$$f_{s4} = \frac{KQZd^{0.33}}{(g^{0.2}s(\gamma^2 - 1)E_0)/\gamma}, \tag{4.7}$$

where f_{s4} is the 3-D scaling parameter that incorporates the variations in all the three parameters. Figures 4.26 and 4.27 effectively demonstrate the validity of the updated 3-D scaling parameter to represent the active shielding systems investigated. A curve-fit was done here to form a mathematical relationship between the flux density reduction factor and the final updated 3-D scaling parameter.

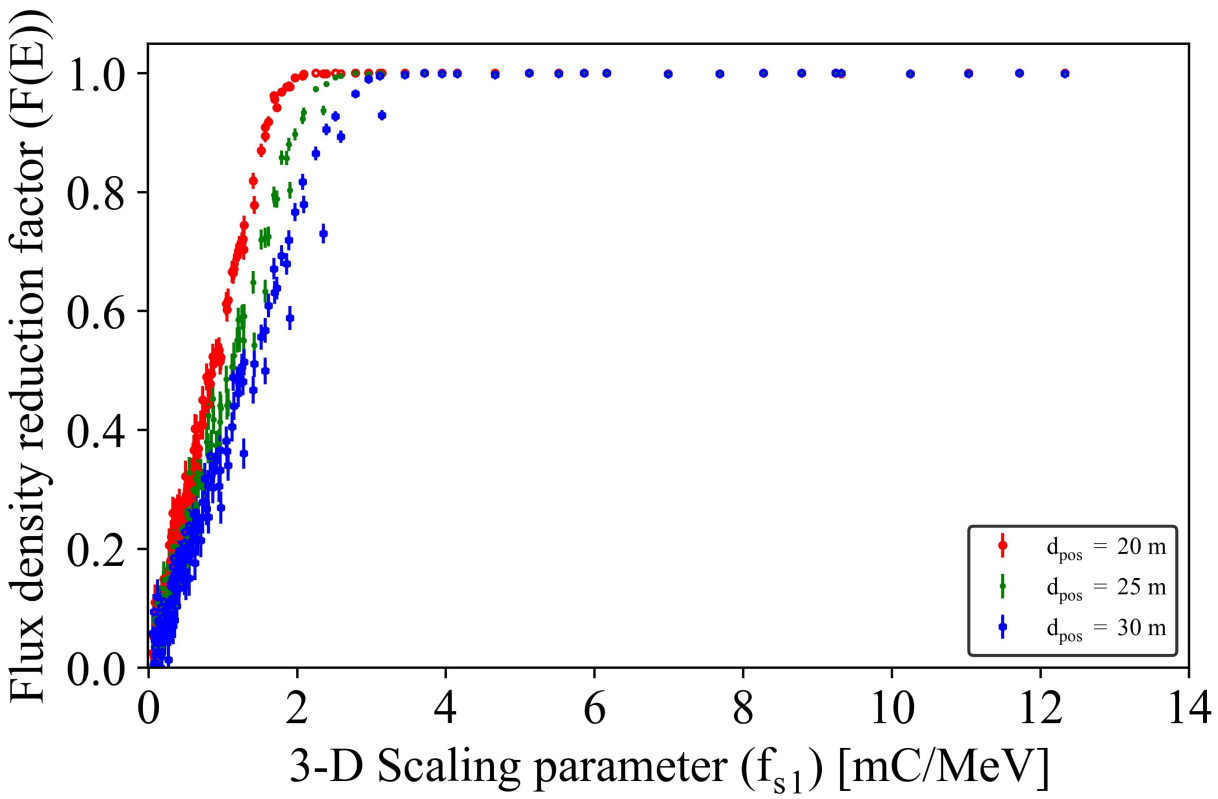

Figure 4.24: 3-D scaling parameter for plane-rod combination (with three planes) without normalized distance to the proximal plane (d_{pos}) scaling

4.10 Summary

In this chapter, different 3-D charge configurations were investigated. The initial approach was to place multiple dipole like nodes along a spherical surface. These types of configurations were only successful if positively charged monopoles were used, which is unrealistic. Later work showed that repetitively aligning these charged nodes over 3-D space lowers the potential requirement. From this idea, a charged array concept emerged where multiple 2-D charged arrays were stacked together, and negatively charged nodes were at the corners of these 2-D charged arrays. Various such configurations were tested for optimization. Of all these configurations, a suitable 3-D charge distribution emerged where 2-D charge planes were positively charged, and the negative points were extended diagonally to achieve better protection. This 3-D charge configuration was converted to a set of regular shaped conductors, and their performance was analyzed via a 3-D scaling study. Later sections show the

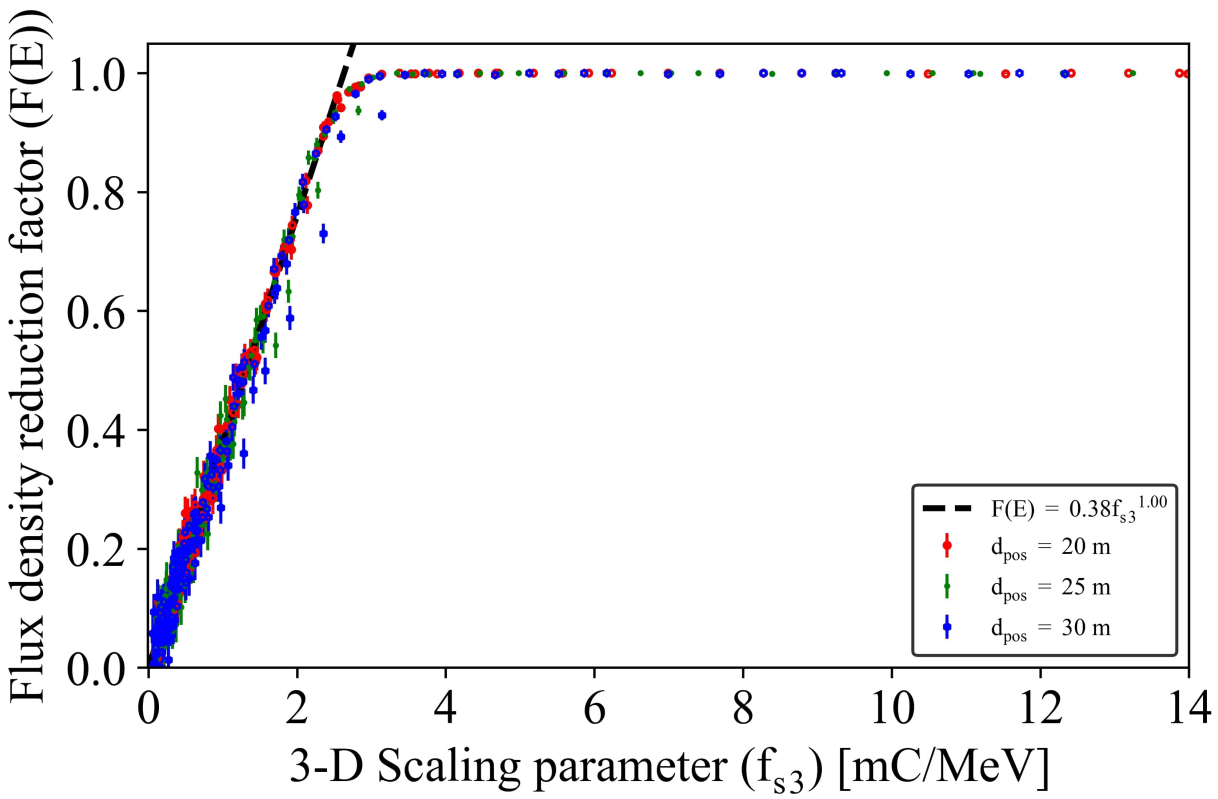

Figure 4.25: 3-D scaling parameter for plane-rod combination (with 3 planes) with normalized distance to the proximal plane (d_{pos}) scaling

improvement of the radiation shielding performance by including this charged plane and rod configuration.

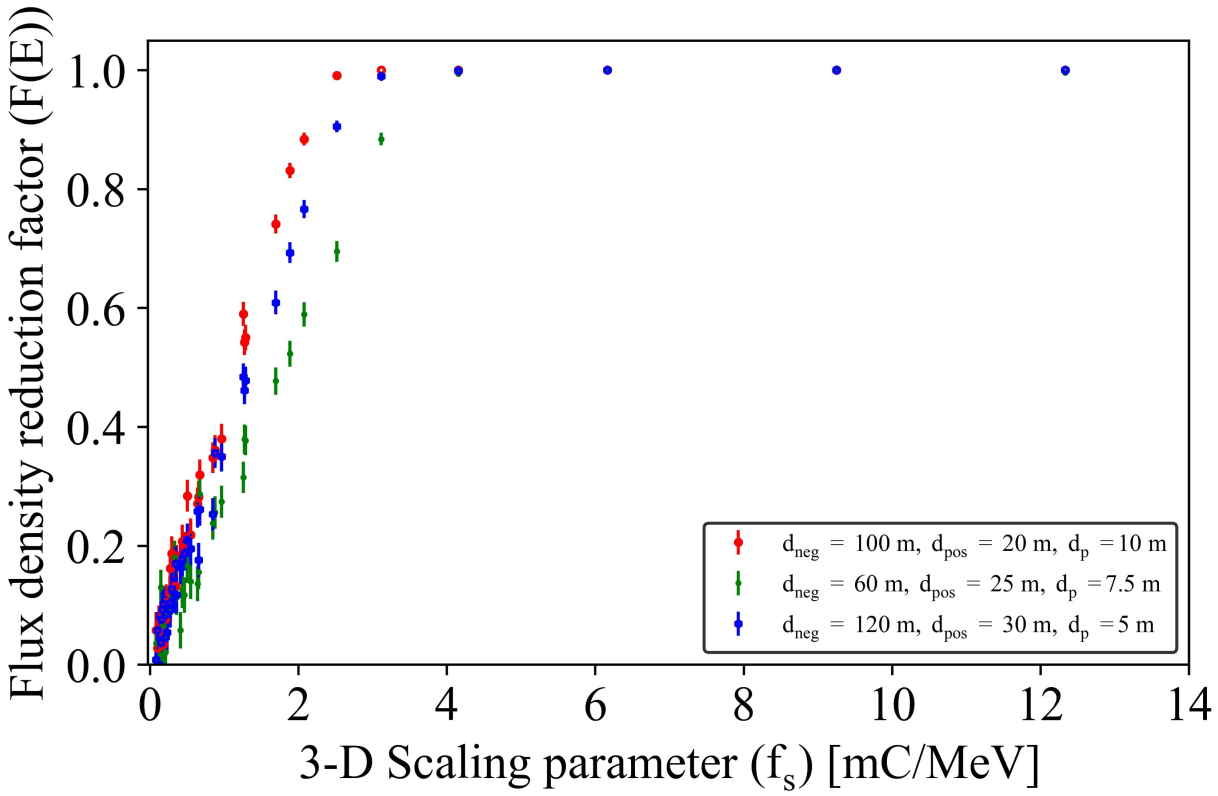

Figure 4.26: 3-D scaling parameter for plane-rod combination (with three planes) with basic scaling

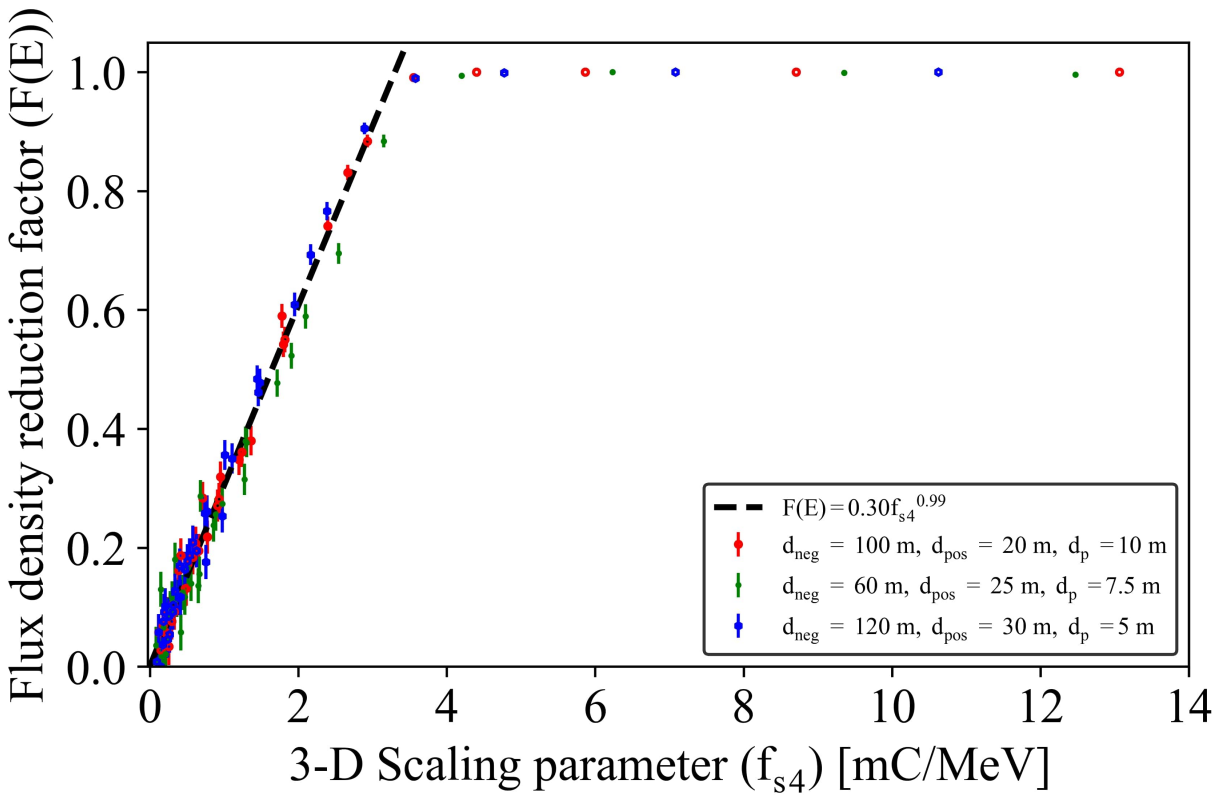

Figure 4.27: 3-D scaling parameter for plane-rod combination (with three planes) with updated 3-D scaling law

Chapter 5

Hybrid Methods of Radiation Shielding against an Extreme SPE

5.1 Motivation

The work presented in this chapter demonstrates the application of the novel active shielding configuration against an extreme, historically significant SPE (October 1989), which would pose a threat to astronauts on a deep space mission. In this section, performance metrics for multiple combinations of active and passive shielding are analyzed. For deep-space missions, storm shelters are planned within spacecraft to protect astronauts from the sudden rise in radiation exposure during severe SPEs. These are thickly shielded regions within the spacecraft where astronauts can take refuge during SPEs [30]. This work concentrates on reducing the mass penalty of the storm shelters and reducing RBE-weighted doses and effective doses for astronauts against large SPEs. The October 1989 SPE was chosen as the representative of the extreme SPE since a previous study has demonstrated that this particular SPE is capable of penetrating nominal spacecraft shielding and has a significant fluence at high energies, which can be damaging to astronauts [30]. Different thicknesses of material shielding that can be used in long-term deep space missions are studied in the presence of the chosen set of active shielding configurations, which were discussed in Chapter 4.

5.2 Description of Electrostatic Field Configurations

Figure 5.1 shows the active shielding system that was investigated in this study. For com-

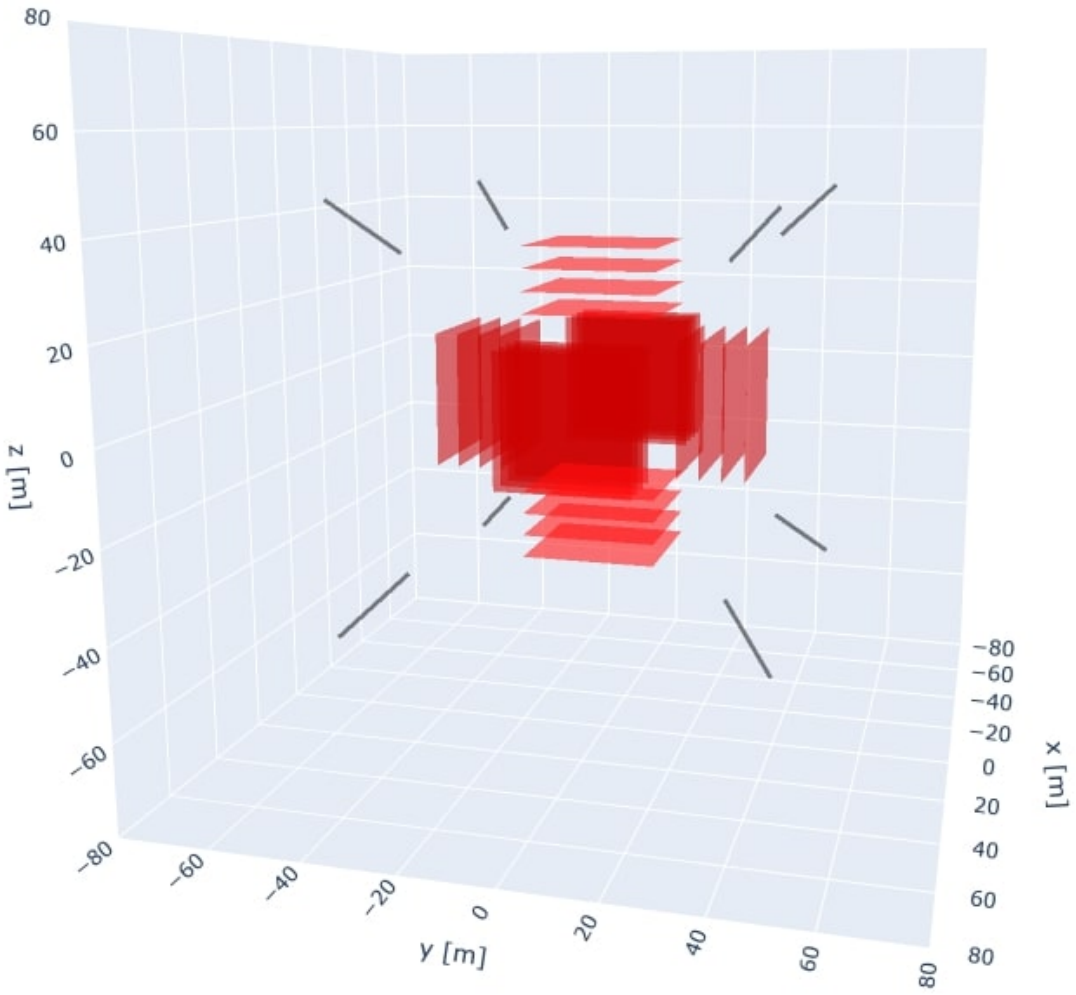

Figure 5.1: 3-D electrostatic shielding configuration with charged planes and rods

putation purposes, three different electrostatic shielding configurations were chosen. These three configurations (shown in Table 5.1) represent three different charge densities (σ) on the positively charged planes. The potentials at the mid-point of these charged planes ($V_{midplane}$) were computed using previously published work [121] and are one to two orders of magnitude lower than the potentials that were used in previous studies [96, 97, 118]. The mathematical formula to compute the potential at the center of the plane is shown in Equation 5.1,

$$V_{midplane} = 4\ln(1+\sqrt{2})\frac{1}{4\pi\epsilon_0}\frac{Q}{L}, \tag{5.1}$$

where Q is the total positive charge on the plane and L is the length of the square plane, and ϵ_0 is the permittivity of free-space.

Table 5.1: Parameter space for the charged plane and rod configuration studies

Parameter	Configuration 1	Configuration 2	Configuration 3
Surface charge density (σ) [μC m^{-2}]	7.57	11.35	15.1
Linear charge density (ρ) [mC m^{-1}]	-1.022	-1.533	-2.044
Potential at the mid-point of the charged plane ($V_{midplane}$) [MV]	7.2	10.8	14.4

In these three configurations, parameters like distance to the proximal plane (d_{pos}), distance to the negatively charged rod (d_{neg}), and gap between planes (d_p) were kept fixed at 20 m, 60 m and 5 m respectively. The total number of positively charged planes in each orthogonal direction ($+x$, $-x$, $+y$, $-y$, $+z$ and $-z$) from the center of the spacecraft was four in all the simulations. The dimension of each charged plane was kept fixed at 30 m $\times$ 30 m in all the simulations. The length of the charged rods was kept fixed at 20 m. The reason for choosing d_{pos} and d_{neg} to be 20 m and 60 m respectively is that these two parameters provided the best performance in terms of flux density reduction by keeping the extent of the active shielding configuration at 80 m, which is within the range of extents discussed in previous literature (50 m to 160 m). Mono-energetic relativistic protons with energy range varying from 10 MeV to 1000 MeV were simulated to compute the flux density reduction factor for the electric fields generated by these three active shielding configurations. No significant flux density reduction ($> 5\%$) was observed beyond 1000 MeV. Multiple random seeds (3) were used to compute the average value of flux density reduction factor and standard error (one standard error) by keeping the standard error within 2%.

Figure 5.2 shows the flux density reduction factor for all the three active shielding con-

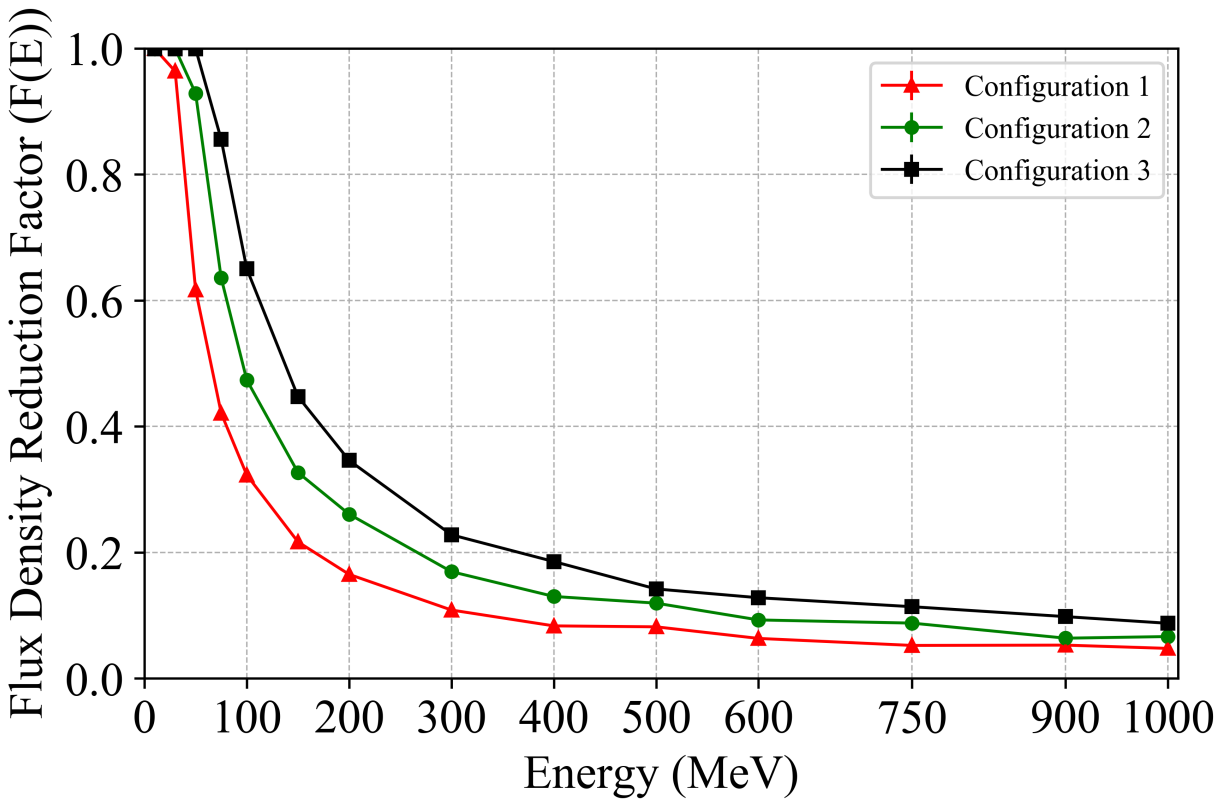

Figure 5.2: Flux density reduction factor for protons for different active shielding configurations

figurations that were investigated for energetic protons. Here, Configuration 1, 2, and 3 represent the three different charge densities of charged planes and rods, as shown in Table 5.1. These three particular charge densities (σ) come from earlier point charge based stacked 2-D array configurations (Figure 4.14). In that configuration, a 7×7 2-D charged array was used. Each point charge of that 2-D charged array was assumed to be a virtual sphere of diameter 2.5 m charged to a potential of 1 MV, 1.5 MV, and 2 MV respectively. It was assumed that the total charge on the surface of the sphere was located at the center. The total positive charge on each of the 2-D array was divided by the area of the array (30 m $\times$ 30 m = 900 m^2) to compute these particular charge densities as shown in Table 5.1. The potential on the charged planes will not be the same as that of the virtual spheres in the 2-D array, as shown in Equation 5.1, because of the difference in the shape and size of the conductors.

The flux density reduction factors for these three cases were used to compute the modified fluence spectrum of the October 1989 SPE. Here, the term flux density reduction factor can be interchangeably used as fluence density reduction factor since SPEs are time-integrated spectra. A logarithmic interpolation algorithm was used using Python software version 2.7 [122] to compute the flux density reduction factor for all the discrete energy bins for the October 1989 SPE fluence spectrum. The flux density reduction factor was assumed to be zero beyond the energy of 1000 MeV Equation 5.2 explains the computation procedure for fluence spectrum subjected to active shielding.

$$\Phi_{ASi}(E) = \Phi(E)(1 - F'_i(E)). \tag{5.2}$$

Here, $\Phi(E)$ is the October 1989 SPE fluence spectra, $F'_i(E)$ is the interpolated flux density reduction factor of the i^{th} active shielding system, and $\Phi_{ASi}(E)$ is the resulting fluence spectrum that passes through the i^{th} active shielding system. The October 1989 SPE spectrum and the proton spectra after passing through the tested active shielding configurations are shown in Figure 5.3.

5.3 Proton Angular Distribution

To use the reduced fluence spectra after the application of the electrostatic shielding ($\Phi_{ASi}(E)$), it was important to determine whether the electric field provides equal protection for all directions of the 4π sr solid angle for incoming protons. Also, to transport the attenuated fluence spectrum through passive shielding, it was important to determine the angular distribution of the incident spectra to be transported. To determine the protection for all directions, the 4π solid angle was divided into 10×10 discrete angular bins in the azimuthal (θ) as well as elevational (ϕ) directions. Here, the angular fluence was computed for each of these bins with and without the presence of the electric field. The angular protection was calculated as the ratio of the angular fluence in case of with and without the active shield in each of these angular bins on the surface of a sphere with radius 5 m and centered at the

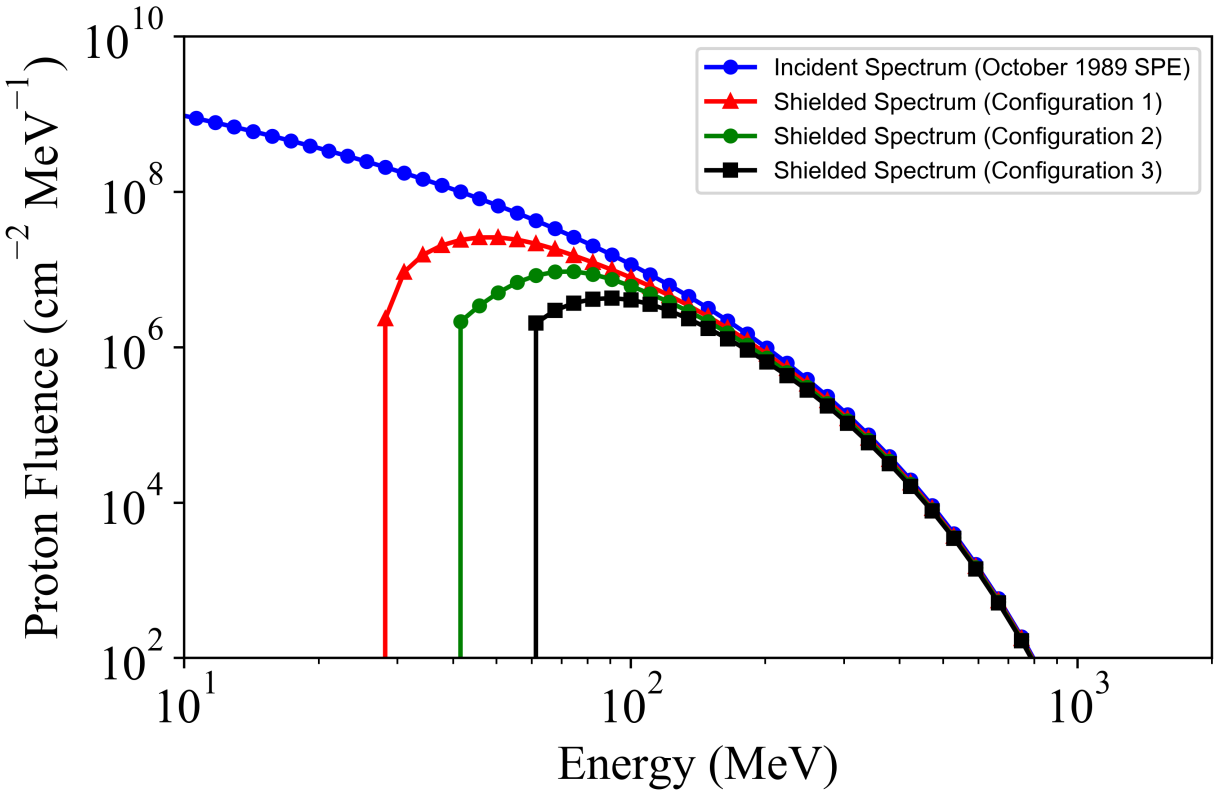

Figure 5.3: Unshielded and shielded proton fluence spectra

origin. This sphere represents spherical crew volume (spacecraft), which was kept constant at 5 m. Protons of kinetic energy 50 MeV to 500 MeV were simulated in the presence of the active shielding Configuration 3. A total of 1.25×10^8 particle histories were simulated for each energy in order to compute the angular fluence. Figures 5.4, 5.5, 5.6, and 5.7 represent the angular protection for each of these bins are represented for protons of kinetic energy 50 MeV to 500 MeV. It is clear from the figures that angular reduction under various angular bins is almost the same for all 100 angular bins. This pattern is observed for all the three active shielding configuration investigated. This shows that the proton spectra, after passing through the active shielding configuration, acts very close to an isotropic distribution. Therefore, the assumption that the fluence spectra after passing through the active shielding will be isotropic is justifiable.

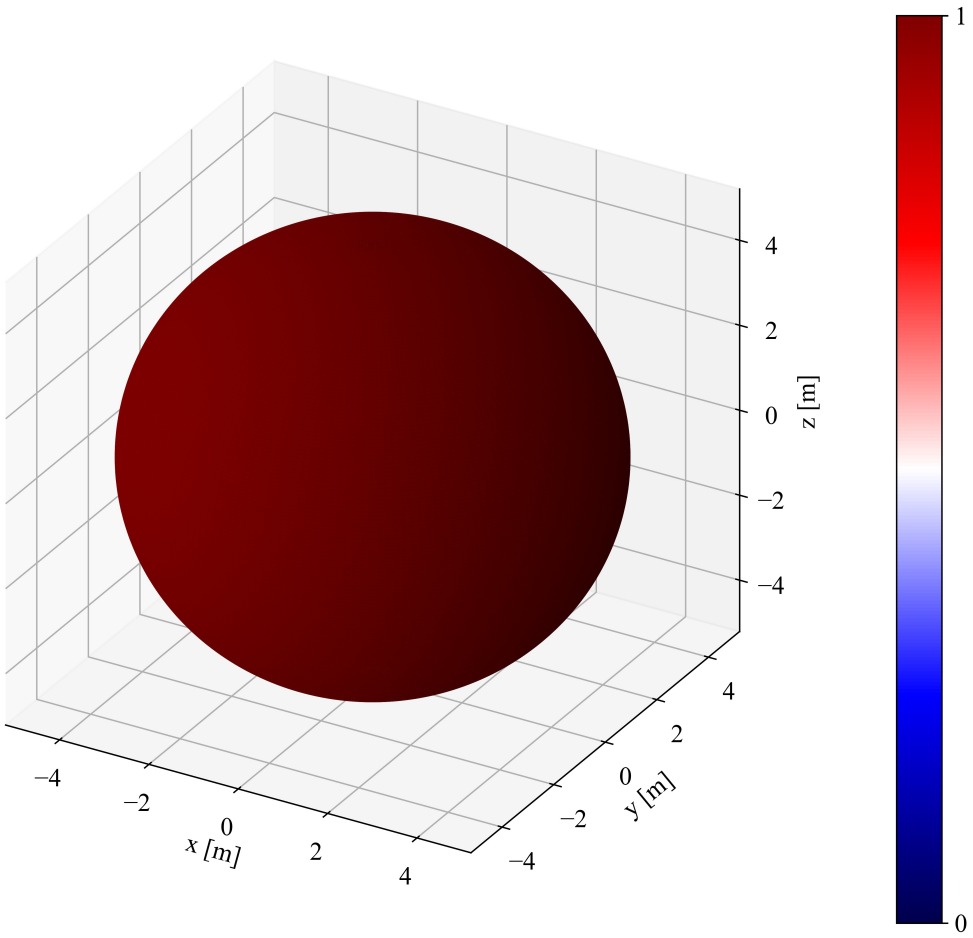

Figure 5.4: Degree of angular reduction in 10×10 angular bin for 50 MeV proton in Configuration 3

5.4 Hybrid Shielding Configurations

In this section, combinations of active and passive shielding are evaluated for shielding efficacy against the October 1989 SPE. The relative performance of these configurations is discussed here. For passive shielding, aluminum was chosen as the standard shielding material as it is the most commonly used material in the case of spacecraft construction. Thicknesses of 5, 10, and 20 $\mathrm{g\,cm^{-2}}$ were used as these thicknesses represent lightly, moderately, and heavily shielded spacecraft. The hybrid shielding configuration was divided into three types. These were: 1) Active-Passive 2) Passive-Active and 3) Passive-Active-Passive. Figures 5.9, 5.10, and 5.11 represent these three different types of hybrid configurations. Besides these

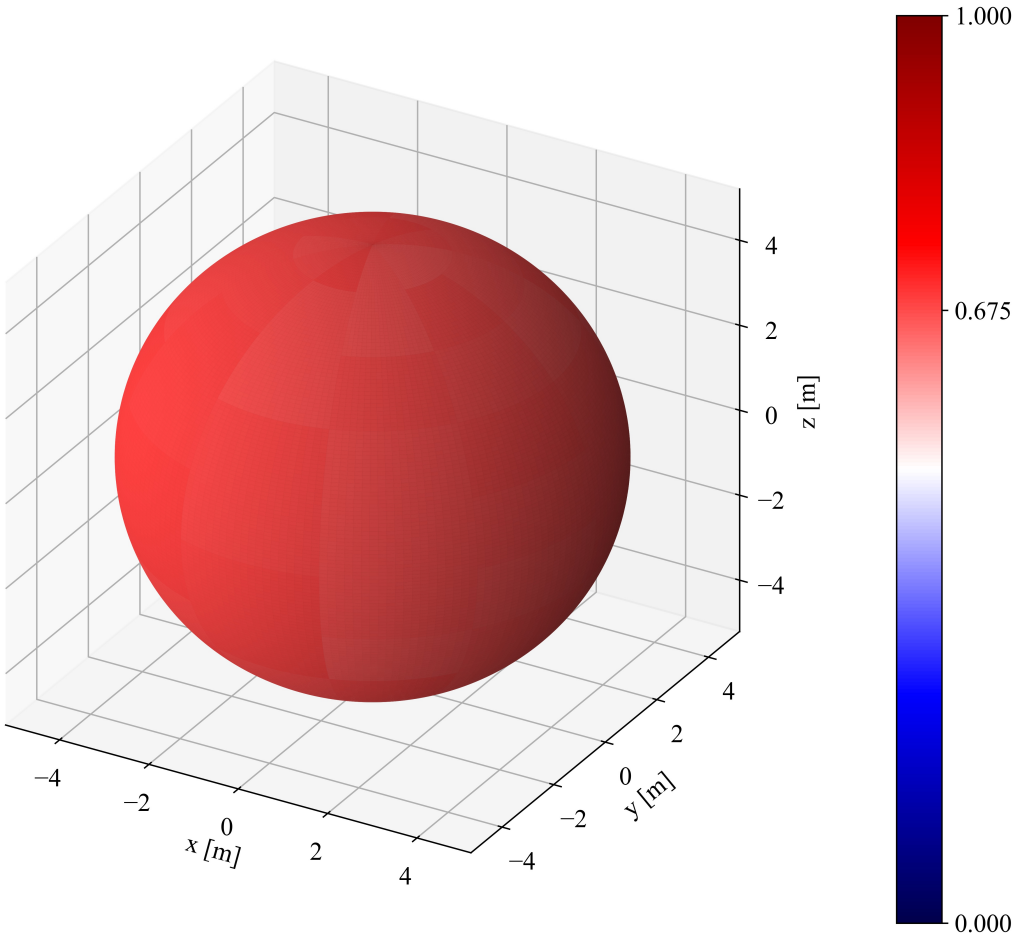

Figure 5.5: Degree of angular reduction in 10×10 angular bin for 100 MeV proton in Configuration 3

three hybrid configurations, passive shielding only was also tested to characterize the performance of these hybrid configurations in terms of their mass savings and reduction of dose and related quantities (Figure 5.8.

The multiple hybrid shielding combinations that have been tested in this study are shown below:

1. $5\,\mathrm{g\,cm^{-2}}$ (Passive),
2. $10\,\mathrm{g\,cm^{-2}}$ (Passive),
3. $20\,\mathrm{g\,cm^{-2}}$ (Passive),

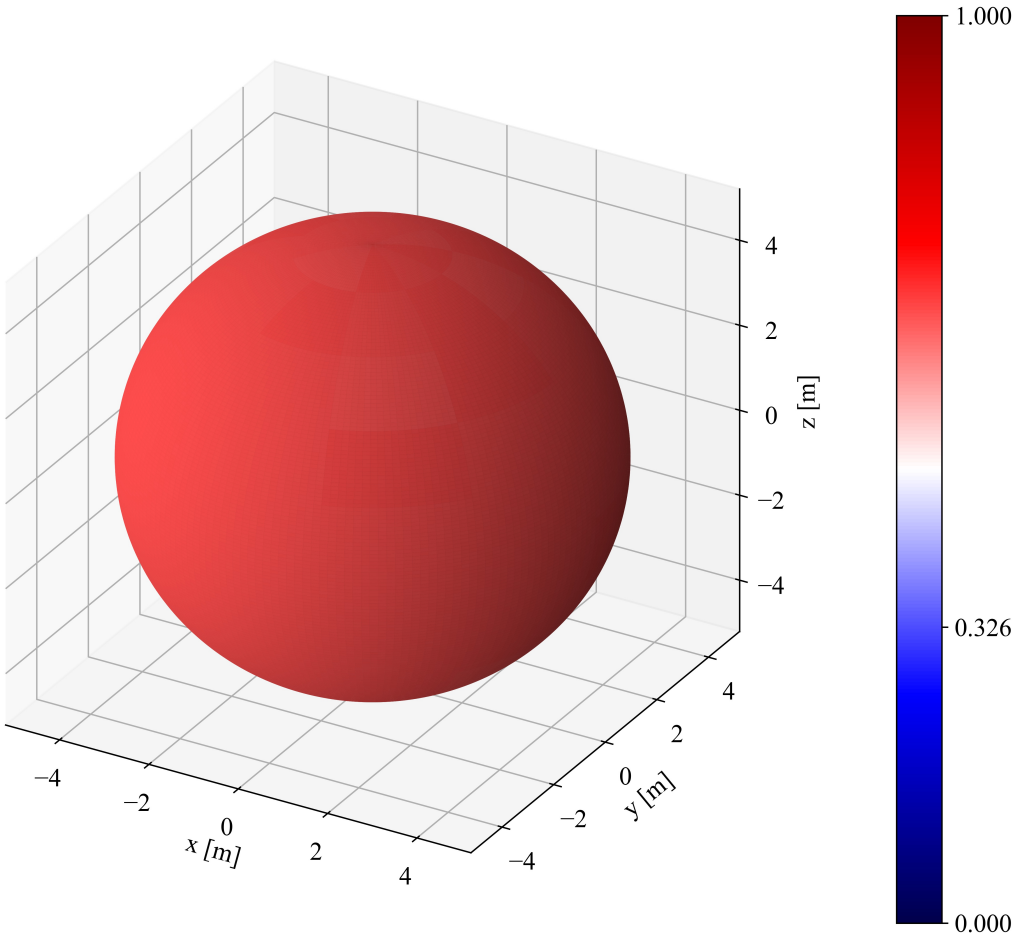

Figure 5.6: Degree of angular reduction in 10×10 angular bin for 200 MeV proton in Configuration 3

4. Configuration 1 + $5\,\mathrm{g\,cm^{-2}}$ (Active-Passive),

5. Configuration 2 + $5\,\mathrm{g\,cm^{-2}}$ (Active-Passive),

6. Configuration 3 + $5\,\mathrm{g\,cm^{-2}}$ (Active-Passive),

7. Configuration 3 + $10\,\mathrm{g\,cm^{-2}}$ (Active-Passive),

8. Configuration 3 + $20\,\mathrm{g\,cm^{-2}}$ (Active-Passive),

9. $5\,\mathrm{g\,cm^{-2}}$ + Configuration 1 (Passive-Active), and

10. $2\,\mathrm{g\,cm^{-2}}$ + Configuration 1 + $3\,\mathrm{g\,cm^{-2}}$ (Passive-Active-Passive).

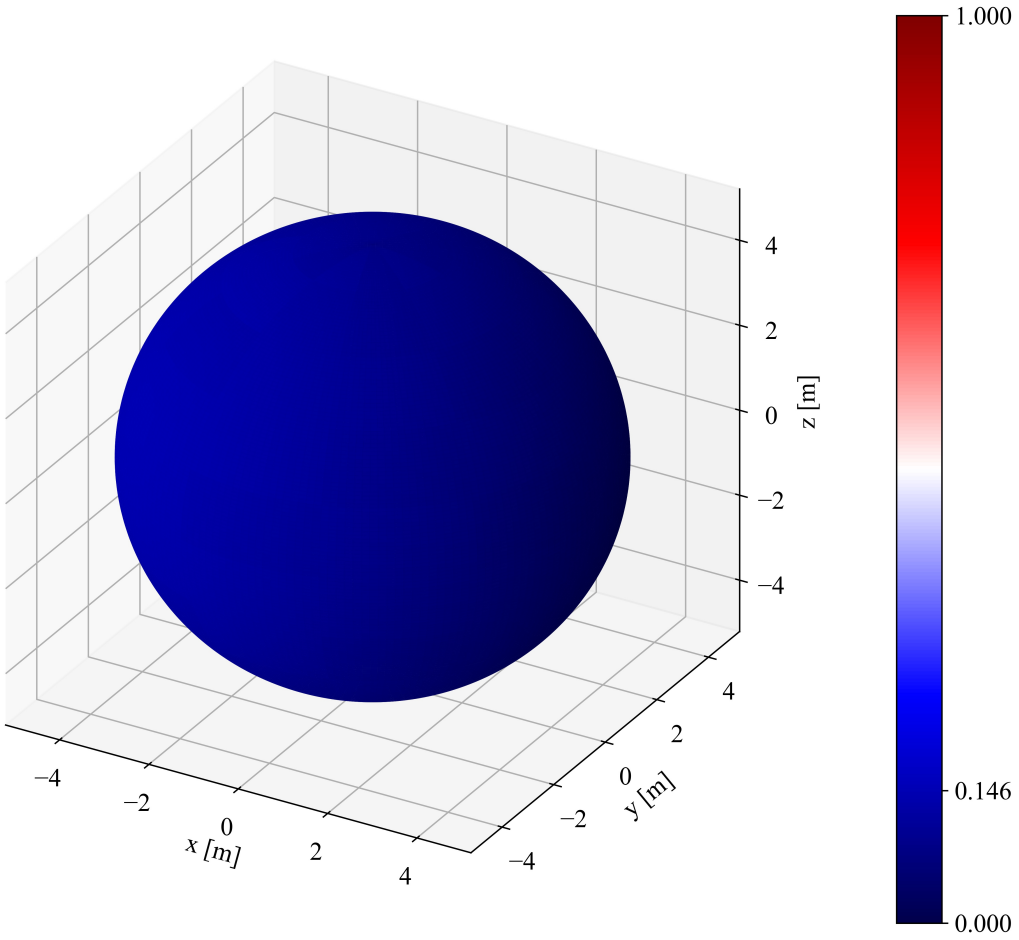

Figure 5.7: Degree of angular reduction in 10×10 angular bin for 500 MeV proton in Configuration 3

In the case of active-passive combination, three active shielding configurations were tested with lightly shielded spacecraft ($5\,\mathrm{g\,cm^{-2}}$) to observe whether any of the three different active shielding configurations could provide a similar degree of protection as that provided by the moderately and heavily shielded spacecraft. The best performing active shielding system (Configuration 3) was also tested with moderately and heavily shielded configurations to assess whether any improvement in performance is gained by appending the best active shielding configuration with these two types of material shielding. The first two active shielding configurations were not tested along with moderately and heavily shielded configurations because these two types of material shielding are capable of completely stopping protons of kinetic energy 100 MeV and 150 MeV respectively, and therefore a significant gain

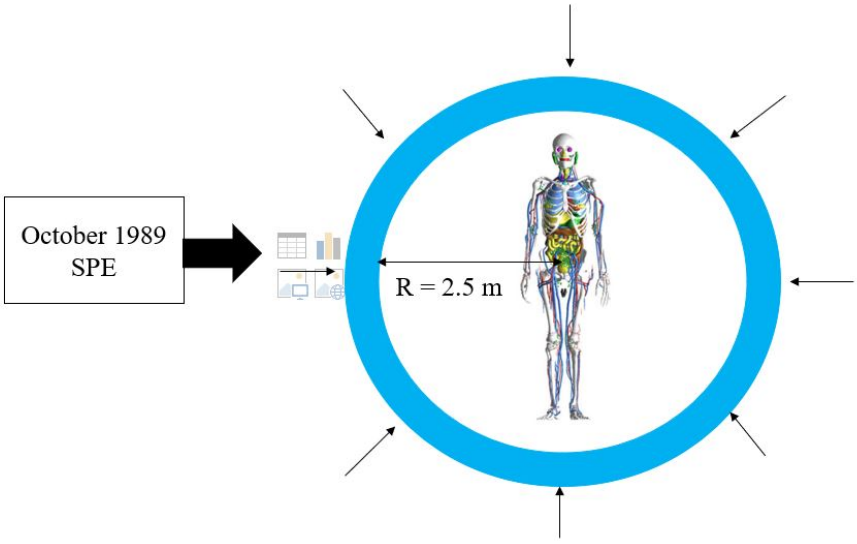

Figure 5.8: Passive shielding configuration

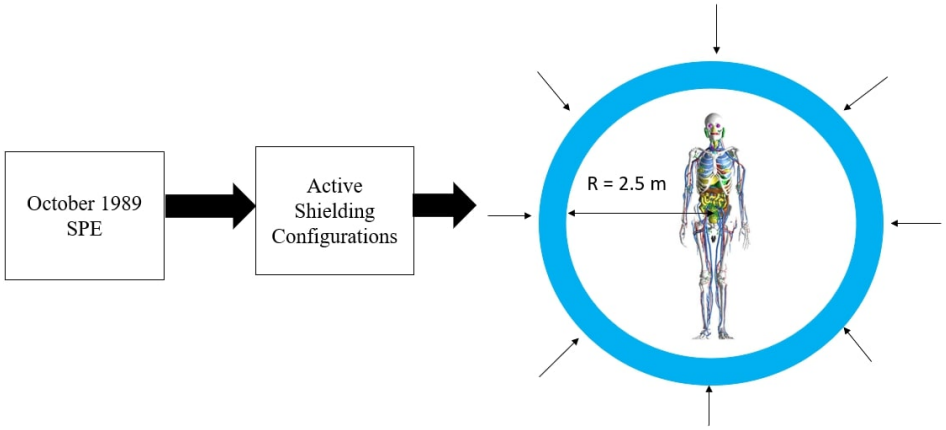

Figure 5.9: Hybrid Active-Passive configuration

could not be achieved by appending the first two active shielding configurations. In the case of passive-active and passive-active-passive configurations, the combination was only tested with lightly shielding materials (less than or equal to $5\,\mathrm{g\,cm^{-2}}$). The rationale was that these configurations were tested as a proof of concept to show that adding passive materials before active shielding can be beneficial. Placing passive materials before active shielding, which is spanned over hundreds of meters is technologically challenging. Therefore, for passive-active or passive-active-passive configurations, only lightly shielded materials were tested. For the

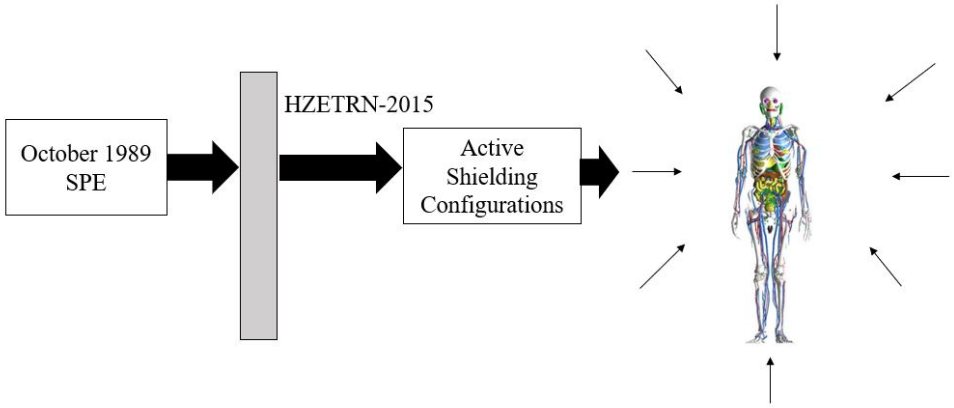

Figure 5.10: Hybrid Passive-Active configuration

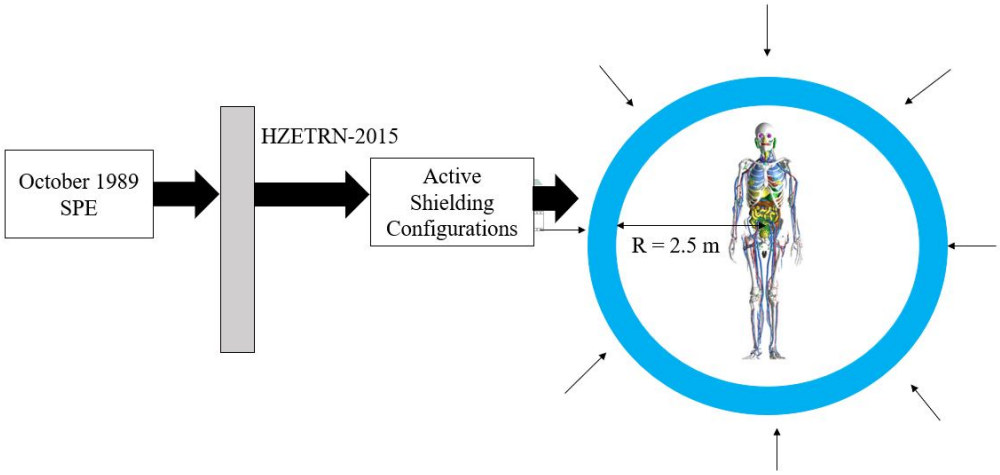

Figure 5.11: Hybrid Passive-Active-Passive configuration

passive-active-passive case, the total material shielding was chosen to be equal to the case of passive-active, to observe whether any advantage can be achieved by distributing the material shielding before and after the active shielding. In the results section, the outcomes of these four different types of shielding combinations (passive, active-passive, passive-active, and passive-active-passive) are demonstrated. To evaluate the performance metric of each of these configurations, the organ dose equivalent and RBE-weighted dose were computed to characterize the risk of the stochastic and deterministic effects, respectively. To calculate organ dose equivalents, the track structure based NASA solid cancer and leukemia qual-

ity factors were used [47]. The organ dose equivalents and RBE-weighted dose [11] were computed for both male and female ICRP-110 computational phantoms [123].

5.5 Ion Scaling

The flux density reduction factor was computed for protons for the configurations is shown in Figure 5.3. The flux density reduction factor was only computed for protons. To assess the performance of passive-active and passive-active-passive configurations, the performance of the active shielding in terms of protection against heavier ions was required, as heavier ions can be generated from target fragmentation. Also, in the case of GCR boundary conditions, there are heavier ions ranging from $Z = 1$ to $Z = 28$ that contribute to organ dose equivalent. Therefore, to compute the flux density reduction factor for all these configurations, all of these ions need to be simulated in different electrostatic field using ASPP, which can be computationally cumbersome. To reduce the required simulation time, a few chosen ions that contribute significantly towards the total effective dose in case of GCR were simulated. The flux reduction factor as a function of kinetic energy of these ions (MeV/n) are shown in Figure 5.12. It is clear that the reduction factor is dependent on the mass and charge of the ions. To remove the dependency, a scaling factor equal to A_{ion}/Z_{ion} was multiplied with each (shown in Equation 5.3). Figure 5.13 shows the flux reduction for each of these ions with the scaling factor. It is evident from the Figure 5.13 that the scaled flux reduction for all energies and all ions coincide. This finding is important as now only the flux density reduction of protons can be simulated using ASPP and flux density reduction factor for all ions can be computed using the mathematical formula shown in Equation 5.3,

$$F_{ion}(E) = F_{proton}(E)\frac{Z_{ion}}{A_{ion}}, \tag{5.3}$$

where $F_{ion}(E)$ represents the flux density reduction of any ion with atomic number and atomic mass Z_{ion} and A_{ion} respectively, whereas $F_{proton}(E)$ represents the flux reduction for protons for the active shielding configuration. All three active shielding configurations show

similar pattern. The resulting ion flux was computed using Equation 5.4,

$$\phi_{ion_i}(E) = \phi_{GCR,ion}(1 - F_{proton_i}(E)\frac{Z_{ion}}{A_{ion}}), \tag{5.4}$$

where $\phi_{ion_i}(E)$ represents the flux of ion ($Z > 1$) after it passes through the i^{th} active shielding configuration. This ion scaling law for active shielding configurations was used for the computational dosimetry throughout this chapter and Chapter 6. Equation 5.3 shows that the lower the Z/A ratio, the more difficult is to deflect the ion using the electric field.

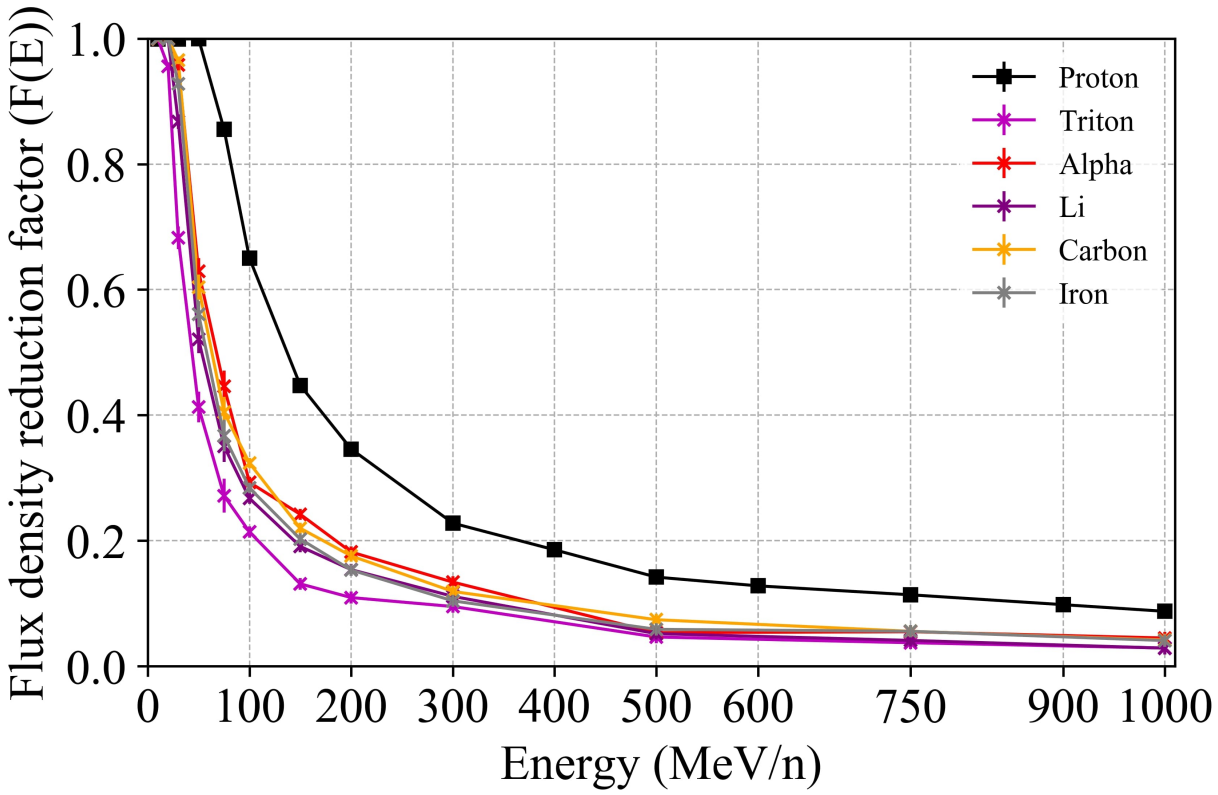

Figure 5.12: Flux density reduction factor for different GCR ions without scaling

5.5.1 Surface Charge Density Scaling

In this section, the effect of increasing the surface charge density of the positively charged plane (σ) of this active shielding system is discussed. In the three active shielding configurations discussed above, the only varying parameter is σ. Figure 5.2 shows the flux density

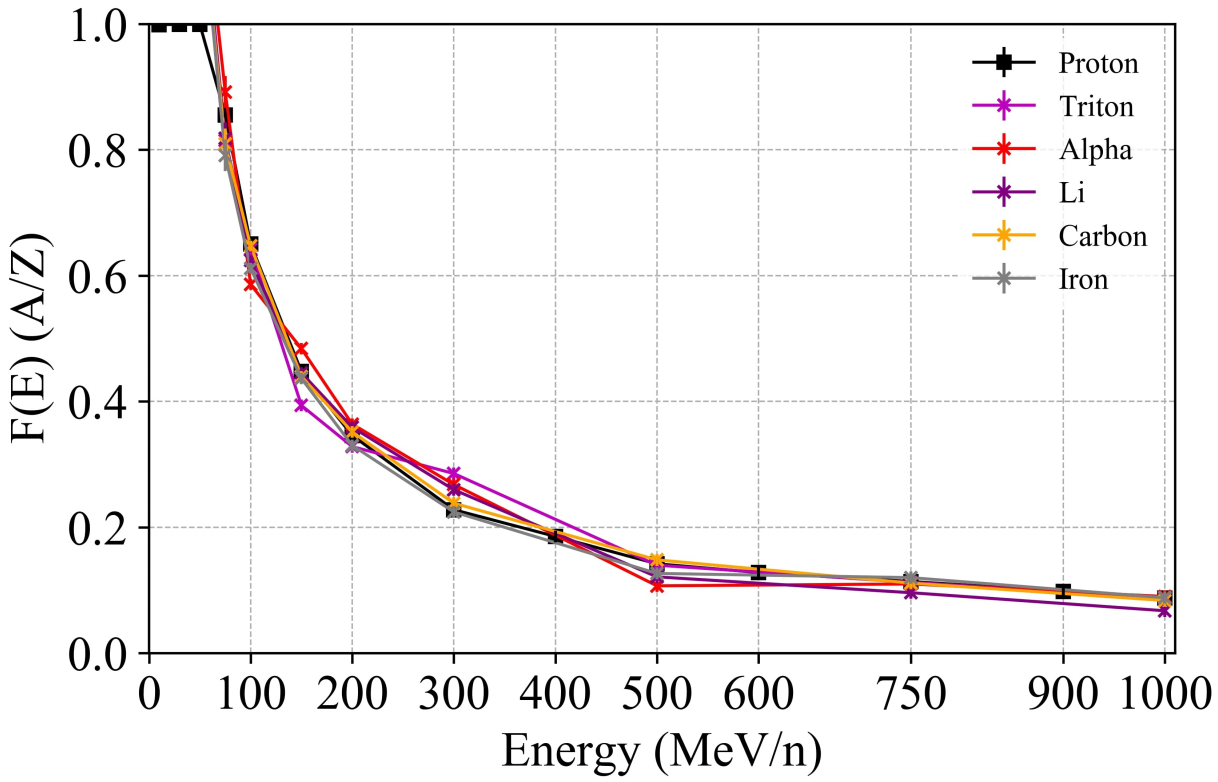

Figure 5.13: Flux density reduction factor for different GCR ions with scaling

reduction factor ($F(E)$) of protons as a function of kinetic energy for all the three active shielding configurations. Figure 5.14, shows the flux density reduction factor scaled by the factor σ_{max}/σ, where σ_{max} is the maximum charge density among the three configurations tested here (Configuration 3)), and σ is the surface charge density for each active shielding configurations. It is evident from Figure 5.14 that when the flux density reduction factor is multiplied by the normalization factor, the three configurations align with each other. This outcome is important as the flux density reduction factor of any surface charge density can be computed using this formula, if all the other parameters remain constant. This work was done for the purpose of demonstration of this property and was not used in any of the radiation transport work.

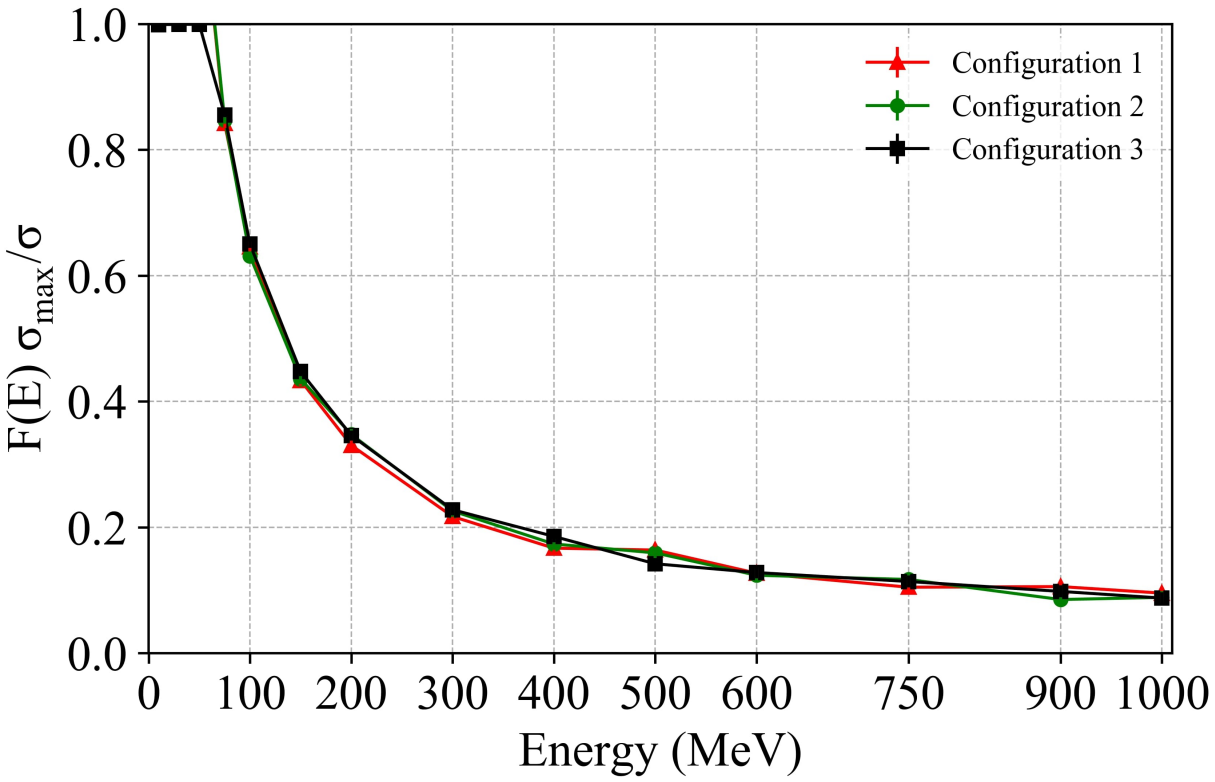

Figure 5.14: Flux density reduction factor normalized with the surface charge density

5.6 Passive Radiation Transport

For radiation transport, stochastic Monte Carlo based code PHITS version 3.17b was used [124] for accurately simulating all the primary and secondary radiation within the voxelized ICRP phantom [123]. The PHITS input file consists of five parts: 1) Definition of the physics modules used 2) Definition of source geometry 3) Material definition 4) Definition of the computational phantom 5) Definition of the output tallies. The source was chosen to be isotropic to represent space-like conditions. For the simulation of RBE-weighted dose, the RBE values shown in Table 1.4 were used. For all other particles that are not listed in this table (Table 1.4), the RBEs are equal to one. In this section, the radiation transport for the three categories of shielding configurations are described.

5.6.1 Description of the Computational Phantoms

For computational phantom, ICRP Publication 110 model was chosen [123]. The ICRP model has both voxel based computational phantoms for both male and female. The voxel phantom had a total of 140 tissue sites that were tallied for computing tissue-specific dose equivalent using NASA solid cancer and leukemia quality factors. Also, dose for each of organ site was computed under different shielding conditions. The male phantom, represents a 38-year-old with height of 176 cm and weight of 76 kg, and consists of 220 slices of 256×256 voxels with 8 mm height and a resolution of 2.08 mm $\times$ 2.08 mm. The female phantom, represents a 43-year-old with height of 167 cm and weight of 60 kg, and consisted of 346 slices of 256×256 voxels with 5 mm height and a resolution of 1.875 mm $\times$ 1.875 mm. Both the male and female computational phantoms were in standing position with arms at side.

5.6.2 Active-Passive Configuration

In case of active-passive combination (Figure 5.9), first the SPE proton spectrum was transported via the different active shielding configurations using Equation 5.2. The resulting spectrum was then transported using PHITS through different material thicknesses and body self shielding to compute dosimetric quantities including effective dose and RBE-weighted dose. Previously, it was shown that the distribution of the SPE fluence remained very close to an isotropic distribution after it passes through the active shielding (Figure 5.6). Using that approximation, the shielded fluence spectrum was assumed to be isotropic prior to encountering the material shielding.

5.6.3 Passive-Active Configuration

In case of passive-active combinations (Figure 5.10), the SPE spectrum was transported through different material thicknesses and resulting particle fluence spectra were computed using 3D-HZETRN [2, 3]. For transport using 3D-HZETRN, 'slab' mode was used which uses bi-directional radiation transport. The October 1989 SPE spectrum was assumed to be incident normally on a slab of thickness 5 g cm^{-2} aluminum. The resulting spectra con-

tained different particles like proton, deuteron, triton, helion, alpha and neutron, which are generated via interactions with the passive shielding. The spectra of charged particles were transported through active shielding configuration using Equations 5.2 and 5.4. The resulting spectra were then transported via body-self shielding using PHITS to compute effective dose and RBE-weighted dose.

5.6.4 Passive-Active-Passive Configuration

This configuration (Figure 5.11) is similar to passive-active configuration, except the fact that the particle fluence spectra, after passing through active shielding, were transported through another layer of thickness of material shielding and body self-shielding to compute the shielding performance metric.

5.6.5 Computation of Effective Dose

To assess the performance of the shielding system, a singular quantity should be defined as the metric for the performance of the active and passive shielding system. The NASA-2010 model for whole-body effective dose was used as the metric [12]. The non-smoker population tissue weight factors were used to compute the effective dose. The tissue-specific weight factors that were used for computation are shown in Table 5.2. The values in parenthesis for the bone marrow represents the tissue weight factor in case of GCR computation.

To compute the blood-forming organs (BFO) dose and dose equivalent, 13 different sites were used, and those are cervical vertebrae, clavicle, cranium, proximal femur, proximal humerus, lumbar vertebrae, mandible, pelvis, ribs, sacrum, scapulae, sternum and thoracic vertebrae. Mass-averaged dose and dose equivalents were computed for each of these sites in order to compute the BFO dose and dose equivalent. The same approach was taken to compute the RBE-weighted dose for BFO.

Table 5.2: Tissue weights for NASA 2010 model for never smokers, after Ref. [12]

Tissue	NASA NS US Male	NASA NS US Female
Colon	0.1	0.09
Stomach	0.12	0.08
Liver	0.07	0.05
Lung	0.19	0.32
Bladder	0.06	0.04
Breast/Prostate	0.03	0.08
Testis	0	0
Brain	0.02	0.01
Esophagus	0.019	0.007
Salivary Glands	0.003	0.003
Oral cavity (OC)	0.003	0.003
Skin	0	0
Thyroid	0.002	0.004
Bone marrow	0.28 (0.21)	0.13 (0.1)
Bone surface	0	0
Remainder	0.07	0.08
Total	1.0	1.0

5.7 Results

In this section, the relative performance of different hybrid shielding arrangements are presented in detail. The plots here demonstrate shielding performances in terms of organ dose equivalent, effective dose and RBE-weighted dose. Figures 5.15 and 5.16 represent the organ dose equivalent for female computational phantoms under various shielding configurations. Similarly, Figures 5.17 and 5.18 represent the organ dose equivalent for male computational phantoms under various shielding configurations.

RBE-weighted dose is calculated for organs where the tissue effects are a concern such as skin, heart, BFO, and eyelens. For the brain, only the dose value (in Gy) is shown. This work shows the relative performance of different shielding configurations in terms of limiting the deterministic effects. The limits for these deterministic effects, were shown in Table 1.6.

The RBE-weighted dose for different shielding configurations for female and male computational phantoms are shown in Figures 5.19, 5.20, 5.21, and 5.22 respectively. The figures

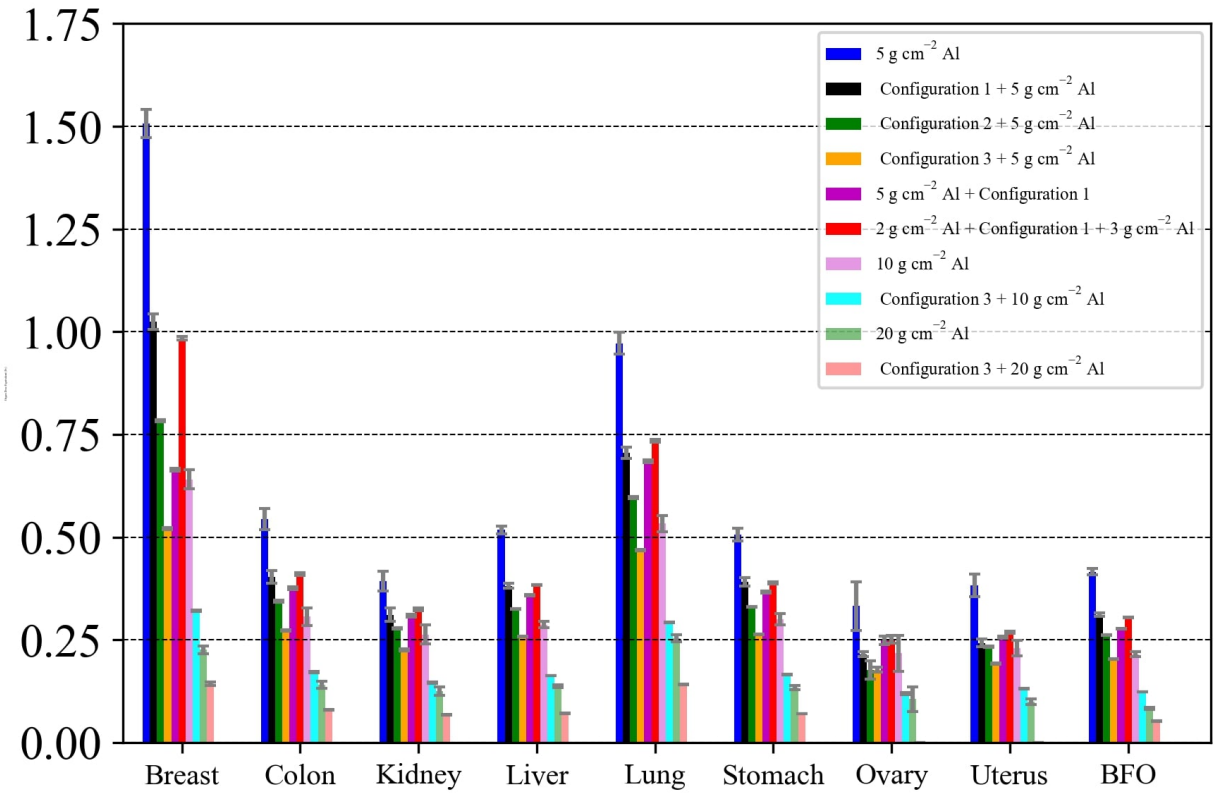

Figure 5.15: Comparison of organ dose equivalent for different important female organs (part 1)

are divided in two subsets representing lightly shielded (material shielding with $\leq 5\,\mathrm{g\,cm^{-2}}$) and heavily shielded (material shielding with $> 5\,\mathrm{g\,cm^{-2}}$). The black and red dotted lines represent the 1-month and 1-year RBE-weighted dose for BFO. It is evident from Figures 5.21 and 5.19 that the RBE-weighted dose for skin is reduced from more than 1500 mGy-Eq (30-day limit) in case of $5\,\mathrm{g\,cm^{-2}}$ shielding to around 500 mGy-Eq when Configuration 3 is used before the $5\,\mathrm{g\,cm^{-2}}$ aluminum. Also, for the heart, the Configuration 3 in conjunction with $10\,\mathrm{g\,cm^{-2}}$ of aluminum reduced the RBE-weighted dose below 250 mGy-Eq (30-day limit) for the male as well as the female, as shown in Figures 5.22 and 5.20. Hybrid shielding configurations are effective in terms of reducing deterministic tissue reactions. It can be concluded that Configuration 3, along with $10\,\mathrm{g\,cm^{-2}}$ worked best among all of them as it lowered the exposure below the specified limit without the use of heavy material shielding. The outcomes for RBE-weighted dose for different thickness of material shielding from $5\,\mathrm{g\,cm^{-2}}$ to $20\,\mathrm{g\,cm^{-2}}$

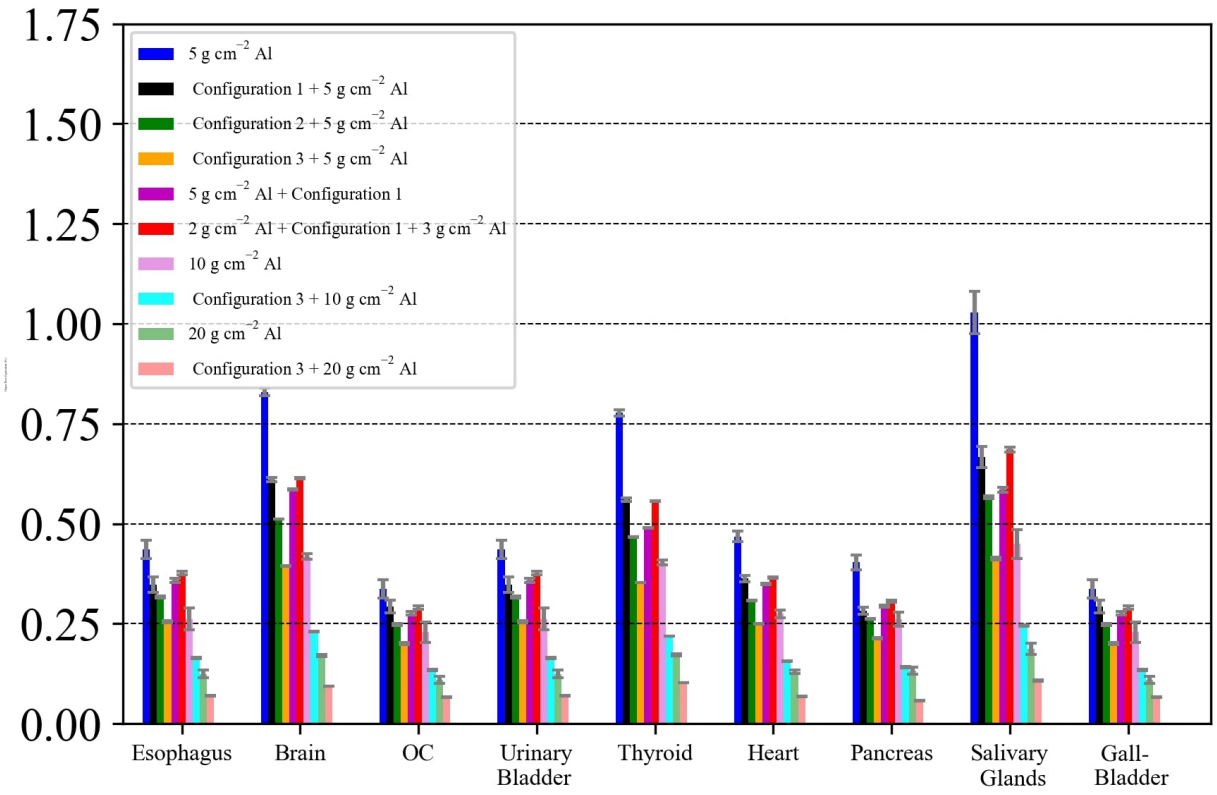

Figure 5.16: Comparison of organ dose equivalent for different important female organs (part 2)

were validated with the outcomes from literature [30]. The RBE-weighted BFO dose under a low and moderate amount of shielding thickness matched very well with the data from literature [30] ($\leq$ 1% relative error), but it did not match with the RBE-weighted dose under heavy shielding (20 g cm^{-2}). The reasons for that can be attributed to the different types of radiation transport tools used for these studies.

Figure 5.23 demonstrates the effective dose under different shielding conditions. In each case, the relative error was kept under 2%. Configuration 3 along with 5 g cm^{-2} provided better performance than only 10 g cm^{-2}. The organ dose and dose equivalent values were validated with outcomes from known literature [11]. It is evident from Figure 5.23 that increasing the potential or charge in different active shielding with a constant value of passive shielding lowers the effective dose linearly. For example, in the case of Configuration 1 + 5 g cm^{-2}, and Configuration 3 + 5 g cm^{-2}, it is shown that the effective dose is reduced by

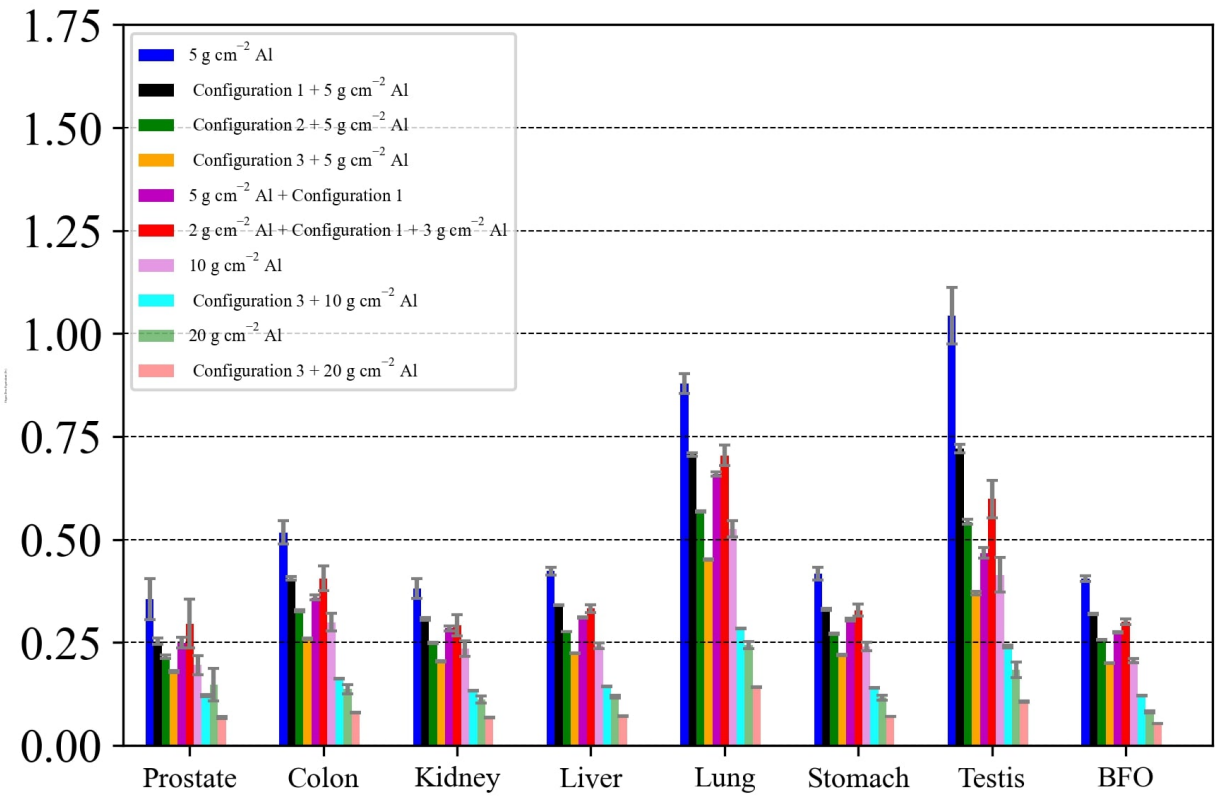

Figure 5.17: Comparison of organ dose equivalent for different important male organs (part 1)

a factor around 2, which is the ratio of the magnitude of surface charge density (electric field) between Configuration 1 and Configuration 3. Configuration 3 along with $10\,\mathrm{g\,cm^{-2}}$, improved the performance from only $10\,\mathrm{g\,cm^{-2}}$ by around 50%. Whereas, Configuration 3 along with $20\,\mathrm{g\,cm^{-2}}$, improved the performance from only $20\,\mathrm{g\,cm^{-2}}$ by 40% and 48% for male and female respectively. Also, it was observed that placing Configuration 1 after the material shielding of $5\,\mathrm{g\,cm^{-2}}$ aluminum improves the performance by around 20% in comparison to placing Configuration 1 before $5\,\mathrm{g\,cm^{-2}}$ aluminum. This is a very important outcome as it validates the hypothesis that passive-active combination can be beneficial in terms of mitigating space radiation risk as it converts the high energetic component of the radiation to lower energetic components which can then be shielded easily with a lower magnitude of an electric field. In Chapter 6, this theory is tested with GCRs. Also, it was observed that the passive-active-passive combination did not perform better than passive-

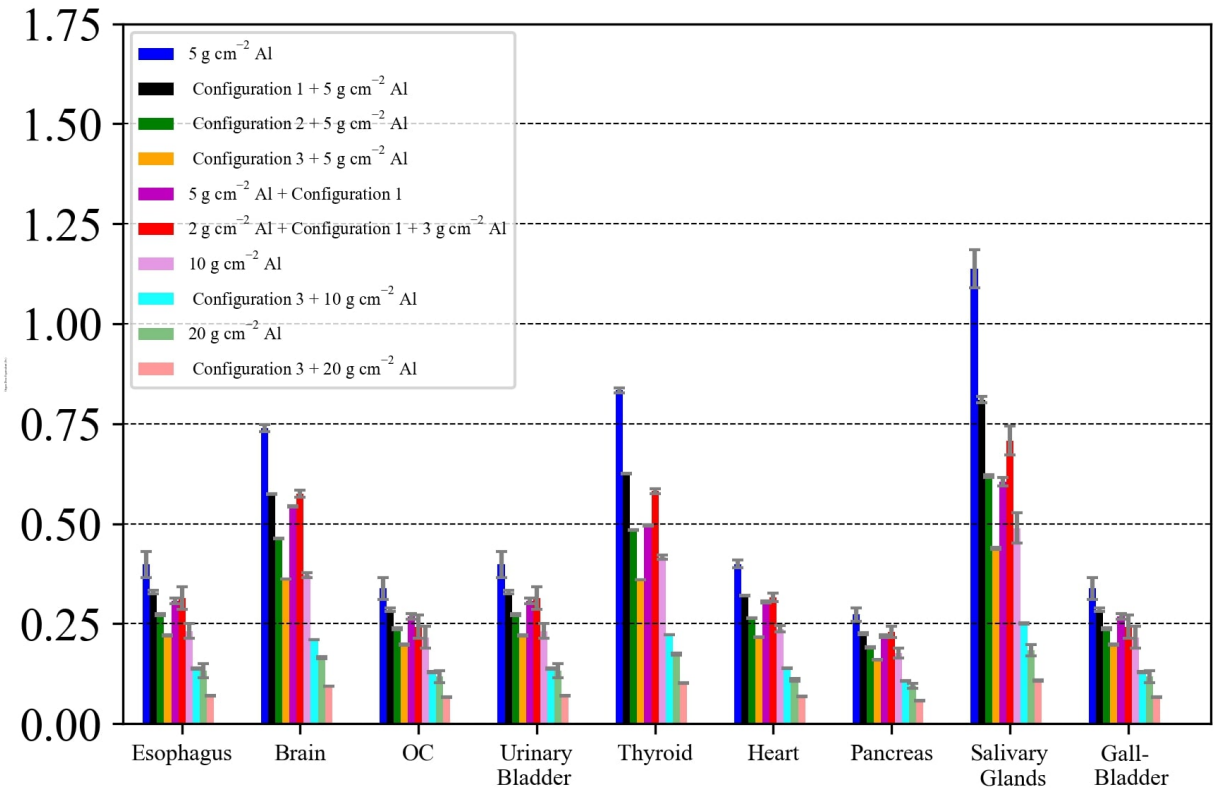

Figure 5.18: Comparison of organ dose equivalent for different important male organs (part 2)

active for low material shielding. Different combinations of this type can be tested in the future to find the optimum configuration.

5.8 Summary

It was observed that implementing active shielding before the passive shielding lowers the exposure quantities and thus can be utilized to reduce the mass penalty. In this work, the effects of hybrid shielding on SPEs were observed in effective doses and RBE-weighted doses. Among all the configurations tested, the active-passive combination of Configuration 3 and $10\,\mathrm{g\,cm^{-2}}$ was chosen to be the best as it was successful in terms of reducing the RBE-weighted dose below specified limit without using heavy material shielding. It was also observed that Configuration 3, when used with $5\,\mathrm{g\,cm^{-2}}$, can perform better than $10\,\mathrm{g\,cm^{-2}}$

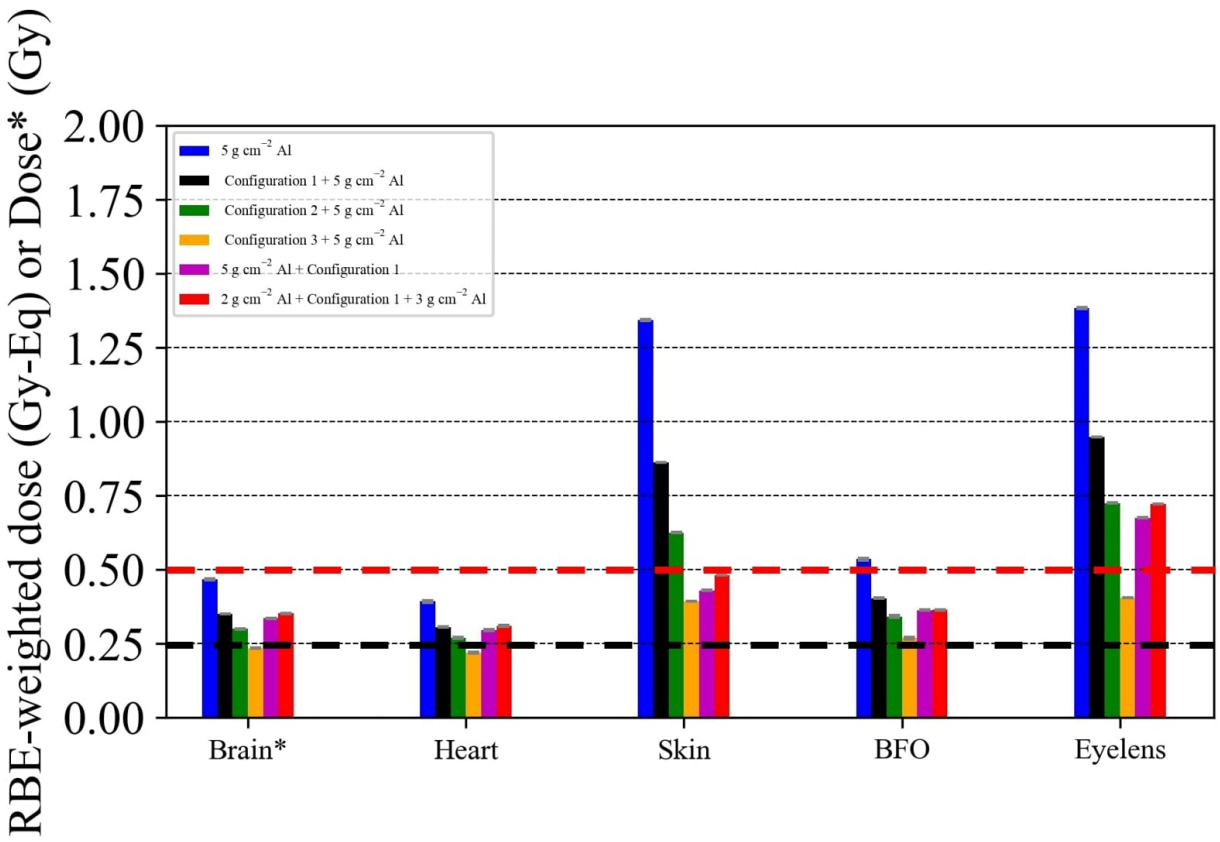

Figure 5.19: Comparison of tissue effects for different organs under different shielding for female (lightly shielded)

alone. This active-passive combination implies that Configuration 3 of the active shielding when placed before $5\,\mathrm{g\,cm^{-2}}$ thickness of aluminum can save a mass penalty of around 15.8 t weight of material, assuming the crew volume to be a sphere of 5 m radius. The concept of passive-active shielding also emerged in this study, an area that had never been investigated before. Evaluated configurations showed the promising outcome of this type of configuration, at least against SPEs.

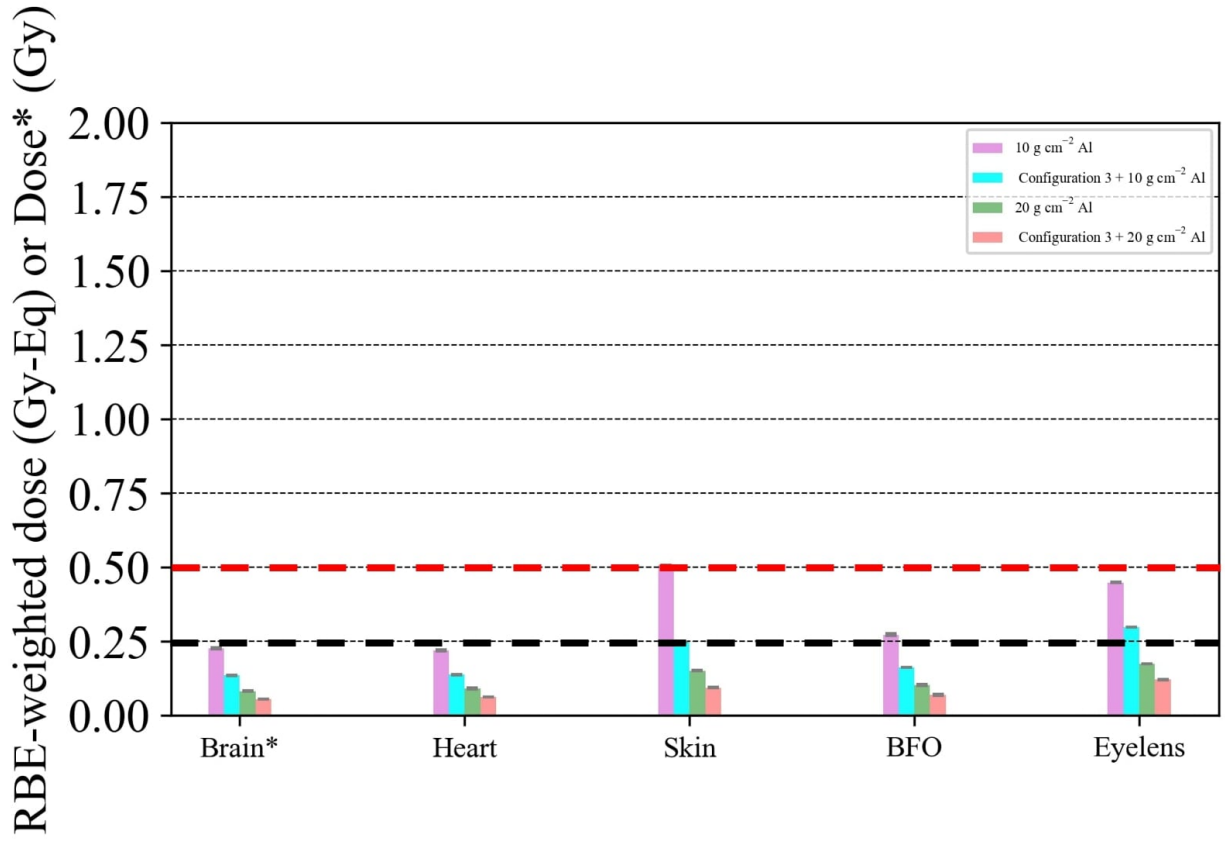

Figure 5.20: Comparison of tissue effects for different organs under different shielding for female (heavily shielded)

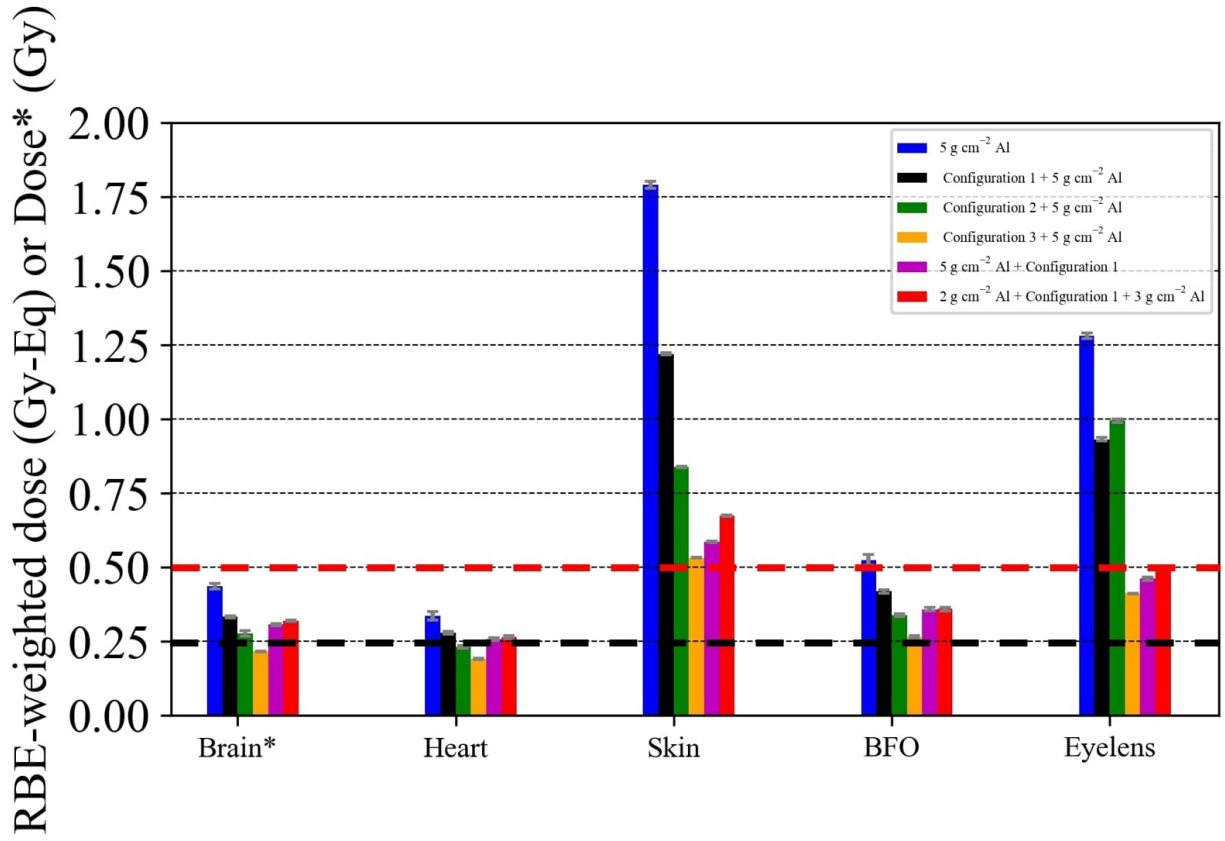

Figure 5.21: Comparison of tissue effects for different organs under different shielding for male (lightly shielded)

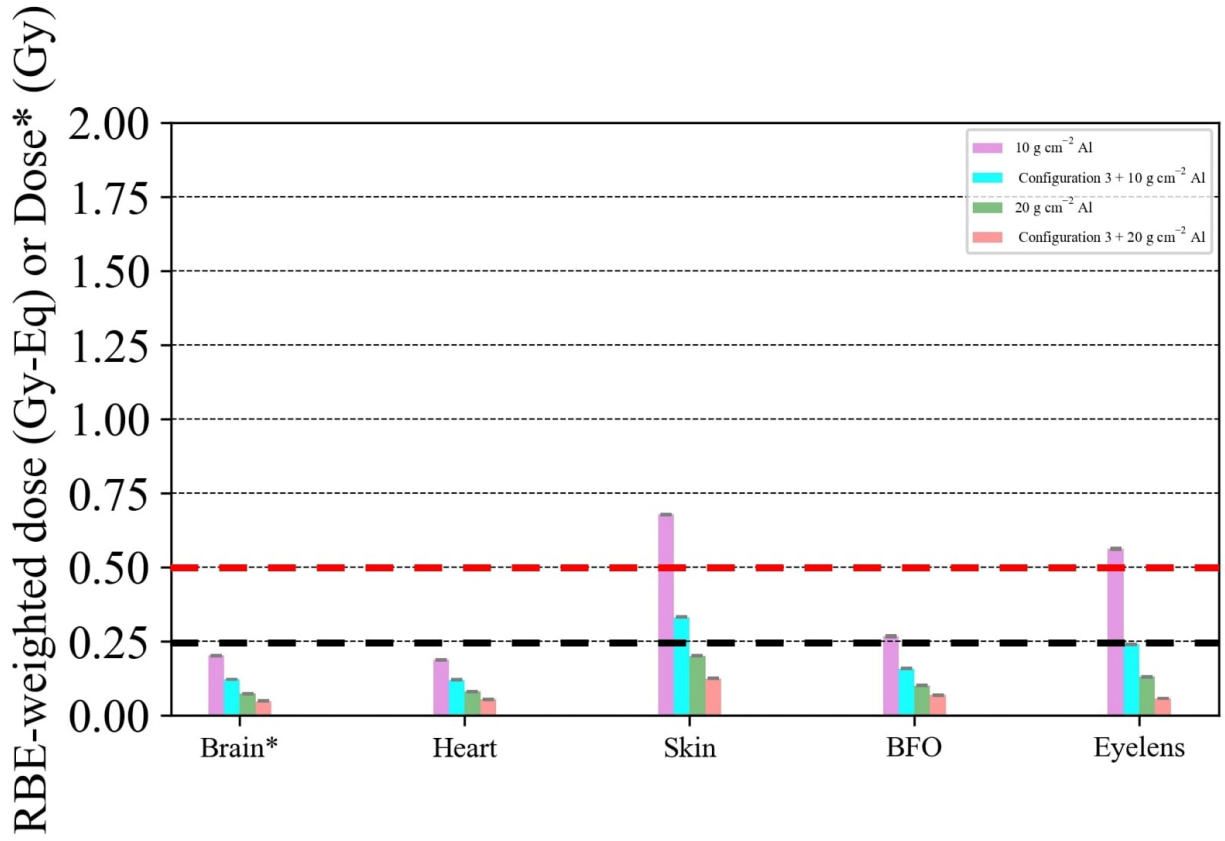

Figure 5.22: Comparison of tissue effects for different organs under different shielding for male (heavily shielded)

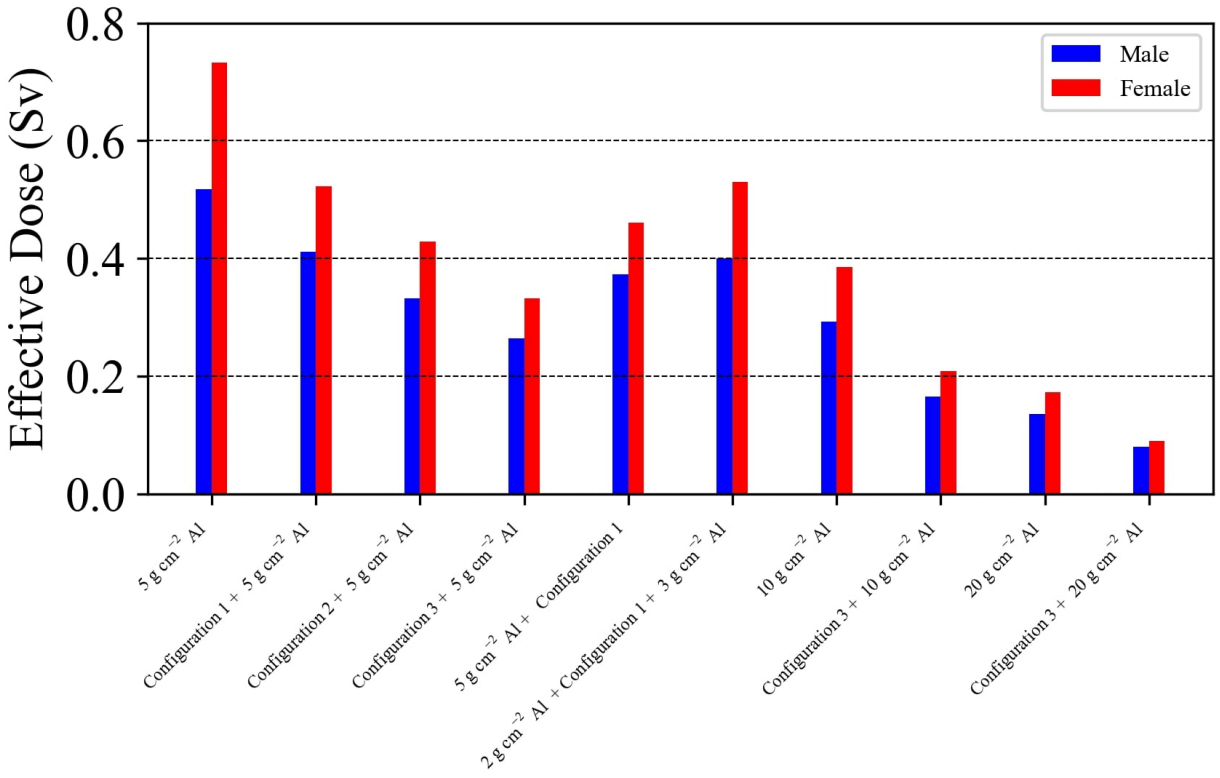

Figure 5.23: Comparison of effective dose for all the tested shielding configurations for male and female

Chapter 6

Hybrid Methods of Radiation Shielding against GCRs

6.1 Motivation

In Chapter 5, the effects of hybrid shielding in terms of protection against SPEs were discussed. In this section, the effects of hybrid shielding are analyzed for protection against GCRs. GCRs are responsible for stochastic effects such as cancer and are considered to be the most harmful space radiation, especially for long-term and deep space missions. The HZE ions encountered in GCR are different from those of SPEs, and the GCR spectra encountered both in case of solar minimum and solar maximum are much more energetic than those of SPEs, with a peak at energy around 1 GeV/n. Therefore, the hybrid shielding configuration was altered from that of SPEs to increase protection. For the validation of results, two methods of stochastic and deterministic radiation transport were used. For stochastic methods, PHITS-v3.17b [124] with ICRP phantoms [123] and the pre-computed fluence to dose conversion factors by Sato [125, 126] were used. Simulation of GCR ions through thick shielding using stochastic transport code such as PHITS is computationally cumbersome, so the validation was limited to smaller thickness aluminum shielding for both solar minimum and solar maximum GCR boundary conditions. For deeper shielding thickness ($20\,\mathrm{g\,cm^{-2}}$),

the output of the Sato's pre-computed fluence to dose conversion factors were compared with results available in literature [12].

6.2 Description of Hybrid Shielding Configuration

GCR spectra are generally more energetic than SPE spectra and therefore a high-magnitude electric field is required to provide any substantial protection. In this study, four electrostatic shielding configurations were tested which showed some degree of protection against the GCR particles. In Chapter 3, Configuration 1, 2, and 3 were tested. In case of GCR a higher electric field was generated (Configuration 4) by increasing the surface charge density of Configuration 3 by a factor of 2. The description of all the electrostatic shielding configurations is shown in Table 6.1. Except the charge density (σ), all other parameters have been kept fixed as discussed in Chapter 5 (Table 5.1)

Table 6.1: Parameter space for the charged plane and rod configuration studies

Parameter	Config 1	Config 2	Config 3	Config 4
Surface charge density (σ) [μC m^{-2}]	7.57	11.35	15.1	30.2
Linear charge density (ρ) [mC m^{-1}]	-1.022	-1.533	-2.044	-4.088
Potential at the midpoint of the charged plane ($V_{midplane}$) [MV]	7.2	10.8	14.4	28.8

The proton flux density reduction factor for Configuration 4 is shown in Figure 6.1. It is clear that the proton reduction is a factor of two greater than that of Configuration 3.

These four active shielding systems were tested along with a material shielding thickness of 20 g cm^{-2} of aluminum. The detailed shielding configurations are described below:

1. Configuration 3 + 20 g cm^{-2} (Active-Passive),

2. Configuration 4 + 20 g cm^{-2} (Active-Passive),

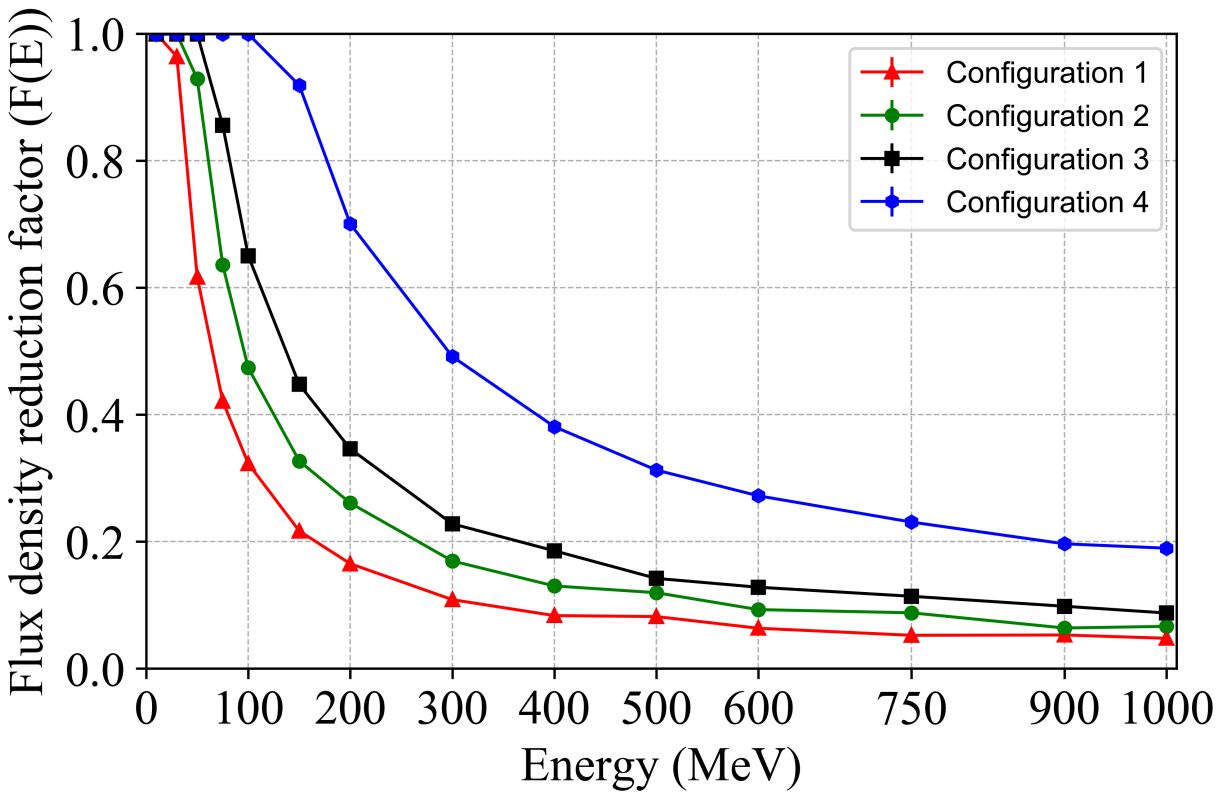

Figure 6.1: Flux density reduction factor for protons for different active shielding configurations relevant for GCR

3. $20\,\mathrm{g\,cm^{-2}}$ + Configuration 3 (Passive-Active), and

4. $20\,\mathrm{g\,cm^{-2}}$ + Configuration 3 (Passive-Active).

In case of GCR, only three hybrid shielding configurations were considered: passive, active-passive and passive-active. It was assumed that $20\,\mathrm{g\,cm^{-2}}$ is the highest material shielding that can be used in a deep-space long-term mission based on data from literature [12, 59, 127]. The goal of this simulation was to observe whether the active shielding along with this thickness of passive shielding can increase the protection. The performance of each passive and hybrid shielding system was determined using effective dose, computed using identical method as in Chapter 5.

6.3 Methods

For radiation transport, two methods were implemented. The first one was a response function based method (Method 1) where ions relevant for GCR boundary conditions ($Z = 1$ to $Z = 28$) were simulated using PHITS version 3.17b [124] for a material shielding thickness of $5\,\mathrm{g\,cm^{-2}}$. The GCR spectra were obtained from HZETRN-2015, where the solar minimum condition was assumed to be when the solar modulation parameter was equal to 475 MV and solar maximum condition was assumed when the solar modulation parameter was equal to 1150 MV [2, 3]. A total of 37 energy bins were used, from 10 MeV/n to 50 GeV/n with a 10 logarithmically placed energy bins per decade. The responses for each of these energy bins in terms of solid cancer and leukemia dose equivalent were computed for the ICRP Publication 110 male and female phantoms [123] using PHITS. The response was then folded with GCR solar mininum and solar maximum spectra obtained from HZETRN-2015 [2, 3]. Method 2 used Sato's pre-computed fluence to dose conversion factors to compute organ dose equivalent and effective dose [125, 126]. Figures 6.2 and 6.3 demonstrate the organ-specific dose equivalents for important organs of male and female phantoms computed using Methods 1 and 2 in case of GCR solar minimum conditions. The results show that these two methods agree with each other and validates the use of Method 2.

After validation of the computational model was complete, Method 2 was used to compute the effective dose for each of these hybrid shielding scenario. The step-by-step details for Method 2 is given below:

1. In case of active-passive shielding arrangement:

   (a) The incident GCR solar minimum and solar maximum boundary conditions were obtained from 3D-HZETRN;

   (b) The flux reduction factor was computed for each GCR ion using the scaled reduction factor as described in Equation 5.4;

   (c) The reduced flux spectra were simulated via passive shielding material using 3D-HZETRN in 'slab' mode;

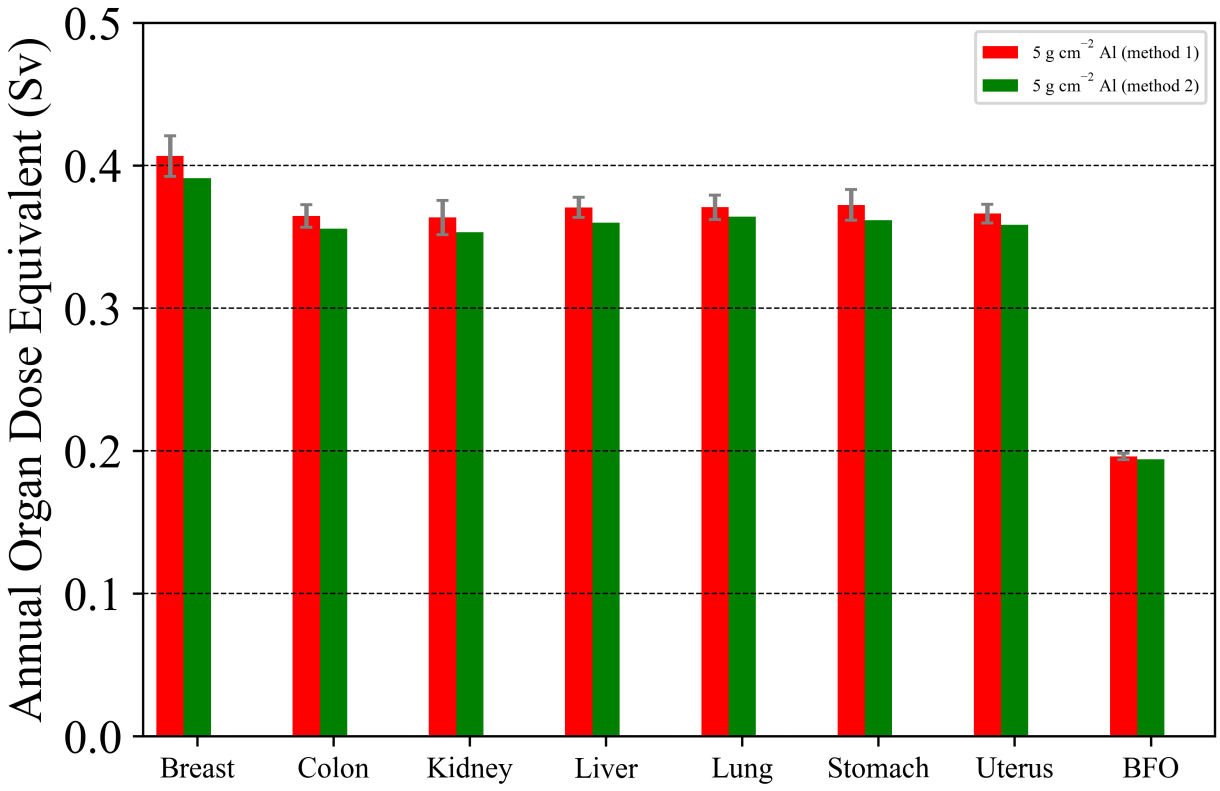

Figure 6.2: Validation of Method 2 in terms of annual organ-specific dose equivalent for solar minimum conditions for female

(d) Resulting flux spectra were folded with flux-to-dose conversion factors for different organs, and organ dose equivalent was computed; and

(e) These organ dose equivalent values were used to compute the whole-body effective dose for male and female.

2. For passive-active configurations:

(a) The solar minimum and maximum GCR spectra were transported through material shielding using HZETRN-2015;

(b) The resulting spectra were transported via active shielding configuration;

(c) These flux spectra were folded with flux-to-dose conversion factors for different organs, and organ dose equivalent was computed; and

(d) These organ dose equivalent values were used to compute the whole-body effective

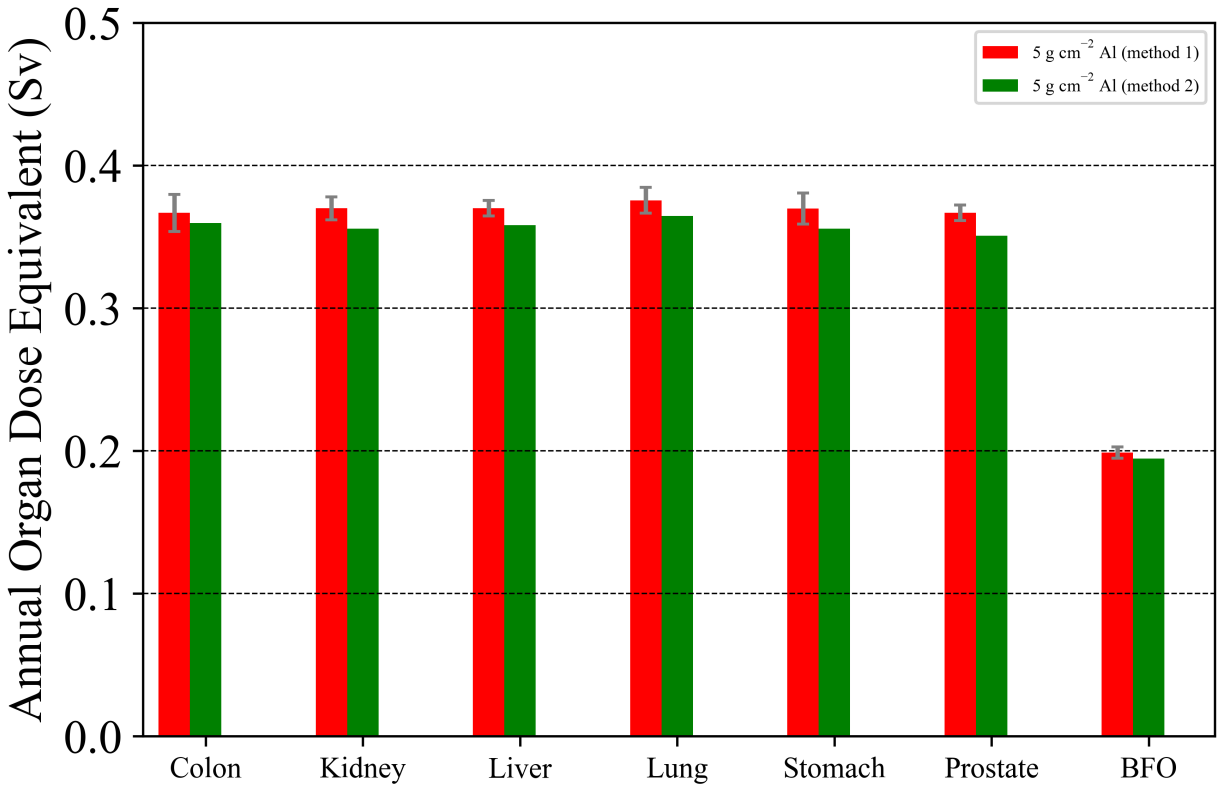

Figure 6.3: Validation of Method 2 in terms of annual organ-specific dose equivalent for solar minimum conditions for male

dose for male and female.

6.4 Results

In this section, the performance of the hybrid shielding against the GCR boundary conditions is discussed. Figures 6.4, 6.5, 6.6, and 6.6 represent the organ dose equivalents for major organs that contribute most towards the effective dose for female and male computational phantoms in case of solar minimum and solar maximum conditions respectively. It is evident from these figures that both Configuration 3 and Configuration 4 are able to reduce the organ dose equivalent compared to 20 g cm^{-2} passive shielding. The reduction is more in case where the active shielding has been placed after the passive shielding because it is easier for the active shielding to deflect lighter fragmented ions compared to heavier ions.

To assess the effect of the hybrid shielding for the whole body, effective dose was com-

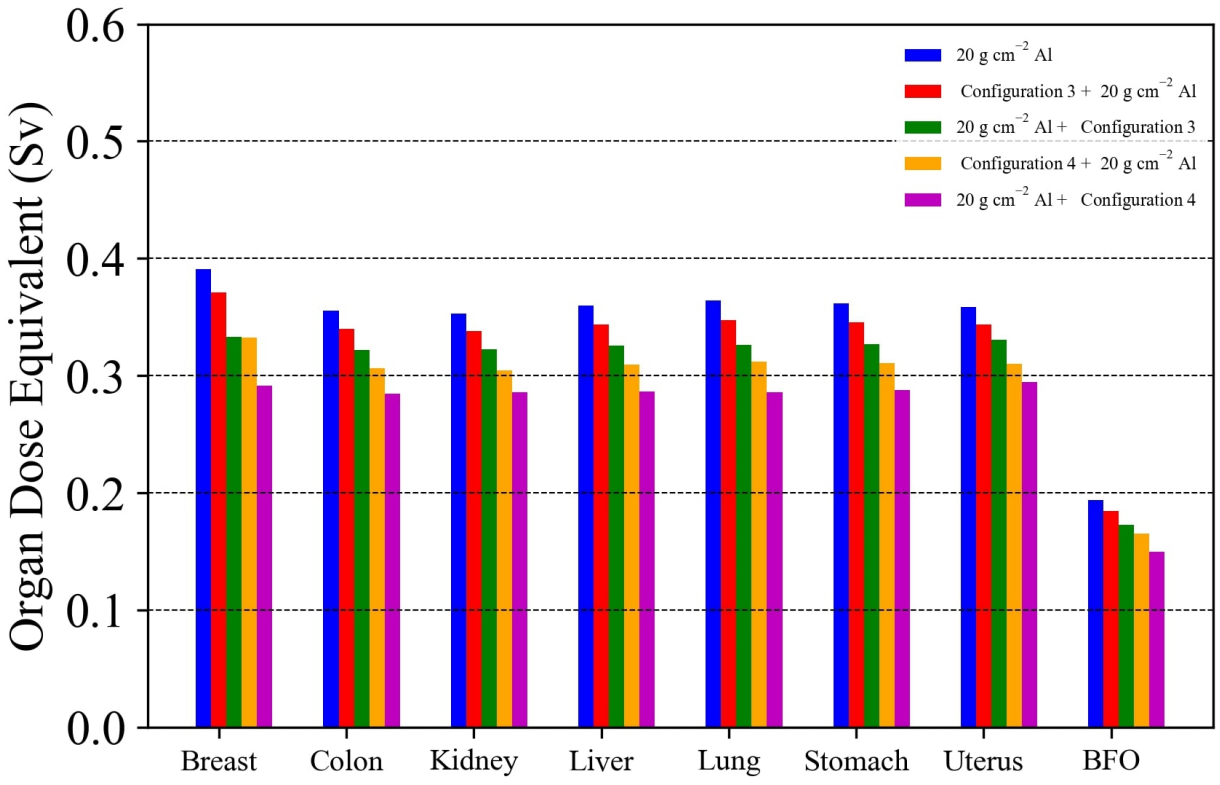

Figure 6.4: Organ dose equivalent for different important organs for female for GCR solar minimum annual exposure

puted for all the shielding configurations. Figures 6.8 and 6.9 demonstrate the effective dose computed under different hybrid shielding configurations under solar minimum and solar maximum conditions respectively. The performance of each of these hybrid configurations was determined by computing their effectiveness to that of the 20 g cm^{-2} of aluminum shielding. It is evident from the figures that for solar minimum boundary condition, around 10% reduction was observed for Configuration 3 + 20 g cm^{-2} aluminum, and around 15% reduction was observed for Configuration 3 is placed after 20 g cm^{-2} aluminum. For Configuration 4, around 15% and 20% reductions were observed when the active shield was placed before and after the material shielding. For solar maximum conditions, these reductions were around 3% and 5% when Configuration 3 were placed before and after the material shielding. For solar maximum boundary condition and Configuration 4, the pre- and post-placement of the active shielding results around 9% and 15% reductions compared to the heavily shielded material.

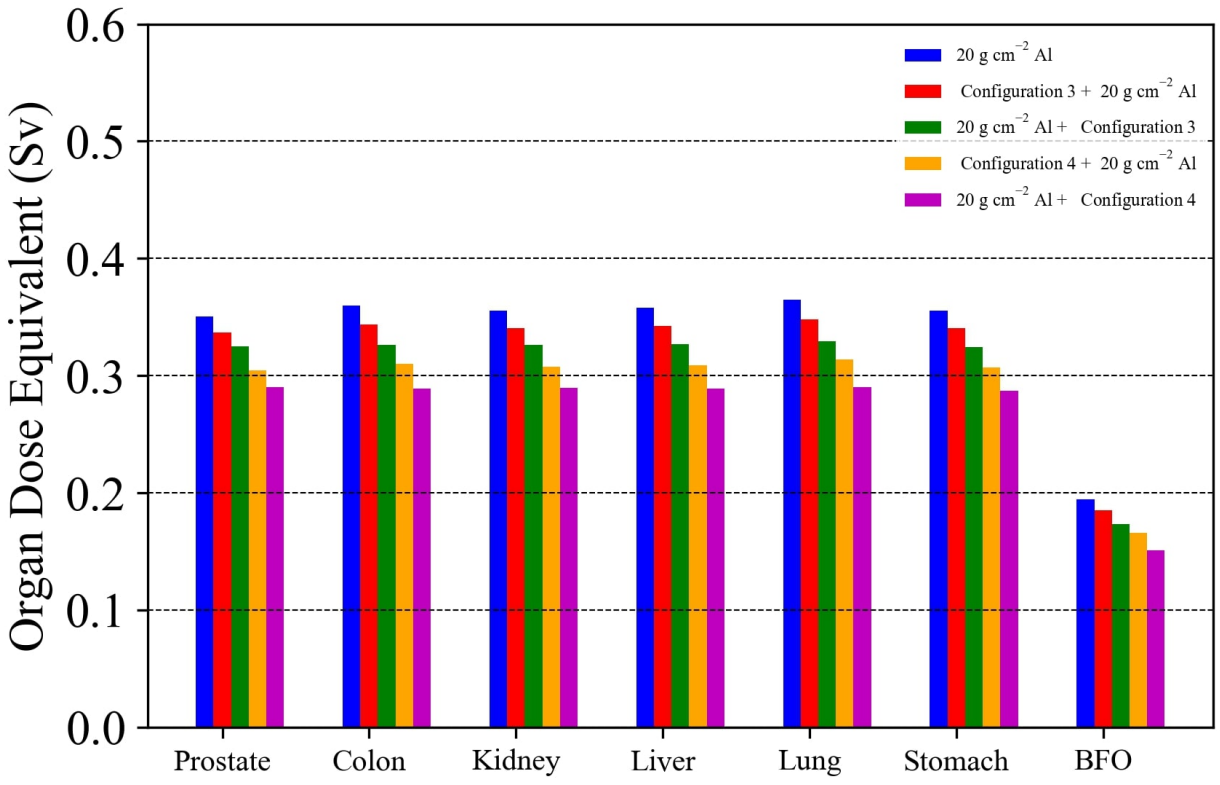

Figure 6.5: Organ dose equivalent for different important organs for male for GCR solar minimum annual exposure

The contributions from different particles towards the total effective dose for female and male computational phantoms for different shielding configurations are shown in Figures 6.10 and 6.11 respectively for solar minimum boundary conditions.

Here, neutral secondary particles refers to neutron and photon, light charged secondaries refer to electrons, positrons, pions, and muons. It can be concluded from Figures 6.10 and 6.11 that when the passive shielding is placed before the active shielding, it lowers the contribution of protons and increases the contribution from neutral secondary particles, which do not contribute much towards dosimetry.

6.5 Summary

In this section, the hybrid shielding configurations were tested against GCR at solar minimum and maximum boundary conditions. The performance of the hybrid shielding configurations

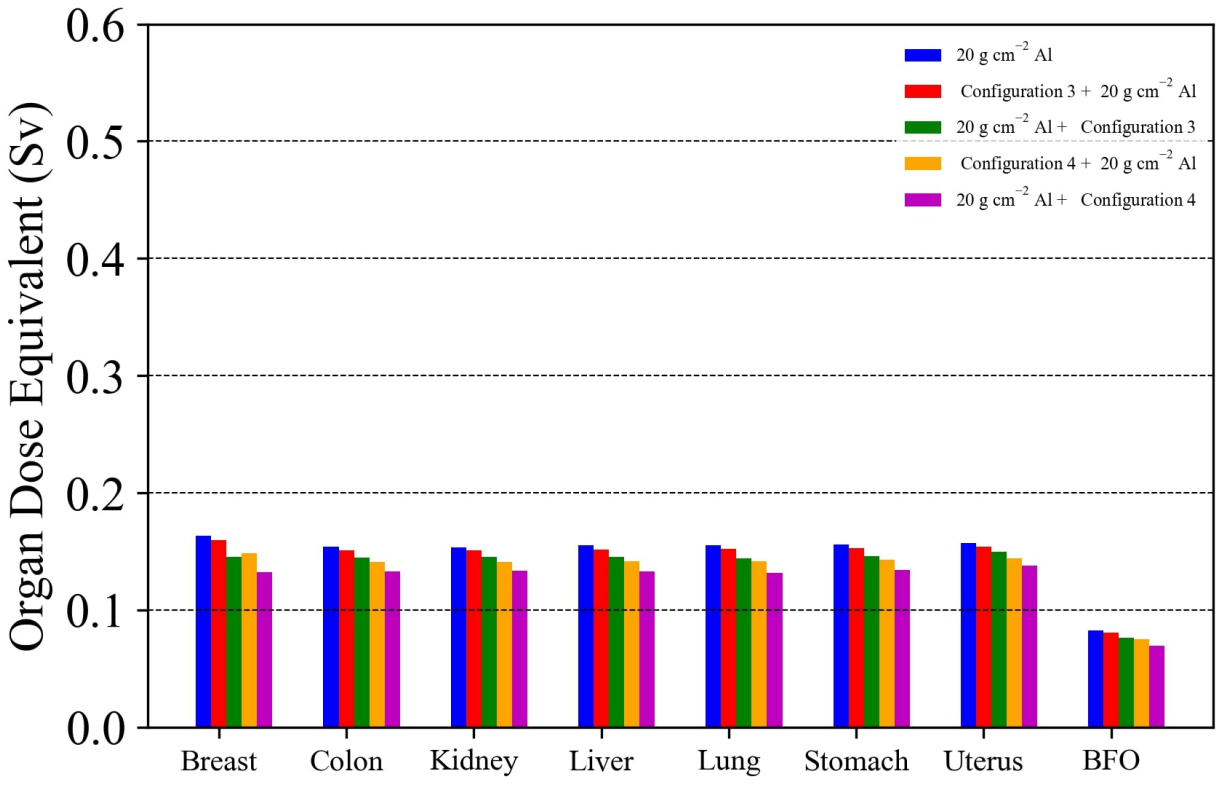

Figure 6.6: Organ dose equivalent for different important organs for female for GCR solar maximum annual exposure

were compared against the performance of a heavily shielded material. It was observed that for the four configurations tested, Configuration 4, when placed after 20 g cm^{-2} provided 20% more reduction for solar minimum conditions and 15% more reduction for solar maximum conditions. The active shielding configuration that provided these reductions requires twice much potential compared to the best performing active shielding configuration in case of SPEs. Nevertheless, the potential required (around 28 MV) is still an order of magnitude less than what have been proposed in the previous studies. Even though the reduction is only 20%, it increases the number of safe days in space for astronauts. The passive-active configurations tested in this section are conceptual and need to be improved to be implemented.

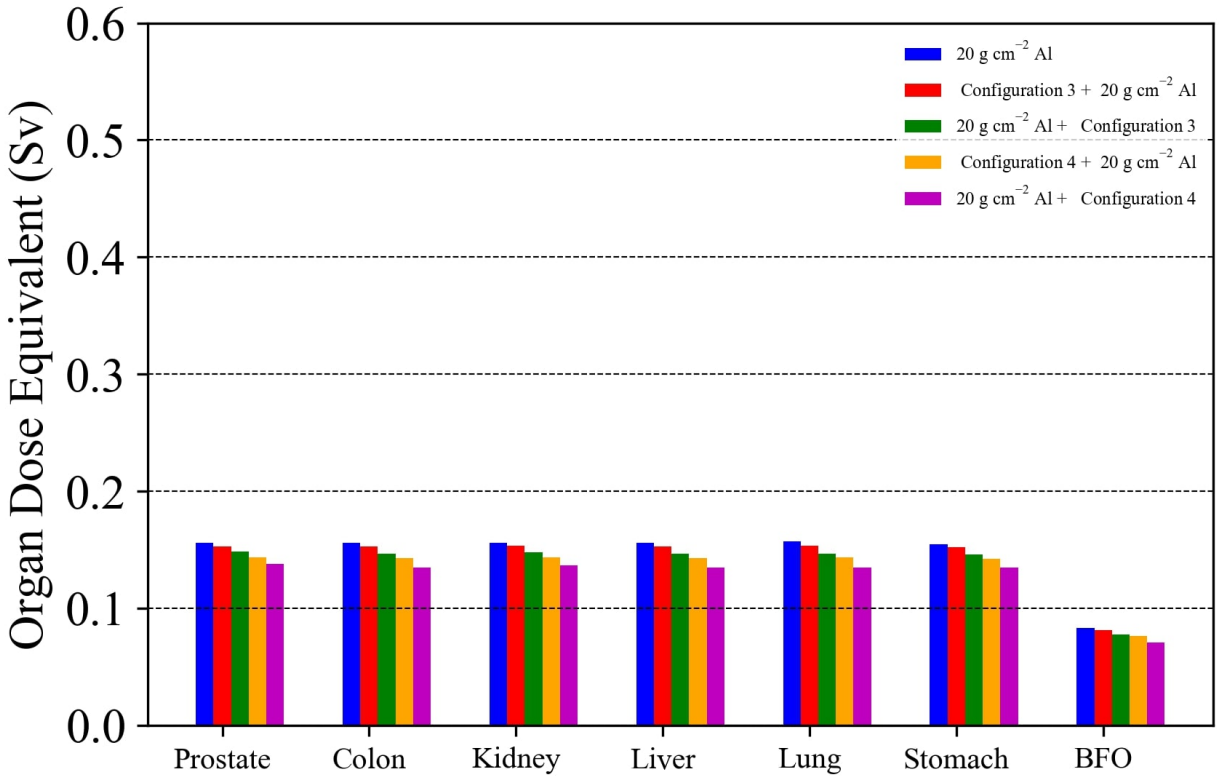

Figure 6.7: Organ dose equivalent for different important organs for male for GCR solar maximum annual exposure

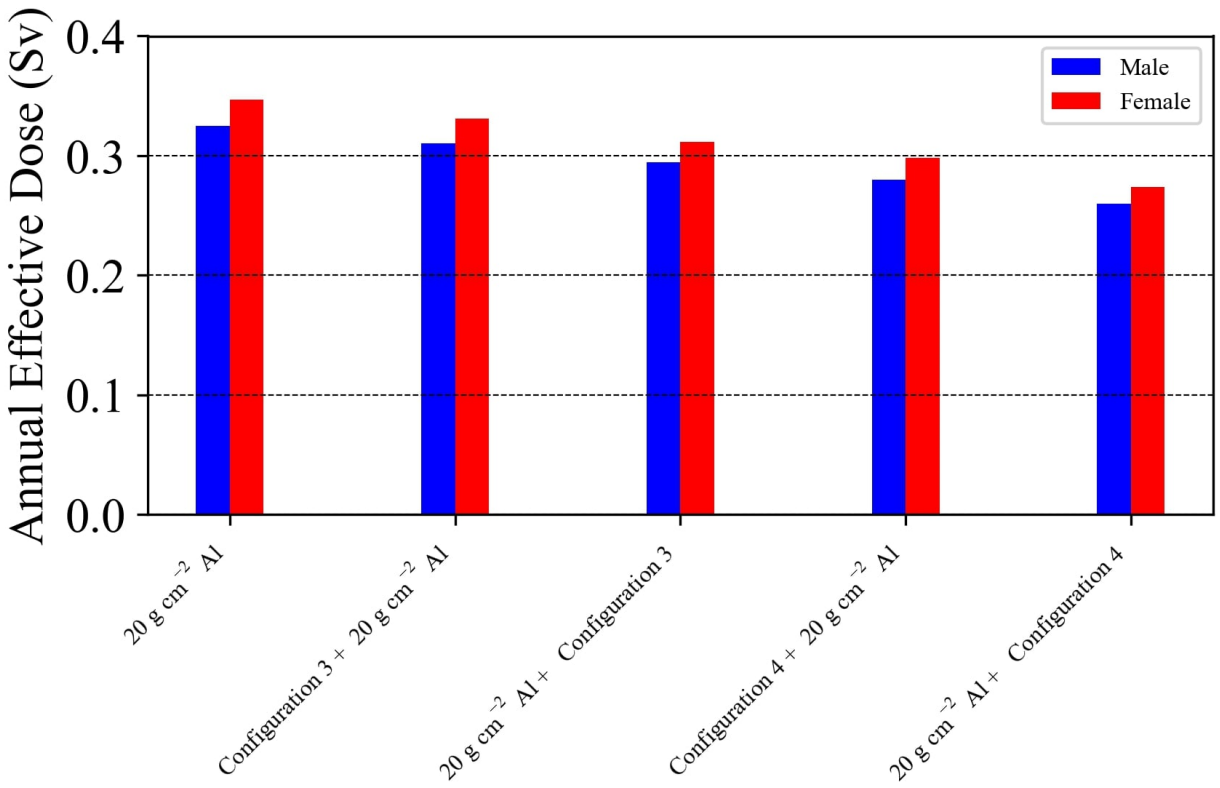

Figure 6.8: Effective dose for different configurations for GCR solar minimum conditions

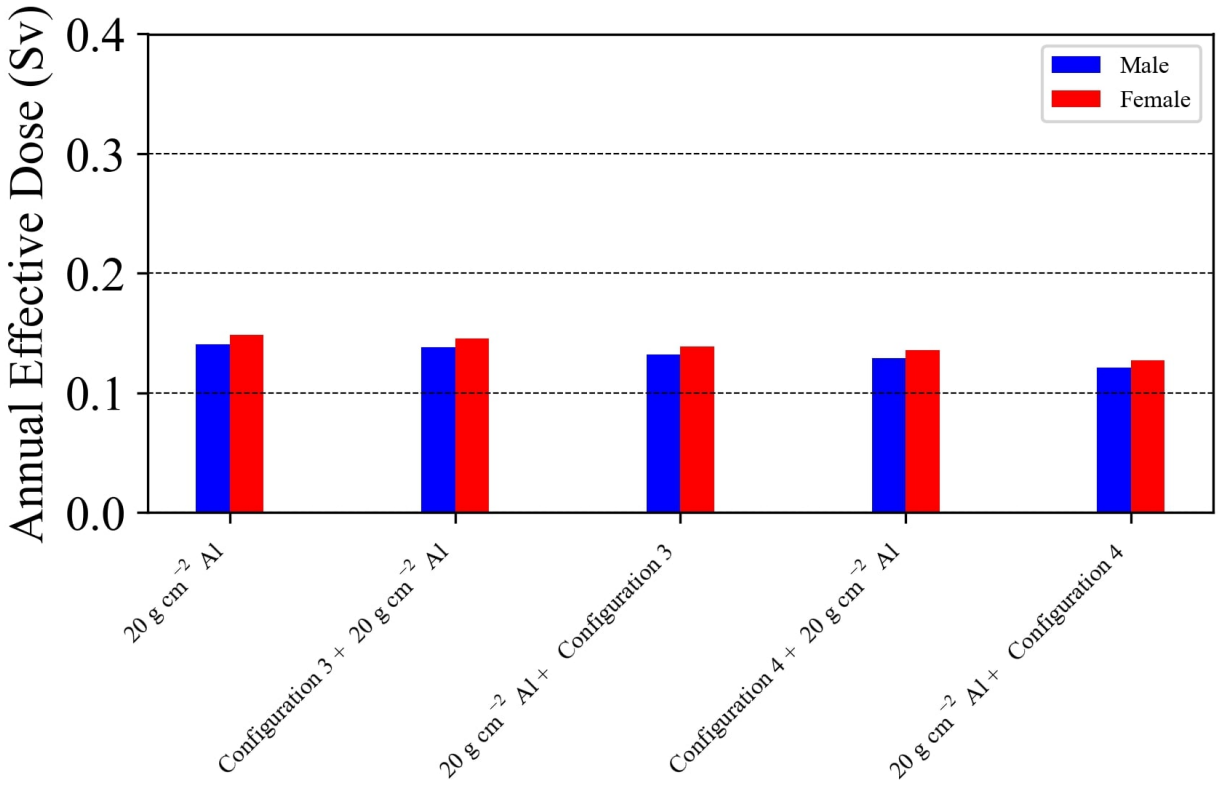

Figure 6.9: Effective dose for different configurations for GCR solar maximum conditions

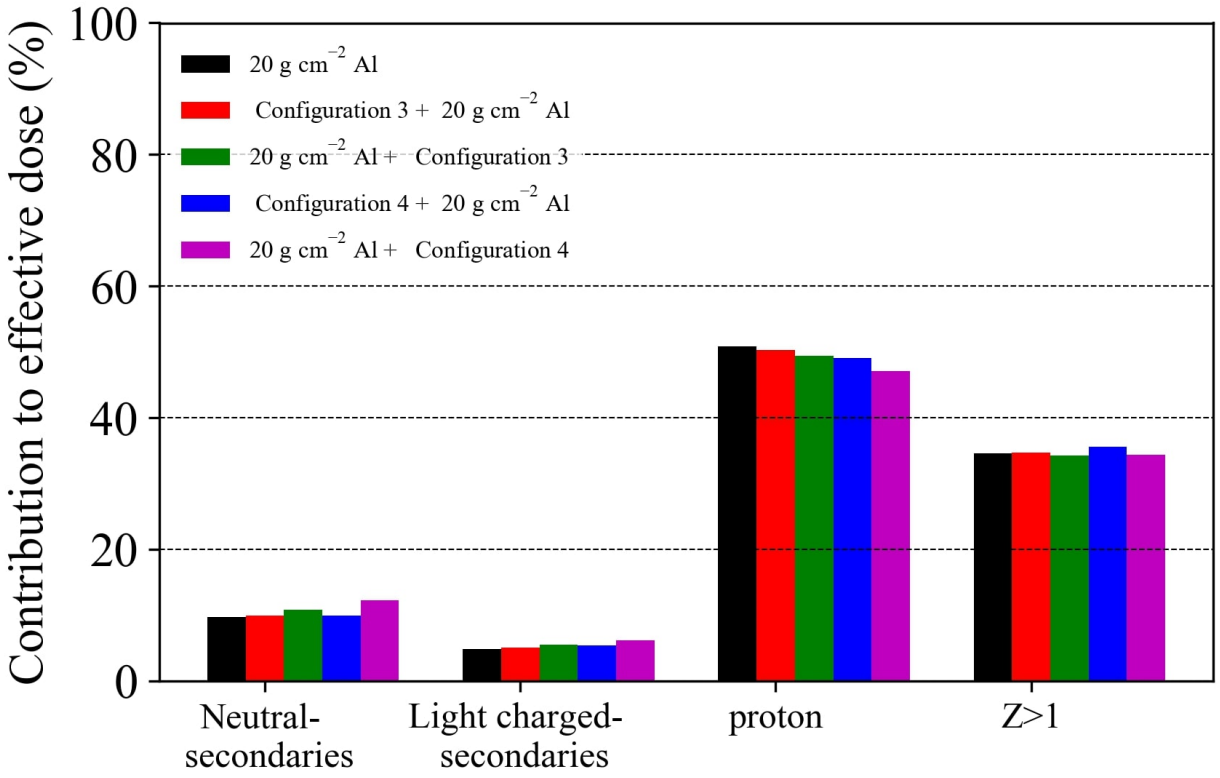

Figure 6.10: Contribution of different particles towards the total effective dose for female computational phantom in solar minimum condition for different shielding configurations

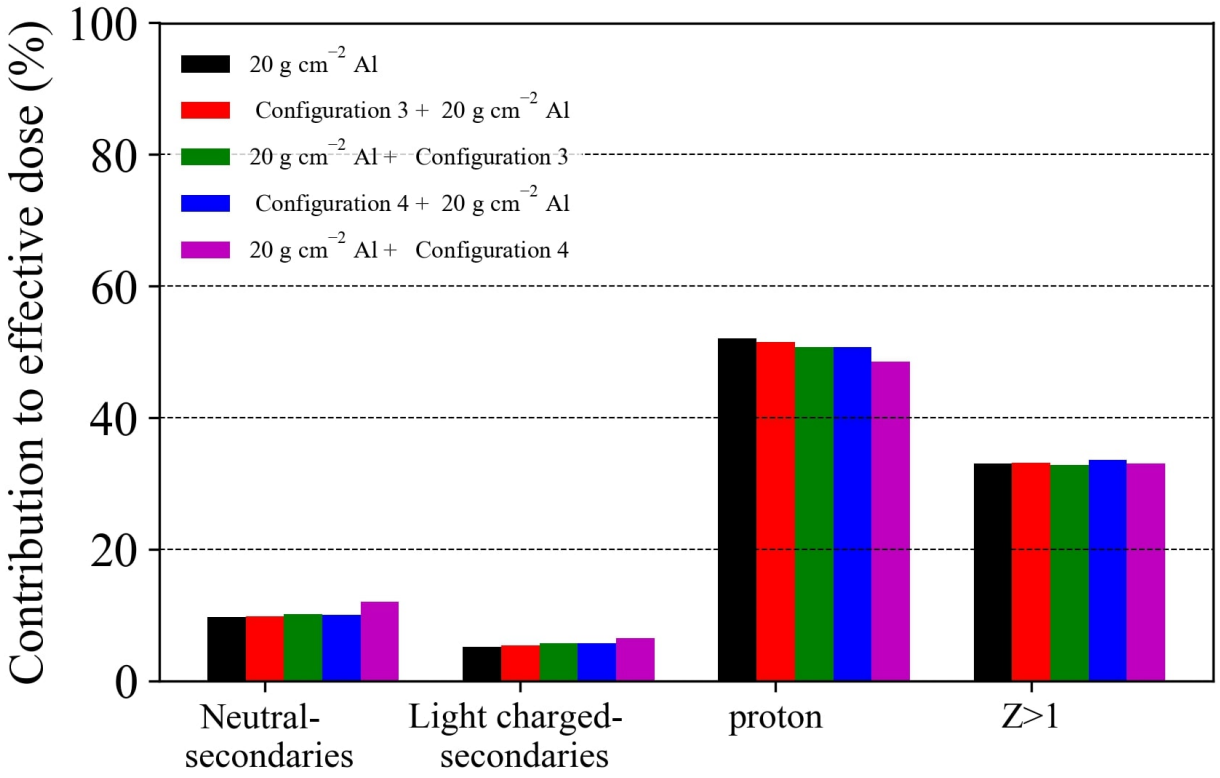

Figure 6.11: Contribution of different particles towards the total effective dose for male computational phantom in solar minimum condition for different shielding configurations

Chapter 7

Conclusions and Future Work

The work done for this dissertation was focused on finding a set of electrostatic shielding configurations that can reduce the radiation risk associated with space radiation. To achieve this goal, multiple steps were taken.

In Chapter 2, the risks involved for male and female astronauts of different ages in different space missions of varying length and radiation environment were shown and a novel population-based approach to compute risks for long-term space missions was presented. This work evolved a method through which a population-based risk for a particular space mission can be defined to avoid sex and age bias. A risk framework considering a realistic spacecraft with the shielding distributions and boundary conditions that closely resemble space missions was used. It was established that passive shielding alone is not sufficient to provide enough protection for long-term exploration missions that can last up to 900 days outside LEO, and that there needs to be some other form of radiation shielding that can reduce the risk. Electrostatic methods of radiation shielding were chosen as an alternative to provide the required protection.

In Chapter 3, the formulation of scaling law for a beam-like configuration that can be used to validate an active shielding configuration at an accelerator-based facility was presented. The work relied on a relativistic charged particle code developed by the collaboration of NASA JSC, University of Utah, and Kansas State University. A beam-like simulation set up

was simulated, and ions with energies relevant to accelerator-based and space-based energies was transported through a dipole electric field to compute a normalized protected area, which is a measure of the degree of protection by the electric field. A 1-D scaling parameter was formulated, which represents the effectiveness of the electric field to deflect a charged ion. Future work will involve the application of this scaling law in an accelerator-based facility to verify the deflection of different charged and energetic ions. This study provided a way of capturing the effectiveness of electrostatic shielding. This work was dedicated to 1-D simulations, but it inspired a move from dipole configuration in 1-D to multiple nodes spread in 3-D over the 4π sr solid angle.

Chapter 4 was dedicated to finding a suitable 3-D electrostatic configuration with the constraint that the potential required to generate the electric field needs to be in the range which is substantially lower than those used in past studies. Initially, the work started from spherical configurations with monopoles, dipoles, and multi-poles spread over different virtual spheres of varying radii. Later the focus shifted to 2-D charged arrays places orthogonally around the spacecraft. It was found that multiple conductors with the lower electric field when arranged repetitively, and negatively charged conductors are decoupled and placed further away from the positively charged conductors, provide better performance. Based on the constraints such as total positive charge, the charge per node, and extent of the active shielding configuration, a set of electrostatic 3-D charge distribution was found. These 3-D charge distributions were then converted to regular shaped charged conductors, and flux density reduction factors were computed for different parameters of the shielding configuration. The chosen configuration consisted of positively charged planes and negatively charged rods placed orthogonally and diagonally, respectively, from the center of the spacecraft (crew volume) with a span ranging from 60 m to 160 m. A set of such configurations (with the span of 60 m) were chosen, and the best of them provided around 32% reduction for protons with kinetic energy equal to 200 MeV. The maximum potential on the planes varied from around 7 MV to 14 MV, one to two orders of magnitude lower than potentials used in literature. A 3-D scaling law was formulated, which related the flux density reduction factor for multiple such configurations through a mathematical expression. By the introduction of this 3-D

scaling law, this work was successful in creating a scalable 3-D active shielding configuration that can be tested in accelerator-based facilities.

Chapters 5 and 6 was dedicated to creating a set of hybrid shielding systems with active and passive shielding and to assess their effectiveness against large SPEs and GCRs. For the SPE, the October 1989 SPE was chosen. The angular flux density reduction factor was also computed for various energies using the active shielding configuration. It was found that the active shielding configuration provides approximately isotropic protection. Different thicknesses of passive materials ranging from light shielding to heavy shielding were investigated along with active shielding. Effective dose and RBE-weighted dose were used as the performance metric. It was found that the best hybrid shielding configuration would be where the best active shielding (Configuration 3) was used prior to a moderate shielding of $10\,\mathrm{g\,cm^{-2}}$ material thickness. This sort of hybrid shielding configuration idea is novel, and it has never been used in previous studies. Previous studies were focused on generating a very high electric field without the use of passive shielding. This study concentrated on using both methods to lower the requirement of potential sources. Also, this study effectively demonstrated that placing passive shielding before active shielding can lower the potential requirement of active shielding, especially in case of SPEs.

For GCRs, the performance of the hybrid shielding system was less effective compared to the SPE. An active shielding configuration was identified that was around 20% more effective when placed after a heavily shielded ($20\,\mathrm{g\,cm^{-2}}$) spacecraft in case of solar minimum conditions and around 15% more effective against GCR at solar maximum conditions when compared with passive shielding alone. This reduction is significant in the sense that it would help to increase the number of safe days in space. If an astronaut could have stayed 300 days in space without exceeding the permissible limit, the addition of this configuration would increase the number of safe days to 360 days. This work also found a pathway through which the flux density reduction factor for different energetic ions can be computed by only computing the flux density reduction factor for protons through the use of a single scaling factor. Also, human computational phantoms were used in this study to use realistic body self-shielding distributions, which was not done in previous studies of active shielding.

To summarize, this work opens up an opportunity to design an active electrostatic radiation shielding system, optimize its performance, and compare multiple parameter sets via the use of a 3-D scaling parameter. This optimized shielding system can be used to compute flux density reduction factors for different energetic ions, and they can be combined with passive shielding to compute dosimetric quantities by simulating relevant space radiation environments through material shielding and computational phantoms.

Future work can be divided into four categories: 1) improvement of current configuration by optimizing different parameters, 2) use of REID instead of effective dose, 3) coupling active and passive shielding together with deterministic HZETRN-2015 instead of PHITS for rapid validation, and 4) addition of the whole hybrid shielding module in real-time with the MeRiT framework of NASA to compute risk for different space missions. These points are briefly discussed here.

The current configuration could be improved by tiling multiple planes along the orthogonal direction or along with different angular directions. Also, further research needs to be conducted on whether adding a small magnetic field can enhance the performance of the active shielding system.

In this work, analysis for REIDs has not been done. Future research should include the performance of the active shielding in terms of reducing the REID. A scaling law could be formulated that directly maps the shielding configuration to its corresponding REID reduction instead of flux density reduction as done in this study. Also, the ability of this configuration in terms of protection against charged particles like electrons, pions, muons, and mesons was not considered in this work. Future work should involve the energy-dependent flux density reduction factors for different active shielding configurations against these particles.

Computation time for SPE and GCR spectra can be substantial with PHITS or any other stochastic transport code. The active-passive shielding system can be coupled with deterministic software like HZETRN-2015 to compute organ dose equivalent.

This work involved the MeRiT software in computing the risk for males and females under varying space radiation environments and shielding. MeRiT takes the radiation environment and transports it through different material thicknesses and body self-shielding. One exten-

siom of this work is to create a module that can produce the radiation environment passing through the active/passive hybrid shielding system, and then simulate transport through the spacecraft and body self-shielding to calculate the REID and other dosimetric quantities such as effective dose and RBE-weighted dose using MeRiT. Then population based risk approach can then be used to better understand population REID on exploration missions employing hybrid shielding.

Bibliography

[1] NASA. The Sun and its atmosphere. https://www.nasa.gov/mission_pages/sunearth/science/Sunlayers.html, 2013.

[2] T. Slaba, J. Wilson, F. Badavi, B. Reddell, and A. Bahadori. Solar Proton Transport within an ICRU Sphere Surrounded by a Complex Shield: Ray-Trace Geometry. Technical Report TP 2015-218994, NASA, 2015.

[3] T. Slaba, J. Wilson, F. Badavi, B. Reddell, and A. Bahadori. Solar Proton Transport within an ICRU Sphere Surrounded by a Complex Shield: Combinatorial Geometry. Technical Report TP 2015-218980, NASA, 2015.

[4] P. O'Neil, S. Golge, and T. Slaba. Badhwar-O'Neill 2014 Galactic Cosmic Ray Flux Model Description. Technical Report TP-2015-218569, NASA, 2015.

[5] ICRP. Recommendations of the International Commission on Radiological Protection. ICRP Publication 26. *Annals of the ICRP*, (1), 1977.

[6] ICRP. 1990 Recommendations of the International Commission on Radiological Protection. ICRP Publication 60. *Annals of the ICRP*, (21), 1991.

[7] R.K. Tripathi. Meeting the Grand Challenge of Protecting Astronaut's Health: Electrostatic Active Space Radiation Shielding for Deep Space Missions. Technical Report NIAC Final Report, National Aeronautics and Space Administration, Hampton, VA, 2011.

[8] D.A. Rajon and W.E. Bolch. Interactions with 3d isotropic and homogeneous radiation fields: a monte carlo simulation algorithm. *Computer Methods and Programs in Biomedicine*, 70(2):167–177, 2003. doi: 10.1016/s0169-2607(02)00008-1. URL https://doi.org/10.1016/s0169-2607(02)00008-1.

[9] Lawrence H. Heilbronn, Thomas B. Borak, Lawrence W. Townsend, Pi-En Tsai, Chelsea A. Burnham, and Rafe A. McBeth. Neutron yields and effective doses produced by galactic cosmic ray interactions in shielded environments in space. *Life Sciences in Space Research*, 7:90–99, November 2015. doi: 10.1016/j.lssr.2015.10.005. URL https://doi.org/10.1016/j.lssr.2015.10.005.

[10] ICRP. The 2007 Recommendations of the International Commission on Radiological Protection. ICRP Publication 103. *Annals of the ICRP*, (37), 2007.

[11] Evidence Report: Risk of Acute Radiation Syndromes due to Solar Particle Events. Technical Report SP–2009–3405, NASA, 2009.

[12] F.A. Cucinotta, M.Y. Kim, and L.J. Chappell. Space Radiation Cancer Risk Projections and Uncertainties – 2012. Technical Report NASA/TP- 2013-217375, 2012.

[13] Tony C. Slaba and Steve R. Blattnig. GCR environmental models I: Sensitivity analysis for GCR environments. *Space Weather*, 12(4):217–224, April 2014. doi: 10.1002/2013sw001025. URL https://doi.org/10.1002/2013sw001025.

[14] White House. Presidential Memorandum on Reinvigorating America's Human Space Exploration Program. https://www.whitehouse.gov/presidential-actions/presidential-memorandum-reinvigorating-americas-human-space-exploration\-program/, 2017.

[15] Bioastronautics Roadmap: A Risk Reduction Strategy for Human Space Exploration. Technical Report SP–2004–6113, NASA, 2005.

[16] Jeffery Chancellor, Graham Scott, and Jeffrey Sutton. Space radiation: The number one risk to astronaut health beyond low earth orbit. *Life*, 4(3):491–510, September 2014. doi: 10.3390/life4030491. URL https://doi.org/10.3390/life4030491.

[17] US Nuclear Regulatory Commission. Standards of Protection against Radiation, 10CFR20. *US Office of the Federal Register, Washington, DC*, 1991.

[18] NASA. National Aeronautics and Space Act of 1958, As Amended, 2006.

[19] NASA Space Flight Human-System Standard Volume 1, Revision A: Crew Health. NASA-STD-3001, National Aeronautics and Space Administration, Washington, DC, 2015.

[20] Francis A. Cucinotta. Space radiation risks for astronauts on multiple international space station missions. *PLOS ONE*, 9(4):1–14, 04 2014. doi: 10.1371/journal.pone.0096099. URL https://doi.org/10.1371/journal.pone.0096099.

[21] Marco Durante and Francis A. Cucinotta. Physical basis of radiation protection in space travel. *Rev. Mod. Phys.*, 83:1245–1281, Nov 2011. doi: 10.1103/RevModPhys.83.1245. URL https://link.aps.org/doi/10.1103/RevModPhys.83.1245.

[22] R.C. Singleterry. Radiation engineering analysis of shielding materials to assess their ability to protect astronauts in deep space from energetic particle radiation. *Acta Astronautica*, 91:49 – 54, 2013. ISSN 0094-5765. doi: https://doi.org/10.1016/j.actaastro.2013.04.013. URL http://www.sciencedirect.com/science/article/pii/S0094576513001252.

[23] Thomas E. Cravens. *Physics of Solar System Plasmas*. Cambridge University Press, September 1997. doi: 10.1017/cbo9780511529467. URL https://doi.org/10.1017/cbo9780511529467.

[24] M.B. BAKER. Geomagnetically trapped radiation. *AIAA Journal*, 3(9):1569–1579, September 1965. doi: 10.2514/3.55177. URL https://doi.org/10.2514/3.55177.

[25] W.L. Brown. Effects of trapped radiation on electronic devices. In *Astrophysics and Space Science Library*, pages 757–792. Springer Netherlands, 1966. doi: 10.1007/978-94-010-3553-8_52. URL https://doi.org/10.1007/978-94-010-3553-8_52.

[26] James A Van Allen. The geomagnetically trapped corpuscular radiation. *Journal of Geophysical Research*, 64(11):1683–1689, 1959.

[27] Francis F. Badavi. Validation of the new trapped environment AE9/AP9/SPM at low Earth orbit. *Advances in Space Research*, 2014.

[28] NOAA. Solar Radiation Storm. https://www.swpc.noaa.gov/phenomena/solar-radiation-storm.

[29] Mihir Desai and Joe Giacalone. Large gradual solar energetic particle events. *Living Reviews in Solar Physics*, 13(1), September 2016. doi: 10.1007/s41116-016-0002-5. URL https://doi.org/10.1007/s41116-016-0002-5.

[30] L.W. Townsend, J.H. Adams, S.R. Blattnig, M.S. Clowdsley, D.J. Fry, I. Jun, C.D. McLeod, J.I. Minow, D.F. Moore, J.W. Norbury, R.B. Norman, D.V. Reames, N.A. Schwadron, E.J. Semones, R.C. Singleterry, T.C. Slaba, C.M. Werneth, and M.A. Xapsos. Solar particle event storm shelter requirements for missions beyond low earth orbit. *Life Sciences in Space Research*, 17:32–39, May 2018. doi: 10.1016/j.lssr.2018.02.002. URL https://doi.org/10.1016/j.lssr.2018.02.002.

[31] Markus J. Aschwanden. GeV particle acceleration in solar flares and ground level enhancement (GLE) events. *Space Science Reviews*, 171(1-4):3–21, Feb 2012. ISSN 1572-9672. doi: 10.1007/s11214-011-9865-x. URL http://dx.doi.org/10.1007/s11214-011-9865-x.

[32] R.A. Mewaldt. Solar energetic particle composition, energy spectra, and space weather. *Space Science Reviews*, 124(1-4):303–316, January 2007. doi: 10.1007/s11214-006-9091-0. URL https://doi.org/10.1007/s11214-006-9091-0.

[33] Jörg R. Hörandel. The origin of galactic cosmic rays. *Nuclear Instruments and Methods in Physics Research Section A: Accelerators, Spectrometers, Detectors and Associated Equipment*, 588(1-2):181–188, April 2008. doi: 10.1016/j.nima.2008.01.036. URL https://doi.org/10.1016/j.nima.2008.01.036.

[34] J.A. Simpson. Elemental and isotopic composition of the galactic cosmic rays. *Annual Review of Nuclear and Particle Science*, 33(1):323–382, December 1983. doi:

10.1146/annurev.ns.33.120183.001543. URL https://doi.org/10.1146/annurev.ns.33.120183.001543.

[35] M. Tanabashi, K. Hagiwara, K. Hikasa, K. Nakamura, Y. Sumino, F. Takahashi, J. Tanaka, K. Agashe, G. Aielli, C. Amsler, M. Antonelli, D. M. Asner, H. Baer, Sw. Banerjee, R. M. Barnett, T. Basaglia, C. W. Bauer, J. J. Beatty, V. I. Belousov, J. Beringer, S. Bethke, A. Bettini, H. Bichsel, O. Biebel, K. M. Black, E. Blucher, O. Buchmuller, V. Burkert, M. A. Bychkov, R. N. Cahn, M. Carena, A. Ceccucci, A. Cerri, D. Chakraborty, M.-C. Chen, R. S. Chivukula, G. Cowan, O. Dahl, G. D'Ambrosio, T. Damour, D. de Florian, A. de Gouvêa, T. DeGrand, P. de Jong, G. Dissertori, B. A. Dobrescu, M. D'Onofrio, M. Doser, M. Drees, H. K. Dreiner, D. A. Dwyer, P. Eerola, S. Eidelman, J. Ellis, J. Erler, V. V. Ezhela, W. Fetscher, B. D. Fields, R. Firestone, B. Foster, A. Freitas, H. Gallagher, L. Garren, H.-J. Gerber, G. Gerbier, T. Gershon, Y. Gershtein, T. Gherghetta, A. A. Godizov, M. Goodman, C. Grab, A. V. Gritsan, C. Grojean, D. E. Groom, M. Grünewald, A. Gurtu, T. Gutsche, H. E. Haber, C. Hanhart, S. Hashimoto, Y. Hayato, K. G. Hayes, A. Hebecker, S. Heinemeyer, B. Heltsley, J. J. Hernández-Rey, J. Hisano, A. Höcker, J. Holder, A. Holtkamp, T. Hyodo, K. D. Irwin, K. F. Johnson, M. Kado, M. Karliner, U. F. Katz, S. R. Klein, E. Klempt, R. V. Kowalewski, F. Krauss, M. Kreps, B. Krusche, Yu. V. Kuyanov, Y. Kwon, O. Lahav, J. Laiho, J. Lesgourgues, A. Liddle, Z. Ligeti, C.-J. Lin, C. Lippmann, T. M. Liss, L. Littenberg, K. S. Lugovsky, S. B. Lugovsky, A. Lusiani, Y. Makida, F. Maltoni, T. Mannel, A. V. Manohar, W. J. Marciano, A. D. Martin, A. Masoni, J. Matthews, U.-G. Meißner, D. Milstead, R. E. Mitchell, K. Mönig, P. Molaro, F. Moortgat, M. Moskovic, H. Murayama, M. Narain, P. Nason, S. Navas, M. Neubert, P. Nevski, Y. Nir, K. A. Olive, S. Pagan Griso, J. Parsons, C. Patrignani, J. A. Peacock, M. Pennington, S. T. Petcov, V. A. Petrov, E. Pianori, A. Piepke, A. Pomarol, A. Quadt, J. Rademacker, G. Raffelt, B. N. Ratcliff, P. Richardson, A. Ringwald, S. Roesler, S. Rolli, A. Romaniouk, L. J. Rosenberg, J. L. Rosner, G. Rybka, R. A. Ryutin, C. T. Sachra-

jda, Y. Sakai, G. P. Salam, S. Sarkar, F. Sauli, O. Schneider, K. Scholberg, A. J. Schwartz, D. Scott, V. Sharma, S. R. Sharpe, T. Shutt, M. Silari, T. Sjöstrand, P. Skands, T. Skwarnicki, J. G. Smith, G. F. Smoot, S. Spanier, H. Spieler, C. Spiering, A. Stahl, S. L. Stone, T. Sumiyoshi, M. J. Syphers, K. Terashi, J. Terning, U. Thoma, R. S. Thorne, L. Tiator, M. Titov, N. P. Tkachenko, N. A. Törnqvist, D. R. Tovey, G. Valencia, R. Van de Water, N. Varelas, G. Venanzoni, L. Verde, M. G. Vincter, P. Vogel, A. Vogt, S. P. Wakely, W. Walkowiak, C. W. Walter, D. Wands, D. R. Ward, M. O. Wascko, G. Weiglein, D. H. Weinberg, E. J. Weinberg, M. White, L. R. Wiencke, S. Willocq, C. G. Wohl, J. Womersley, C. L. Woody, R. L. Workman, W.-M. Yao, G. P. Zeller, O. V. Zenin, R.-Y. Zhu, S.-L. Zhu, F. Zimmermann, P. A. Zyla, J. Anderson, L. Fuller, V. S. Lugovsky, and P. Schaffner. Review of particle physics. *Phys. Rev. D*, 98:030001, Aug 2018. doi: 10.1103/PhysRevD.98.030001. URL https://link.aps.org/doi/10.1103/PhysRevD.98.030001.

[36] A. A. Abdo, M. Ackermann, M. Ajello, W. B. Atwood, M. Axelsson, L. Baldini, J. Ballet, G. Barbiellini, D. Bastieri, M. Battelino, B. M. Baughman, K. Bechtol, R. Bellazzini, B. Berenji, R. D. Blandford, E. D. Bloom, G. Bogaert, E. Bonamente, A. W. Borgland, J. Bregeon, A. Brez, M. Brigida, P. Bruel, T. H. Burnett, G. A. Caliandro, R. A. Cameron, P. A. Caraveo, P. Carlson, J. M. Casandjian, C. Cecchi, E. Charles, A. Chekhtman, C. C. Cheung, J. Chiang, S. Ciprini, R. Claus, J. Cohen-Tanugi, L. R. Cominsky, J. Conrad, S. Cutini, C. D. Dermer, A. de Angelis, F. de Palma, S. W. Digel, G. Di Bernardo, E. do Couto e Silva, P. S. Drell, R. Dubois, D. Dumora, Y. Edmonds, C. Farnier, C. Favuzzi, W. B. Focke, M. Frailis, Y. Fukazawa, S. Funk, P. Fusco, D. Gaggero, F. Gargano, D. Gasparrini, N. Gehrels, S. Germani, B. Giebels, N. Giglietto, F. Giordano, T. Glanzman, G. Godfrey, D. Grasso, I. A. Grenier, M.-H. Grondin, J. E. Grove, L. Guillemot, S. Guiriec, Y. Hanabata, A. K. Harding, R. C. Hartman, M. Hayashida, E. Hays, R. E. Hughes, G. Jóhannesson, A. S. Johnson, R. P. Johnson, W. N. Johnson, T. Kamae, H. Katagiri, J. Kataoka, N. Kawai, M. Kerr, J. Knödlseder, D. Kocevski, F. Kuehn, M. Kuss, J. Lande, L. Latronico, M. Lemoine-Goumard,

F. Longo, F. Loparco, B. Lott, M. N. Lovellette, P. Lubrano, G. M. Madejski, A. Makeev, M. M. Massai, M. N. Mazziotta, W. McConville, J. E. McEnery, C. Meurer, P. F. Michelson, W. Mitthumsiri, T. Mizuno, A. A. Moiseev, C. Monte, M. E. Monzani, E. Moretti, A. Morselli, I. V. Moskalenko, S. Murgia, P. L. Nolan, J. P. Norris, E. Nuss, T. Ohsugi, N. Omodei, E. Orlando, J. F. Ormes, M. Ozaki, D. Paneque, J. H. Panetta, D. Parent, V. Pelassa, M. Pepe, M. Pesce-Rollins, F. Piron, M. Pohl, T. A. Porter, S. Profumo, S. Rainò, R. Rando, M. Razzano, A. Reimer, O. Reimer, T. Reposeur, S. Ritz, L. S. Rochester, A. Y. Rodriguez, R. W. Romani, M. Roth, F. Ryde, H. F.-W. Sadrozinski, D. Sanchez, A. Sander, P. M. Saz Parkinson, J. D. Scargle, T. L. Schalk, A. Sellerholm, C. Sgrò, D. A. Smith, P. D. Smith, G. Spandre, P. Spinelli, J.-L. Starck, T. E. Stephens, M. S. Strickman, A. W. Strong, D. J. Suson, H. Tajima, H. Takahashi, T. Takahashi, T. Tanaka, J. B. Thayer, J. G. Thayer, D. J. Thompson, L. Tibaldo, O. Tibolla, D. F. Torres, G. Tosti, A. Tramacere, Y. Uchiyama, T. L. Usher, A. Van Etten, V. Vasileiou, N. Vilchez, V. Vitale, A. P. Waite, E. Wallace, P. Wang, B. L. Winer, K. S. Wood, T. Ylinen, and M. Ziegler. Measurement of the cosmic rayee-spectrum from 20 GeV to 1 TeV with the fermi large area telescope. *Physical Review Letters*, 102(18), May 2009. doi: 10.1103/physrevlett.102.181101. URL https://doi.org/10.1103/physrevlett.102.181101.

[37] R.A. Nymmik, M.I. Panasyuk, T.I. Pervaja, and A.A. Suslov. A model of galactic cosmic ray fluxes. *International Journal of Radiation Applications and Instrumentation. Part D. Nuclear Tracks and Radiation Measurements*, 20(3):427–429, July 1992. doi: 10.1016/1359-0189(92)90028-t. URL https://doi.org/10.1016/1359-0189(92)90028-t.

[38] E.N. Parker. The passage of energetic charged particles through interplanetary space. *Planetary and Space Science*, 13(1):9–49, January 1965. doi: 10.1016/0032-0633(65)90131-5. URL https://doi.org/10.1016/0032-0633(65)90131-5.

[39] Vanderbilt University. Creme2009. https://creme.isde.vanderbilt.edu.

[40] Ilya G. Usoskin, Agnieszka Gil, Gennady A. Kovaltsov, Alexander L. Mishev, and Vladimir V. Mikhailov. Heliospheric modulation of cosmic rays during the neutron monitor era: Calibration using PAMELA data for 2006-2010. *Journal of Geophysical Research: Space Physics*, 122(4):3875–3887, April 2017. doi: 10.1002/2016ja023819. URL https://doi.org/10.1002/2016ja023819.

[41] Patrick M. O'Neill. Badhwar-O'neill 2010 Galactic Cosmic Ray Flux Model-revised. *IEEE Transactions on Nuclear Science*, December 2010. doi: 10.1109/tns.2010.2083688. URL https://doi.org/10.1109/tns.2010.2083688.

[42] Alankrita Isha Mrigakshi, Daniel Matthiä, Thomas Berger, Günther Reitz, and Robert F. Wimmer-Schweingruber. Assessment of galactic cosmic ray models. *Journal of Geophysical Research: Space Physics*, 117(A8):n/a–n/a, August 2012. doi: 10.1029/2012ja017611. URL https://doi.org/10.1029/2012ja017611.

[43] I. The Determination of Absorbed Dose. *Journal of the International Commission on Radiation Units and Measurements*, os6(1):1–30, March 1964. doi: 10.1093/jicru/os6.1.1. URL https://doi.org/10.1093/jicru/os6.1.1.

[44] Andreo Pedro, David T Burns, Alan E Nahum, Jan Seuntjens, and Frank H Attix. *Fundamentals of Ionizing Radiation Dosimetry*. Wiley-VCH, 2014.

[45] D.J. BRENNER. Effective dose: a flawed concept that could and should be replaced. *The British Journal of Radiology*, 81(967):521–523, July 2008. doi: 10.1259/bjr/22942198. URL https://doi.org/10.1259/bjr/22942198.

[46] K.W Cho, M.C Cantone, C Kurihara-Saio, B. Le Guen, N. Martinez, D. Oughton, T. Schneider, R. Toohey, and F. ZöLzer. Ethical Foundations of the System of Radiological Protection. ICRP Publication 138. *Annals of the ICRP*, 47(1):1–65, 2018.

[47] Thomas B. Borak, Lawrence H. Heilbronn, Lawrence W. Townsend, Rafe A. McBeth, and Wouter De Wet. Quality factors for space radiation: A new approach. *Life Sciences in Space Research*, 2014. ISSN 22145532. doi: 10.1016/j.lssr.2014.02.005.

[48] Francis A. Cucinotta and Marco Durante. Cancer risk from exposure to galactic cosmic rays: implications for space exploration by human beings. *The Lancet Oncology*, 7(5): 431–435, May 2006. doi: 10.1016/s1470-2045(06)70695-7. URL https://doi.org/10.1016/s1470-2045(06)70695-7.

[49] Francis A. Cucinotta, Murat Alp, Frank M. Sulzman, and Minli Wang. Space radiation risks to the central nervous system. *Life Sciences in Space Research*, 2:54 – 69, 2014. ISSN 2214-5524.

[50] John E Baker, John E Moulder, and John W Hopewell. Radiation as a risk factor for cardiovascular disease. *Antioxidants & redox signaling*, 15(7):1945–1956, 2011.

[51] Shaowen Hu, Myung-Hee Y. Kim, Gene E. McClellan, and Francis A. Cucinotta. MODELING THE ACUTE HEALTH EFFECTS OF ASTRONAUTS FROM EXPOSURE TO LARGE SOLAR PARTICLE EVENTS. *Health Physics*, 96(4):465–476, April 2009. doi: 10.1097/01.hp.0000339020.92837.61. URL https://doi.org/10.1097/01.hp.0000339020.92837.61.

[52] R.E. Shore, H.L. Beck, J.D. Boice, E.A. Caffrey, S Davis, H.A. Grogan, F.A. Mettler, R.J. Preston, J.E. Till, R Wakeford, et al. Implications of recent epidemiologic studies for the linear nonthreshold model and radiation protection. *Journal of Radiological Protection*, 38(3):1217, 2018.

[53] M. Kroupa, T. Campbell-Ricketts, A. A. Bahadori, R. Pal Chowdhury, A. Empl, S. P. George, and T. P. O'Brien. Extravehicular electron measurement based on an intravehicular pixel detector. *Journal of Geophysical Research: Space Physics*, 124(11): 8271–8279, November 2019. doi: 10.1029/2019ja026495. URL https://doi.org/10.1029/2019ja026495.

[54] Kotaro Ozasa, Eric J Grant, and Kazunori Kodama. Japanese legacy cohorts: The life span study atomic bomb survivor cohort and survivors' offspring. *Journal*

of Epidemiology, 28(4):162–169, 2018. doi: 10.2188/jea.je20170321. URL https://doi.org/10.2188/jea.je20170321.

[55] H.M. Cullings, E.J. Grant, S.D. Egbert, T. Watanabe, T. Oda, F. Nakamura, T. Yamashita, H. Fuchi, S. Funamoto, K. Marumo, R. Sakata, Y. Kodama, K. Ozasa, and K. Kodama. DS02r1. *Health Physics*, 112(1):56–97, January 2017. doi: 10.1097/hp.0000000000000598. URL https://doi.org/10.1097/hp.0000000000000598.

[56] NRC Committee to Assess Health Risks from Exposure to Low Levels of Ionizing Radiation. Health Risks from Exposure to Low Levels of Ionizing Radiation: BEIR VII – Phase 2, 2006.

[57] D. L. Preston, E. Ron, S. Tokuoka, S. Funamoto, N. Nishi, M. Soda, K. Mabuchi, and K. Kodama. Solid cancer incidence in atomic bomb survivors: 1958–1998. *Radiation Research*, 168(1):1–64, July 2007. doi: 10.1667/rr0763.1. URL https://doi.org/10.1667/rr0763.1.

[58] United Nations and Scientific Committee. Sources and effects of ionizing radiation United Nations Scientific Committee on the Effects of Atomic Radiation, 2008.

[59] Francis A. Cucinotta, Murat Alp, Blake Rowedder, and Myung-Hee Y. Kim. Safe days in space with acceptable uncertainty from space radiation exposure. *Life Sciences in Space Research*, 5:31–38, April 2015. doi: 10.1016/j.lssr.2015.04.002. URL https://doi.org/10.1016/j.lssr.2015.04.002.

[60] Tatsuhiko Sato, Koji Niita, Norihiro Matsuda, Shintaro Hashimoto, Yosuke Iwamoto, Takuya Furuta, Shusaku Noda, Tatsuhiko Ogawa, Hiroshi Iwase, Hiroshi Nakashima, Tokio Fukahori, Keisuke Okumura, Tetsuya Kai, Satoshi Chiba, and Lembit Sihver. Overview of particle and heavy ion transport code system PHITS. *Annals of Nuclear Energy*, 82:110–115, August 2015. doi: 10.1016/j.anucene.2014.08.023. URL https://doi.org/10.1016/j.anucene.2014.08.023.

[61] Giuseppe Battistoni, Till Boehlen, Francesco Cerutti, Pik Wai Chin, Luigi Salvatore Esposito, Alberto Fassò, Alfredo Ferrari, Anton Lechner, Anton Empl, Andrea Mairani, Alessio Mereghetti, Pablo Garcia Ortega, Johannes Ranft, Stefan Roesler, Paola R. Sala, Vasilis Vlachoudis, and George Smirnov. Overview of the FLUKA code. *Annals of Nuclear Energy*, 82:10–18, August 2015. doi: 10.1016/j.anucene.2014.11.007. URL https://doi.org/10.1016/j.anucene.2014.11.007.

[62] S. Agostinelli, J. Allison, K. Amako, J. Apostolakis, H. Araujo, P. Arce, M. Asai, D. Axen, S. Banerjee, G. Barrand, F. Behner, L. Bellagamba, J. Boudreau, L. Broglia, A. Brunengo, H. Burkhardt, S. Chauvie, J. Chuma, R. Chytracek, G. Cooperman, G. Cosmo, P. Degtyarenko, A. DellAcqua, G. Depaola, D. Dietrich, R. Enami, A. Feliciello, C. Ferguson, H. Fesefeldt, G. Folger, F. Foppiano, A. Forti, S. Garelli, S. Giani, R. Giannitrapani, D. Gibin, J.J. Gómez Cadenas, I. González, G. Gracia Abril, G. Greeniaus, W. Greiner, V. Grichine, A. Grossheim, S. Guatelli, P. Gumplinger, R. Hamatsu, K. Hashimoto, H. Hasui, A. Heikkinen, A. Howard, V. Ivanchenko, A. Johnson, F.W. Jones, J. Kallenbach, N. Kanaya, M. Kawabata, Y. Kawabata, M. Kawaguti, S. Kelner, P. Kent, A. Kimura, T. Kodama, R. Kokoulin, M. Kossov, H. Kurashige, E. Lamanna, T. Lampén, V. Lara, V. Lefebure, F. Lei, M. Liendl, W. Lockman, F. Longo, S. Magni, M. Maire, E. Medernach, K. Minamimoto, P. Mora de Freitas, Y. Morita, K. Murakami, M. Nagamatu, R. Nartallo, P. Nieminen, T. Nishimura, K. Ohtsubo, M. Okamura, S. ONeale, Y. Oohata, K. Paech, J. Perl, A. Pfeiffer, M.G. Pia, F. Ranjard, A. Rybin, S. Sadilov, E. Di Salvo, G. Santin, T. Sasaki, N. Savvas, Y. Sawada, S. Scherer, S. Sei, V. Sirotenko, D. Smith, N. Starkov, H. Stoecker, J. Sulkimo, M. Takahata, S. Tanaka, E. Tcherniaev, E. Safai Tehrani, M. Tropeano, P. Truscott, H. Uno, L. Urban, P. Urban, M. Verderi, A. Walkden, W. Wander, H. Weber, J.P. Wellisch, T. Wenaus, D.C. Williams, D. Wright, T. Yamada, H. Yoshida, and D. Zschiesche. Geant4 a simulation toolkit. *Nuclear Instruments and Methods in Physics Research Section A: Accelerators, Spectrometers, Detectors and Associated Equipment*, 506(3):250–303, July 2003. doi: 10.1016/s0168-9002(03)

01368-8. URL https://doi.org/10.1016/s0168-9002(03)01368-8.

[63] C.J. Solomon F.B. Brown G.W. McKinney M.E. Rising D.A. Dixon R.L. Martz H.G. Hughes L.J. Cox A. J. Zukaitis J.C. Armstrong1 R. A. Forster L. Casswell C.J. Werner, J.S. Bull. MCNP6.2 Release Notes, Los Alamos National Laboratory, report LA-UR-18-20808 , 2018.

[64] Y. Nara, N. Otuka, A. Ohnishi, K. Niita, and S. Chiba. Relativistic nuclear collisions at 10a gev energies from p+Be to au+au with the hadronic cascade model. *Phys. Rev. C*, 61:024901, Dec 1999. doi: 10.1103/PhysRevC.61.024901. URL https://link.aps.org/doi/10.1103/PhysRevC.61.024901.

[65] A. Boudard, J. Cugnon, J.-C. David, S. Leray, and D. Mancusi. New potentialities of the liège intranuclear cascade model for reactions induced by nucleons and light charged particles. *Physical Review C*, 87(1), January 2013. doi: 10.1103/physrevc.87.014606. URL https://doi.org/10.1103/physrevc.87.014606.

[66] T. Ogawa, T. Sato, S. Hashimoto, D. Satoh, S. Tsuda, and K. Niita. Publisher's note: Energy-dependent fragmentation cross sections of relativistic ^{12}C [phys. rev. c 92, 024614 (2015)]. *Phys. Rev. C*, 92:029904, Aug 2015. doi: 10.1103/PhysRevC.92.029904. URL https://link.aps.org/doi/10.1103/PhysRevC.92.029904.

[67] T.W. Armstrong and K.C. Chandler. SPAR, a FORTRAN program for computing stopping powers and ranges for muons, charged pions, protons, and heavy ions. Technical report, May 1973. URL https://doi.org/10.2172/4477546.

[68] Tatsuhiko Sato, Koji Niita, Norihiro Matsuda, Shintaro Hashimoto, Yosuke Iwamoto, Shusaku Noda, Tatsuhiko Ogawa, Hiroshi Iwase, Hiroshi Nakashima, Tokio Fukahori, et al. Particle and heavy ion transport code system, PHITS, version 2.52. *Journal of Nuclear Science and Technology*, 50(9):913–923, 2013.

[69] Koji Niita, Yosuke Iwamoto, Tatsuhiko Sato, Hiroshi Iwase, Norihiro Matsuda, Yukio Sakamoto, and Hiroshi Nakashima. A new treatment of radiation behaviour beyond

one-body observables. In *ND2007*. EDP Sciences, 2007. doi: 10.1051/ndata:07398. URL https://doi.org/10.1051/ndata:07398.

[70] Hideo Hirayama, Yoshihito Namito, Alex F. Bielajew, Scott J. Wilderman, Michigan U., and Walter R. Nelson. The EGS5 code system. Technical report, December 2005. URL https://doi.org/10.2172/877459.

[71] W R Phillips. Heavy-ion transfer reactions. *Reports on Progress in Physics*, 40(4): 345–407, April 1977. doi: 10.1088/0034-4885/40/4/001. URL https://doi.org/10.1088/0034-4885/40/4/001.

[72] ON THE ENERGY LOSS OF FAST PARTICLES BY IONISATION. In *Collected Papers of L.D. Landau*, pages 417–424. Elsevier, 1965. doi: 10.1016/b978-0-08-010586-4.50061-4. URL https://doi.org/10.1016/b978-0-08-010586-4.50061-4.

[73] P V VAVILOV. Ionization losses of high-energy heavy particles. *Exptl. Theoret. Phys*, 5(4):920–923, November 1957.

[74] J.W. Wilson, L.W. Townsend, J.E. Nealy, S.Y. Chun, B.S. Hong, W.W. Buck, S.L. Lamkin, B.D. Ganapol, F Khan, and F.A. Cucinotta. BRYNTRN : A Baryon Transport Model. Technical Report NASA/TP- 2887, 1989.

[75] Tony Slaba, Steve Blattnig, F. Badavi, Ryan Norman, A. Adamczyk, L. Townsend, Indi Sriprisan, and J. Norbury. HZETRN2010 - a space radiation analysis tool for research and engineering applications (invited). *AGU Fall Meeting Abstracts*, 12 2010.

[76] John W. Wilson, Lawrence W. Townsend, Walter Schimmerling, Govind S. Khandelwal, Ferdous Khan, John E. Nealy, Francis A. Cucinotta, and John W. Norbury. Transport Methods and Interactions for Space Radiations. Technical Report NASA/TP 1257, NASA Langley Research Center, Hampton, Virginia, 1991.

[77] John W. Wilson, Tony C. Slaba, Francis F. Badavi, Brandon D. Reddell, and Amir A. Bahadori. Advances in NASA radiation transport research: 3dhzetrn. *Life Sciences*

in Space Research, 2:6–22, July 2014. doi: 10.1016/j.lssr.2014.05.003. URL https://doi.org/10.1016/j.lssr.2014.05.003.

[78] Tony C. Slaba, Steve R. Blattnig, Brandon Reddell, Amir Bahadori, Ryan B. Norman, and Francis F. Badavi. Pion and electromagnetic contribution to dose: Comparisons of HZETRN to monte carlo results and ISS data. *Advances in Space Research*, 52(1): 62–78, July 2013. doi: 10.1016/j.asr.2013.02.015. URL https://doi.org/10.1016/j.asr.2013.02.015.

[79] D. Fry, M. Lund, A. A. Bahadori, R. Pal. Chowdhury, L. Stegeman, and S. Madzunkov. Active shielding particle pusher(aspp): Charged-particle tracking through electromagnetic fields. Technical Report NASA/TP–2020–20205002408, NASA, 2020.

[80] Loup Verlet. Computer "Experiments" on Classical Fluids. I. Thermodynamical Properties of Lennard-Jones Molecules. *Phys. Rev.*, 159:98–103, Jul (1967). doi: 10.1103/PhysRev.159.98. URL https://link.aps.org/doi/10.1103/PhysRev.159.98.

[81] Seiji Zenitani and Takayuki Umeda. On the boris solver in particle-in-cell simulation. *Physics of Plasmas*, 25(11):112110, November 2018. doi: 10.1063/1.5051077. URL https://doi.org/10.1063/1.5051077.

[82] Evaluating Shielding Approaches to Reduce Space Radiation Cancer Risks . NASA TM-2012-217361, National Aeronautics and Space Administration, Washington, DC, 2012.

[83] Tony C. Slaba, Amir A. Bahadori, Brandon D. Reddell, Robert C. Singleterry, Martha S. Clowdsley, and Steve R. Blattnig. Optimal shielding thickness for galactic cosmic ray environments. *Life Sciences in Space Research*, 12:1–15, February 2017. doi: 10.1016/j.lssr.2016.12.003. URL https://doi.org/10.1016/j.lssr.2016.12.003.

[84] Richard H. Levy. RADIATION SHIELDING OF SPACE VEHICLES BY MEANS OF SUPERCONDUCTING COILS. In *Design and Reliability, and Invited Addresses*,

pages 119–155. Elsevier, 1961. doi: 10.1016/b978-1-4832-2899-0.50011-1. URL https://doi.org/10.1016/b978-1-4832-2899-0.50011-1.

[85] Richard H. Levy and G. Sargent Janes. Plasma radiation shielding. *AIAA Journal*, 2(10):1835–1838, October 1964. doi: 10.2514/3.2683. URL https://doi.org/10.2514/3.2683.

[86] Richard H. Levy and Francis W. French. Plasma radiation shield - concept and applications to space vehicles. *Journal of Spacecraft and Rockets*, 5(5):570–577, May 1968. doi: 10.2514/3.29306. URL https://doi.org/10.2514/3.29306.

[87] P. Spillantini, M. Casolino, M. Durante, R. Mueller-Mellin, G. Reitz, L. Rossi, V. Shurshakov, and M. Sorbi. Shielding from cosmic radiation for interplanetary missions: Active and passive methods. *Radiation Measurements*, 42(1):14–23, January 2007. doi: 10.1016/j.radmeas.2006.04.028. URL https://doi.org/10.1016/j.radmeas.2006.04.028.

[88] J. Hoffman, P. Fisher, and O. Batischev. Use of Superconducting Magnet Technology for Astronaut Radiation Protection. NIAC Phase I Contract CP04-01, National Aeronautics and Space Administration, Cambridge, MA, 2015.

[89] Changran Geng, Xiaobin Tang, Chunhui Gong, Fada Guan, Jesse Johns, Diyun Shu, and Da Chen. A monte carlo-based radiation safety assessment for astronauts in an environment with confined magnetic field shielding. *Journal of Radiological Protection*, 35(4):777–788, oct 2015. doi: 10.1088/0952-4746/35/4/777. URL https://doi.org/10.1088%2F0952-4746%2F35%2F4%2F777.

[90] Piero Spillantini. Active shielding for long duration interplanetary manned missions. *Advances in Space Research*, 45(7):900–916, April 2010. doi: 10.1016/j.asr.2010.01.025. URL https://doi.org/10.1016/j.asr.2010.01.025.

[91] L.W Townsend. Overview of Active Methods for Shielding Spacecraft from Energetic Space Radiation. *Physica medica : PM : an international journal devoted to the appli-*

cations of physics to medicine and biology : official journal of the Italian Association of Biomedical Physics (AIFB), 2001. ISSN 1120-1797.

[92] L Gargaté, R Bingham, R A Fonseca, R Bamford, A Thornton, K Gibson, J Bradford, and L O Silva. Hybrid simulations of mini-magnetospheres in the laboratory. 50(7): 074017, June 2008. doi: 10.1088/0741-3335/50/7/074017. URL https://doi.org/10.1088/0741-3335/50/7/074017.

[93] R.A. Bamford, B. Kellett, J. Bradford, T.N. Todd, M.G. Benton, R. Stafford-Allen, E.P. Alves, L. Silva, C. Collingwood, I.A. Crawford, and R. Bingham. An exploration of the effectiveness of artificial mini-magnetospheres as a potential solar storm shelter for long term human space missions. 105(2):385–394, December 2014. doi: 10.1016/j.actaastro.2014.10.012. URL https://doi.org/10.1016/j.actaastro.2014.10.012.

[94] F. H. Vogler. Analysis of an Electrostatic Shield for Space Vehicles. *AIAA Journal*, 2(5):872–878, may 1964. doi: 10.2514/3.2451. URL https://doi.org/10.2514/3.2451.

[95] Warren Frisina. Optimizing electrostatic radiation shielding for manned space vehicles. *Acta Astronautica*, 12(12):995–1003, December 1985. doi: 10.1016/0094-5765(85)90028-1. URL https://doi.org/10.1016/0094-5765(85)90028-1.

[96] R.K. Tripathi, J.W. Wilson, and R.C. Youngquist. Electrostatic Active Radiation Shielding - Revisited. *Aerospace Conference, IEEE*, (2006). ISSN 1095323X. doi: 10.1109/AERO.2006.1655760.

[97] R.P. Joshi, H. Qiu, and R.K. Tripathi. Configuration Studies for Active Electrostatic Space Radiation Shielding. *Acta Astronautica*, 88:138–145, Jul (2013). doi: 10.1016/j.actaastro.2013.03.011. URL https://doi.org/10.1016/j.actaastro.2013.03.011.

[98] ICNIRP STATEMENT ON THE "GUIDELINES FOR LIMITING EXPOSURE TO TIME-VARYING ELECTRIC, MAGNETIC, AND ELECTROMAGNETIC FIELDS

(UP TO 300 GHz)". *Health Physics*, 97(3):257–258, September 2009. doi: 10.1097/hp.0b013e3181aff9db. URL https://doi.org/10.1097/hp.0b013e3181aff9db.

[99] Loyd S Swenson Jr, James M Grimwood, and Charles C Alexander. This New Ocean: A History of Project Mercury. Technical Report SP-4201, NASA, 1998.

[100] NAS/NRC. National Academy of Sciences/National Research Council, Radiobiological Factors in Manned Space Flight, Report of a Panel of the Space Science Board, 1967.

[101] NCRP. National Council on Radiation Protection and Measurements, Guidance on Radiation Received in Space Activities, NCRP Report No. 98, National Council on Radiation Protection and Measurements , 1989.

[102] NCRP. National Council on Radiation Protection and Measurements, Radiation Protection Guidance for Activities in Low-Earth Orbit, NCRP Report No. 132, National Council on Radiation Protection and Measurements, 2000.

[103] Institute of Medicine. Health Standards for Long Duration and Exploration Spaceflight: Ethics Principles, Responsibilities, and Decision Framework, 2014.

[104] US Nuclear Regulatory Commission. 10CFR19: Notices, instructions, and reports to workers: Inspection and investigations, 1995.

[105] Paul A. Locke and Michael M. Weil. Personalized cancer risk assessments for space radiation exposures. *Frontiers in Oncology*, 6, February 2016. doi: 10.3389/fonc.2016.00038. URL https://doi.org/10.3389/fonc.2016.00038.

[106] NASA. NPR 8900.1B NASA Health and Medical Requirements for Human Space Exploration. *NASA Procedural Requirement*, 2016.

[107] NAS/NRC. National Academy of Sciences/National Research Council, Radiation Protection Guides and Constraints for Space Mission and Vehicle-Design Involving Nuclear Systems, Radiobiological Advisory Panel, Committee on Space Medicine, 1970.

[108] Douglas A. Reynolds, Thomas F. Quatieri, and Robert B. Dunn. Speaker verification using adapted gaussian mixture models. *Digital Signal Processing*, 10(1-3):19–41, January 2000. doi: 10.1006/dspr.1999.0361. URL https://doi.org/10.1006/dspr.1999.0361.

[109] B. W. Silverman. Density Estimation: For Statistics and Data Analysis, 2018.

[110] Serkan Golge. MeRiT: Multi-environment cancer Risk analysis Tool. Technical Report SRAG-INT-PHOG-2015-005, NASA JSC SRAG, 2016.

[111] Donald M. Sawyer and James I. Vette. AP-8 trapped proton environment for solar maximum and solar minimum. *NASA STI/Recon Technical Report N*, 77, 1976.

[112] T.P. O'Brien, W.R. Johnston, S.L. Huston, C.J. Roth, T.B. Guild, Y-J Su, and R.A. Quinn. Changes in AE9/AP9-Irene version 1.5. *IEEE Transactions on Nuclear Science*, 65(1):462–466, 2017.

[113] Robert Kramer, HJ Khoury, JW Vieira, and VJM Lima. MAX06 and FAX06: update of two adult human phantoms for radiation protection dosimetry. *Physics in Medicine & Biology*, 51(14):3331, 2006.

[114] T.C. Slaba, G.D. Qualls, M.S. Clowdsley, S.R. Blattnig, L.C. Simonsen, S.A. Walker, and R.C. Singleterry. Analysis of mass averaged tissue doses in CAM, CAF, MAX, and FAX. Technical Report TP-2009-215562, NASA, 2009.

[115] D. Fry, S. Madzunkov, J. Simcic, and A. W. Hunt. Application of scaling methods to foster ground development of active shielding concepts for space exploration. *submitted to Acta Astronautica*, 2020.

[116] J. Canny. A computational approach to edge detection. *IEEE Trans. Pattern Anal. Mach. Intell.*, 8(6):679–698, June 1986. ISSN 0162-8828. doi: 10.1109/TPAMI.1986.4767851. URL https://doi.org/10.1109/TPAMI.1986.4767851.

[117] B. M. Adams, M. S. Ebeida, M. S. Eldred, J. D. Jakeman, L. P. Swiler, J. A. Stephens, D. M. Vigil, T. M. Wildey, W. J. Bohnhoff, K. R. Dalbey, J. P. Eddy, K. T. Hu, L. E. Bauman, and P. D. Hough. Dakota, A Multilevel Parallel Object-Oriented Framework for Design Optimization, Parameter Estimation, Uncertainty Quantification, and Sensitivity Analysis: Version 6.2 User's Manual. *Sandia Technical Report SAND2014-4633*, (July), 2014. URL https://dakota.sandia.gov/sites/default/files/docs/6.2/Users-6.2.0.pdf.

[118] R.K. Tripathi, J.W. Wilson, and R.C. Youngquist. Electrostatic Space Radiation Shielding. *Advances in Space Research*, (2008). ISSN 02731177. doi: 10.1016/j.asr.2007.09.015.

[119] Leslie Glasser and A G. Every. Energies and Spacings of Point Charges on a Sphere. *Journal of Physics A-Mathematical and General*, 25:2473–2482, May (1992). doi: 10.1088/0305-4470/25/9/020.

[120] Jonathan Swinton and Erinma Ochu and. Novel Fibonacci and non-Fibonacci structure in the sunflower: results of a citizen science experiment. *Royal Society Open Science*, 3(5):160091, May 2016. doi: 10.1098/rsos.160091. URL https://doi.org/10.1098/rsos.160091.

[121] Orion Ciftja. Electric potential of a uniformly charged square on its plane. *European Journal of Physics*, 32(6):L55–L57, October 2011. doi: 10.1088/0143-0807/32/6/l06. URL https://doi.org/10.1088/0143-0807/32/6/l06.

[122] Guido Van Rossum and Fred L Drake Jr. *Python tutorial*. Centrum voor Wiskunde en Informatica Amsterdam, The Netherlands, 1995.

[123] ICRP. Adult reference computational phantoms. ICRP Publication 110. *Annals of the ICRP*, 39(2), 2009.

[124] Tatsuhiko Sato, Yosuke Iwamoto, Shintaro Hashimoto, Tatsuhiko Ogawa, Takuya Furuta, Shin ichiro Abe, Takeshi Kai, Pi-En Tsai, Norihiro Matsuda, Hiroshi Iwase,

Nobuhiro Shigyo, Lembit Sihver, and Koji Niita. Features of particle and heavy ion transport code system (PHITS) version 3.02. *Journal of Nuclear Science and Technology*, 55(6):684–690, January 2018. doi: 10.1080/00223131.2017.1419890. URL https://doi.org/10.1080/00223131.2017.1419890.

[125] Tatsuhiko Sato, Akira Endo, Maria Zankl, Nina Petoussi-Henss, and Koji Niita. Fluence-to-dose conversion coefficients for neutrons and protons calculated using the PHITS code and ICRP/ICRU adult reference computational phantoms. *Physics in Medicine and Biology*, 54(7):1997–2014, March 2009. doi: 10.1088/0031-9155/54/7/009. URL https://doi.org/10.1088/0031-9155/54/7/009.

[126] Tatsuhiko Sato, Akira Endo, and Koji Niita. Fluence-to-dose conversion coefficients for heavy ions calculated using the PHITS code and the ICRP/ICRU adult reference computational phantoms. *Physics in Medicine and Biology*, 55(8):2235–2246, March 2010. doi: 10.1088/0031-9155/55/8/008. URL https://doi.org/10.1088/0031-9155/55/8/008.

[127] Francis A. Cucinotta, Khiet To, and Eliedonna Cacao. Predictions of space radiation fatality risk for exploration missions. *Life Sciences in Space Research*, 13:1–11, May 2017. doi: 10.1016/j.lssr.2017.01.005. URL https://doi.org/10.1016/j.lssr.2017.01.005.